

University of Nottingham
School of Mechanical, Materials, Manufacturing
Engineering and Management

**Finite Element Analysis of Glass Fibre Reinforced
Thermoplastic Composites for
Structural Automotive Components**

Martin J Wilson
MEng (Hons)

Thesis submitted to the University of Nottingham
for the degree of Doctor of Philosophy
September 2003

Contents

Abstract	vii
Acknowledgements	viii
Glossary	ix
Nomenclature	xi

Chapter 1 Introduction

1.1 Fibre Reinforced Thermoplastic Composites	1-1
1.2 Application of Thermoplastic Composites to Automotive Structures	1-1
1.3 Modelling Damage Development in Thermoplastic Composites	1-4
1.4 Theme of this Research	1-5

Chapter 2 Literature Review

2.1 Introduction	2-1
2.2 Manufacture and Testing of Commingled Thermoplastic Composites	2-1
2.2.1 Processing Commingled Thermoplastic Composites	2-1
2.2.2 Characterisation and Mechanical Testing of Composites	2-4
2.3 Crashworthy Applications of Composite Materials	2-5
2.3.1 Energy Absorption Mechanisms in Composite Materials	2-5
2.3.2 Automotive Applications for Structural Composite Materials	2-7
2.3.3 Composite Materials for Side Impact Protection	2-9
2.4 Damage Modelling Techniques	2-13
2.4.1 General Macroscopic Progressive Damage Models	2-14
2.4.2 Chang Model	2-17
2.4.3 Ladeveze Model	2-19
2.4.4 PAM-CRASH Bi-Phase Model	2-22
2.5 Assessment of Complex Composite Geometries Using Finite Element Damage Models	2-23
2.6 Conclusion	2-25
2.7 Tables	2-28
2.8 Figures	2-30

Chapter 3 Experimental Methods

3.1	Introduction	3-1
3.2	Material Form	3-1
3.3	Compression Moulding Commingled Thermoplastic Composites	3-1
3.3.1	Tooling Concept	3-2
3.4	Material Model Calibration Data	3-2
3.4.1	0°/90° Tensile Test	3-3
3.4.2	0°/90° Compressive Test	3-4
3.4.3	+45°/-45° Tensile Test	3-4
3.5	Coupon Tests for Model Validation	3-4
3.5.1	+45°/-45° Compressive Test	3-5
3.5.2	0°/90° Tensile Hole in Plate Test	3-5
3.5.3	+45°/-45° Tensile Hole in Plate Test	3-6
3.5.4	+45°/-45° Compressive Hole in Plate Test	3-6
3.6	Conclusion	3-7
3.7	Tables	3-8
3.8	Figures	3-10

Chapter 4 Implicit Finite Element Damage Modelling

4.1	Introduction	4-1
4.2	Analysis Technique	4-2
4.2.1	Finite Element Code	4-2
4.2.2	Material Model	4-3
4.2.3	Element Definition and Formulation	4-3
4.2.4	Section Definition	4-4
4.2.5	Definition of Orthotropy Direction	4-4
4.3	Development of the Damage Model	4-5
4.3.1	Tensile Failure Model	4-5
4.3.2	Compressive Failure Model	4-6
4.3.3	Shear Damage and Failure Model	4-7
4.3.4	Implementation	4-7

4.4	Calibration	4-8
4.4.1	Simulation of Calibration Coupon Tests	4-8
4.4.2	Tensile 0°/90° Test Simulation	4-9
4.4.3	Compressive 0°/90° Test Simulation	4-10
4.4.4	Tensile +45°/-45° Test Simulation	4-10
4.5	Validation	4-11
4.5.1	Compressive +45°/-45° Test Simulation	4-11
4.5.2	Tensile 0°/90° Hole in Plate Test Simulation	4-12
4.5.3	Tensile +45°/-45° Hole in Plate Test Simulation	4-13
4.5.4	Compressive +45°/-45° Hole in Plate Test Simulation	4-13
4.6	Model Sensitivity	4-14
4.6.1	Sensitivity to Analysis Step	4-15
4.6.2	Sensitivity to Shear Non-Linearity Parameter	4-15
4.6.3	Sensitivity to Calibration of Damaged Shear Modulus	4-16
4.6.4	Sensitivity to Element Formulation	4-16
4.6.5	Sensitivity to Mesh Refinement	4-18
4.7	Conclusion	4-19
4.8	Figures	4-21

Chapter 5 Explicit Finite Element Modelling

5.1	Introduction	5-1
5.2	Analysis Technique	5-1
5.2.1	Finite Element Code	5-1
5.2.2	Material Model	5-2
5.2.3	Element Definition and Formulation	5-2
5.2.4	Section Definition	5-3
5.2.5	Definition of Orthotropy Direction	5-3
5.3	Bi-Phase Damage Model	5-3
5.3.1	Degenerate Bi-Phase Damage Model	5-3

5.4	Calibration	5-4
5.4.1	Calibration of Composite Material Elastic Constants	5-5
5.4.2	Calibration of Composite Material Damage Parameters	5-5
5.4.3	Simulation of Calibration Coupon Tests	5-6
5.4.4	Tensile 0°/90° Test Simulation	5-6
5.4.5	Compressive 0°/90° Test Simulation	5-7
5.4.6	Tensile +45°/-45° Test Simulation	5-8
5.5	Validation	5-8
5.5.1	Compressive +45°/-45° Test Simulation	5-8
5.5.2	Tensile 0°/90° Hole in Plate Test Simulation	5-9
5.5.3	Tensile +45°/-45° Hole in Plate Test Simulation	5-10
5.5.4	Compressive +45°/-45° Hole in Plate Test Simulation	5-11
5.6	Model Sensitivity	5-11
5.6.1	Sensitivity to Damage Model Parameters	5-12
5.6.2	Sensitivity to Mesh Refinement	5-12
5.7	Conclusion	5-13
5.8	Tables	5-14
5.9	Figures	5-15

Chapter 6 Application to an Automotive Demonstrator Component

6.1	Introduction	6-1
6.2	Side Intrusion Beam Test Methods	6-2
6.2.1	Small-Scale 3-Point Flexure Test	6-2
6.2.2	Large-Scale 3-Point Flexure Test	6-3
6.2.3	FMVSS214 Side Intrusion Test	6-3
6.3	Phase 1 Demonstrator Component	6-4
6.3.1	Phase 1 Demonstrator Component Design	6-4
6.3.2	Phase 1 Demonstrator Component Manufacture	6-5
6.3.3	Phase 1 Demonstrator Component Small-Scale 3-Point Flexure Test	6-5
6.3.4	Phase 1 Demonstrator Component Large-Scale 3-Point Flexure Test	6-6
6.3.5	Phase 1 Demonstrator Implicit Finite Element Damage Modelling	6-8
6.3.6	Phase 1 Demonstrator Explicit Finite Element Damage Modelling	6-10

6.4	Phase 2 Demonstrator Component	6-12
6.4.1	Phase 2 Demonstrator Component Design	6-12
6.4.2	Phase 2 Demonstrator Component Manufacture	6-13
6.4.3	Phase 2 Demonstrator Component Large-Scale 3-Point Flexure Test	6-14
6.4.4	Phase 2 Demonstrator Implicit Finite Element Damage Modelling	6-16
6.4.5	Phase 2 Demonstrator Explicit Finite Element Damage Modelling	6-18
6.5	Vehicle Testing	6-21
6.5.1	Installation of Beam in Target Vehicle	6-21
6.5.2	FMVSS 214 Vehicle Test	6-21
6.6	Conclusion	6-22
6.7	Tables	6-24
6.8	Figures	6-25

Chapter 7 Discussion and Conclusions

7.1	Introduction	7-1
7.2	Coupon Test Methods for Calibration and Validation of Finite Element Damage Models	7-2
7.2.1	Quantity of Specimens Tested and Scatter of Results	7-2
7.2.2	Strain Measurement Techniques	7-3
7.2.3	Shear Behaviour During Off Axis Tests	7-3
7.2.4	Out of Plane Deformation During Compressive Test	7-4
7.2.5	Damage Development in Hole in Plate Specimens	7-4
7.3	Implicit Finite Element Damage Modelling	7-5
7.3.1	The Treatment of Fibre Direction and Shear Damage	7-5
7.3.2	Accuracy of Fibre Direction Damaging Behaviour	7-6
7.3.3	Accuracy of Shear Damaging Behaviour	7-6
7.3.4	Application of the Implicit Damage Model to a Complex Component	7-7
7.3.5	Suitability of the Implicit Finite Element Method for Large Displacements	7-8

7.4	Explicit Finite Element Damage Modelling	7-9
7.4.1	The Treatment of Fibre Direction and Shear Damage	7-9
7.4.2	Accuracy of Fibre Direction Damaging Behaviour	7-9
7.4.3	Accuracy of Shear Damaging Behaviour	7-10
7.4.4	Sensitivity to Calibration Parameters	7-11
7.4.5	Application of the Explicit Damage Model to a Complex Component	7-11
7.4.6	Applicability of Damage Model to Thermoplastics	7-12
7.4.7	Suitability of the Explicit Finite Element Method for Large Displacements	7-13
7.5	Application of Thermoplastic Composites to Crashworthy Automotive Structures	7-13
7.5.1	Industrial Processing Techniques for Thermoplastic Composite	7-14
7.5.2	The Effect of Process Variability	7-15
7.5.3	The Need for Part Integration	7-15
7.6	Recommendations for Future Work	7-16
7.6.1	Inclusion of Residual Load Carrying Capacity in the Implicit Model	7-16
7.6.2	Implementation of the Implicit Damage Model in an Explicit Code	7-16
7.6.3	Assessment of Alternative Damage Models	7-17
7.6.4	Assessment of Relevance of Delamination as a Damage Mechanism	7-17
7.6.5	Rate Dependency	7-17
7.6.6	Development of a Fully Thermoplastic Door Concept	7-17
7.7	Conclusions	7-18

Chapter 8 References

Appendices

Appendix A	ABAQUS/Standard User Defined Field	A-1
Appendix B	Derivation of Shear Damage Formulation	A-3
Appendix C	ABAQUS/Standard Material Cards	A-6
Appendix D	PAM-CRASH Material Cards	A-7
Appendix E	CRACKTAC Project Publications	A-8

Abstract

This thesis describes the investigation and development of damage modelling techniques for woven long glass fibre reinforced polypropylene matrix composites. The objective of the work was to develop and validate predictive models for the intralaminar damage behaviour of these materials, with the aim of applying the results to an industrial demonstrator component.

Two damage modelling methods were investigated. The first, based on ply-level failure criteria and implemented in an implicit finite element code, was developed and validated using a range of coupon tests for a balanced weave 60% weight fraction commingled glass/polypropylene composite. The second method utilised a model previously implemented in the commercial explicit finite element code, PAM-CRASH. This model was calibrated and validated using the same coupon tests as the first model.

The models were subsequently used to simulate an industrial demonstrator component, during a two-phase design and development programme. The demonstrator, an automotive side intrusion beam, was designed and predictively modelled using the two damage modelling techniques investigated.

Finally, the composite component was compared to a steel side intrusion beam, using a quasi-static vehicle test to a current legislative standard. This test showed comparable performance in terms of strength and stiffness for the two beams.

It was concluded that the implicit finite element damage modelling technique can account for the damage and failure modes observed in a woven glass fibre reinforced polypropylene composite, but is limited when considering high levels of material non-linearity and damage development, due to the stability of the implicit finite element method. It was also concluded that the explicit finite element technique was more suited to the simulation of damage development in thermoplastic matrix composite components, although the research showed that the model investigated was limited when considering shear damaging behaviour in a woven fibre reinforced composite.

Acknowledgements

The author would like to thank the supervisors of this work, Dr N. A. Warrior, Dr R. Brooks and Professor C. D. Rudd, for their guidance.

The research was jointly funded by the EPSRC, the University of Nottingham and the CRACTAC project consortium, including: Ford Motor Company, Jaguar Cars, BMW, Borealis, DOW Automotive, ESI Group, Magna, Mapleline, MIRA, Polynorm Plastics, Park Hill Textiles, SCL, Saint-Gobain Vetrotex and Symalit.

The School of Mechanical, Materials, Manufacturing Engineering and Management is thanked for the use of departmental facilities and the support of the technical staff, including Roger Smith, Paul Johns and Dave Smith is acknowledged.

Thanks also go to the other members of the Polymer Composites Research Group, particularly Nuno Lourenço, Dan Bailey, Chris Curtis, Ed Cooper, Richard Fernie, Craig Wilks and Carlo Santulli, for their invaluable advice and assistance.

Finally, thank you to my friends and family who have supported and encouraged me throughout this work, my trusty Ford Capri Calypso for reliably getting me to the office every day and Sallyanne for her belief in me and her love.

Glossary

1:1 weave	Weave pattern with equal number of reinforcing fibres in the two principal directions
3D fabric	1:1 weave fabric with 1% z-axis fibres
4:1 weave	Weave pattern with twice the number of reinforcing fibres in one of the two principal directions in-plane
ABAQUS/Standard	Commercial implicit finite element code
Blank	Piece of preconsolidated commingled composite cut to size prior to heating and moulding
CAD	Computer aided design
Commingled	Intimately combined polymer and reinforcement fibres
CRACKTAC	Crashworthy Automotive Components Using Thermoplastic Composites - Research Programme
Door cassette	Automotive module used to mount door hardware
FEA	Finite element analysis
FORTRAN	Computer programming language
FV	Field variable used in implicit damage model
GMT	Glass mat thermoplastic
Interlaminar	Between plies
Intralaminar	Within a ply
Isothermal moulding	Moulding process where consolidation occurs in a hot tool - at or above the matrix melt temperature
Lay-up	Combination of plies stacked to form a laminate
Non-isothermal moulding	Moulding process where consolidation occurs in a cool tool - below the matrix melt temperature
PAM-CRASH	Commercial explicit finite element code
PEEK	Polyetherether-ketone
Ply	Single layer of a laminate
PP	Polypropylene

Preconsolidated	Commingled fabric that has been partially consolidated to improve moulding and ease of handling
RTM	Resin transfer moulding
SMC	Sheet moulding compound
StaMax	Glass reinforced polypropylene injection moulding material
Thermoplastic	Polymer softened by heating and hardened by cooling in a reversible process
Thermoset	Polymer hardened by irreversible chemical change
Tow	Bundle of fibres
TowFlex	Powder impregnated reinforced thermoplastic composite
Twintex	Commingled glass reinforced thermoplastic composite
UD	Unidirectional
VF	Volume fraction
WF	Weight fraction

Nomenclature

ABAQUS/Standard model parameters

E_{11}	Young's Modulus in first in-plane principal fibre direction
E_{22}	Young's Modulus in second in-plane principal fibre direction
ν	Poisson's Ratio in-plane
G_{12}	Shear modulus in-plane
G_{13}	Shear modulus through thickness
G_{23}	Shear modulus through thickness
σ_{T1U}	Ultimate tensile strength in first in-plane principal fibre direction
σ_{T2U}	Ultimate tensile strength in second in-plane principal fibre direction
σ_{C1U}	Ultimate compressive strength in first in-plane principal fibre direction
σ_{C2U}	Ultimate compressive strength in second in-plane principal fibre direction
α	Shear damage nonlinearity parameter
d_s	Shear damage level
σ_{12}	In-plane shear stress
ϵ_{12}	In-plane shear strain
ϵ_{12U}	Ultimate in-plane shear strain
E_{11F}	Failed Young's Modulus in first in-plane principal fibre direction
E_{22F}	Failed Young's Modulus in second in-plane principal fibre direction
ν_F	Failed Poisson's Ratio in-plane
G_{12D}	Fully damaged shear modulus in-plane
G_{12F}	Failed shear modulus in-plane

PAM-CRASH bi-phase model parameters

E_{11T}	Tensile Young's Modulus in first in-plane principal fibre direction
E_{11C}	Compressive Young's Modulus in first in-plane principal fibre direction
E_{22T}	Tensile Young's Modulus in second in-plane principal fibre direction
E_{22C}	Compressive Young's Modulus in second in-plane principal fibre direction
E_{33T}	Tensile Young's Modulus through thickness
E_{33C}	Compressive Young's Modulus through thickness
ν_{12}	Poisson's Ratio in-plane

ν_{13}	Poisson's Ratio through thickness
ν_{23}	Poisson's Ratio through thickness
G_{12}	Shear modulus in-plane
G_{13}	Shear modulus through thickness
G_{23}	Shear modulus through thickness
ϵ_{iT}	Tensile initial damage strain
ϵ_{iT}	Tensile intermediate damage strain
ϵ_{uT}	Tensile ultimate damage strain
d_{iT}	Tensile intermediate damage magnitude
d_{uT}	Tensile ultimate damage magnitude
ϵ_{iC}	Compressive initial damage strain
ϵ_{iC}	Compressive intermediate damage strain
ϵ_{uC}	Compressive ultimate damage strain
d_{iC}	Compressive intermediate damage magnitude
d_{uC}	Compressive ultimate damage magnitude

[] Numbers in square parenthesis refer to References in Chapter 8

[°] Angles (in degrees) in square parenthesis refer to laminate lay-up

Chapter 1 Introduction

1.1 Fibre Reinforced Thermoplastic Composites

Composites combine high strength fibres and lightweight matrices, creating materials with high specific properties. Through careful selection of fibre length, material and architecture and the matrix polymer, it is possible to create an extensive range of engineering materials.

Applications for these materials are varied and wide ranging, from short fibre reinforced injection moulded thermoplastics for high volume manufacturing, through to high performance aligned long fibre composites for more demanding applications. There is a broad range of commercially available resin systems, fibres and pre-impregnated composite materials. Each offers a different level of mechanical performance, surface finish, recyclability, formability and cost.

Thermoplastic matrix based composites have become popular for large volume production of components and structures, as they offer a number of advantages over thermosetting composites. They are tough, can be formed or moulded quickly through the application of heat, they can be recycled easily and produce very little waste during manufacture. These factors combine to make them appeal strongly to medium to high volume automotive manufacturers.

1.2 Application of Thermoplastic Composites to Automotive Structures

Legislation is constantly demanding improvements to every aspect of new passenger vehicles. This legislation can be simplified into two key requirements. Firstly, cars must be more environmentally friendly in terms of both fuel efficiency and recyclability and secondly, they must be safer, offering more protection to both passengers and pedestrians in the event of an accident. Composites materials can offer solutions to both these problems.

Increased efficiency is achievable through weight saving since up to 40% of fuel consumption can be attributed to inertia due to the mass of the vehicle, particularly

when looking at the urban test cycle [1]. Significant weight reduction, especially in the body in white, can be achieved by novel design and the use of composites with higher specific properties than traditional materials such as steel and aluminium.

Recyclability of thermoplastic matrix based composites is also good, components can be melted to separate the polymer matrix from fibres or the whole composite can be chopped to produce pelletised materials suitable for injection moulding.

Safety and in particular crashworthiness can also be significantly improved by the use of composites. Metallic crash structures absorb energy during an impact primarily through plastic deformation. Composites have the potential to absorb considerably larger amounts of energy [2] due to damage modes, including matrix deformation, delamination, local cracking and crushing. The specific energy absorption of composites has been well documented and shown to offer substantial performance improvements.

The final requirement and probably the most important to manufacturers in today's highly competitive passenger vehicle sector is cost. A recent survey by DuPont Automotive, of automotive design engineers, showed that 50% rated cost as the number one challenge when designing a new vehicle [3]. This means that as well as cheap raw materials, cost effective design and manufacturing routes are also required.

Low cost engineering fibres preimpregnated with bulk thermoplastic matrices lend themselves to forming routes such as non-isothermal stamping or flow moulding. These materials offer a relatively cheap raw material combined with the rapid manufacturing technology required by the high volume automotive sector.

Random long glass fibre reinforced polypropylene Glass Mat Thermoplastic (GMT), is already used widely by the automotive industry for numerous semi-structural applications. In the year 2000, 37,000 tonnes of GMT were used in the manufacture of European automotive components, with a further 19,000 tonnes being used in Asia and the USA. Current production applications include a number of noise shields and front end structures, as well as the Mercedes A Class rear hatch and double floor structure, the Volvo 850 rear seat structure and Volvo truck dashboards [4]. Currently

though, the properties of polypropylene based GMT products preclude them from being used in fully crashworthy structures.

To produce automotive crash structures with a polypropylene matrix based composite an aligned or woven fibre composite is required. One such, commercially available, material is Twintex, a commingled thermoplastic composite produced by Saint-Gobain Vetrotex. Twintex is available in a number of forms, including various woven commingled fabrics and preconsolidated sheets. Although much stronger and stiffer than GMT, Twintex has only found limited use in the automotive sector. Examples of current applications are rear load floor structures produced by Nissan, off-road vehicle skid plates by General Motors and a number of truck load area liners and HGV trailer panels [5]. These structures are still not fully crashworthy applications and offer little or no contribution towards collision energy absorption in impact situations; they are being used simply as tough and lightweight semi-structural and low energy impact protection components.

A key issue facing engineers trying to use these materials is that the forming process and geometries that can be created using a woven composite are limited when compared to a flow material such as GMT, which impacts on the cost effectiveness of using such fabrics. Often to overcome this problem, woven materials are co-moulded with flow materials to create a structure with complex geometry and improved structural performance. An example of a production application is Peugeot's 806, glass reinforced polypropylene, bumper structure, which uses GMT co-moulded with Twintex to significantly increase the flexural stiffness and strength of the part [5].

To fully exploit the crashworthy potential of aligned fibre thermoplastic composite materials for high volume automotive applications they first need to be shown to offer one or more advantages over steel or aluminium. The proven ability to mould complex shapes using co-moulded GMT should allow engineers to produce highly integrated structures, with aligned fibre materials providing high levels of energy absorption in critical areas. Before this type of design becomes a reality though, aligned fibre thermoplastics must be proven as crashworthy materials and design and analysis tools must be reliable and available to industry.

1.3 Modelling Damage Development in Thermoplastic Composites

Of the three cost components of a new part: raw materials, manufacture and cost to design and test, the latter can be considerable, especially when selecting a new material for a high volume application [6]. A designer needs to be able to develop a component that will perform satisfactorily, without the need for expensive iterative testing programmes.

Car designers can, with some level of confidence, design and fully crash test a new vehicle with primarily metal crash structures, using analysis software, before a single component has been produced. What manufacturers require is an ability to predict the performance of thermoplastic composite structures in the same way. Engineers must be able to model them as they undergo the large amounts of damage seen in vehicle crash tests or real life accident situations.

There are two basic approaches to modelling the behaviour of a composite material. A highly detailed micro model of the matrix and fibre system can be used to predict the development of microcracks and delaminations as the composite material is deformed and hence a complete and detailed description of the material at all stages can be obtained. Alternatively a more global approach can be taken. Instead of trying to describe the complex behaviour of the material at a microstructural level, a macroscopic approach to identifying damage can be used.

The advantage of the macroscopic approach is that material models can be developed and calibrated from simple testing of the composite under certain load cases. These calibrated models can then be used in simulations of large components to predict global structural behaviour and performance. If understood and used correctly they can offer designers a much more computationally economic solution to the problem of simulating damage within composite structures.

Research into the damage modelling of composite materials was primarily undertaken to aid the design of high performance aerospace structures. The techniques developed are now being applied to more varied situations. Often in costly aerospace applications, combinations of high performance matrix and fibre materials have been

used to produce stiff and lightweight components, designed with large *safety factors* and replaced when minimal damage has been identified. Modelling of these structures has in the past therefore often only required the use of a failure criterion or a simple and limited damage model. For crashworthy automotive structures these criteria are not adequate. Vehicle components during a crash undergo large deformations and can damage extensively before ultimate failure, often progressively absorbing a large amount of energy.

A designer therefore needs an accurate and computationally efficient solution to the problem of damage modelling of structures manufactured from composite materials.

1.4 Theme of this Research

This research is part of the CRACTAC (Crashworthy Automotive Components Using Thermoplastic Composites) project, see Appendix E for publications. The CRACTAC project is a jointly funded industrial and academic research initiative investigating the use of reinforced thermoplastics for crashworthy automotive structures. The focus of this work, within the framework of the CRACTAC project, is the development and validation of predictive modelling techniques for the in-plane damage behaviour of long glass fibre reinforced polypropylene composites, with the aim of applying the results to an industrial demonstrator component.

A review of current work in the field, presented in Chapter 2, has identified a considerable amount of research into the analysis of damage and failure in thermoset matrix composites structures, where damage models have been shown to offer the ability to predict damage initiation and progression. The application of these techniques to bulk thermoplastic composites is less well documented and little work has been published on the use of these models for large or complex composite structures.

In the present work, initial efforts, detailed in Chapter 4, were focussed on the application and subsequent further development of a thermoset matrix composite damage model to thermoplastic matrix composites using the ABAQUS/Standard implicit finite element code. The second stage of the work, presented in Chapter 5,

was an investigation of the bi-phase material and damage model available to the analyst in the PAM-CRASH explicit finite element code. Research included an investigation of the calibration strategies for these damage models and their sensitivity to the required input parameters.

Current manufacturing and testing methods for thermoplastic composite materials were also investigated within the scope of the work. These are presented in Chapter 3 and discussed in terms of both the acquisition of relevant data for material model calibration and the subsequent validation of the models using in-plane damaging test specimens.

Finally, in Chapter 6, these approaches to the damage modelling of long glass fibre reinforced polypropylene matrix composites have been compared and contrasted in terms of the design and modelling of a crashworthy automotive industrial demonstrator component. This component, a structural side intrusion protection beam was designed, manufactured and tested, using the techniques developed during the earlier phases of the study. The demonstrator study has shown that large deformation and global fibre direction damage development prediction is possible for glass reinforced thermoplastic composite materials, where the loading is such that damage modes are predominantly in plane.

To conclude the programme, the concept of a crashworthy glass reinforced thermoplastic door module, installed in a target vehicle, was tested and compared to a current steel door structure. This was used to validate the materials and concept as a viable alternative to steels, when considering structural performance.

Chapter 2 Literature Review

2.1 Introduction

This chapter presents a review of literature on the manufacturing, testing, design and predictive damage modelling of woven glass reinforced polypropylene composites. The review is therefore presented in four sections, the first covering manufacturing and testing techniques, the second presenting applications of composite materials to structural automotive components and the final sections reviewing damage modelling techniques and implementation strategies for finite element analysis codes and their application to 3D geometries.

2.2 Manufacture and Testing of Commingled Thermoplastic Composites

Long fibre reinforced thermoplastic composites, due to their high matrix viscosity, compared to thermoset matrix composites, initially present a challenge for manufacturing. It is difficult to flow the polymer material to produce a fully consolidated composite using moulding techniques optimised for thermosets. For this reason, a range of partially impregnated material forms have been developed, which allow rapid processing. These combine the thermoplastic and fibre reinforcement intimately, prior to the main component manufacture phase. Examples of intimately combined long fibre reinforced thermoplastics include commingled, co-wrapped and core spun yarns [7], see Figure 2.1.

2.2.1 Processing Commingled Thermoplastic Composites

Twintex is a commingled glass reinforced polypropylene material, which offers cost effective processing routes, for low, medium and high volume components. It is available in various states including yarn, woven fabric and pre-consolidated woven sheets, see Figure 2.2. In this study, the pre-consolidated woven form of the material is used.

Woven Twintex can be formed into complex parts using a range of manufacturing methods, which all include three basic stages. Initially the material must be heated above the melt temperature of the matrix, pressure is then applied to form the

component and consolidate the composite and finally the material is cooled. The two most widely used industrial manufacturing processes are compression moulding and vacuum consolidation. Of the two, compression moulding allows the shorter cycle time and therefore is the most applicable to medium and high volume automotive components. It is for this reason that the compression moulding technique was selected for this study. Compression moulding can be separated further into two distinct methods, isothermal and non-isothermal moulding. The variation between the two is predominantly in the moulding and cooling cycle.

An isothermal moulding process forms the pre-heated material in tooling which is at a temperature high enough to keep the matrix in a molten state. The formed component is then slowly cooled in the tool while pressure is continuously applied. Non-isothermal moulding uses cool tooling, maintained at a constant temperature, below the melt temperature of the matrix. The preheated material is transferred to the tool and pressure is applied, while the matrix rapidly cools and the part is formed. The non-isothermal process, due to the rapid cooling of the formed part, reduces cycle time significantly when compared to isothermal moulding. This reduction in cycle time and the reduced cost associated with cool tooling make this process more suitable for automotive components.

Isothermal processing of commingled glass reinforced polypropylene has been thoroughly investigated by Ye et al [8]. Three processing variables are identified as critical to composite quality. These variables, pressure, time at pressure and moulding temperature are related to void content, flexural modulus and transverse tensile modulus, to identify the minimum values required to achieve a satisfactory moulding. Results from this work show that optimum mechanical properties are achieved when void content is below 2%. This requires a holding time of over 18 minutes at a pressure of 1MPa and a temperature of 185°C. The work of Klinkmuller et al [9] [10] confirms this result, suggesting that acceptable moulding quality is achievable with temperatures and pressures of 175°C and 10 bar (~1MPa) respectively, with relatively small improvement in composite properties above these levels. This shows that although the isothermal moulding process produces high quality composites, it requires cycle times that are too long and tool temperatures that are too high for medium to high volume automotive structures.

Wakeman et al [11] have investigated the non-isothermal moulding of commingled glass/polypropylene Twintex fabric. A design of experiments technique was used to optimise processing variables including, tool temperature, preheat temperature, moulding pressure and time at pressure. Flexural modulus, flexural strength and void content were used to measure composite quality. It was shown that preheat temperature had the largest effect on the quality of the moulding. Results were relatively insensitive to moulding pressure and time at pressure, as long as these were above a level of 15MPa and 40s respectively. Below these 'cut-off' values composite quality was significantly worse, with a void content of over 50% observed in the poorest specimens, compared to <0.5% in the highest quality mouldings. From the results of this study, the authors propose processing conditions for optimised mechanical performance of flat plaques manufactured from woven glass/polypropylene commingled fabric, see Table 2.1.

This study was limited to flat plaque specimens manufactured from commingled fabric using 'low cost' tooling methods. Wakeman [12] suggests that further investigation using preconsolidated Twintex and matched metal tooling could lead to equivalent quality mouldings being produced using a shorter time at pressure. Expansion of this research to more complex three-dimensional geometries, including curvature, would lead to identification of suitable moulding parameters for an industrial process.

Osten et al [13] have also presented the moulding of Twintex combined with glass mat thermoplastic (GMT). During this study, flat plaque specimens of Twintex were moulded and shown to have a flexural modulus and strength of 12GPa and 300MPa respectively. This compares to a maximum strength of 259.9MPa and modulus of 13.2GPa reported by Wakeman [11]. The results achieved by Osten et al used metal tooling and a preheat temperature of 225°C.

Bruer and Neitzel [14] present general issues concerning the quality of non-isothermal compression moulded glass fibre/polyamide commingled thermoplastic composites. Control of defects such as fibre damage, part distortion, wrinkling and delamination are discussed. It is suggested that to control wrinkling during forming a fabric

clamping device is used to tension the fibres as they are drawn into the tool. The authors also recommend that consolidation pressure is limited to <50MPa to avoid fibre damage.

2.2.2 Characterisation and Mechanical Testing of Composites

Non-linear composite material models often require a large quantity of calibration data when compared to models for metallic materials. This data can include both elastic material properties and a range of post first-ply failure and damage characteristics, if the model accounts for this behaviour.

Depending on the treatment of damage and consequent effect on mechanical properties, the range of data required varies significantly. Models that separate fibre and matrix behaviour can require characterisation of both phases of the composite, whereas techniques that evaluate damage on a macro scale may require less rigorous test programmes for calibration. Models may also need experimentally observed fitting or coupling parameters to be quantified. The calibration parameters required for various damage models are discussed in more detail in section 2.4.

Curtis [15] proposes a range of tests for full characterisation of a composite material, for calibration of a homogenous damaging material model, including through-thickness and interlaminar behaviour. Problems were encountered when investigating through-thickness properties due to the thickness of the moulding required for specimen manufacture. This is a particular issue for a non-isothermal compression moulded thermoplastic composite where maximum thickness is limited by the manufacturing process. Lourenço [16] has also shown the proposed test methods to yield suitable data for the full, ply level characterisation of a thermoset matrix composite material, for non-linear finite element analysis. The material properties and associated physical tests are detailed in Table 2.2 and corresponding test specimens are shown in Figure 2.3.

A certain amount of published data is available for Twintex. Saint-Gobain Vetrotex present a range of mechanical properties, including elastic constants and failure data for 60% WF glass/polypropylene Twintex [17]. This data was obtained through a thorough test programme undertaken by the University of Wyoming (2001) and is

summarised in Table 2.3. The data differs from published information available in 1998 from the manufacturer [18], also presented in Table 2.3. Variation in modulus and strength are explained by continuous material improvement undertaken during the past five years, which is particularly apparent when comparing in-plane shear modulus. It is also noted that the data presented is dependant on the quality of manufacturing techniques.

When considering the characterisation of shear behaviour, Pieron and Vautrin [19] suggest that the 45° tensile test method yields results that are comparable with the Iosipescu method, in terms of both absolute value and scatter. The 45° tensile test also offers significant advantages in terms of specimen preparation, investment in test rigs and complexity of method.

2.3 Crashworthy Applications of Composite Materials

Aligned fibre composite materials, in general, offer a combination of high specific stiffness, strength and energy absorption when compared to metals. This is observed, not only in ‘exotic’ materials, but even when considering bulk thermoplastic matrix materials such as polypropylene reinforced with glass fibres, see Table 2.4 [12][18][20][21][22]. Composites therefore have the potential to replace metallic crash energy management structures in transport applications, where low mass and high strength and energy absorption are key economic drivers.

2.3.1 Energy Absorption Mechanisms in Composite Materials

Composites absorb energy through elastic/plastic deformation and a range of damage mechanisms. These mechanisms have been characterised as fibre debonding, matrix cracking and fibre failure [23]. An ideal energy absorber exhibits one or more of these damage characteristics without catastrophic failure and can be achieved through a combination of careful design and materials selection.

The final failure modes exhibited by a UD composite ply are presented by Hull [23] and related to longitudinal, transverse and shear loading, see Figure 2.4. These are applicable to a thermoplastic matrix composite, although Cantwell and Morten [24] report that the matrix toughness could significantly affect resistance to certain failure

modes. In their review of impact resistance of composites they state that selection of a matrix material with a tensile strain to failure of 4% could lead to improved impact resistance. Svrinivasan et al [25] confirm this through comparative tangential impact testing of epoxy and PEEK matrix composites. The post impact damage areas of various composite plates were investigated and two damage propagation modes were identified. Damage in the thermoset matrix samples was shown to progress through the composite by inter-ply delamination and in the thermoplastic matrix samples by localised shear failure.

Jouri and Shortall [26] performed similar tangential impact tests on random glass reinforced Nylon 6 composite at various temperatures. Scanning electron microscopy was used to characterise failure in the composite, post-test. Specimens tested at ambient temperature exhibited various damage mechanisms including fibre fracture, localised matrix yielding and cracking, fibre pull out and fibre debonding. No global delamination is reported in any of the specimens tested. Santulli et al [27] report similar results for falling weight impact specimens manufactured from woven commingled glass/ polypropylene composite. Infrared thermography showed that for plaques impacted with between 15J and 45J of energy, damage remained localised to the zone of contact with the impactor. Micrographs of the damage zones were used to identify the damage present in the plaques. None of the balanced weave plaques tested exhibited any delamination. In most cases, through thickness matrix cracking was observed as the dominant failure mode.

The most widely investigated energy absorbing composite structure is the crush tube. This type of structure has the potential to absorb large amounts of energy per unit mass, through a range of damage mechanisms occurring at, or close to, the crush front. The energy absorbing crushing modes of a composite tube have been generally characterised as splaying, fragmentation and local buckling. Predominantly, research in this area has focussed on composites with thermosetting resin systems [28]. Crush tubes, although potentially offering a very high level of energy absorption, are sensitive to various factors, which can lead to unstable collapse. A tube crushed at an angle can fail catastrophically and only absorb a small percentage of its quoted capability. Small levels of pre-damage can also significantly affect the performance of composite crush tubes, making it difficult to assess reparability in crash damaged

vehicles. Consequently, composite crush tubes have found only limited application in frontal crash structures, where steel and aluminium are used extensively.

Flexural deformation of composites under tangential loading also produces damage in the material and can absorb energy. The damage and failure throughout the material is, in general, not as widespread as that seen in a progressively crushing tube, although the modes and overall behaviour are not as dependant on such factors as loading angle and failure initiator geometry. A composite beam in flexure deforms elastically and then progressively damages. The stability of such components depends primarily on geometry and material and therefore, for structural components, allows control over the performance under a range of load cases.

2.3.2 Automotive Applications for Structural Composite Materials

Traditional barriers to composite materials entering high volume passenger vehicle design, such as processing time, cost and recyclability are being overcome by thermoplastic matrix composites.

Glass reinforced polypropylene GMT is used extensively in the Mercedes A Class, where the rear hatch is manufactured as a module, produced and delivered by an external supplier. This module saves 3kg over a conventional pressed steel structure, which equates to approximately 25% of the component mass [2]. The BMW Mini also uses thermoplastic composites in a semi-structural application [29]. In this vehicle a complete front-end carrier component is manufactured using StaMax, an injection moulded glass-reinforced polypropylene material. This structure requires 40 fewer parts when compared to a steel front-end carrier [30], and offers a cost and weight advantage. This material is also used in front-end applications on the Porsche Cayenne and the Volkswagen Toureg [31] and in the door module of the Ford Fiesta [32].

Long glass fibre reinforced polypropylene Twintex has been used for a bumper beam structure in the Peugeot 806/Evasion van, see Figure 2.5, where the beam has been shown to perform effectively in both low and high speed collisions [1][33], remaining in one piece after testing and overcoming the problems of catastrophic collapse and failure associated with thermosetting matrix composites. Twintex has also been used,

by Nissan, for the rear load floor of the Primera Break [33], see Figure 2.6. In this component, aligned fibre reinforced composite facings are moulded as a sandwich structure with polypropylene honeycomb and polypropylene trim fabric. This use of 100% polypropylene and glass fibre allows relatively easy recycling of the complete part.

TowFlex, a long fibre, glass reinforced Nylon 6 composite is used in a crashworthy application on the current BMW M3 [34]. The front and rear bumper beam structures are thermoformed from preconsolidated sheets of thermoplastic powder impregnated glass fibres. The bumper crush tubes are also manufactured from the same material, produced using a continuous compression moulding process. The bumper system, when tested, was shown to offer improved crash performance, with a weight saving of 60%, over a comparable metallic bumper system [35].

The Lotus Elise uses Resin Transfer Moulding (RTM) to produce structural and crashworthy components from glass fibre reinforced thermoset resin composites. These parts include a crush cone structure specifically designed for crash energy management [1].

Probably the most recent, high profile, use of composites in the automotive industry has been the Aston Martin Vanquish. This vehicle, launched in 2001 uses carbon fibre reinforced composites in the crash energy management structures, A-pillars and transmission tunnel. These parts, not only provide increased stiffness and enhanced levels of crashworthiness, but offer significant weight saving over similarly performing steel structures [36].

As well as production parts, research and development work is ongoing, to develop new composite components for the automotive industry. Some published applications include structural instrument panels and cross car beams developed by Delphi, Beyer and General Motors Inc. [37][38][39], a glass fibre reinforced B-post developed in conjunction with Volvo [40] and an energy absorbing knee bolster designed and tested by GE Plastics [41]. Much of the current industrial research work remains unpublished though, due to its commercially sensitive nature [42].

Two significant barriers to the use of composites in automotive structural design still remain. The first of these is the End of Life Vehicle Directive [43], which specifies requirements for recyclability. The second is the relatively high component cost of composite parts when compared to metals. Aligned fibre reinforced thermoplastic composites therefore seem a promising option for high volume automotive applications, if they can be proven to meet both structural and crashworthiness requirements.

2.3.3 Composite Materials for Side Impact Protection

A large part of this research work was the design and development of a thermoplastic composite side intrusion protection system. A review of current crashworthiness requirements and solutions was performed, with a particular focus on the use of composites in this area.

The two main methods for side impact performance evaluation are the Euro NCAP test [44] and the Federal Motor Vehicle Safety Standard (FMVSS214) [45]. The Euro NCAP test uses a deformable barrier mounted on a sled, which is impacted into the test vehicle. Data is acquired from a fully instrumented ‘dummy’ mounted in the driving seat, which is used to evaluate the injury severity of the impact. The FMVSS214 test has a similar barrier impact, but also includes a simpler quasi-static pole intrusion. This test evaluates the stiffness of the door and has a pass/fail criteria based on the resistive force against displacement.

Both tests have been shown to offer an improvement in performance in ‘real life’ side impact collision scenarios. A side impact collision involving a car receiving a high ranking Euro NCAP score, of 4 stars, is 30% less likely to result in fatal or serious injuries [46]. Similarly, after the introduction of FMVSS214 it was shown that cars complying to the standard showed a 25% reduction in the risk of serious casualty, in both vehicle to stationary object and vehicle to vehicle side impact collisions [47]. Further research has shown that although developments are ongoing in the field of side impact protection, there is still potential for improvement in performance, both in collisions with fixed roadside objects [48] and with other vehicles [49][50]. In collisions with other vehicles, pelvic fracture is seen in 85% of cases [49], suggesting that improved performance of the door and side impact structure could potentially

reduce the severity and occurrence of the types of injuries seen in the majority of vehicle to vehicle impacts. Research in Japan, measuring the injury and fatality rate in all collisions registered by Japanese law enforcement, between 1992 and 1995, has shown that the side impact fatal injury rate in all reported collisions is 0.32%, which is considerably higher than the 0.24% fatality rate observed in frontal impacts [51]. It has also been observed that design of the interior panel of a passenger vehicle door and the structural collapse mechanism of the B-pillar during side impact can influence the level of abdominal and thoracic injury [52].

Current production passenger vehicles traditionally use either a pressed or tubular, high strength steel beam structure for side impact protection. Work has been undertaken to modularise steel doors [53] and concepts have been shown to offer weight savings of up to 30% for a full door structure, validated to FMVSS214. These weight savings were achieved through selection of stronger materials than are currently used in automotive door structures and through novel design, moving the side intrusion protection beam to the lower and upper section of the door frame.

Composite materials, as an alternative to steel, have also been investigated, with varying levels of success. Cheon et al [54] manufactured and tested various side intrusion protection beam structures from glass fibre-epoxy composite. A square tube, circular tube and I-beam were tested quasi-statically in three point flexure. Load was applied to the beams supported over a 470mm span, using a 12 inch diameter impactor. Results from static tests showed localised catastrophic failure at the point of load application, between 25mm and 50mm displacement, in all the beams tested. The square section beam performed better than the other two geometries tested, giving a peak load of 25.3kN at approximately 30mm displacement. This is similar to the peak load of 27.3kN observed when testing a steel side intrusion beam, although the steel beam yielded and failed progressively, resisting load up to the maximum test displacement of 100mm.

With a catastrophic failure at less than 50mm displacement it is unlikely though that a beam of this geometry and material combination could meet even the basic quasi-static side intrusion requirement of the Federal Motor Vehicle Safety Standard.

A hexagonal cross section, glass fibre reinforced epoxy, beam design has also been proposed by Kamil and Saunders [55] as part of an undergraduate research study. The beam has been analysed using a linear static finite element technique and assessed against a maximum stress failure criteria, which showed that the concept could potentially meet the load displacement performance criteria of FMVSS214. A prototype beam was not manufactured and this work has not been validated. It is unlikely that the beam, although a novel design, would meet the structural requirements of the Federal Standard, since only a basic modelling approach was used during the design phase.

Patberg et al [56] have investigated an integrated composite door and side impact protection structure concept. Both thermoset matrix and thermoplastic matrix composite structures have been designed. The thermoplastic beam was manufactured from hybrid glass/polypropylene yarns using a combination of braiding and tape winding, followed by a thermoforming stage. The thermoset composite beam was manufactured from braided glass fibre reinforced epoxy composite. Basic simulation of the performance of both concepts has been investigated, although for the thermoplastic concept it was observed that modelling, using current techniques, was difficult due to the rigorous material characterisation required. Simulation results are not presented for either of the concepts. A range of static and dynamic test procedures has been identified and initial testing of the thermoset concept using a FMVSS214 style pole intrusion has been undertaken. Absolute values are not given, but the concept appears to perform comparably to a similar steel door structure. The result does show that the composite concept is initially stiffer than the steel beam and then undergoes a damage event that reduces the load by approximately 40%, followed by a steady re-loading. This indicates that a certain amount of catastrophic failure is occurring in part of the side impact structure. The damage observed in the test is not discussed so it is difficult to identify whether this failure occurs in the beam or the door structure.

Twintex glass reinforced polypropylene composite has been used by Erzen et al [57] to produce a side intrusion beam design that has been investigated using finite element analysis techniques. The first-ply failure of the composite beam, predicted using a maximum stress failure criteria, was compared to a steel beam assessed using

a von Mises yield criteria. Simulation showed that the optimised Twintex beam would start to fail at approximately 60mm compared to a yield displacement of 84mm for the reference steel beam. No post failure behaviour modelling or physical testing of components was undertaken. The study is therefore incomplete in terms of full validation of either the concept or modelling technique.

A Twintex composite side intrusion beam was also proposed and developed as a technology demonstrator component for the SACTAC research programme at the University of Nottingham [58][59], see Figure 2.7. The beam was initially designed through analysis performed using the ABAQUS/Standard finite element code, with subsequent simulations being performed using an unvalidated material model for Twintex implemented in the LS-Dyna explicit finite element analysis code. The final beam design was manufactured using low cost tooling and tested using a rig developed for FMVSS214 vehicle testing. The composite beam underperformed by between 8% and 18% when comparing peak loads and energy absorption with those of an equivalent steel beam. The major conclusions from this work were that:

- Despite the low failure strain of glass/PP composite when compared to steel, a correctly designed beam could perform as well as a steel beam.
- Due regard must be given to the difference in failure stress in tension and compression for Twintex.

Further work is suggested to improve the design by increasing the dimensions of the compressive face of the beam to augment the strength. It is also recommended that simulation techniques should be used to further understand the damage mechanisms and behaviour of the beam. Development of the component as part of a crashworthy door module, or inclusion of the beam in a fully thermoplastic door structure, could also provide significant improvement in performance as well as providing commercial advantages through parts integration.

Side impact protection is therefore an area where thermoplastic composites have been shown, by Patberg et al [56] and the work undertaken at Nottingham University [58][59], to offer the potential to provide a similar level of performance as current

steel beams. Further work is required including the development and validation of reliable modelling techniques and the production and testing, to a current standard, of a composite beam mounted in a vehicle.

2.4 Damage Modelling Techniques

To be able to design composite structures for large deformation, structural and crashworthy applications, it is important that the behaviour of the material can be accurately predicted. The basic in-plane damage mechanisms identified for composite materials and specifically those with thermoplastic matrices have been introduced previously. In this section of the review, some methods for quantifying this damage and relating it to degradation in material properties are described. These models will be discussed with particular focus on their implementation into finite element analysis codes.

Priston [60] suggests that approaches towards the assessment and quantification of damage in composite materials can be separated into two distinct concepts. These are, micromechanical models, which relate individual stresses to distinct microstructural damage mechanisms and macroscopic models, which describe the damage in a representative volume of composite. Both these methods can then be used to predict changes in properties and behaviour of the damaged composite.

The use of micromechanical models as a basis for finite element simulation of composite materials is computationally expensive, since meshes need to be defined with a resolution high enough to capture individual damage mechanisms. This would lead to impractically high mesh density if the models were to be applied to large test specimens or more complex components. When discussing the use of damage models with the finite element method, for simulation at component level, the scope is therefore, in general, constrained to macroscopic approaches.

The volume of literature in this field is extensive and is represented here by a range of modelling techniques which have been applied to in-plane damage development. Three of these modelling approaches are discussed in further detail and in section 2.5

literature regarding the application of damage models to more complex geometries is presented.

2.4.1 General Macroscopic Progressive Damage Models

The fundamental differences between the majority of published macroscopic damage modelling techniques are the methods used to identify damage and the subsequent relationship between the damage identified and the elastic properties of the composite.

Various authors have selected and used failure criteria as the basis of their damage model, developing a subsequent material property degradation regime based on the damage mode identified by the criteria. Cheikh [61] presents this type of model in its simplest form. Maximum longitudinal, transverse and shear stress criteria are used to identify three distinct damage modes in the composite. These damages, when identified, lead to a step reduction in the corresponding modulus to zero. The model proposed is used to simulate progressive damage in a unidirectional composite tensile test, with various ply orientations, using a stepped analysis, where load is incremented and damage is computed over a range of small displacements. The methodology appears to work successfully, although no experimental results are presented, so it is impossible to validate either the damage identification or modulus reduction methods. The maximum stress criteria could potentially offer an effective method of identifying fibre direction damage, where behaviour is dominated by a linear elastic then fracturing fibre behaviour. It is unlikely that the maximum shear stress criteria could accurately model shear damage, which is usually a progressive type of damage, dependant on the matrix material.

A similar method is presented by Belingardi et al [62] who propose a modified Hashin criteria to describe the failure surface for a composite, with identified failure leading to a strain-softening behaviour. This model is used to simulate impact damage during a drop dart test on an E-glass/epoxy plate. In the case of both a 5J and 50J impact, agreement between experiment and simulation is good. This is in part due to the introduction of a time dependant behaviour and presumably a calibration of strain-softening based on experimental observations. Feng et al [63] and Gamble et al [64] present similar failure criteria based models although the modulus degradation regimes associated with identified damage, in both cases, do not include a strain-

softening behaviour. Both models use criteria to identify three distinct failure modes, these are: matrix cracking, fibre matrix shear and fibre breakage. Experimental validation of the Feng model for a composite plate under a uniform pressure loading, shows good agreement between experiment and simulation, except in the case of strain levels close to the edge of the plate, where the simulation of boundary conditions lead to uncharacteristically high strains due to over-constrained edges. The Gamble model is validated with a hole in plate specimen, where the location and magnitude of predicted damage is shown to compare well to experimentally observed results. The authors have suggested that ongoing work to develop and implement a more physically based, strain dependant damage mechanics model, will improve the performance of the technique.

Further models of this type presented by Tan and Perez [65], Padhi et al [66] and Ochoa and Engblom [67] have been validated using a hole in plate under compression, a plate loaded with a uniform tangential pressure and a plate under four point bending, respectively. All of these models implement failure criteria in an incremented finite element analysis, with elastic property degradation based on the identified damage mode. Chang and Chang [68] also present a failure criteria based damage model, which is discussed in section 2.4.2.

Chow and Yang [69] describe a more complex damage law based on the deviation from elastic behaviour, due to a damaged component of the strain, associated with microcracks and voids in the composite. Similar approaches, described as continuum damage mechanics models, are also used by Williams et al [70] to simulate crack propagation in a notched plate and by Vang et al [71] to successfully model the behaviour of a braided carbon composite tube under cycled pressure loading. Comparison is made by Vang, between predicted and experimental hoop and axial strain and shows good agreement for the model. Oytana [72] also presents a damage mechanics model based on a recoverable, but non-reversible phenomenon treated separately to damage, which produces an associated permanent plastic deformation. Results from simulations using this model are compared to experimental results for composite plates in tension. In the experiment, damage in translucent plates is measured using an optical technique and is shown to be similar in location and magnitude to the predicted damage from the model.

Coats and Harris [73][74] have also undertaken research in the field of continuum damage mechanics and proposed a volume strain based damage accumulation model. Experimental validation of the model for a graphite/epoxy composite plate under tensile loading is presented [75], comparing numerically predicted residual strength with experimentally obtained results. The model, in this case is within 10% of the experimental results for a range of notch lengths between 2mm and 23mm.

Iannucci et al [76][77][78] have presented a damage mechanics approach, using variables which relate to the dissipated energy associated with certain damage modes, including fibre fracture and fibre-matrix deterioration. These variables are then related to material characteristics, to represent the reduction in load carrying capacity of a composite ply associated with accumulated damage. The authors suggest that this type of approach, implemented in the LS-Dyna explicit finite element analysis code, is a significantly improved method for predicting impact damage, than traditional stress based failure criteria modelling techniques [68][79]. Good agreement between experiment and test is seen for a tangential impact on a woven carbon composite plate and for a simulation of bird strike on the leading edge of a composite aircraft tail component. Simulations of the tangential impact using a stress based damage model shows significant overprediction of laminate strength.

Both the Ladeveze model [80] and the PAM-CRASH bi-phase model [81], discussed in subsequent sections, are further examples of damage mechanics models, which have been successfully implemented in commercial finite element codes.

In general, failure criteria based models, which result in material property degradation based on identified damage modes, can be calibrated using absolute values obtained through physical test, for example, the tensile failure strength of a ply, or the compressive strength of the matrix. In contrast, the damage mechanics models require the user to identify the relation between a theoretical damage level in a volume of composite and the associated effect on the behaviour in terms of elastic constants, as well as the plastic behaviour caused by a level of non recoverable deformation due to cracking in the composite.

2.4.2 Chang Model

Chang and Chang [68] presented a failure criteria based progressive damage model for laminated composite plates. The model identifies critical in-plane damage modes and relates these to reduction in material properties in the damaged areas. The three in-plane failure modes, describing the failure envelope of the composite, proposed for a fibre dominated material are: matrix cracking, fibre-matrix shearing and fibre breakage. The matrix cracking criteria is developed by the authors, based on the transverse tensile and shear stress in a ply. The fibre/matrix shear damage and fibre breakage is based on a modified Yamada-Sun failure criterion. The model also includes a non-linear shear stress-strain relationship based on work by Hahn and Tsai [82]. Assessment of the performance of the model was made through comparison of analytical results with experimental results for a carbon/epoxy composite plate, with a stress concentrator, under tensile loading. Predicted strength and damage showed good agreement with experiment for various hole diameters.

Subsequently, Chang and Lessard [79] have developed the modelling approach further, incorporating matrix tensile and compressive failure, fibre buckling and fibre-matrix shearing failure. Again, during analysis of composite plates containing a hole in compression, reduction in material properties based on the type of failure identified is possible due to the assessment of a range of separate damage mechanisms. Lessard and Chang [83] have undertaken validation of this model by comparison of experimental results with the predicted performance of graphite/epoxy composite plates with various ply orientations. Good agreement is observed between experiment and simulation for a range of ply angles. The model accurately predicts damage location and magnitude and the consequent reduction in material performance, as well as capturing the final failure load of the test specimens.

Further work based on the damage modelling techniques developed by Chang et al was undertaken by Chang, Liu and Chang [84] to validate the method for tensile loading on specimens with a stress concentrating hole. The model, previously only validated for compressive loadings [68][79] was applied to a hole in tensile plate specimen with various ply orientations. Good agreement was observed between predicted and observed failure loads and the simulated load/strain behaviour, up to approximately 1% strain over a 1 inch (25.4mm) gauge length. Since the stress

concentration is a 0.25 inch diameter hole, this 1% strain over the gauge length potentially represents up to 4% strain, if deformation is concentrated about the hole. This simulation of the tensile hole in plate specimen has been repeated by Avalle et al [85], using a version of the model implemented in LS-Dyna, an explicit finite element code. The authors state that the models are validated, although no direct comparison of experimental and analytical results is given.

Shahid and Chang [86] have presented continuing work on accumulative damage modelling based on damage prediction, using failure criteria developed by Hashin. Damage, quantified in terms of crack density, is related to composite load carrying capacity and hence material constants, using ply constitutive equations proposed by the authors. The model is compared to experimental data for tensile and rail shear loadings. Stress/strain predictions for various tensile specimens agreed well up to the point where extensive damage in the specimen resulted in a significant drop in load carrying capacity. Load and displacement behaviour during the rail shear simulation is not compared to experimental results, although failure load appears to show good agreement with experiment. In general the model is accurate when damage is predominantly in-plane. The authors comment that in laminates which are prone to delamination, the model may overestimate laminate strength. This is because delamination damage, which can occur at strain levels significantly below ultimate failure, results in matrix cracking which can influence global composite strength.

Davila et al [87] have applied the compressive damage model proposed by Chang and Lessard [79] to the simulation of a ribbed wing-box cover panel manufactured from graphite reinforced epoxy composite. Experimental results are in good agreement with the model up to the point at which out of plane deformation occurs in the panel. Since the model does not include a delamination damage mode, this result was expected. It is noted that the load displacement response of the panel, up to the point where out of plane damage occurs, is fairly linear. The model is therefore not fully validated for highly non-linear behaviour in large components.

In all the work presented by Chang et al [68][79][83], finite element analysis is undertaken using software tools developed for the purpose of composite plate analysis. Subsequently, the model proposed by Chang and Lessard [79] has been

presented as a worked example, input as a 'user defined' material model in the commercial finite element analysis code, ABAQUS/Standard [88]. The example analysis presented by the publishers of the code, shows simulation of a carbon/epoxy composite plate, with a stress concentration, under compressive loading. Experimental and numerical load displacement curves for this test show excellent agreement up to 1% strain in the 25.4mm (1 inch) gauge length, although above this level, the model is less able to accurately simulate material behaviour. Experimentally observed ultimate failure occurs at 2.8% strain with an applied load of 13440N (3000lbs), compared to 2.4% and 11200N (2500lbs) seen in the most accurate of the numerical results. In the strain range over 1%, the model appears to underestimate the load carrying capacity of the damaged composite. It is therefore overpredicting either the level of damage in the composite or the reduction in material properties related to the level of damage identified. In either case, the result is that the model appears to become less stable, with larger displacements occurring during the final steps of the analysis, compared to the start.

In general, these models give a good agreement with experiment, when considering in-plane damage development in a brittle matrix composite, such as carbon reinforced epoxy. They accurately capture both fibre direction and shear damage especially during the initial stages of damage development, although correlation with experiment appears to reduce at higher strains. There is also little evidence in the literature that these models have been applied to other materials, especially bulk thermoplastic matrix composites, such as the one under consideration in this study.

2.4.3 Ladeveze Model

Ladeveze [80][89][90] has proposed a damage mechanics model for laminated composite materials. This model is based on a damage concept, which relates the material moduli to parameters describing the damage state of the material, where a macroscopic damage kinematic is used to quantify the damage parameters. The model also includes a plasticity coupled to damage, which accounts for the inelastic strains observed in composites, relating to deterioration of the fibre-matrix interface.

The author proposes that only the shear and transverse tensile moduli vary with damage state and that the other elastic characteristics remain constant up to a rupture

point, resulting in the requirement for only two damage parameters for a composite ply, d the shear damage parameter:

$$d = 1 - \frac{G_{12}}{G_{12}^0} \quad (2.1)$$

and d' the transverse damage parameter:

$$d' = 1 - \frac{E_{22}}{E_{22}^0} \quad (2.2)$$

where G_{12}^0 and E_{22}^0 denote the undamaged shear modulus and transverse modulus and G_{12} and E_{22} denote the shear modulus at a damage level d and the transverse modulus at a damage level d' . These parameters combined with the rupture criteria and plasticity behaviour therefore describe the progressive damaging and failure behaviour of the composite.

Ladeveze [80] states that this model has been ‘checked on numerous experimental tests’, although only selected results for T300-914 thermoset composite are presented. It is observed that the model is in good agreement for tensile tests on various fibre angles, particularly for a tensile test on a $[\pm 45]_{2s}$ laminate. Limitations regarding the final failure or rupture identification when the model is implemented using the finite element method are also discussed. The post critical behaviour is strongly dependent on the discretisation of the test specimen, suggesting that convergence studies are needed to accurately capture cracking damage in the fibre direction.

Ladeveze and Le Dantec [91] present a thorough review of the calibration scheme required to fully characterise the behaviour of a composite using the model presented previously. Three tensile tests and a compressive test on various laminates are needed to derive the parameters used to calibrate the model. These are summarised in Table 2.5. Experimentally these tests do not present a particular challenge although they do require measurement of transverse laminate strain. It is not possible to apply the model and calibration strategy, in this form, to a woven fabric reinforced composite.

This is due to the $[\pm 67.5]_{2s}$ tensile test specimen, which cannot exist when considering a balanced weave composite.

Allix et al [92][93][94][95] have subsequently utilised the homogenous ply model proposed by Ladeveze [80], combined with an interface layer to create a mesomodel of a composite laminate. This approach has been used to successfully model the intralaminar and interlaminar damage in a carbon fibre/epoxy matrix composite plate with a stress concentration loaded in tension, when comparing the size and location of delamination and damage zones [95]. Touchard et al [96] have repeated this study for an APC-2 carbon fibre/thermoplastic matrix composite. The authors report that when considering the $[\pm 45]_{2s}$ laminate, strain levels in excess of 25% were observed compared to <10% for the thermoset matrix composite. It is also reported that the $[45]_8$ specimen for the determination of the transverse damage law only resulted in calibration up to a damage level of 0.2, since catastrophic failure occurred very rapidly after damage initiation. The nature of damage observed in the notched tensile test, showed significant difference in both the type and size of the damage areas when comparing the thermoset to the thermoplastic matrix composite. No delamination and only small matrix cracks are observed in the thermoplastic composite, which the authors conclude, suggests that the model may need some adaptation if it is to be applied to such materials.

Coutelier and Rozycki [97] have used a version of the model implemented in the PAM-CRASH finite element code to simulate the behaviour of an E-Glass/Epoxy composite. The authors conclude that the model is in good agreement when compared to experiment for a tensile test on a $[\pm 45]_{2s}$ laminate and for a dynamic 3 point bending test on a $[90_2 0_2]_s$ laminate. Results are also discussed for the simulation of a steel/composite laminated tube crush, although experimental curves are not presented.

Hochard et al [98] have modified the original model present by Ladeveze [68] to simulate the damaging behaviour of a woven carbon fibre reinforced composite. A further damage parameter has been included to account for transverse fibre direction damage. This model, like the work of Coutelier and Rozycki [97] confirms that the agreement between experimental and simulation results obtained by the original author [68] are repeatable. Johnson and Simon [99] have also presented preliminary

work on the implementation of a fabric composite model, based on the unidirectional model presented previously, in the PAM-CRASH explicit finite element code. The model has been calibrated for a woven glass fibre reinforced epoxy composite with verification performed by regenerating the cyclic shear stress/strain curve for the material. Simulation of a tangential impact on a composite plate is presented, but no experimental data is shown to validate the result, since this work is part of an ongoing research programme.

2.4.4 PAM-CRASH Bi-Phase Model

Two material models are available, in the PAM-CRASH finite element code, for the simulation of damage in composite materials [81]. One of these, the bi-phase model is described by de Rouvray and Haug [100][101] as an elastic-brittle fibre phase, superimposed over an elastic-plastic/brittle matrix phase, with a strain based, linear damaging, ply degradation and failure regime. Pickett et al [102] present an introduction to the model and detail the implementation in the PAM-CRASH explicit finite element code. A bi-linear damaging version of then model is also introduced in this work, see Figure 2.8. Using this version of the model a comparison is made by Pickett et al [102] between experiment and simulation for impact on a SMC composite plate, showing good agreement between the test and predicted results.

De Rouvray et al [103] present a numerical investigation of the effect of notches on the strength of composite plates, using the bi-linear damaging version of the model. This model is of the same form as that currently available in the commercial analysis code, PAM-CRASH. Results from this study show that for various ply orientations, the model can accurately predict ultimate strength. It is noted that the model, in certain cases, overpredicts the strength of $+45^{\circ}/-45^{\circ}$ plies, by up to 17%, due to the lack of an interface layer to capture interlaminar matrix damage. This phenomenon, also observed by Shahid and Chang [86], reiterates the importance of delamination as a failure mode in certain laminates. It is expected that this would not have a significant influence on the performance of a thermoplastic matrix composite though, for example glass reinforced/PP Twintex, where the tough matrix eliminates delamination as a critical failure mode.

In subsequent work, the concept of a ‘modified’ form of the bi-phase model is also introduced, where, for cloth or cross-ply laminates the orthotropic constants of the matrix phase of the model can be used to represent the composite as a whole. Haug and de Rouvray [104] suggested that this approach is well suited for modelling a composite laminate using a multi-layered shell element. This use of the ‘modified’ or ‘degenerate’ form of the material model with multi-layered shells has subsequently been used with some success by Curtis [15] and Lourenco [16].

Haug and Jamjian [105] also propose a programme including 0° and 90° tension, 90° compression and a shear test, as a suitable range of experimental data collection for the calibration of the model. This is again verified by the work of both Lourenco [16] and Curtis [15]. It is noted that all of the development, calibration and validation work presented, concentrates on the use of the model for the simulation of thermosetting matrix composites. The use of a bulk thermoplastic matrix, such as polypropylene, is not addressed.

2.5 Assessment of Complex Composite Geometries Using Finite Element Damage Models

There are predominantly two methods used to solve finite element models, the implicit and the explicit technique. Due to the nature of these numerical methods, the implicit and explicit techniques are often applied to two different classes of problem [122].

An implicit solution is calculated by solving a global stiffness matrix for an equilibrium loading, to give nodal displacements, and is therefore generally used for linear or static problems. For problems involving non-linear material behaviour and dynamic loading, the stiffness matrix is not constant, leading to the need for iterative schemes to converge a solution for a particular loading. The implicit technique can therefore become computationally expensive in such situations. Recently, the explicit technique has become popular for non-linear problems, especially in the field of crashworthiness, where contact and dynamic effects are critical to the solution.

An explicit solution, unlike the implicit equilibrium solution, treats the problem as a dynamic event, considering the equations of motion for nodal displacement, solved in the time domain. Nodal velocities and displacements, in this case, are obtained by integrating Newton's second law over a small time-step on an element by element basis. This leads to a set of uncoupled equations, unlike the implicit technique which requires assembly and inversion of the complete stiffness matrix.

In general, the explicit technique is therefore selected when significantly high levels of material nonlinearity and deformation are expected, although the implicit technique can be used if dynamic effects are negligible and a solution is required for a relatively small displacement.

Predominantly, the majority of literature in the field of composite materials and damage modelling focuses on the development and validation of numerical techniques for the simulation of test coupons or components with 'simple' geometries, using either the implicit or explicit finite element technique.

In the work presented by Chang et al [68][79][83] the damage modelling techniques developed are applied only to plates with stress concentrations. There is little evidence in the current literature that this type of model, implemented in an implicit finite element code, has been used to simulate more complex geometries. Conversely, the bi-phase model, implemented in the PAM-CRASH explicit code [81], has been used for various industrial component failure studies. These include both automotive and aerospace structures manufactured from composite materials.

Haug and de Rouvray [104], Haug and Jamjian [105][106], Haug et al [107] and Nakada and Haug [108] present simulations using the model, validated against experimental data. These include impact on composite plates, composite tube crush and the simulation and test of a prototype composite car in both side and frontal impact. The car, manufactured from carbon/epoxy and aramid/epoxy composite shows that simulation of the response of thermoset matrix composites can yield realistic load and displacement characteristics when compared to test. Good agreement is observed between the experimental result of a dynamic side intrusion

test and simulation, when comparing both the acceleration/time and absorbed energy/time histories.

Significant further work has been ongoing regarding the application of the bi-phase model to the simulation of composite materials in the aerospace industry. The concept of explicit codes being applied to such components was discussed by Johnson et al [109]. Investigation and calibration of the bi-phase model for these applications was presented by Kohlgruber and Kamoulakos [110]. This work suggests that for the two types of fabric composite in question, carbon/epoxy and aramid/epoxy, the degenerate form of the bi-phase model is most suitable. This is confirmed by the research of Deletombe et al [111] and McCarthy et al [112] who present the results from simulation and test of a composite helicopter sub-floor component crush. Agreement between experimental results and those predicted by the degenerate bi-phase model in PAM-CRASH are generally acceptable, although some limitations with the model are suggested. Future research, developing material models specifically for fabric composites and the consideration of strain rate effects and delamination, is ongoing by the authors.

Recently, McCarthy and Wiggeraad [113] further reinforced previous findings, drawing various conclusions, including that the degenerate bi-phase material model did not allow matching of off-axis behaviour satisfactorily for the materials under investigation and that a new fabric model, under development at the time of publication could provide better results in future. This work also addressed the issue of the need for a residual strength characteristic to be included past the failure observed in coupon tests, to allow correct prediction of energy absorption. It is suggested that calibration of post ultimate failure behaviour, a non-physical material characteristic included to maintain stability during dynamic analysis, could be achieved through sub-component testing and modelling.

2.6 Conclusion

This chapter has presented an introduction to Twintex, a woven glass fibre reinforced polypropylene matrix composite material, summarising current applications and material property information available in the public domain. The non-isothermal compression moulding technique has been introduced and a processing window has been defined based on work at the University of Nottingham by Wakeman et al [11][12]. General testing of composites for characterisation and specifically the mechanical performance of Twintex has also been discussed. Furthermore, a range of tests has been identified as suitable for acquisition of the material properties required in this study.

A review of current structural applications of composite materials in the automotive industry has also been performed. Areas where composites potentially offer an alternative to metallic structures have been discussed. Side intrusion protection has been identified as a suitable application for the candidate material in this study. Limited work has been undertaken in this area, although initial results appear to suggest that there is the potential for a high performance composite side intrusion protection structure to offer a viable alternative to current metallic design solutions.

The final area of the review has been the application of predictive damage models and finite element analysis to composites. A range of techniques have been developed and validated, predominantly for simple geometries, although some research has applied these methods to more complex structures. There is very little literature available investigating the use of these techniques for predicting accumulated damage in bulk thermoplastic matrix composites, such as glass reinforced polypropylene, the candidate material in this study.

The following three areas have therefore been identified as requiring further investigation:

1. The application of failure criteria based damage modelling techniques to woven glass fibre reinforced polypropylene matrix composites.

2. The use of the bi-phase material model, implemented in the PAM-CRASH explicit finite element analysis code, for the simulation of the behaviour of woven glass fibre reinforced polypropylene matrix composites.

3. The use of glass fibre reinforced polypropylene composite materials for side impact protection and the application of finite element damage modelling techniques to the design of such components.

2.7 Tables

Processing Parameter	Optimised Value
Tool temperature	60°C
Commingled fabric preheat temperature	220°C
Moulding pressure	40 bar
Consolidation time at pressure	80s

Table 2.1 Optimised processing parameters for non-isothermal compression moulding of commingled glass polypropylene composites [11]

Required Properties	Evaluating Test
$E_{1t}, \nu_{12}, \nu_{13}$	In-plane 0° Tensile Test
$E_{2t}, \nu_{21}, \nu_{23}$	In-plane 90° Tensile Test
$E_{3t}, \nu_{31}, \nu_{32}$	Through-Thickness Tensile Test
E_{1c}	In-plane 0° Compressive Test
E_{2c}	In-plane 90° Compressive Test
E_{3c}	Through-Thickness Compressive Test
G_{12}	Iosipescu Shear Test
G_{23}	Iosipescu Shear Test
G_{31}	Iosipescu Shear Test

Table 2.2 Material properties and associated physical tests [16]

Material Constants	Published 2003	Published 1998
E_{11}	13.79 GPa	13.6 GPa
E_{22}	12.97 GPa	13.6 GPa
E_{33}	- GPa	5.3 GPa
ν_{12}	0.10	0.08
ν_{21}	0.12	0.08
G_{12}	1.72 GPa	1.20 GPa
G_{13}	1.79 GPa	1.52 GPa
G_{23}	1.66 GPa	1.52 GPa

Strength	Published 2003	Published 1998
σ_{T1U}	287.6 MPa	313 MPa
σ_{T2U}	265.9 MPa	313 MPa
σ_{C1U}	154.5 MPa	125 MPa
σ_{C2U}	151.1 MPa	125 MPa
τ_{12U}	18.8 MPa	25 MPa
τ_{13U}	13.7 MPa	31 MPa
τ_{23U}	12.1 MPa	31 MPa

Table 2.3 60% WF balanced weave Twintex properties, 2003[17] and 1998 [18]

Material	WF (%)	Density (tonne/m ³)	E (GPa)	σ_{TU} (MPa)	$\sigma_{specific}$
SMC Chopped Glass	30	1.9	9.0	76	40.0
Random Glass/Vinyl-ester	38	-	8.6	124	-
GMT Random Glass/PP	40	1.2	6.6	120	100.0
Twintex 1:1 Glass/PP (2003)	60	1.5	13.79	288	191.7
Twintex 1:1 Glass/PP (1998)	60	1.5	13.6	313	208.7
Twintex 1:1 Glass/PP (1998)	75	1.75	21	420	240.0
Twintex 4:1 Glass/PP (1998)	60	1.5	24	500	333.3
Twintex UD Glass/PP	75	1.75	38	800	457.1
Plytron UD Glass/PP	60	1.48	28	650	439.2
Commingled 1:1 Carbon/PEEK	61	1.6	63	780	487.5
Commingled UD Carbon/PEEK	61	1.5	145	1840	1226.7
Aluminium 6061 T6	-	2.71	69	310	114.4
Steel SAE 1010	-	7.87	200	365	46.4
Steel SAE 4340	-	7.83	200	1034	132.1

Table 2.4 Comparison of the mechanical properties of composite and metallic materials [12][18][20][21][22]

Test	Calibration
Tensile test on [0,90] _{2s} laminate	Fibre tensile strain limit
Compressive test on [0,90] _{4s} laminate	Fibre compressive strain limit
Tensile test on [±45] _{2s} laminate	Damage and plasticity laws
Tensile test on [±67.5] _{2s} laminate	Transverse tension damage master curve

Table 2.5 Tests used to calibrate Ladeveze damage model [74]

2.8 Figures

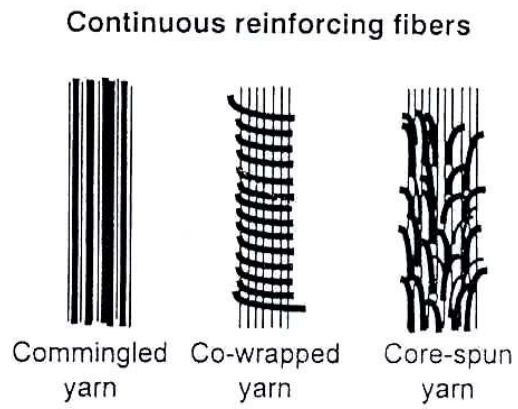


Figure 2.1 Methods for intimately combining thermoplastic matrix and long fibre reinforcement [7]

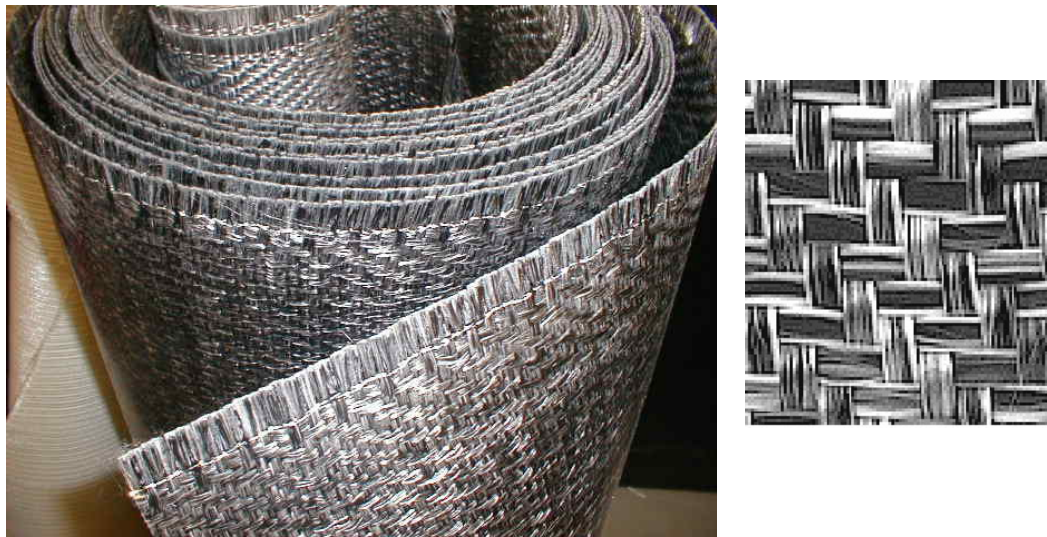


Figure 2.2 Woven commingled Twintex sheet and fabric

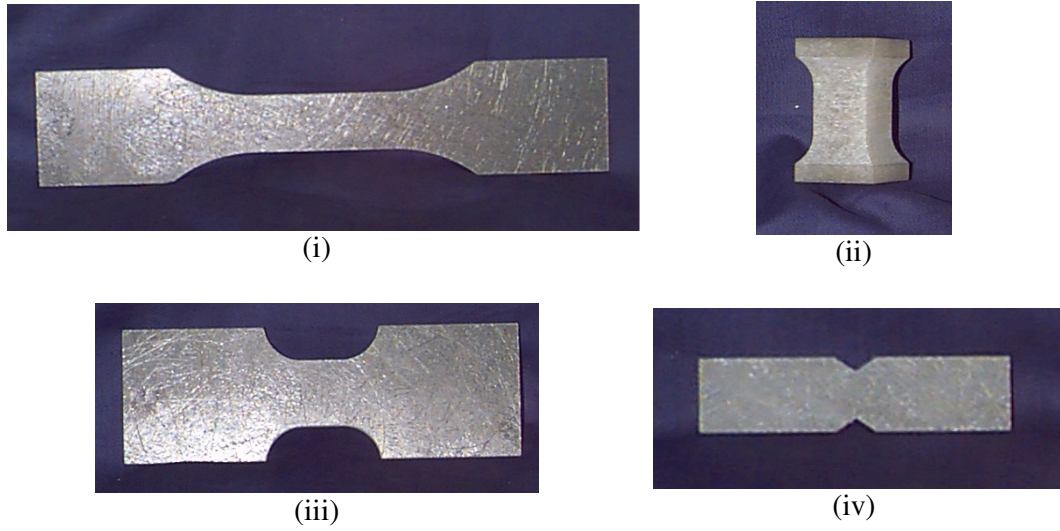


Figure 2.3 Coupon test specimens: (i) Tensile, (ii) Through-thickness, (iii) Compressive, (iv) Shear [16]

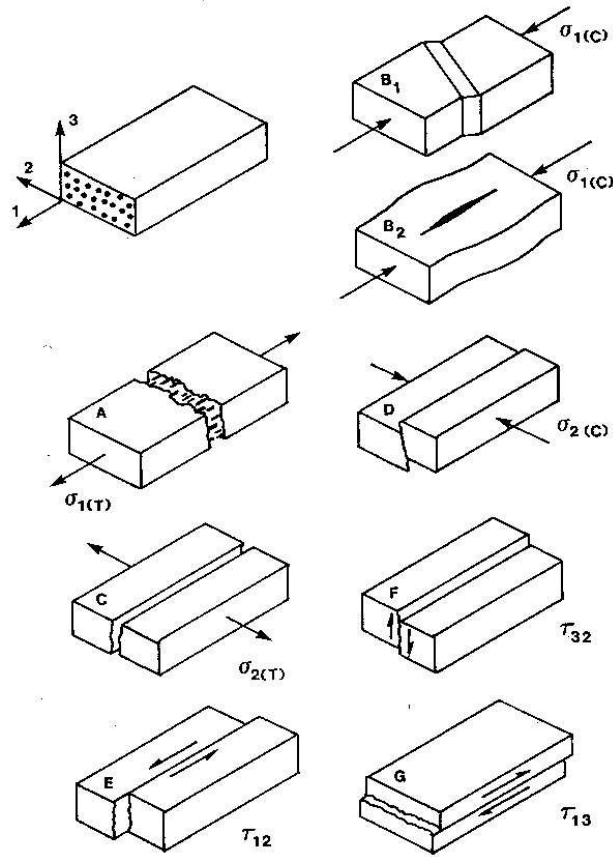
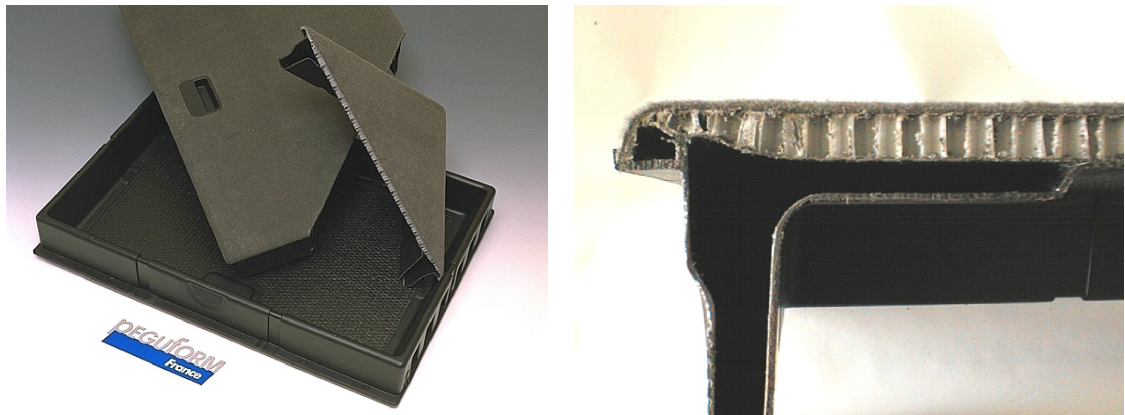


Figure 2.4 Unidirectional composite failure modes [23]



Photograph: Peguform, France

Figure 2.5 Peugeot 806/Evasion glass/PP GMT/Twintex bumper beam structure



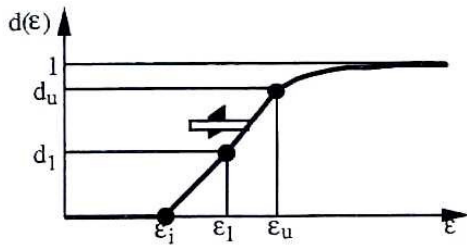
Photograph: Peguform, France

Figure 2.6 Nissan Primera Break PP Twintex/honeycomb structural load floor



Figure 2.7 SACTAC Project PP Twintex side intrusion beam component

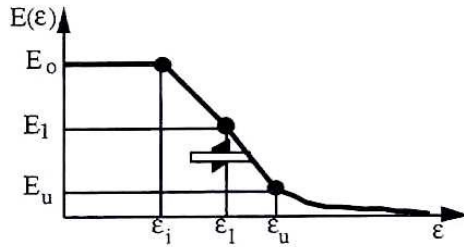
(i) fracturing damage function :



damage function $d(\epsilon)$	range
$\frac{\epsilon - \epsilon_i}{\epsilon_1 - \epsilon_i} d_1$	$\epsilon_i < \epsilon < \epsilon_1$
$\frac{\epsilon - \epsilon_1}{\epsilon_u - \epsilon_1} (d_u - d_1) + d_1$	$\epsilon_1 < \epsilon < \epsilon_u$
$1 - (1 - d_u) \epsilon_u / \epsilon$	$\epsilon_u < \epsilon < \infty$

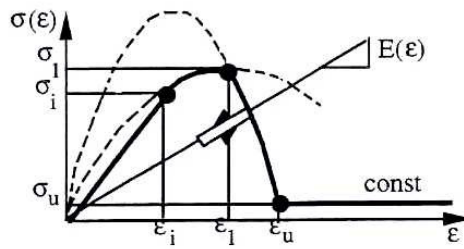
ϵ = equivalent strain E_0 = initial elastic modulus
 ϵ_i = initial threshold strain σ_u = residual constant stress level
 ϵ_1 = intermediate ϵ_u = ultimate strain
 d_1 = intermediate damage d_u = ultimate damage

(ii) modulus damage :



modulus damage
$E(\epsilon) = (1 - d(\epsilon)) E_0$

(iii) stress-strain diagram :



stress-strain relation $\sigma(\epsilon)$	range
$E_0 \epsilon \left(1 - \frac{d_1}{\epsilon_1 - \epsilon_i} (\epsilon - \epsilon_i) \right)$	$\epsilon_i < \epsilon < \epsilon_1$
$E_0 \epsilon \left(1 - d_1 \frac{d_u - d_1}{\epsilon_u - \epsilon_1} (\epsilon - \epsilon_1) \right)$	$\epsilon_1 < \epsilon < \epsilon_u$
$\sigma_u = E_0 \epsilon_u (1 - d_u) = \text{const}$	$\epsilon_u < \epsilon < \infty$

Figure 2.8 Bi-Phase composite material damage model [81]

Chapter 3 Experimental Methods

3.1 Introduction

The numerical material models developed during this work required a number of composite material coupon tests to generate calibration data. To validate the models a further set of coupons were tested.

To support the calibration and validation test work, manufacturing techniques were developed and novel tooling was designed. This technology, applicable to both laboratory and industrial scale processes, was used for the manufacture of the demonstrator components, described in Chapter 6.

3.2 Material Form

The material used for this study is Twintex, a commingled glass fibre reinforced polypropylene matrix composite. Twintex is supplied in various forms including rovings, woven fabric and preconsolidated sheets. A balanced 2 x 2 twill weave (10 ends/in. x 5 double ends/in.) preconsolidated form of the material, with 60% glass fibres by weight, is used during the development of material models in this study. Figure 3.1 shows preconsolidated woven fabric Twintex. The polymer in this case is coloured black and the glass fibres appear white. In the later demonstrator component stages of the work, described in Chapter 6, Twintex with white polypropylene was used. The properties are unchanged between the two and the switch was based on material availability.

Figure 3.2 shows a schematic view of the cross section of one commingled tow. Glass fibres and polymer fibres are bundled together to facilitate rapid forming through preheat and compression moulding.

3.3 Compression Moulding Commingled Thermoplastic Composites

A non-isothermal compression moulding process was used to manufacture all test coupons and the demonstrator components in this work. The process involves preheating, rapid transfer to a press tool and cooling during application of pressure,

see Figure 3.3. The processing parameters, used for compression moulding, were taken from previous work by Wakeman [11][12].

Figure 3.4 shows a schematic representation of the microstructure of a preconsolidated and a fully consolidated thermoplastic composite material. The small voids present in the preconsolidated material are removed as air is expelled from the composite during the forming process.

3.3.1 Tooling Concept

A novel flat plaque tool was developed to produce the mouldings from which all in-plane test coupons were cut. The tool included a blankholder, to maintain tension in the fibres during forming and a shear edge to minimise matrix flow from the tool during the application of pressure and to allow co-moulding with flow materials such as GMT. The blankholder is sprung to put a slight amount of tension in the aligned fibre of the woven material, with the intention of giving improved and more repeatable mechanical properties and to aid formability for more complex components [14].

Figure 3.5 shows the lower half of the tool; the upper half consisted of a simple flat face. The shear edge is also sprung to allow moulding of different thickness plaques using the tool. Figure 3.6 shows the location of these springs. These features were included on the flat plaque tool to validate the concept before application to a larger more complex tool for the demonstrator component programme.

3.4 Material Model Calibration Data

Both the ABAQUS/Standard implementation of the model proposed by Chang et al [79], presented in modified form in Chapter 4 and the PAM-CRASH bi-phase composite model [81] presented in Chapter 5, require a range of material properties for full calibration. This work combines experimental test generated data and published values to produce the required datasets.

Table 3.1 shows the material constants and damage parameters required for the ABAQUS composite material damage model and the source of the values used in this work. Table 3.2 shows the material constants and damage parameters required for the PAM-CRASH bi-phase composite material damage model and the source of the values used.

It was important that data was accurate and gathered under standardised and repeatable conditions. Where possible BS/ISO or ASTM standard test methods were used. Where stress/strain behaviour is presented, the stress is the nominal stress based on the original cross section area of the test specimen.

3.4.1 0°/90° Tensile Test

The 0°/90° tensile test was used to calibrate the Young's Modulus for the fibre direction as well as the failure strength for the ABAQUS damage model. The nominal stress/strain curves were also used to calibrate the PAM-CRASH bi-phase model damage parameters.

The British Standard method for determination of tensile properties of isotropic and orthotropic fibre reinforced composite materials [114] was selected for these tests. Nominally 4mm thick specimens were cut from plaques moulded using the method described in section 3.3. The specimens were produced to the dimensions given in Figure 3.7. Specimens were tested to ultimate failure in an Instron 1195 test machine with a 50 kN load cell, shown in Figure 3.8. The specimen was mounted in shear-locking jaws and a linear extensometer, calibrated to measure up to 10% strain in the longitudinal direction over a 50mm gauge length, was mounted across the central section of the test specimen, see Figure 3.9. Specimens were tested at a displacement rate of 1mm/minute.

Nominal stress/strain results from the tests are presented in Figure 3.10. Ultimate tensile strength was averaged from the results of the eleven specimens tested and Young's Modulus was calculated over a 0% to 0.5% strain range and averaged for the specimens. The mean Young's Modulus was 12.17 GPa and the mean tensile strength was 279 MPa. A typical failed specimen is shown in Figure 3.11.

3.4.2 0°/90° Compressive Test

The ASTM standard [115] was used for testing compressive specimens. The dimensions of the test specimens are shown in Figure 3.12. Experimental results are taken from the work of Wan and Tham [116], who tested four specimens to failure. The tests were performed in the Instron 1195 test machine, using the compressive test fixture shown in Figure 3.13. Strain was measured using a single electrical resistance strain gauge, within the 20mm gauge length. Specimens were tested at a displacement rate of 1mm/minute.

Nominal stress/strain results from the tests are presented in Figure 3.14 and a characteristic failure for one of the four compressive test specimens is shown in Figure 3.15. Ultimate strength was averaged from the results of the four specimens tested. The compressive strength was used for calibration of the ABAQUS damage model and the full stress/strain response was used for calibration of the PAM-CRASH model.

3.4.3 +45°/-45° Tensile Test

The off-axis tensile test was performed using the same specimen geometry, test method, fixture and machine as the 0°/90° tensile test. The specimens were cut from a plaque manufactured with the fibre directions aligned at 45° to the principal axes of the mould tool. Nominal stress/strain results from the tests are shown in Figure 3.16. A typical failed specimen is shown in Figure 3.17. Specimens were tested at a displacement rate of 2mm/minute.

The results from this test were used to confirm the in-plane shear modulus from manufacturers data. The curves were also used during the calibration of the ABAQUS shear degradation and failure model.

3.5 Coupon Tests for Model Validation

For validation of the models described in Chapter 4 and Chapter 5, further tests were used, where possible based on existing techniques. Four test specimen geometries were selected. A compressive +45°/-45° specimen, two tensile specimens with a stress

concentrator, $0^\circ/90^\circ$ and $+45^\circ/-45^\circ$ and a compressive $+45^\circ/-45^\circ$ specimen with a stress concentrator.

3.5.1 $+45^\circ/-45^\circ$ Compressive Test

The geometry of the test specimen for the off-axis compressive test was the same as that used for the $0^\circ/90^\circ$ compressive test. The specimens were cut from plaques manufactured from blanks of material cut at 45° to the principal fibre direction. The specimen was tested in the same rig as the $0^\circ/90^\circ$ compressive specimen, although strain across the gauge length was measured from crosshead displacement and not using strain gauges. Specimens were tested at a displacement rate of 1mm/minute.

The nominal stress/strain results from the tests are shown in Figure 3.18 and a typical failed specimen is shown in Figure 3.19. The side view of the specimen shows that, as well as in-plane damage, out of plane buckling occurred at higher compressive strain levels.

3.5.2 $0^\circ/90^\circ$ Tensile Hole in Plate Test

The geometry of the tensile hole in plate specimen is shown in Figure 3.20. The specimen dimensions are the same as the standard tensile test, but the specimen has a 6.35mm (0.25 inch) hole drilled centrally, to act as a stress concentrator. The test method and rig used were also the same as that used for the standard tensile tests. Strain was measured using an extensometer across a 50mm gauge length of the specimen. Specimens were tested at a displacement rate of 1mm/minute.

Nominal stress/strain results from the tests are shown in Figure 3.21 and a typical failed specimen is shown in Figure 3.22. Photographs were also taken during the test to investigate the visible progressive damage development. Figure 3.23 shows that damage is only visible post failure, due to the rapid development of damage in this test. Figure 3.24 shows a detailed view of the failed area of the specimen, where the glass fibres have broken and the matrix has cracked.

3.5.3 +45°/-45° Tensile Hole in Plate Test

The +45°/-45° tensile hole in plate test used the same specimen geometry and test method as the fibre direction hole in plate specimen. The strain across the 50mm gauge length was measured using an extensometer. Specimens were tested at a displacement rate of 2mm/minute.

Nominal stress/strain results from this test are shown in Figure 3.25 and a typical failed specimen is shown in Figure 3.26. This specimen shows that necking occurred around the hole during the test. This can also be seen in Figure 3.27, which shows the specimen during the test. Clearly, strain in the specimen predominantly occurs around the centrally placed stress concentrator. Figure 3.28 shows the failed part of the specimen, post-test. It can be seen that little fibre failure has occurred and that the ultimate failure mode is fibre pull-out from the polypropylene matrix.

3.5.4 +45°/-45° Compressive Hole in Plate Test

A +45°/-45° compressive test coupon with a stress concentrator, in the form of a central hole was also tested. The specimen was based on the tests carried out by Lessard and Chang [83] in their original damage model development work. The specimen geometry is shown in Figure 3.29. The specimen was tested in a different rig to the other compressive specimens. The rig, specifically developed by Duckett [117], shown in Figure 3.30, end loads the specimen rather than shear loading and has guide plates screwed on to promote in-plane damage in the specimen and minimise buckling. The specimen was tested to a higher displacement than those in Lessard and Chang's [83] work, due to the ductile nature of the thermoplastic matrix. Specimens were tested at a displacement rate of 1mm/minute.

Nominal stress/strain results from the tests are shown in Figure 3.31. A typical failed specimen is shown in Figure 3.32. Like the +45°/-45° compressive test specimens, out-of-plane deformation was observed during the test. This buckling can be clearly seen in the side view of the tested specimen.

3.6 Conclusion

Optimised non-isothermal manufacturing parameters for Twintex have been used throughout this research to manufacture flat plaques. The flat plaques were manufactured using a novel tool design.

Test specimen data has been obtained through a varied programme including standard and novel test methods. This data has subsequently been used to calibrate and validate two material models for predicting the damaging behaviour of Twintex. Fibre direction test results for both tension and compression gave good results up to failure. Off axis tests in compression showed some buckling, which gave uncharacteristic stress results at large strain levels, since the buckling load for the specimens is lower than the load required to deform the test specimens purely in-plane.

3.7 Tables

Material Constants			Source
E_{11}	12.17	GPa	Experimental Test
E_{22}	12.17	GPa	Experimental Test
ν	0.08		Manufacturers Data
G_{12}	1.04	GPa	Manufacturers Data
G_{13}	1.52	GPa	Manufacturers Data
G_{23}	1.52	GPa	Manufacturers Data

Damage Model Parameters			Source
σ_{T1U}	279	MPa	Experimental Test
σ_{T2U}	279	MPa	Experimental Test
σ_{C1U}	137	MPa	Experimental Test
σ_{C2U}	137	MPa	Experimental Test
α	1.4×10^{-5}		Simulation of Experimental Test
ϵ_{12U}	0.45		Simulation of Experimental Test

Failed Material Constants			Source
E_{11F}	1	MPa	Nominal Value
E_{22F}	1	MPa	Nominal Value
ν_F	0	MPa	Nominal Value
G_{12D}	25	MPa	Simulation of Experimental Test
G_{12F}	1	MPa	Nominal Value

Table 3.1 Material constants and damage parameters for ABAQUS model

Material Constants			Source
E_{11T}	12.17	GPa	Experimental Test
E_{11C}	12.17	GPa	Experimental Test
E_{22T}	11.40	GPa	Experimental Test
E_{22C}	11.40	GPa	Experimental Test
E_{33T}	5.3	GPa	Manufacturers Data
E_{33C}	5.3	GPa	Manufacturers Data
ν_{12}	0.08		Manufacturers Data
ν_{13}	0.08		Manufacturers Data
ν_{23}	0.36		Manufacturers Data
G_{12}	1.04	GPa	Manufacturers Data
G_{13}	1.52	GPa	Manufacturers Data
G_{23}	1.52	GPa	Manufacturers Data

Damage Model Parameters		Source
ϵ_{iT}	0.0053	Experimental Test
ϵ_{1T}	0.017	Experimental Test
ϵ_{uT}	0.039	Experimental Test
d_{1T}	0.25	Experimental Test
d_{uT}	0.9	Experimental Test
ϵ_{iC}	0.0053	Experimental Test
ϵ_{1C}	0.017	Experimental Test
ϵ_{uC}	0.039	Experimental Test
d_{1C}	0.50	Experimental Test
d_{uC}	0.9	Experimental Test

Table 3.2 Material constants and damage parameters for PAM-CRASH deviatoric bi-phase model

3.8 Figures

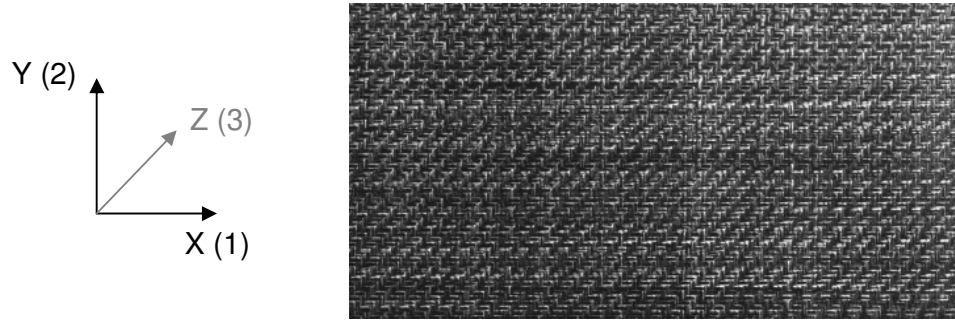


Figure 3.1 Preconsolidated woven commingled Twintex fabric

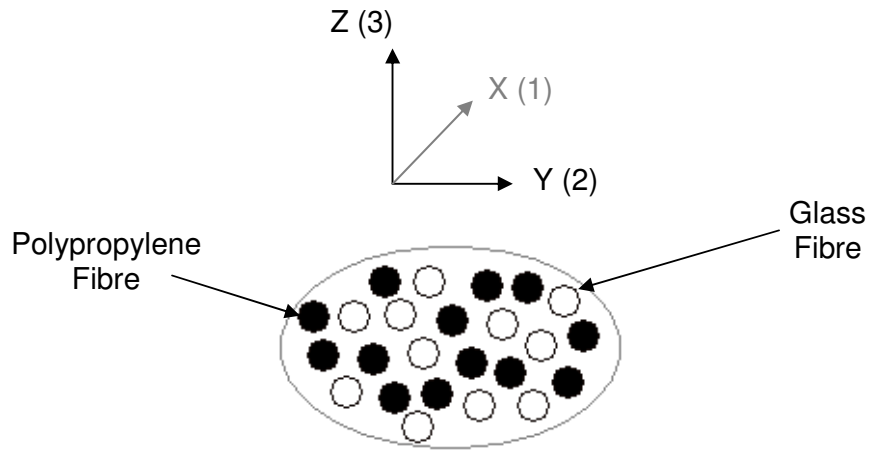


Figure 3.2 Section through commingled tow

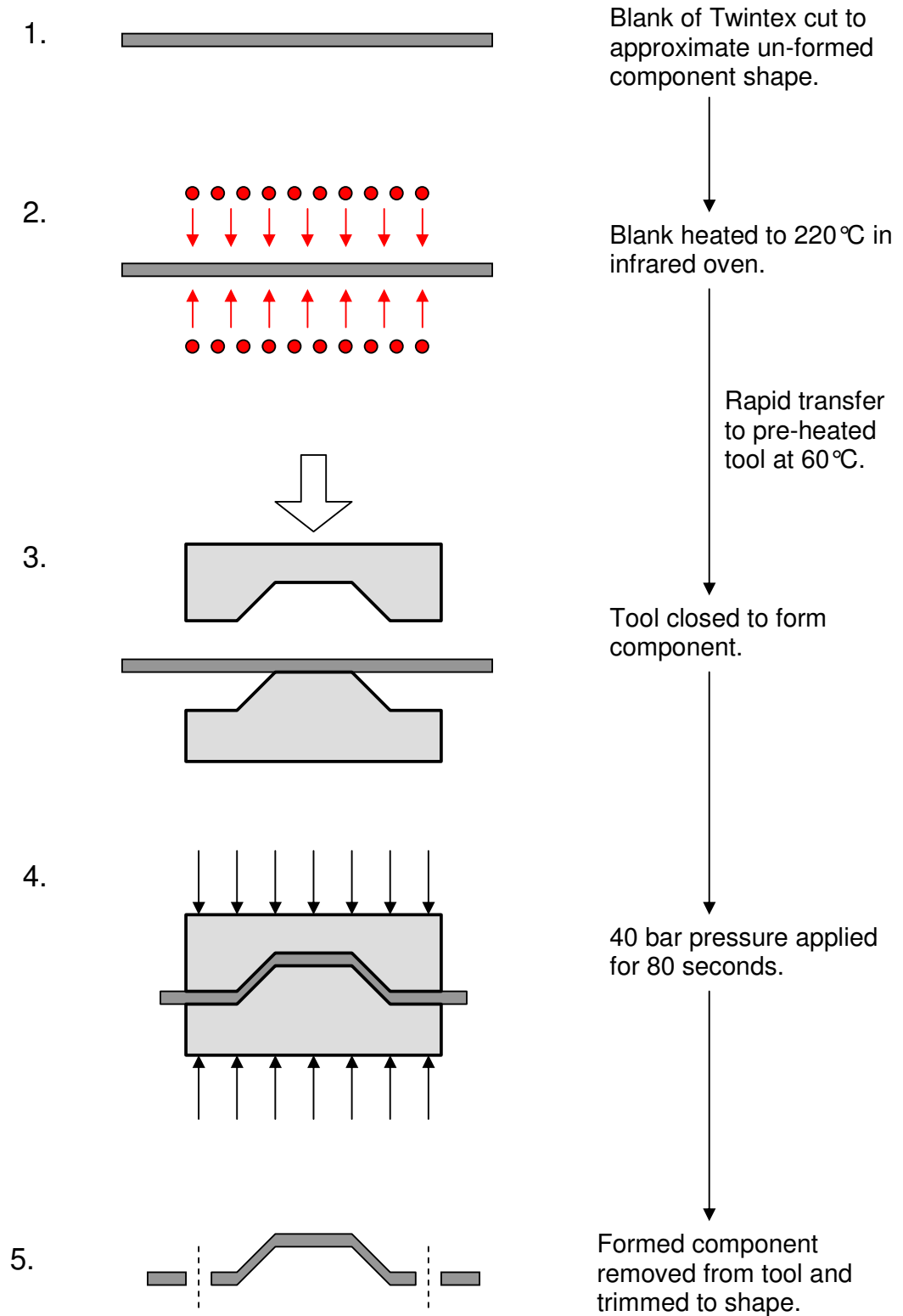


Figure 3.3 Schematic diagram of non-isothermal compression moulding process

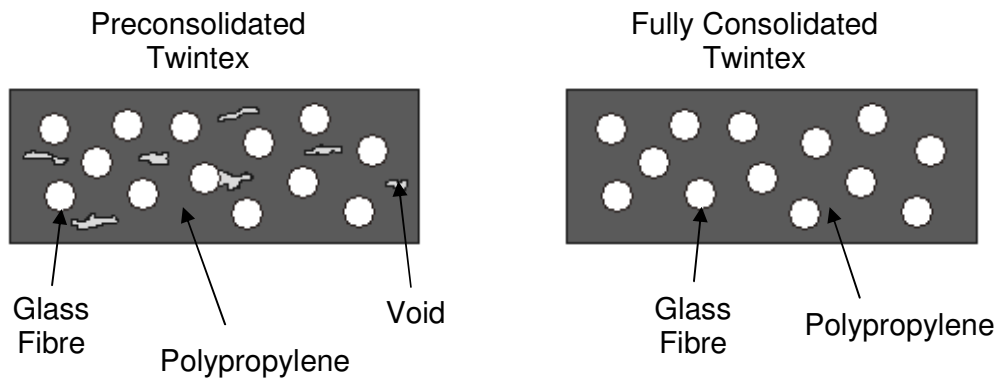


Figure 3.4 Preconsolidated and fully consolidated Twintex micro structure

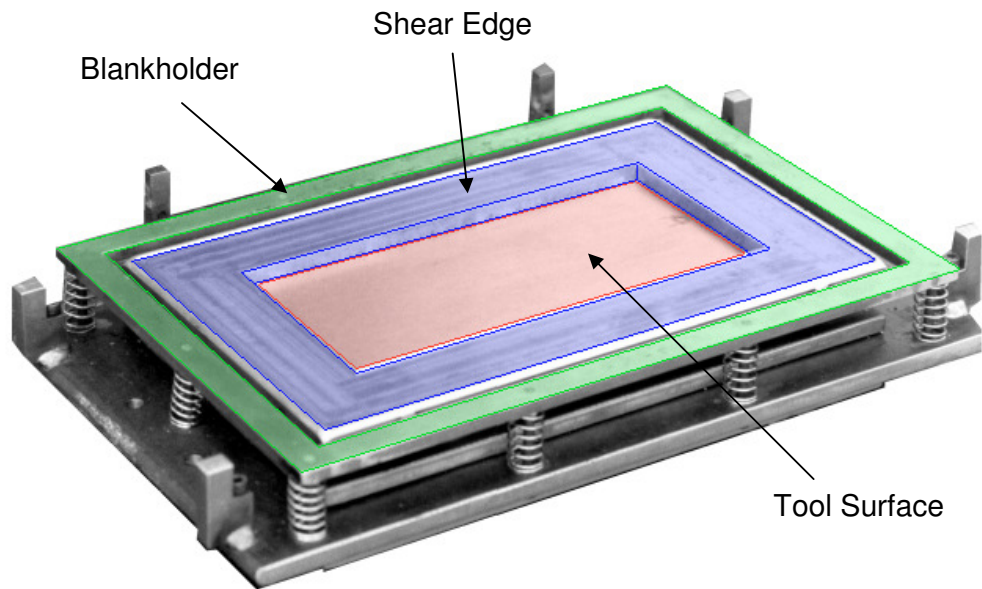


Figure 3.5 Top half of combined shear edge and blankholder tooling concept

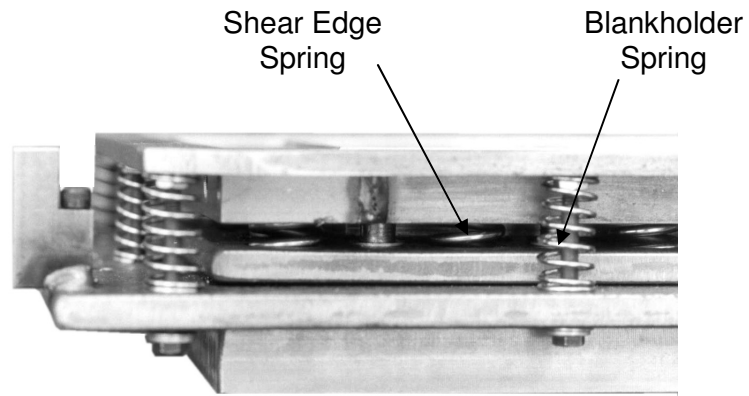


Figure 3.6 Side of tooling concept showing shear edge and blankholder springs

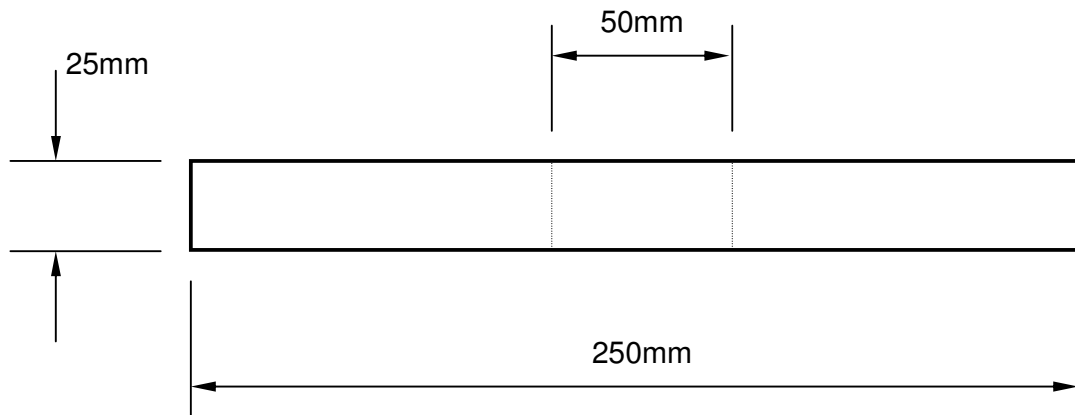


Figure 3.7 Tensile tests specimen geometry



Figure 3.8 Instron 1195 test machine used for tensile coupon tests



Figure 3.9 Tensile test specimen with extensometer mounted

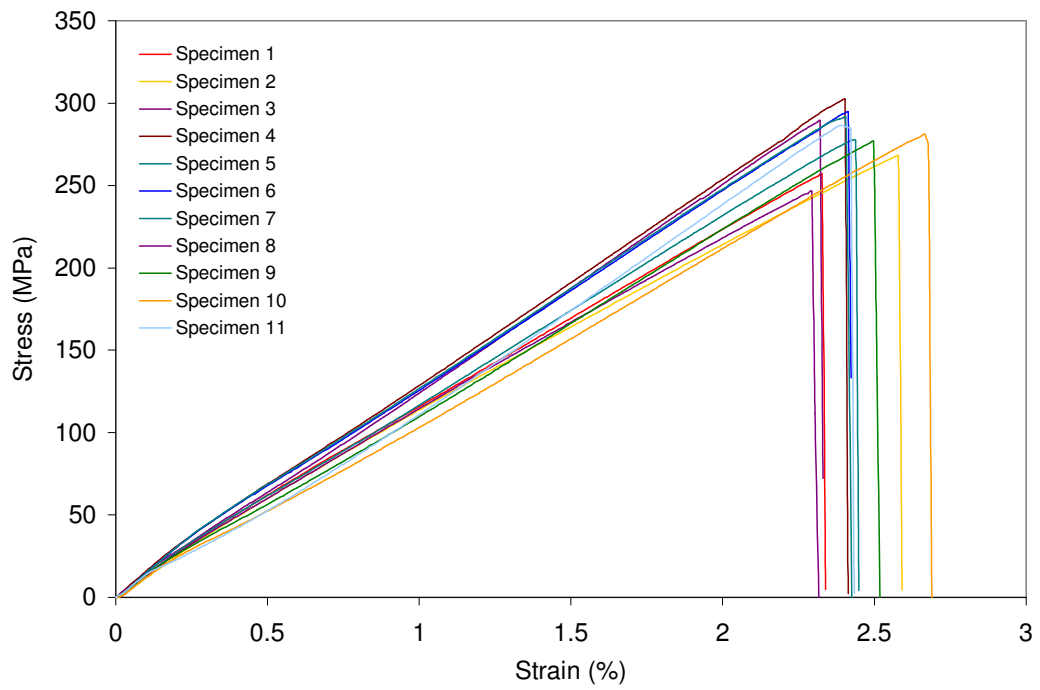


Figure 3.10 0°/90° tensile test results

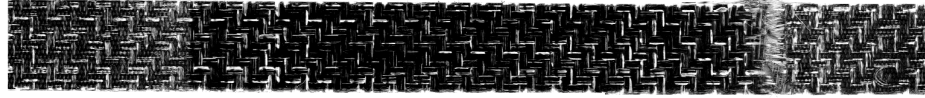


Figure 3.11 Post test tensile $0^{\circ}/90^{\circ}$ specimen

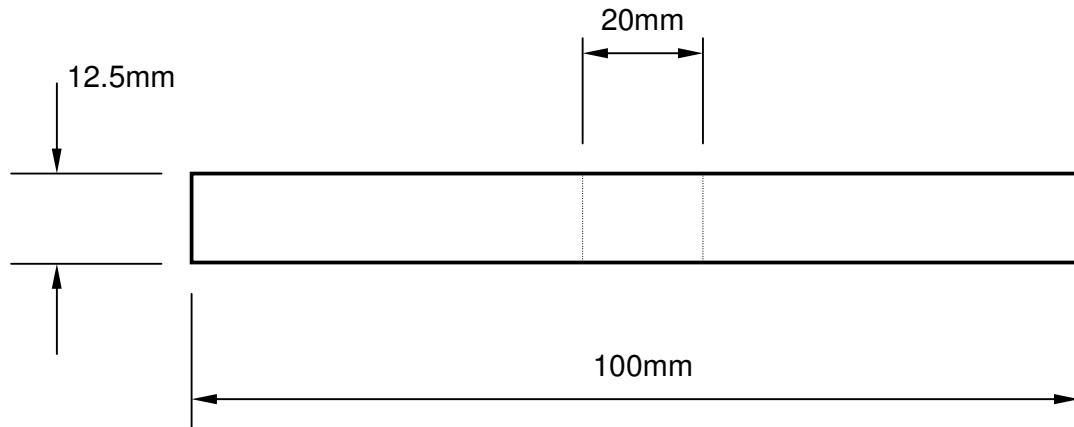


Figure 3.12 Compressive tests specimen geometry



Figure 3.13 Shear loaded compressive test fixture

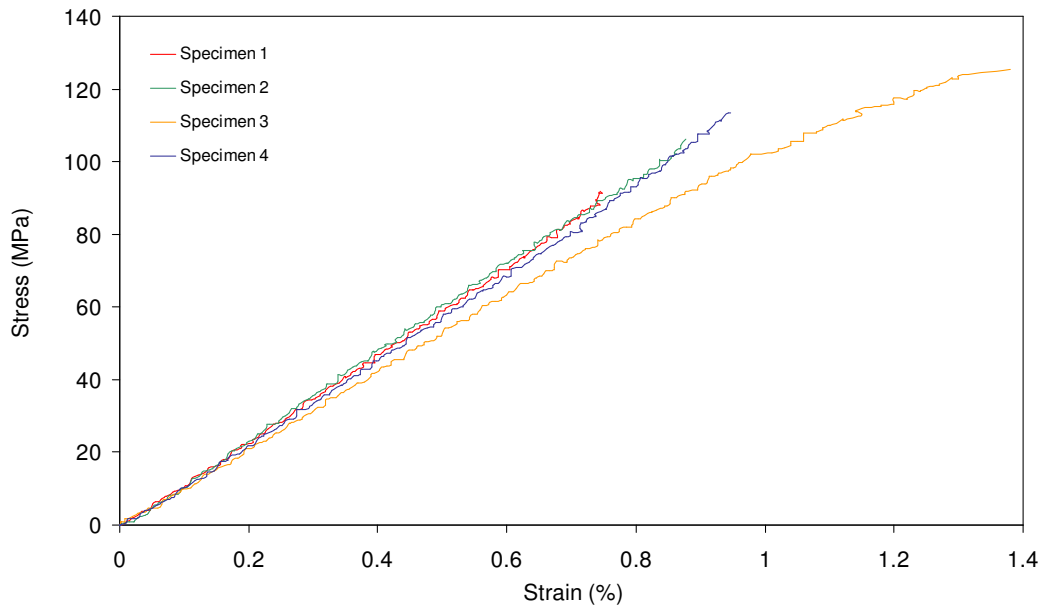


Figure 3.14 0°/90° compressive test results [116]



Figure 3.15 Post test compressive 90°/90° specimen [116]

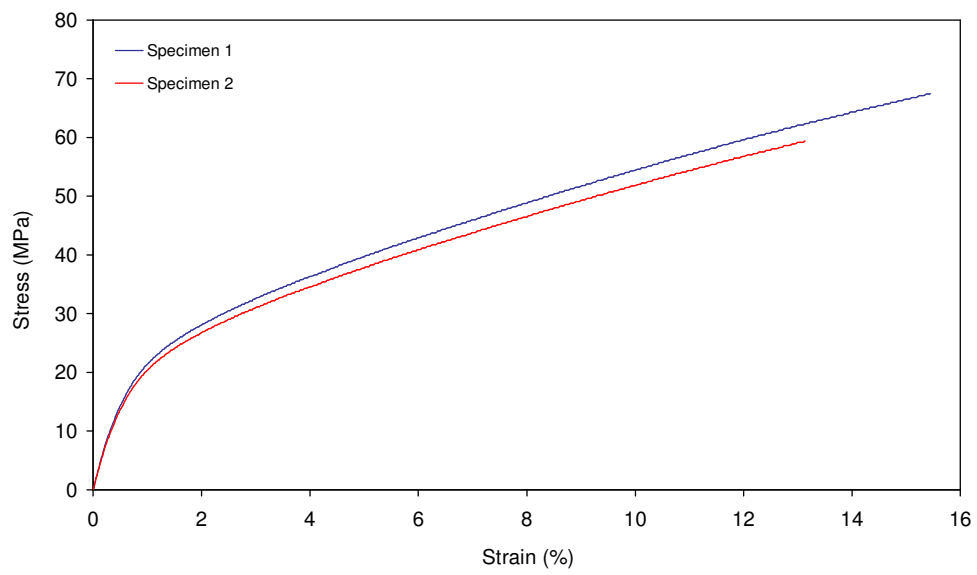


Figure 3.16 +45°/-45° tensile test results



Figure 3.17 Post test tensile +45°/-45° specimen

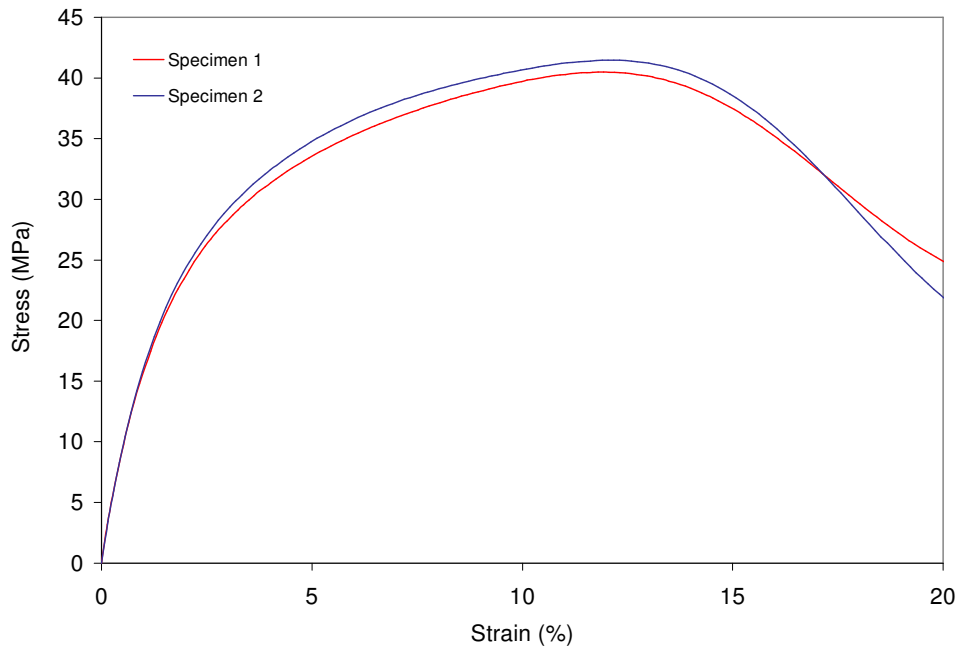


Figure 3.18 +45°/-45° compressive test results



Figure 3.19 Post test compressive +45°/-45° specimen

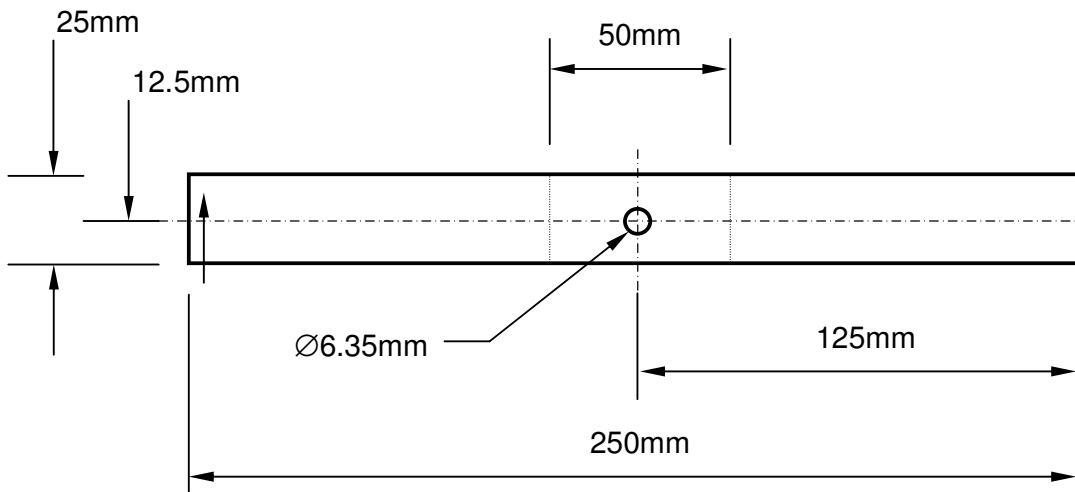


Figure 3.20 Tensile tests specimen with stress concentrator geometry

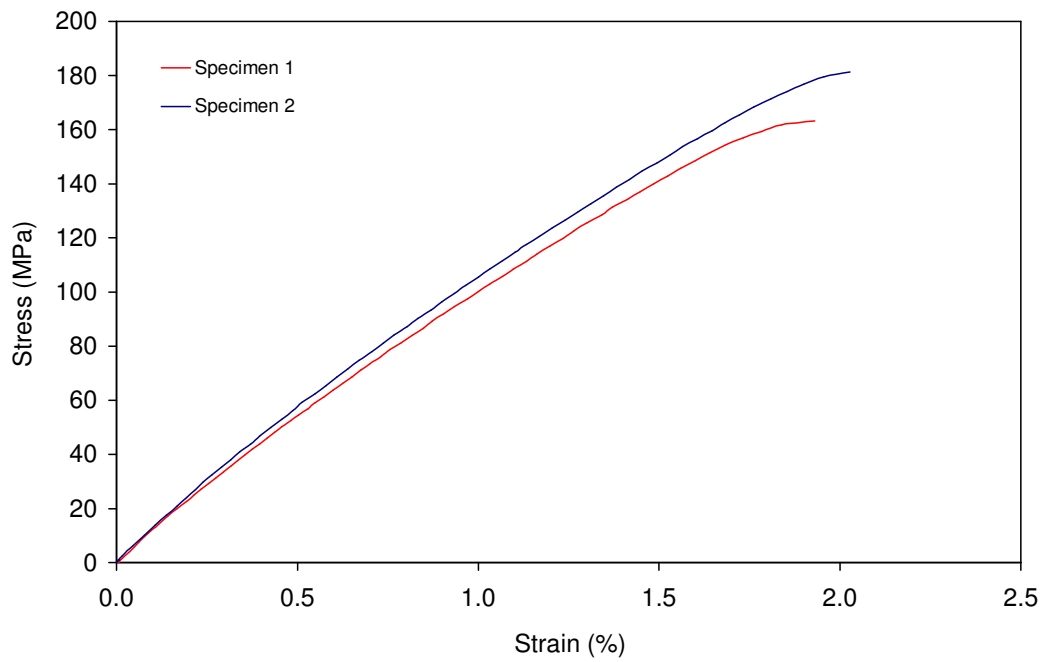


Figure 3.21 0°/90° tensile hole in plate test results



Figure 3.22 Post test tensile 0°/90° specimen with stress concentrator

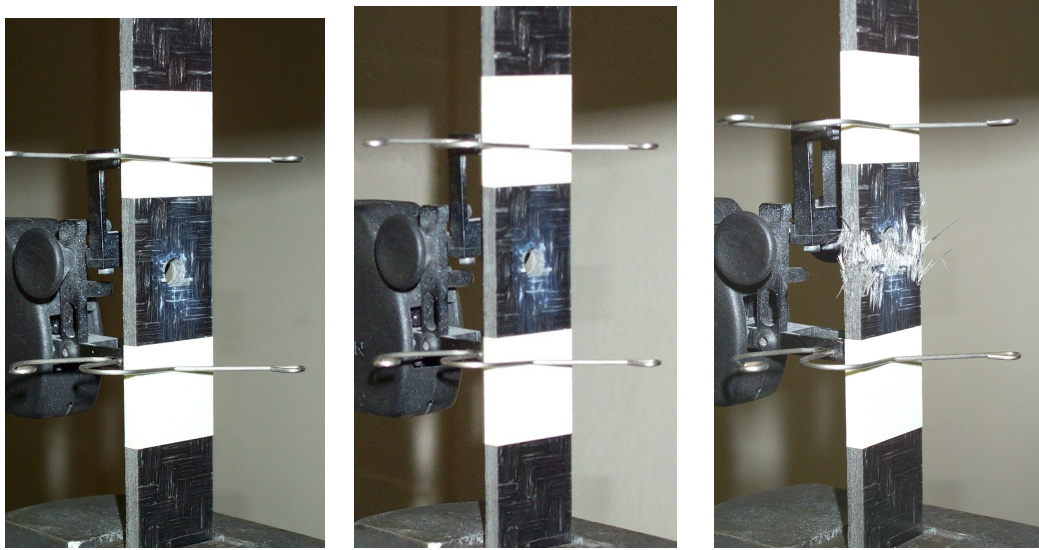


Figure 3.23 Damage development in 0°/90° tensile hole in plate test

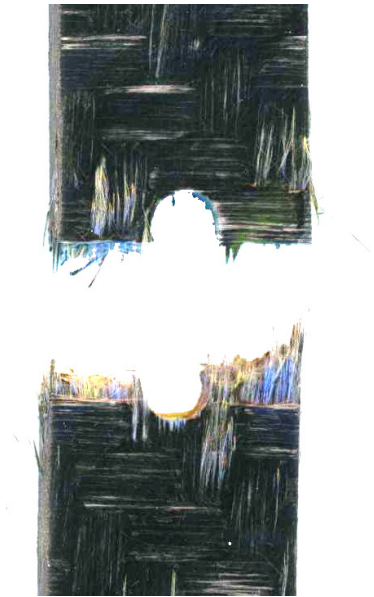


Figure 3.24 Typical failure in 0°/90° tensile hole in plate test

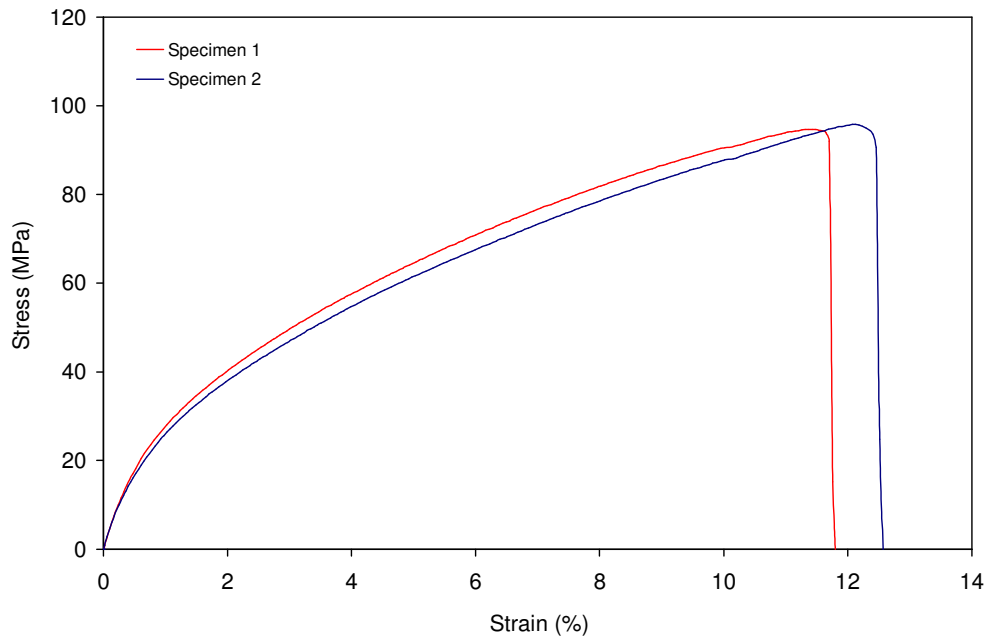


Figure 3.25 +45°/-45° tensile hole in plate test results



Figure 3.26 Post test tensile +45°/-45° specimen with stress concentrator

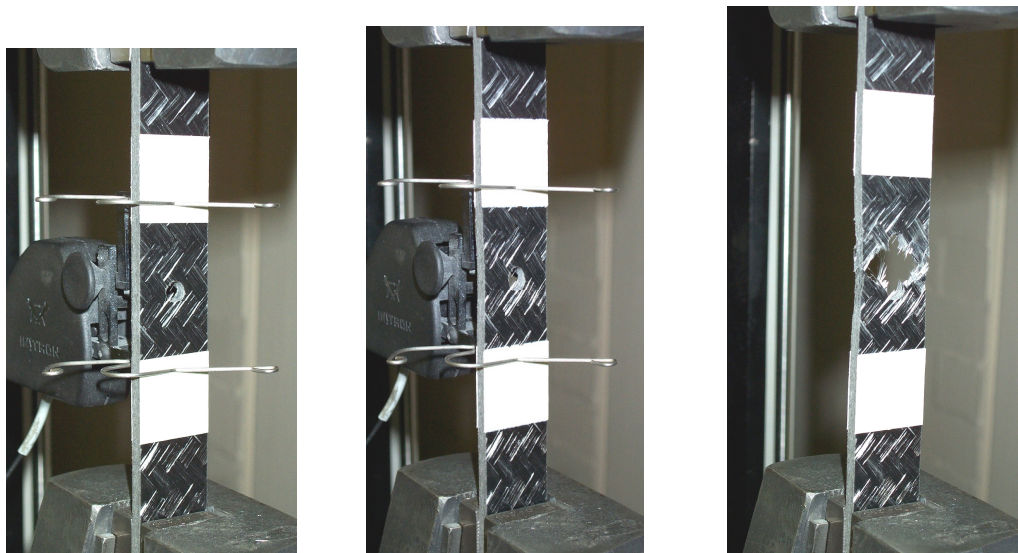


Figure 3.27 Damage development in 0°/90° tensile hole in plate test



Figure 3.28 Typical failure in $+45^\circ/-45^\circ$ tensile hole in plate test

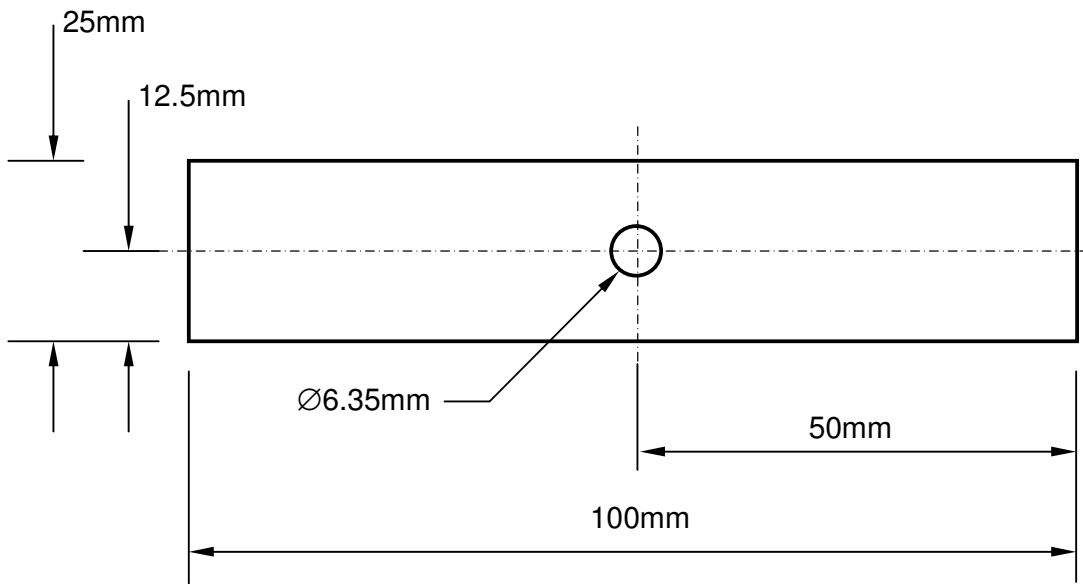


Figure 3.29 Compressive test specimen with stress concentrator geometry

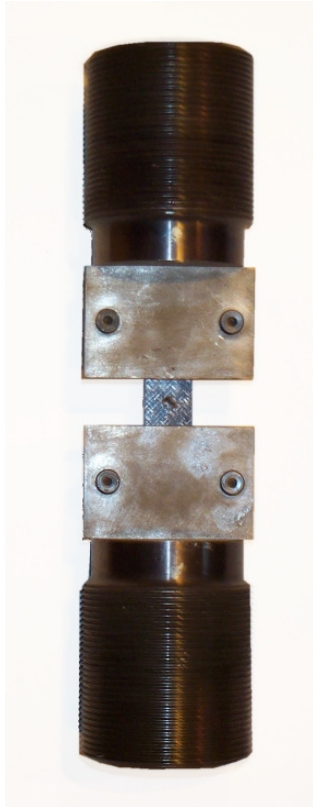


Figure 3.30 End loaded compressive test fixture

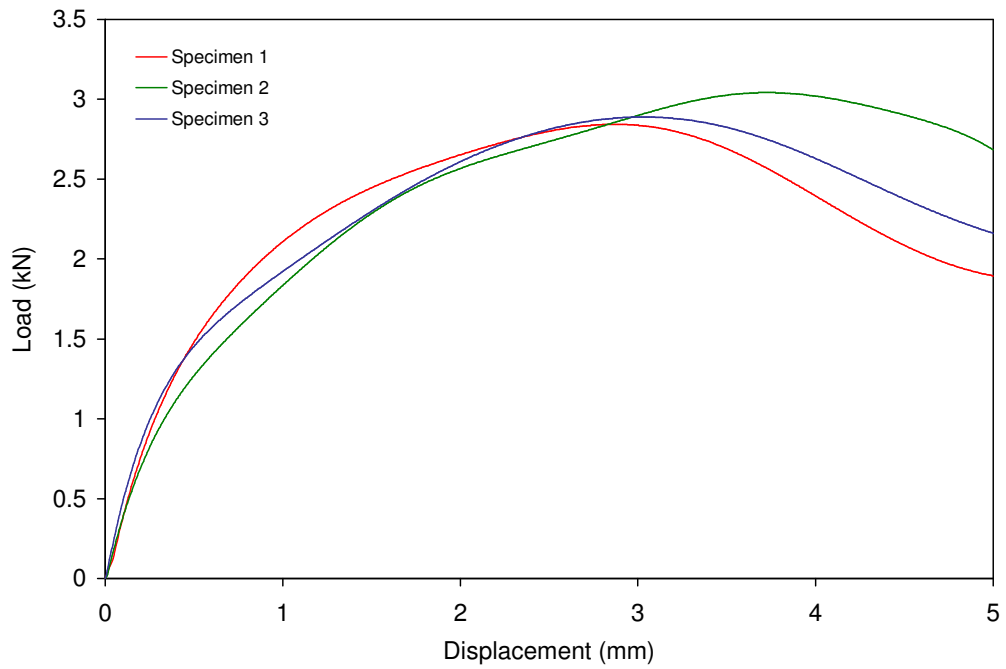


Figure 3.31 +45°/-45° compressive hole in plate test results



Figure 3.32 Post test compressive $+45^{\circ}/-45^{\circ}$ specimen with stress concentrator

Chapter 4 Implicit Finite Element Damage Modelling

4.1 Introduction

An implicit finite element analysis technique is usually employed for small displacement stress analysis. An iterative solution of this type is therefore usually not particularly suited to the large displacement analysis of composite materials, whose post first-ply failure behaviour is often highly non-linear. The method can though be adapted to cope with the onset of damage in composites and the consequent reduction in material properties.

Rather than analysing a single displacement step, an incremented technique with relatively small displacements can be used. If failure criteria are implemented in the material model, leading to progressive degradation of elastic material properties, a composite component can be simulated as it displaces and continuum damage evolves. An example of this type of analysis, implementing a progressive damage model developed by Chang and Lessard [79], is described in Chapter 2, where it is shown that this method can be used with some success to model in-plane damage development around a stress concentration for thermoset matrix composites.

This part of the work attempts to retain the methodology, but develop the model proposed by Chang and apply this to thermoplastic matrix composites. Since the Chang model was developed for unidirectional thermoset matrix composites, the ductility of the matrix and the fibre architecture differ significantly from those used in this study. Failure in the composite, modelled by Chang using either fibre or matrix failure criteria, is therefore represented here using a ply based maximum strength approach, although the shear damage methodology is retained. The modification of the damage and failure prediction laws allows more accurate simulation of the behaviour of a woven composite and enables the model to be calibrated with a small range of standard coupon tests.

The model is implemented as a user defined material within the ABAQUS/Standard implicit finite element code [118]. Failure checks and elastic property reduction are performed by a FORTRAN subroutine subsequent to each load step.

Validation of the model is performed for a number of in-plane load cases including tension and compression and for an in-plane specimen with a stress concentrator, both in the fibre direction and for off axis loading.

4.2 Analysis Technique

Since the modelling strategy developed during this research was to be implemented in larger analyses with more complex geometry than those used for laboratory scale validation tests, a primary requirement was that the methodology used could be efficiently scaled up to larger components. Often, techniques for modelling progressive damage in composite materials rely heavily on highly refined meshes, mixed shell and solid elements, multi-layered shells or complex and numerically expensive sub models to capture behaviours such as micro-cracking and delamination [15]. The material damage model developed here is used with standard, full and reduced integration, shell elements. These are typical of the types of elements used in industry for stress analysis solutions. Hence the material model can be transferred to larger simulations without the need for costly refinement of, or alteration to, existing meshes.

Single layer shell element models were generated using HyperMesh version 4.0. Subsequent editing of input decks was carried out to modify the material cards and implement the damage model.

4.2.1 Finite Element Code

The choice of an implicit finite element code for non-linear problems of this sort is often overlooked. However through careful material model development an implicit stepped solution has the potential to offer a computationally efficient solution when compared to an explicit code. The ABAQUS/Standard implicit finite element code [118] was selected for this work, as it allows a significant degree of user input within available material models. This versatility is facilitated by the *user defined material* card within the ABAQUS input deck, which gives control over the elastic material constants used by the analysis.

4.2.2 Material Model

The material model selected for the analysis was *ELASTIC TYPE=LAMINA. The model allows the definition of a single ply of an anisotropic lamina material using the following elastic material constants E_1 , E_2 , ν_{12} , G_{12} , G_{13} , and G_{23} .

The model includes the switch, DEPENDENCIES=3, which gives user control over the elastic constants at the start of each load increment. 3 field variables are used to define the values assigned to the material properties, relative to their initial, undamaged, state. The field variables are flags, which range from 1 to 0 and define a variation of the elastic material constants between the initial state, given in the first line of the material model, and the minimum values described in the field variable dependent lines of the material model.

Field variables can be set at the start of each increment by calling a USDFLD subroutine from the *USER DEFINED FIELD card. The USDFLD routine allows output variables from the analysis to be used to compute current values of field variables and return these to the material model. In the case of the damage model developed for this work, the subroutine uses stress and strain results from the analysis to calculate accumulated damage and adjusts the field variables accordingly.

4.2.3 Element Definition and Formulation

For all the analyses performed in this section of the research, Kirchhoff thin shell elements are used [118]. These elements were selected as they can be used to accurately model the behaviour of structures, which have a section thickness that is small relative to the overall dimensions of the component. Test specimens modelled are typically over 100mm long and have a section thickness of less than 4mm. The final demonstrator component, described in chapter seven, is over 1000mm in length and has a maximum section thickness of 8mm. In practice, considering the limitations of the non-isothermal compression moulding technique used in this research, it would be unlikely that a component could be produced for which a shell element model was not the most suitable analysis technique.

The shell elements used, are, in the case of quadrilateral elements, defined by four nodal points. These nodes describe the spatial position of the element and also, using the 'right-hand rule', define the normal direction of the shell. This normal is critical for correct definition of laminate ply sequences. During the calibration and validation of the model a comparison of the full and reduced integration elements available in ABAQUS was made. All test specimen simulations were run with both element types, those being S4 and S4R. Where the element code relates to the following:

S4 - Stress/displacement element, **4** nodes

and:

S4R - Stress/displacement element, **4** nodes, **Reduced** integration.

ABAQUS stress/displacement shell elements use a Lagrangian formulation where the element displaces according to the behaviour of the constituent material. Gaussian Quadrature is used to solve for static equilibrium at each integration point within the element.

4.2.4 Section Definition

Shell elements are defined in ABAQUS using the *SHELL SECTION card. This card specifies the shell element thickness, material and number of through thickness integration points. The optional COMPOSITE parameter allows the user to define discrete layers and orientations. Using this type of section definition a complex, multiple layered, laminate can be accurately described and assigned to shell elements.

Details of the various ply and orientation section definitions, used in the analysis of each of the in-plane damaging specimens simulated, are given later in this chapter.

4.2.5 Definition of Orthotropy Direction

The orientation of the fibre direction for each composite material ply can be defined independently. The *ORIENTATION card is used to, with either a local or the global coordinate system, assign the fibre directions of the woven composite. In this case, for the analysis of flat rectangular test specimens, all materials are oriented relative to the

global coordinate system. If the model were to be used for a spherical or cylindrical component a local coordinate system could be defined and the composite oriented accordingly. This global coordinate orientation technique, when used in conjunction with shell elements, identifies the orientation direction which lies closest to the plane of each shell and projects the principle fibre directions to that plane accordingly. This feature is used extensively in the analysis performed on demonstrator components, detailed in Chapter 6.

4.3 Development of the Damage Model

The model was developed to represent the in-plane damaging behaviours of a balanced weave composite material. Three critical, ply level, damage modes were identified through review of previous work. These were tensile, compressive and shear damage. These modes represent, at a ply level, more complex micro damage accumulation. For example, in the case of tensile damage, degradation of material properties could be the result of matrix cracking, fibre matrix debonding, fibre failure or a combination of all three. The model, although not identifying these discrete damage types, represents the accumulated effect of them through calibration from physical test. The assumption is therefore made that the type of damage seen in laboratory tests is similar to that developed in a more complex geometry under large displacement loading. The initial testing and simulation and subsequent validation work substantiates this hypothesis.

The model implements numerical representations of the global ply damage and failure modes identified. Within the user defined damage model subroutine, these criteria are used to directly alter the elastic material properties within the composite material model.

4.3.1 Tensile Failure Model

In this model, the basic anisotropic linear elastic tensile behaviour of the standard ABAQUS composite material is modified, by including a failure check. It was felt after analysis of results from tensile test specimens that degradation of the modulus prior to failure was not required, since the behaviour of Twintex is dominated by the glass fibres. This leads to a characteristic linear elastic behaviour with catastrophic

failure caused by fibre breakage. To simulate this, a maximum stress criteria is implemented in the fibre direction, which when exceeded results in a reduction of the Young's modulus in both the 1 and 2 direction to a nominal value of 1MPa and the reduction of Poisson's Ratio to 0. This represents the loss of local tensile load carrying capacity in both directions when fibre failure occurs in a composite ply (eqn. 3.1).

$$\text{Failure identified if:} \quad \sigma_{11T} > \sigma_{T1U} \quad (3.1)$$

Since Twintex is a balanced weave composite, the behaviour in the two principal in-plane directions is identical. Hence the tensile failure check in the 2 direction also uses a maximum stress criteria (eqn. 3.2), which in this case reduces the elastic constants in the same way as if tensile failure in the 1 direction were identified.

$$\text{Failure identified if:} \quad \sigma_{22T} > \sigma_{T2U} \quad (3.2)$$

4.3.2 Compressive Failure Model

The Young's modulus of the composite ply applies to both the tensile and compressive elastic behaviour of the material. Therefore, if tensile failure has occurred and the corresponding modulus has been reduced to a nominal value, the composites ability to carry compressive load is also compromised. In turn if compressive failure has been identified the compressive and tensile load carrying capacity is reduced, again to a nominal modulus of 1MPa. The compressive failure of Twintex if evaluated in-plane, i.e. buckling effects are discounted, can also be represented as a linear elastic behaviour followed by catastrophic failure. Hence the compressive failure model uses, like the tensile model, a maximum stress criteria. This criteria is used in both the 1 and 2 directions of the composite ply (see eqn. 3.3 and eqn. 3.4).

$$\text{Failure identified if:} \quad \sigma_{11C} > \sigma_{C1U} \quad (3.3)$$

$$\text{Failure identified if} \quad \sigma_{22C} > \sigma_{C2U} \quad (3.4)$$

4.3.3 Shear Damage and Failure Model

The shear damaging behaviour of the composite is more complex than the relatively simple linear elastic followed by ultimate failure of the tensile and compressive models. When the woven ply is loaded in shear, matrix damage is accumulated over a large strain range before ultimate failure. It is therefore not possible to use a maximum stress based failure criteria to describe the ply.

Following Chang's approach [79], the shear properties of the material are degraded as a cubic function of the shear stress. For each load/displacement increment, at each integration point, the value of the shear stress is used to adjust the in-plane shear modulus, G_{12} (see eqn. 3.5). In the model, α is a fitting parameter and defines the non-linear relationship between shear stress and strain.

$$\epsilon_{12} = \frac{\sigma_{12}}{G_{12}} + \alpha \sigma_{12}^3 \quad (3.5)$$

In the model, G_{12} tends to a value of 25MPa, denoted G_{12D} . This modulus when reached is used up to the point at which ultimate ply shear failure is identified. The value of this damaged, but not failed, shear modulus was arrived at through calibration from experimental test.

In Chang's work an ultimate shear failure criteria is included, based on the fibre buckling strength and laminate shear strength. In this study, where calibration from a basic suite of experimental tests was a primary requirement, a maximum shear strain criteria is used (see eqn. 3.6). When this failure is identified, shear loads can no longer be carried, therefore the in plane shear modulus, G_{12} , is reduced to a nominal value of 1MPa.

$$\text{Failure identified if:} \quad \epsilon_{12} > \epsilon_{12U} \quad (3.6)$$

4.3.4 Implementation

As mentioned previously, the material model includes the `DEPENDENCIES=3` switch, which allows the elastic material properties to varied using user defined field variables. Within the model these dependency variables are returned at each step of the analysis by calling the `USDFLD` subroutine. This routine is written using the

FORTRAN programming language and implements the mathematical damage and failure checks of the model. Appendix A gives the code used for the model and includes the tensile compressive and shear failure checks and the shear damaging behaviour. The form of the mathematical implementation of the shear damage model is arrived at through manipulation of Equation 3.5. A derivation of the shear damage formulation is given in Appendix B.

The field variables used for the variation of the material properties are output during the analysis and identify damage or failure in the specimen. Field variable 1 (FV1) denotes tensile or compressive fibre direction failure. This variable is set initially at 0, no failure, and rises to 1 when ultimate failure is identified. Similarly, field variable 2 (FV2), is initially 0 and becomes 1 when shear failure is identified. Field variable 3 (FV3) relates to shear damage and varies between 0 and 1 as shear damage accumulates during the analysis. Figure 4.1 summarises the implementation of the damage model as a FORTRAN subroutine in the ABAQUS/Standard finite element package.

4.4 Calibration

To calibrate the damage model, material properties were taken from Saint-Gobain Vetrotex published information [18] and calibration tests. The tests were used to confirm manufacturer's information for the processing techniques employed and to identify the material ultimate strengths and fitting parameters required for the model. A detailed description of experimental test work and a summary of the material properties, failure criteria and calibration parameters used in the model are given in Chapter 3. The calibrated input cards for the ABAQUS field dependant material are given in Appendix C. Throughout this section of the work, simulation results, like the experimental results in Chapter 3, are presented as nominal stress/strain.

4.4.1 Simulation of Calibration Coupon Tests

The tests used to derive the model parameters were simulated using the damage model to confirm that calibration coefficients and material properties were correct and that the experimentally identified failure mode was being predicted in the correct location and at the correct nominal stress and strain level.

4.4.2 Tensile 0°/90° Test Simulation

The finite element mesh used to model the 0°/90° tensile coupon tests is shown in Figure 4.2. 170 reduced integration four node shell elements were used, with a nominal edge length of 5mm. The aspect ratio of the elements in the areas where the specimen is gripped in the test is increased, since these nodes were either constrained in all degrees of freedom at the fixed end, or constrained with a constant displacement boundary condition at the moving end. This boundary condition arrangement was felt to be the most accurate representation of the shear loading jaws used to clamp the coupon during experimental test.

The simulation was set to run to a total displacement of 5mm, which equates to a strain level of approximately 3.33% in the gauge length of the specimen. The increment for each analysis step was set to 0.025mm or 0.0167% strain. This increment was selected to allow the model to accurately identify the point at which damage starts to occur in the test. Larger increment sizes could lead to failure being identified at an incorrect displacement due to the resolution of the solution. Further investigation of the sensitivity of the model to increment size was undertaken and a minimum solution resolution is recommended in section 4.6.1.

Element stress/strain and field variable status output from the analysis was requested after every fifth increment. This was chosen to minimise the size of output files from the analysis, since reaching the disk quota limit before completion of an analysis would cause premature termination. Nodal output was requested every second increment, resulting in 100 data-points for a full tensile test simulation run. This was felt to be sufficient to provide output for comparison with experimentally derived stress/strain curves.

Since the experimentally derived stress/strain behaviour in the fibre direction is predominantly linear elastic with a catastrophic failure, the finite element simulation curve shows good correlation, see Figure 4.3. The strain at failure for the simulation is slightly lower than experiment, since in the test, material behaviour is not truly linear elastic throughout. As the coupon nears the ultimate stress of the material, there is a slight reduction in modulus. This is observed from approximately 1% strain where the experimental curve dips below the simulation result. This effect is negligible though

when considering the spread of failure strain results from experiment. The calibration for tensile failure is therefore shown to be accurate and the model successfully predicts the behaviour of Twintex in tension.

The final damaged state of the specimen is shown for test and simulation to compare the damage prediction, see Figure 4.4. In this case it is not possible to visually draw conclusions from the result as the final plot state of the field variable for tensile damage is prior to the failure event. Once failure has occurred a large amount of element deformation takes place and a static equilibrium solution cannot be converged and hence a plot of the failed element(s) cannot be generated.

4.4.3 Compressive 0°/90° Test Simulation

The finite element mesh used to model the compressive coupon tests is shown in Figure 4.5. 224 reduced integration four node shell elements were used, with a nominal edge length of approximately 1.5mm within the gauge length area of the specimen. Although the full specimen is modelled, the majority of the specimen in this case is constrained, since the loading is applied with locking jaws which transmit the compressive load to the specimen. The gauge length of the specimen is minimised to alleviate the problem of buckling as the specimen is loaded.

The compression test results in Figure 4.6 show good correlation between FE and experimental stress/strain behaviour. The form of the curve is similar to that seen in the tensile test. The behaviour is predominantly linear elastic with an ultimate failure. Figure 4.7 shows the predicted damage at the end of the simulation. Compressive damage is predicted throughout the gauge length of the specimen. The damage seen in test shows a line of failure in the gauge length of the specimen.

4.4.4 Tensile +45°/-45° Test Simulation

+45°/-45° tensile tests were used to calibrate the shear degradation part of the damage model. Figure 4.2 shows the mesh used for simulation of these specimens. This mesh is identical to that used in the 0°/90° tensile test simulations, although the material is oriented differently.

Figure 4.8 shows the comparison between experimentally observed stress/strain in the gauge length and simulation result. The fitting parameter, α , and the damaged shear modulus was calibrated iteratively using this simulation and test result. These specimens exhibited a much larger strain to failure than the $0^\circ/90^\circ$ tensile specimens, due to gradual reduction of the shear modulus during the test. The results show that at strains of up to 20% in the gauge length, the implicit elements and the shear degradation model can reproduce the shear properties of the woven material. Figure 4.9 shows a comparison between an experimentally damaged specimen and the predicted damage from simulation. The simulation plot shows that the specimen damages is shear from the early stages of the simulation, but does not fail in a catastrophic manner until very high strain levels. During this calibration process, the in plane shear modulus, G_{12} , was also adjusted from 1.20GPa to 1.04GPa to improve the correlation between simulation and test.

The ultimate shear failure, which is also calibrated from this experimental test, shows that the simulation predicts failure at approximately 19% strain in the gauge length of the specimen.

4.5 Validation

Various coupon tests were simulated to validate the damage model calibration. These simulations are classed as validations, since no alteration of properties or damage parameters was undertaken after the calibration from the three simple tests detailed in sections 4.4.2 to 4.4.4. These specimens were similar to those used for the calibration, but included a stress concentration in the form of a circular hole, except in the case of the $+45^\circ/-45^\circ$ compressive specimen, which did not include a stress concentration.

4.5.1 Compressive $+45^\circ/-45^\circ$ Test Simulation

The compressive $+45^\circ/-45^\circ$ simulation uses the same finite element mesh as the $0^\circ/90^\circ$ compressive specimen, see Figure 4.5. Since the parameters describing the shear behaviour of the material were calibrated from the off axis tensile test, there were no parameters taken from this test specimen.

The stress/strain response from experiment and simulation are shown in Figure 4.10. The correlation between the curves is not as good as that seen in previous tests, and the simulation is predicting the specimen to be stiffer than is actually observed in experiment. This phenomenon can be explained by observing the damaged specimen and predicted damage in the model, see Figure 4.11. The simulation shows a steady build up of in-plane shear damage, whereas the test specimen has clearly deformed out of the plane of the test. This out of plane deformation explains why the experimentally derived curve shows a lower stress level than the simulation result.

The simulation result also shows a stepped response. This is caused by fibre compressive failure occurring in the model and resultant reduction of the local fibre direction modulus of the specimen in certain elements. The location of this failure can be seen in Figure 4.30, where a similar behaviour is observed in the full integration shell element model of the test. This stepped behaviour continues to occur after 5% strain in the gauge length of the specimen.

This result shows that the model is accurate for in-plane damage modes, but when material deformation occurs out of plane, the model cannot accurately capture the behaviour. This shows that the model should be used with care if out of plane, buckling deformation is expected.

4.5.2 Tensile 0°/90° Hole in Plate Test Simulation

Figure 4.12 shows the finite element mesh used to simulate the tensile hole in plate specimen. The specimen was manufactured exactly as the plain tensile test specimens, but subsequently a hole was drilled to represent initial damage.

Figure 4.13 shows the stress/strain response over the central 500mm gauge length for the test and simulation result. The simulation shows good correlation with experiment, although damage and subsequent ultimate failure is predicted to occur at a lower stress level than that seen in experiment. This is due to a whole element being ‘failed’ when stress levels around the hole reach the failure strength of Twintex. In the experimental test, the stress concentrator causes only a small amount of failure, initially at the edge of the hole, which does not fail the specimen catastrophically. This can be seen in the experimental curve as a slight reduction in modulus and

shallowing of the stress/strain curve. In the simulation, as soon as failure has occurred in one element, load is transferred and the surrounding elements also fail catastrophically.

The damage variable plot and failed test specimen, shown in Figure 4.14, highlight this catastrophic failure seen in the simulation, where at the final step of the analysis a whole group of elements has failed during the same iteration. This large failure occurs at a higher load in the experimental test, but as expected, in the same location, around the stress concentration.

4.5.3 Tensile +45°/-45° Hole in Plate Test Simulation

The +45°/-45° tensile test with a stress concentrator uses the same mesh as the fibre direction test, see Figure 4.12. As in the fibre direction test, the shear damage part of the model over predicts damage around the hole for the tensile stress concentrator situation. This is shown by Figure 4.15 where the experimental stress/strain plot shows a much stiffer response than the simulation. In this case, like the previous 0°/90° specimen with a stress concentrator, the model over predicts damage, resulting in reduced stiffness in the simulation. This result could also be explained by the inability of the model to account for the reorientation of fibres in areas of high shear strain. This could potentially lead to a stiffening effect around the hole, which is not modelled accurately. This phenomenon is discussed in more detail in Chapter 7.

The damage contours from the model, in Figure 4.16, show shear damage developing throughout the specimen and particularly around the hole from the early stages of the simulation. The damage model predicts a distribution of damage throughout the specimen, with necking occurring along the entire length. This was not seen in the experimental test, where the necking phenomenon was only observed around the area of the hole.

4.5.4 Compressive +45°/-45° Hole in Plate Test Simulation

The mesh used for the +45°/-45° compressive test coupon with a stress concentrator is shown in Figure 4.17. Since the test used an end loading rig, the specimen is modelled with constraints only along the edge nodes at one end, with displacement applied at the other. Tests results are given as load/displacement, since in this test no strain

gauge or extensometer was used, see Figure 4.18. The correlation between test and experiment is good up to 2mm displacement, where the experimental test shows a reduction in load, that is not reflected in the simulation. This is explained by the specimen deformation seen in experiment, see Figure 4.19. During test, the Twintex deforms out of plane in a buckling mode, which is not accounted for by the damage model. The load therefore begins to reduce after 3.5mm displacement, whilst the simulation result suggests that the damage will gradually accumulate as the load increases.

The lack of correct treatment of fibre reorientation in areas of high shear strain, mentioned in section 4.5.3, when discussing the under-stiff response of the model for the tensile test, could also be used to explain the over-stiff response observed for this simulation. Again, this is discussed in more detail in Chapter 7.

4.6 Model Sensitivity

The model was developed and calibrated from the results of experimental test. The sensitivity of the model to parameters such as Young's Modulus and tensile and compressive failure strain taken from these tests is predictable. For example increasing the tensile failure stress in the damage model will result in the model failing at a higher stress level. Similarly, variation of the material constants results in a predictable change in the linear elastic behaviour of the model. There are however parameters in the model for which the sensitivity is not as easy to estimate. The variables that were investigated can be split into two distinct groups, material model constants and analysis parameters.

The constants that were investigated, were both part of the shear damage model, since the fibre direction damage models are calibrated with exact values taken directly from test results. These parameters were, α , the shear damage parameter and the damaged shear modulus G_{12D} .

The analysis parameters that were investigated were, the number of analysis steps, the element formulation (full or reduced integration) and mesh refinement.

4.6.1 Sensitivity to Analysis Step

The sensitivity to analysis step was investigated for the +45°/-45° tensile test, since this test undergoes a large amount of deformation, with progressive damage throughout. The analysis was set to run to a total displacement of 30mm, which equates to a total strain of approximately 20%. Five analyses were run with a total number of steps of 20, 50, 100, 200 and 500, or approximate steps of 1%, 0.4%, 0.2%, 0.1% and 0.04% strain. Stress/strain responses from each of these simulations were plotted and compared to experimental test data, see Figure 4.20. The results are shown up to 10% strain to highlight the region of the analysis where the result is most sensitive to step size.

It can be seen from the results that the solution has converged by the 200 step simulation although the 100 step solution shows a satisfactory level of convergence. The step size of 0.1% strain, from the 200 step solution, was selected as a minimum for the analysis of Twintex.

4.6.2 Sensitivity to Shear Non-Linearity Parameter α

The +45°/-45° tensile test simulation was also used to investigate the sensitivity of the model to α , the shear damage parameter. This sensitivity analysis was used as part of the calibration of the model, since the result was used to select the value of α used for all simulations.

Figure 4.21 shows the result of the five sensitivity simulations run against the result from experimental test. The five α values used were 1.4×10^{-6} , 6.3×10^{-6} , 1.4×10^{-5} , 6.3×10^{-5} and 1.4×10^{-4} . The stress/strain curves show that the region between 0.5% and 2% strain is the area that is most sensitive to the shear damage parameter calibration. As the magnitude of the parameter is reduced, the magnitude of the identified damage and hence the reduction of shear modulus is also reduced. From this result, an α value of 1.4×10^{-5} was selected as most accurately representing the relationship between damage and modulus reduction for Twintex undergoing shear deformation.

4.6.3 Sensitivity to Calibration of Damaged Shear Modulus

The third of the calibration parameters investigated was G_{12D} , the damaged shear modulus. Again, five values were selected to investigate the sensitivity in the $+45^\circ/-45^\circ$ tensile test simulation. The values chosen were 5MPa, 15MPa, 25MPa, 45MPa and 60MPa.

Figure 4.22 shows the stress/strain results from this sensitivity analysis, compared to the experimental test result, up to a strain level of 10%. The plot shows that the region of the analysis that is sensitive to the damaged shear modulus, G_{12D} , is above approximately 2% strain. The best correlation between experiment and analysis is for a G_{12D} value of 25MPa. This value was selected and used for all simulations.

4.6.4 Sensitivity to Element Formulation

An in depth investigation into the effect of element formulation was also undertaken. All calibration and validation simulations, originally run with reduced integration shell elements were simulated with full integration elements. The meshes used were identical to the original simulations.

Figure 4.23 shows the stress/strain result for the $0^\circ/90^\circ$ tensile test. The simulation shows almost identical response, although the full integration elements predict failure slightly before the reduced integration and the analysis remains stable after first failure is predicted. This is shown graphically by the damage contour plot in Figure 4.24, where the full integration simulation gives damage output showing the areas where failure has been identified. The elements showing failure levels of 0.25 and 0.5 are average values for the four integration points of the element. A smoothed contour plot was not used, since this would not allow easy identification of ‘fully’ failed elements.

The results from the compressive $0^\circ/90^\circ$ simulation show a similar result to the tensile test. Figure 4.25 shows that the stress/strain response is identical for both the full and reduced integration elements. The damage plot, Figure 4.26, shows a slight difference in the level of damage identified and the shape of the damage area, when comparing the two simulations. The full integration elements predict damage slightly earlier than the reduced integration, in the elements adjacent to the area where the boundary

conditions are applied. This is due to the stress concentration effect of the nodal constraints used.

The effect of element integration is more marked for the simulations where shear damage is being predicted. This is shown by Figure 4.27. The $+45^\circ/-45^\circ$ tensile test simulation predicts ultimate failure sooner with full integration, at around 16% strain, compared to 19% strain in the reduced integration simulation. The plot comparing field variable 3 for the two simulations, Figure 4.28, shows that the prediction of damage development in the early stages of the simulation is very similar for the two types of element formulation.

The result for the $+45^\circ/-45^\circ$ compressive test simulation shows the most significant difference between the two formulations, see Figure 4.29. The stress/strain response is similar up to approximately 2% strain, where the responses diverge considerably. In the full integration simulation, much more severe damage is predicted. This damage is shown in Figure 4.30. The full integration elements, as well as identifying a similar level of shear damage, seen in the comparison of field variable 3, show compressive fibre direction damage highlighted by the plot of field variable 1.

The tensile $0^\circ/90^\circ$ specimen with a stress concentrating hole also gives a differing result dependant on the type of element used. The stress/strain plot, Figure 4.31, shows that in the case of full integration, damage is predicted at just over 1% strain, whereas in the reduced integration elements this is not predicted until 1.5% strain. The damage in the full integration elements occurs earlier due to the proximity of the integration point to the stress concentration. Higher stress means that failure is reached sooner in the analysis. Figure 4.32 shows that the full integration elements remain stable and converge a solution after damage has occurred. The reduced integration solution fails to converge soon after the first point at which damage is predicted to occur.

The $+45^\circ/-45^\circ$ tensile specimen with a stress concentration models under-predict the stiffness, with either element type, see Figure 4.33. Figure 4.34 shows the field variables representing damage during the simulation. The full integration solution

predicts damage and failure sooner than the reduced integration elements. Again this is due to the proximity of the integration points to the stress concentration.

Figure 4.35 shows the stress/strain response from the $+45^\circ/-45^\circ$ compressive specimen with a hole stress concentration. The results are similar to previous observations, where the full integration elements predict a slightly higher level of damage. At around 4mm displacement the response of the full integration simulation shows a drop in load, which is not seen in the reduced integration simulation. The comparative plot of field variable 3 for each simulation highlights this difference in damage prediction, see Figure 4.36. In both cases the solutions do not predict the drop off in load seen as the specimen starts to deform out of plane. As explained earlier, during the validation section of the work, this phenomenon is not simulated by the model.

4.6.5 Sensitivity to Mesh Refinement

The sensitivity of the solution to mesh refinement was also investigated. Figures 4.37 and 4.38 show two meshes used to simulate the $+45^\circ/-45^\circ$ compressive specimen with a stress concentration. This coarse and fine mesh were compared to the standard density mesh used during the validation of the model. Figure 4.39 shows the stress/strain response for the coarse mesh. Both full and reduced integration solutions are shown, since the mesh density also affects sensitivity to element formulation. In both cases the simulations predict shear damage, although it is noted that the full integration solution does not show the load drop off at 4mm predicted by the medium density mesh. The full integration elements also show a significantly higher stiffness than their reduced integration counterparts. The field variable 3 plots in Figure 4.40 also show a significant difference in the level and pattern of damage.

The fine mesh results in Figure 4.41 show that when the mesh is refined, the effect of the number of integration points on the stiffness of the elements is far lower. The load/displacement response up to 3.5mm is very similar for both models. The full integration solution does though predict a load drop off due to damage development in the specimen, at approximately 3.5mm, which is not seen in the reduced integration solution. A comparison of field variable 3 during the simulation is shown in Figure 4.42. The level of shear damage predicted by the full integration solution is slightly

higher, although the difference is not as marked as that displayed by the coarser meshes.

In general for a reduced integration element formulation, the load/displacement response does not appear to be particularly sensitive to element formulation. Even the coarse mesh gives a good representation of the specimens behaviour up to the point at which out of plane damage begins to occur. The main difference between the meshes can be seen when comparing the field variable plots, especially for the full integration solution.

4.7 Conclusion

A damage model based on a maximum stress fibre direction failure criteria, a strain based shear failure and a shear degradation behaviour has been developed and calibrated for woven Twintex. The calibration method suggested can be performed and the material fully characterised with only 3 test geometries.

Modelling of calibration and validation specimens has shown that the model is accurate when predicting the behaviour of Twintex for situations where loading is in the principal fibre directions. The shear behaviour of the material can also be accurately simulated, although when shear deformation is unevenly distributed in a specimen such as the tensile $+45^\circ/-45^\circ$ test with a stress concentration, the model under-predicts the stiffness. The only test specimen behaviour that the model cannot accurately predict is out of plane buckling. This is seen in some of the compressive tests, where the in-plane model over-predicts the stiffness of test specimens.

A further limitation of the model for small coupon tests, such as those presented in this chapter, is the ability of an implicit code to converge an equilibrium solution after material properties have been significantly reduced. The property reduction results in high levels of element deformation and subsequent failure of the analysis, not just the material model.

The model has been shown to be sensitive to calibration parameters, solution step size, element formulation and mesh density. The calibration parameters and step size were found to be the most critical of these variables.

The results from this piece of work demonstrate that in general, prediction of in-plane damage development is possible for a woven composite material, using a stepped implicit finite element solution, with a basic damage model.

4.8 Figures

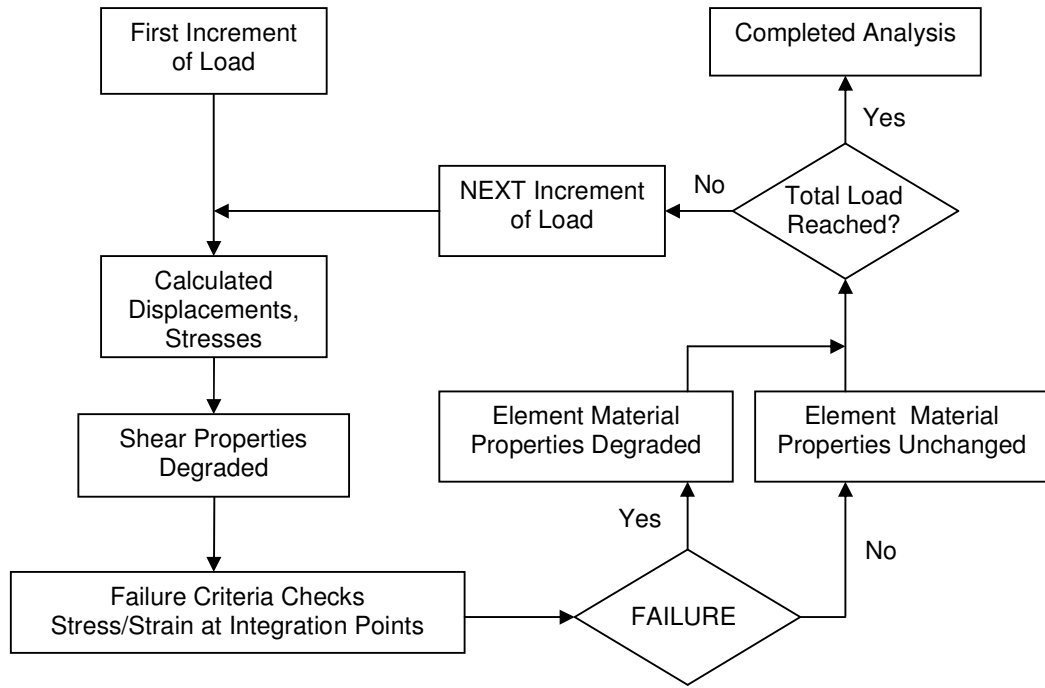


Figure 4.1 Schematic of damage model implementation as an ABAQUS user defined FORTRAN subroutine

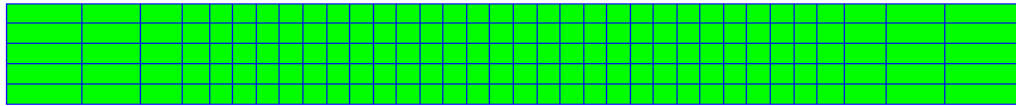


Figure 4.2 Tensile test - shell element mesh

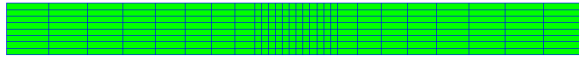


Figure 4.5 Compressive test - shell element mesh

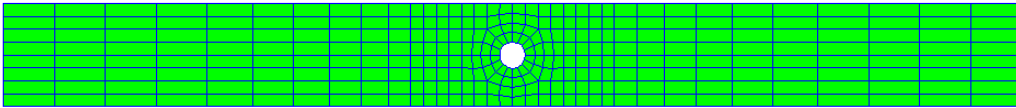


Figure 4.12 Tensile hole in plate test - shell element mesh

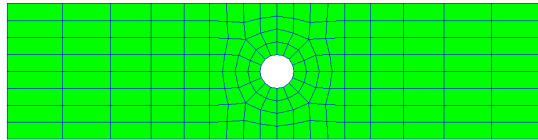


Figure 4.17 Compressive hole in plate test - shell element mesh

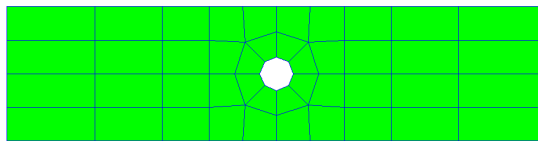


Figure 4.37 Compressive hole in plate test - shell element mesh (coarse)

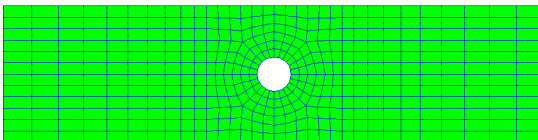


Figure 4.38 Compressive hole in plate test - shell element mesh (refined)

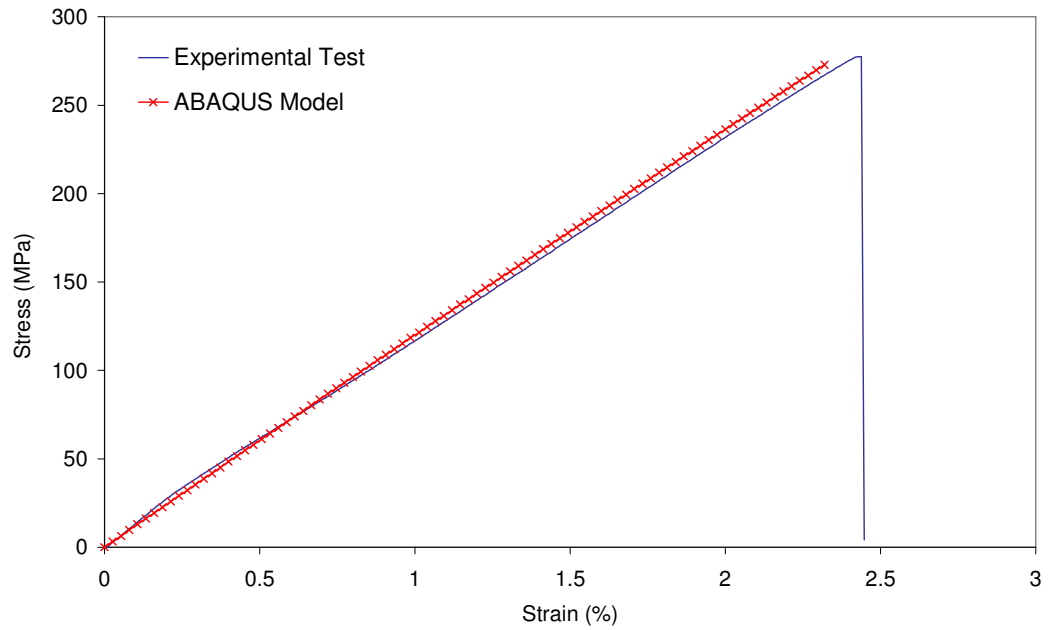


Figure 4.3 0°/90° tensile test simulation - stress/strain

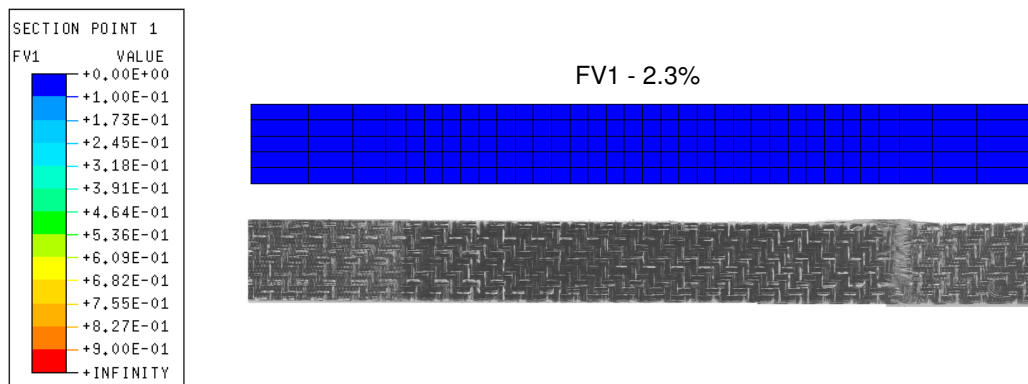


Figure 4.4 0°/90° tensile test simulation - experimental and predicted damage

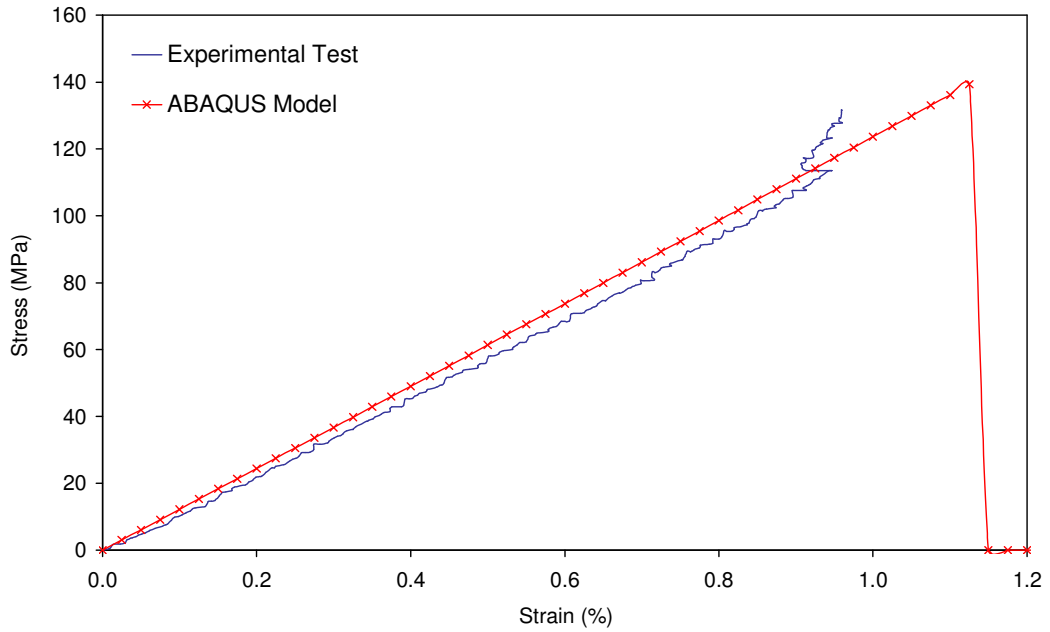


Figure 4.6 0°/90° compressive test simulation - stress/strain

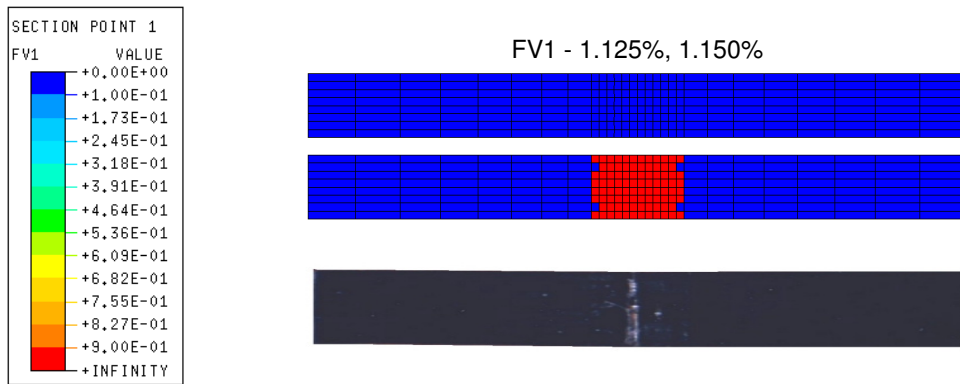


Figure 4.7 0°/90° compressive test simulation - experimental and predicted damage

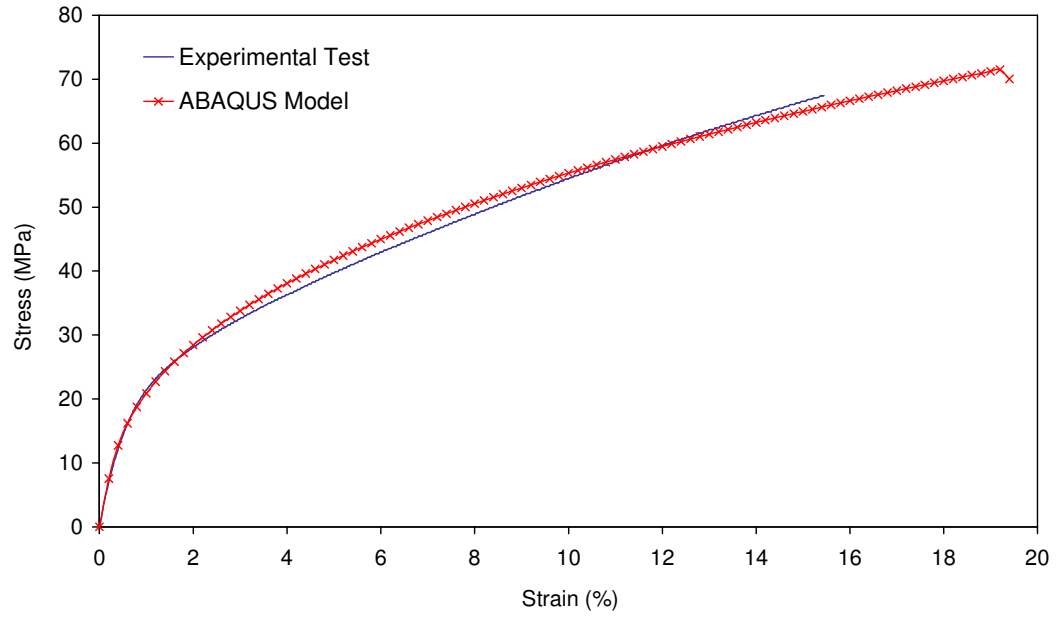


Figure 4.8 +45°/-45° tensile test simulation - stress/strain

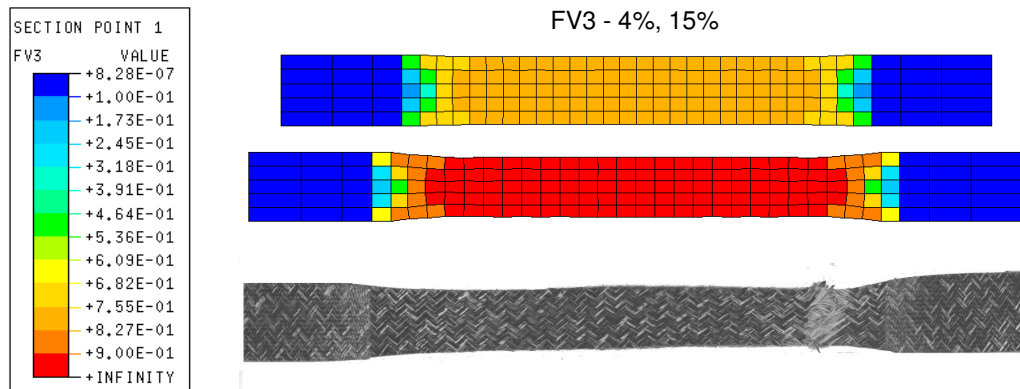


Figure 4.9 +45°/-45° tensile test simulation - experimental and predicted damage

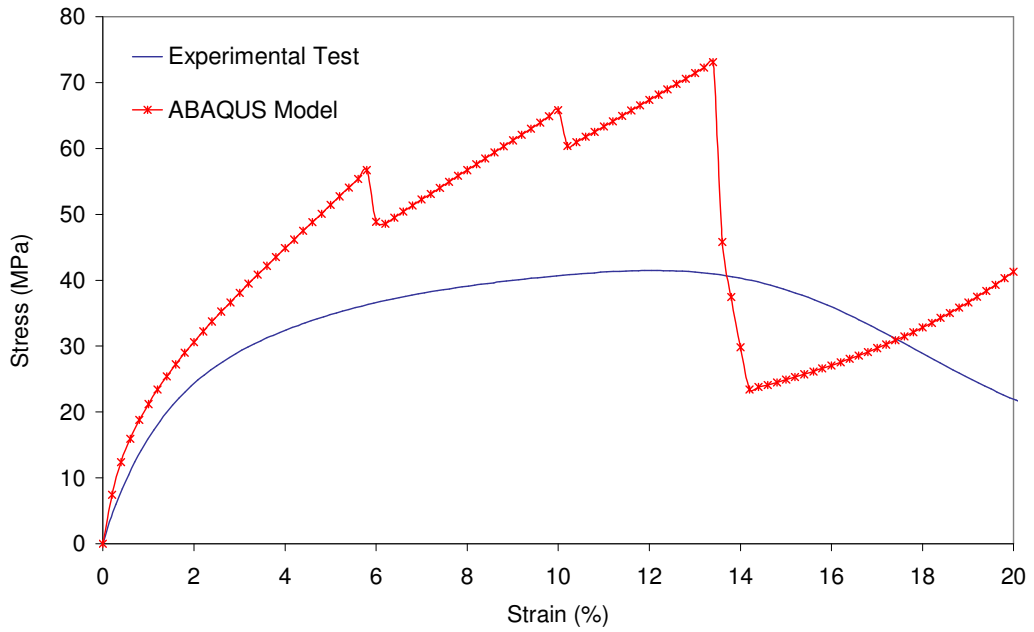


Figure 4.10 +45°/-45° compressive test simulation - stress/strain

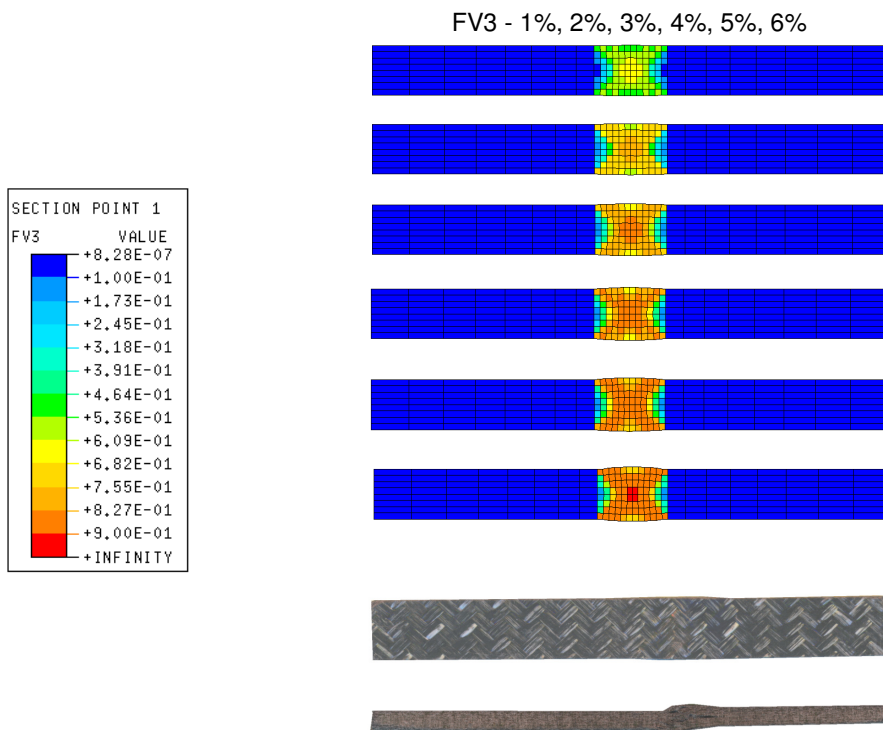


Figure 4.11 +45°/-45° compressive test simulation - experimental and predicted damage

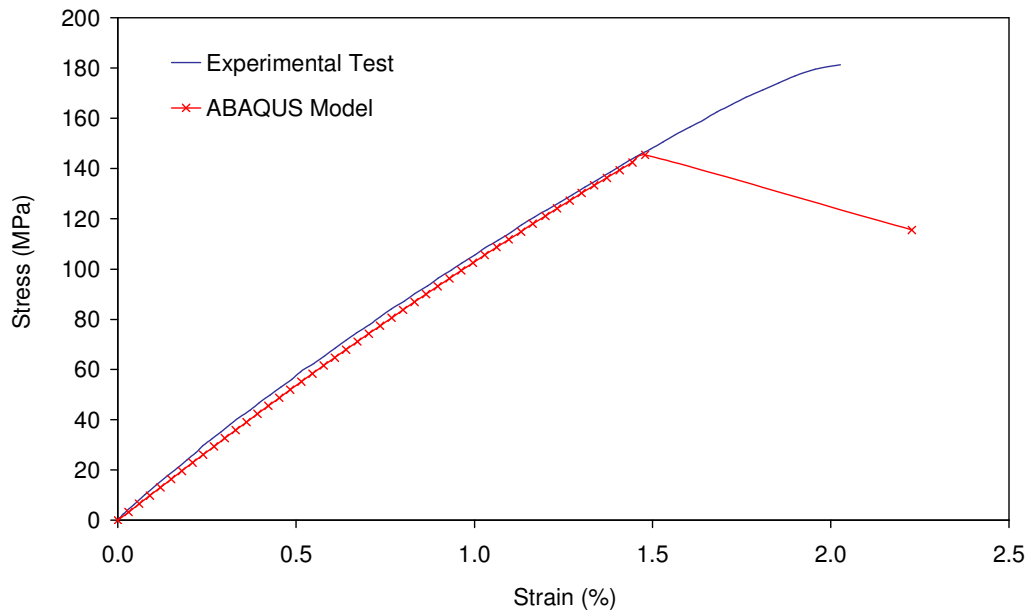


Figure 4.13 0°/90° tensile hole in plate test simulation - stress/strain

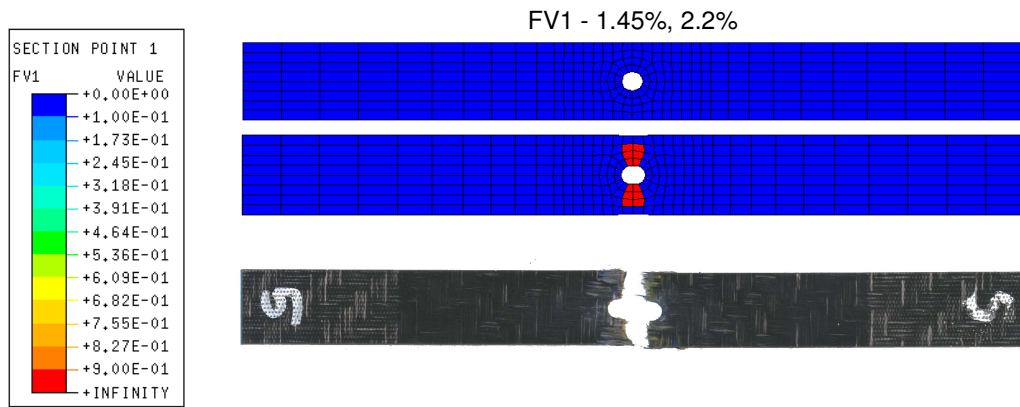


Figure 4.14 0°/90° tensile hole in plate test simulation - experimental and predicted damage

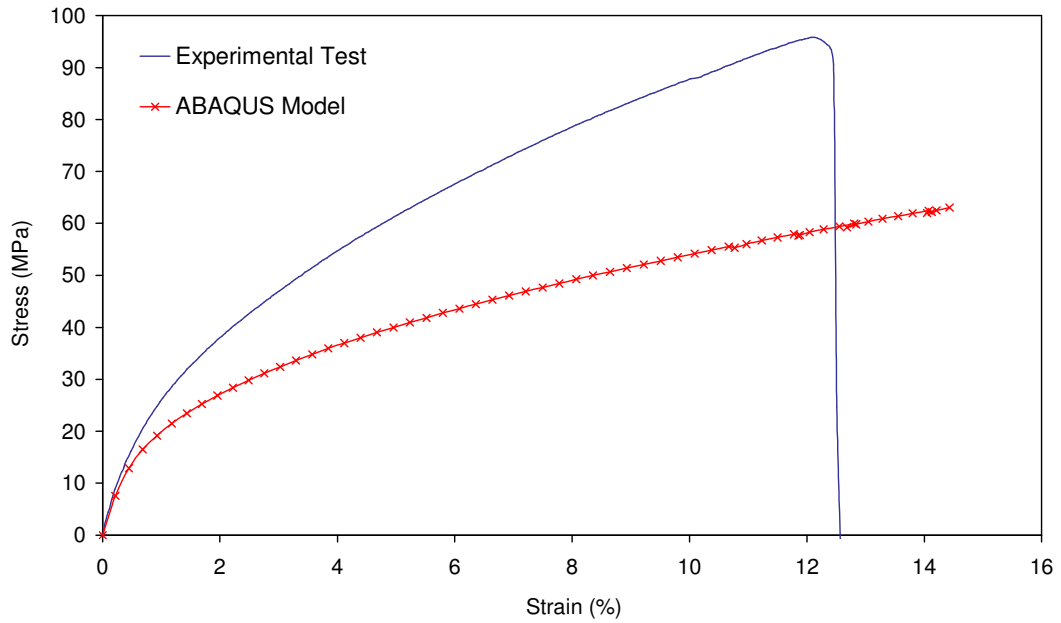


Figure 4.15 +45°/-45° tensile hole in plate test simulation - stress/strain

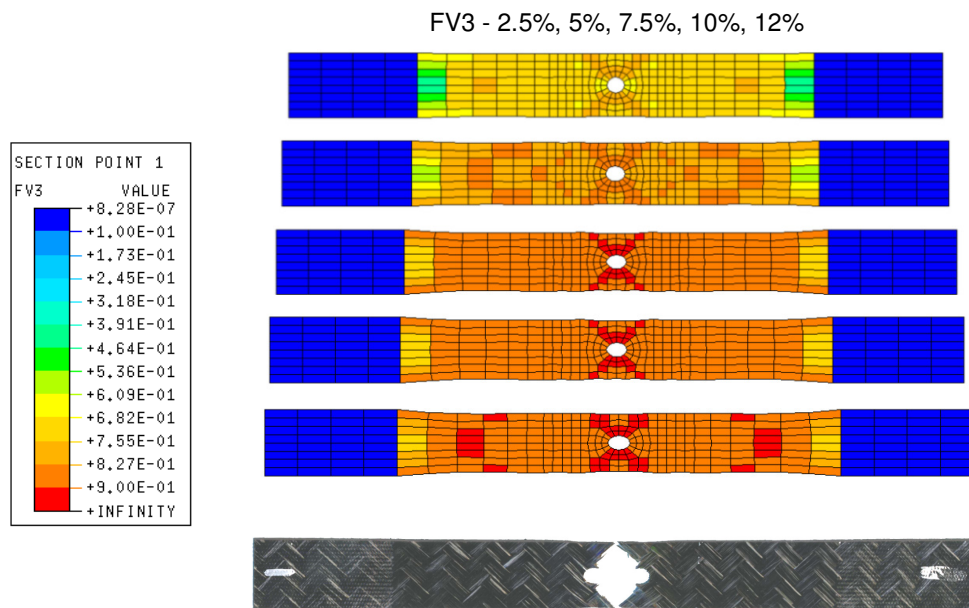


Figure 4.16 +45°/-45° tensile hole in plate test simulation - experimental and predicted damage

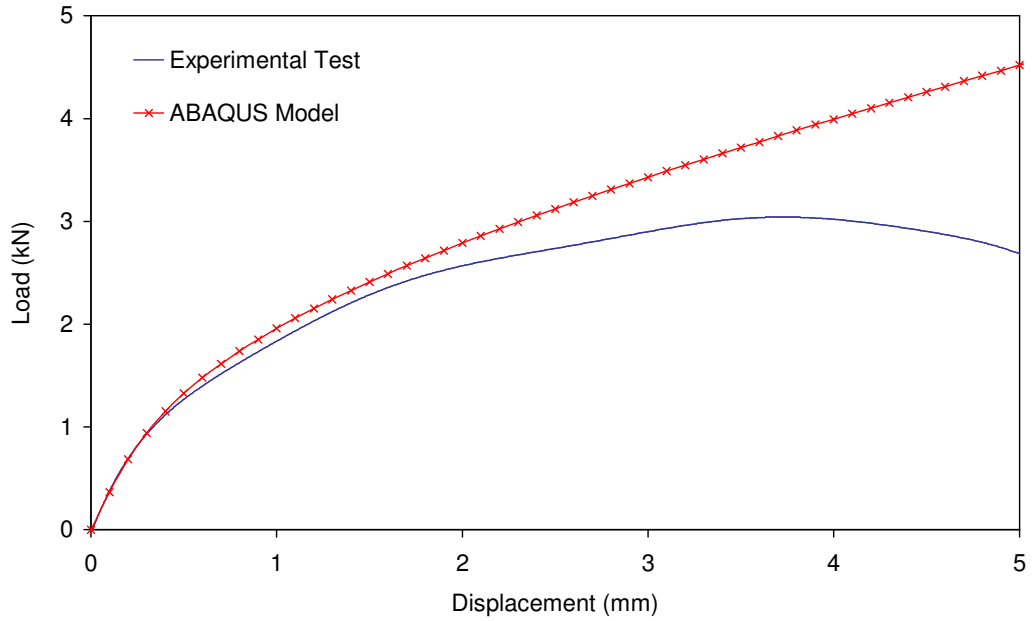


Figure 4.18 +45°/-45° compressive hole in plate test simulation - load/displacement

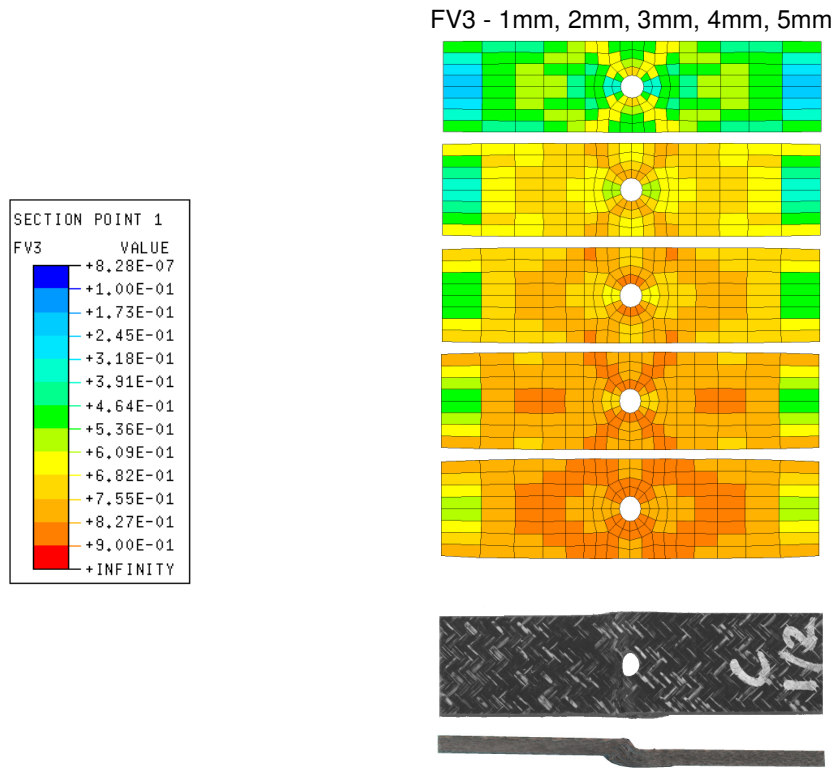


Figure 4.19 +45°/-45° compressive hole in plate test simulation - experimental and predicted damage

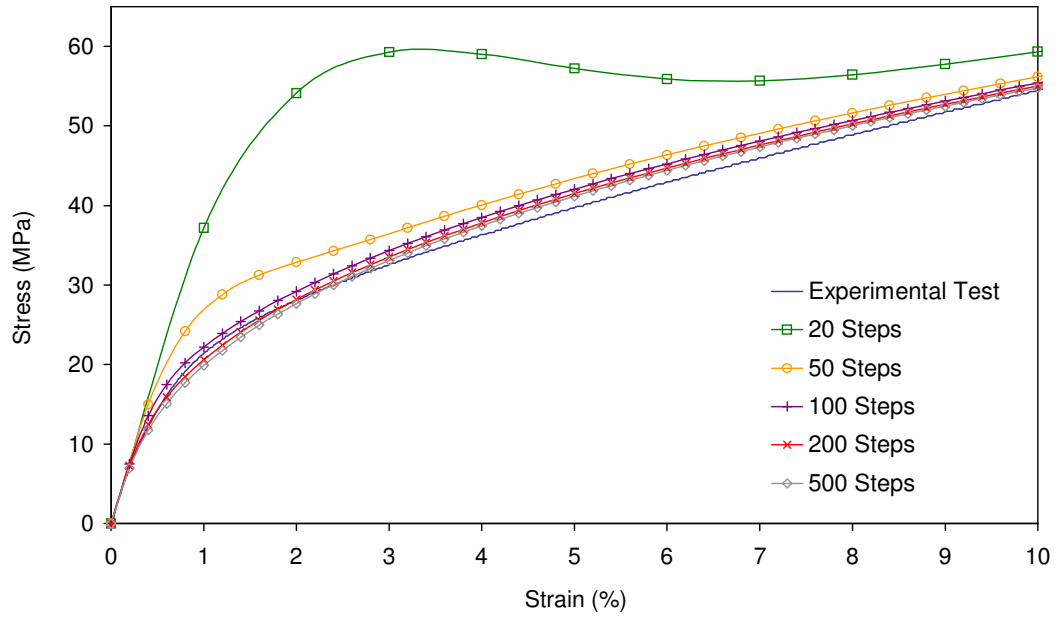


Figure 4.20 +45°/-45° tensile test simulation - sensitivity to analysis steps

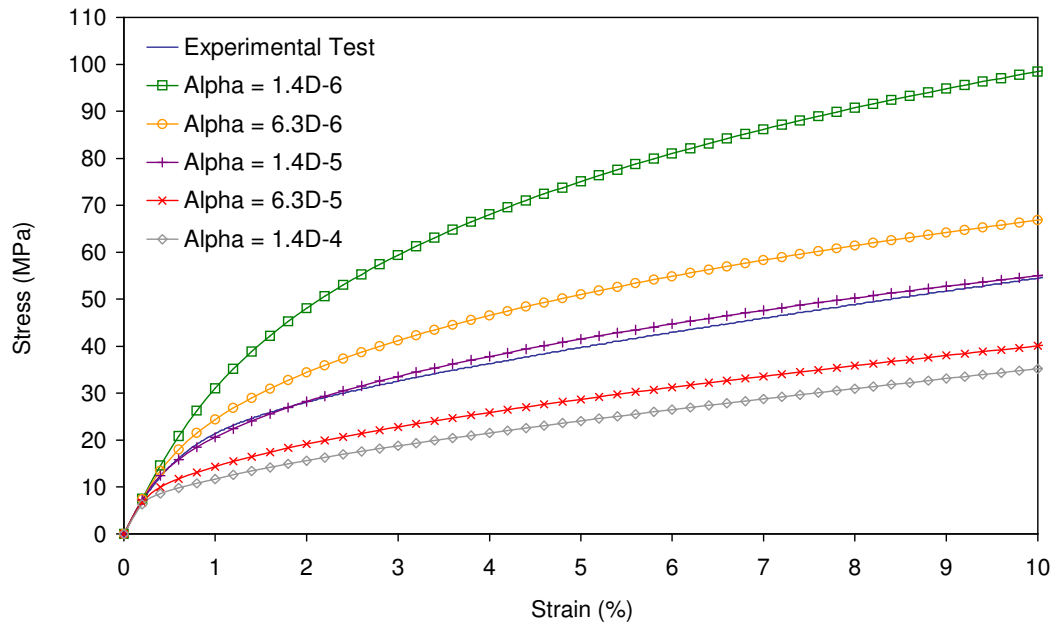


Figure 4.21 +45°/-45° tensile test simulation - sensitivity to shear damage parameter alpha - α

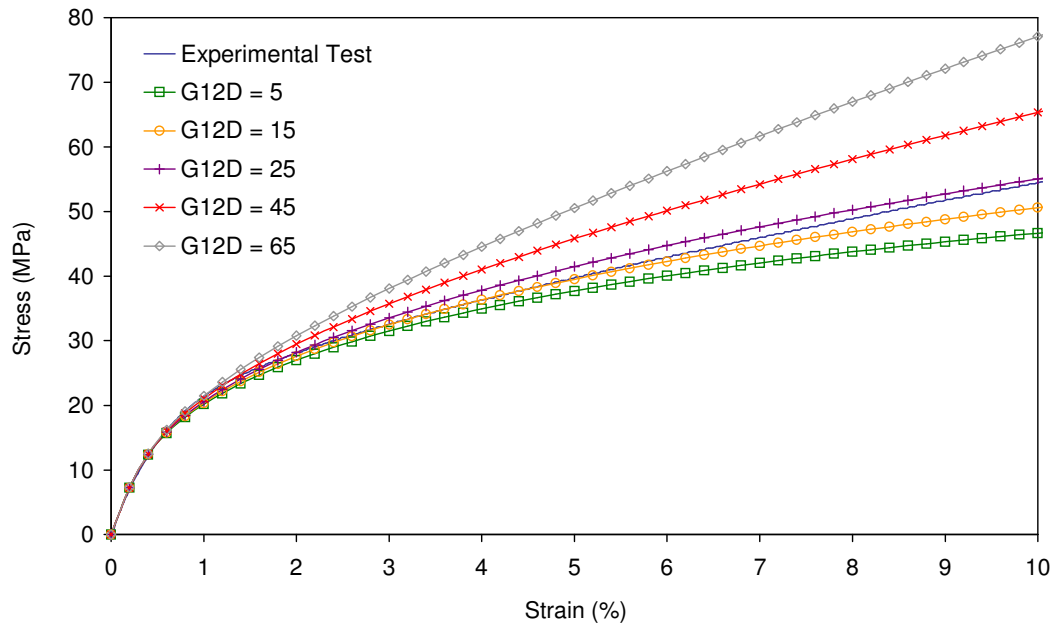


Figure 4.22 +45°/-45° tensile test simulation - sensitivity to damaged shear modulus - G_{12D}

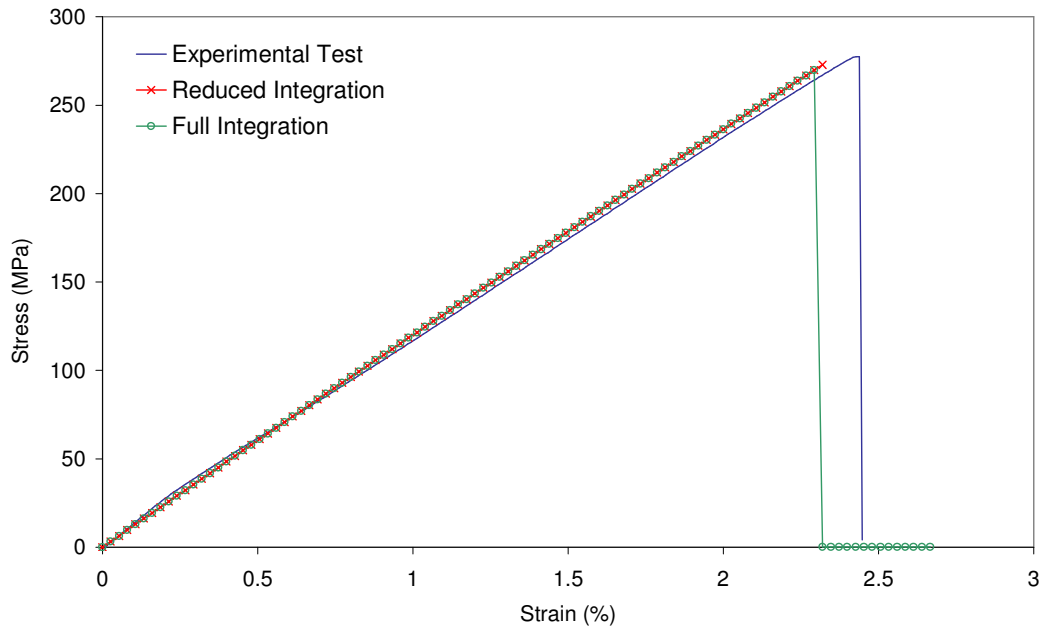


Figure 4.23 0°/90° tensile test simulation - sensitivity to element formulation

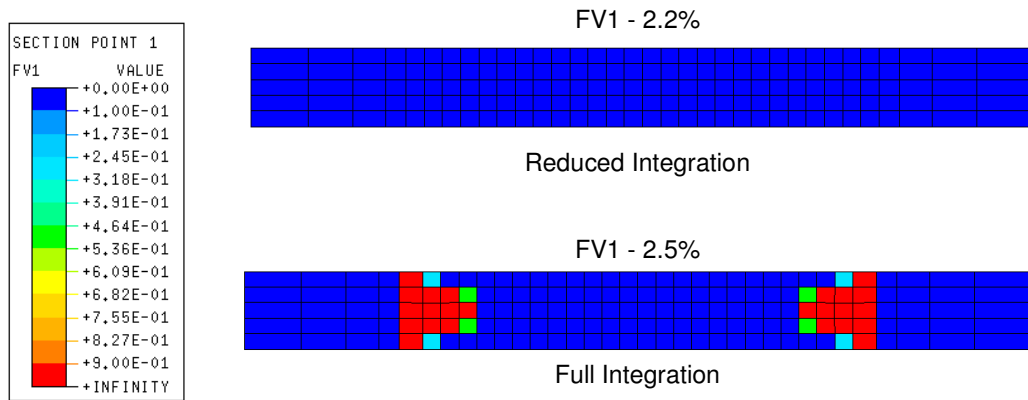


Figure 4.24 0°/90° tensile test simulation - predicted damage

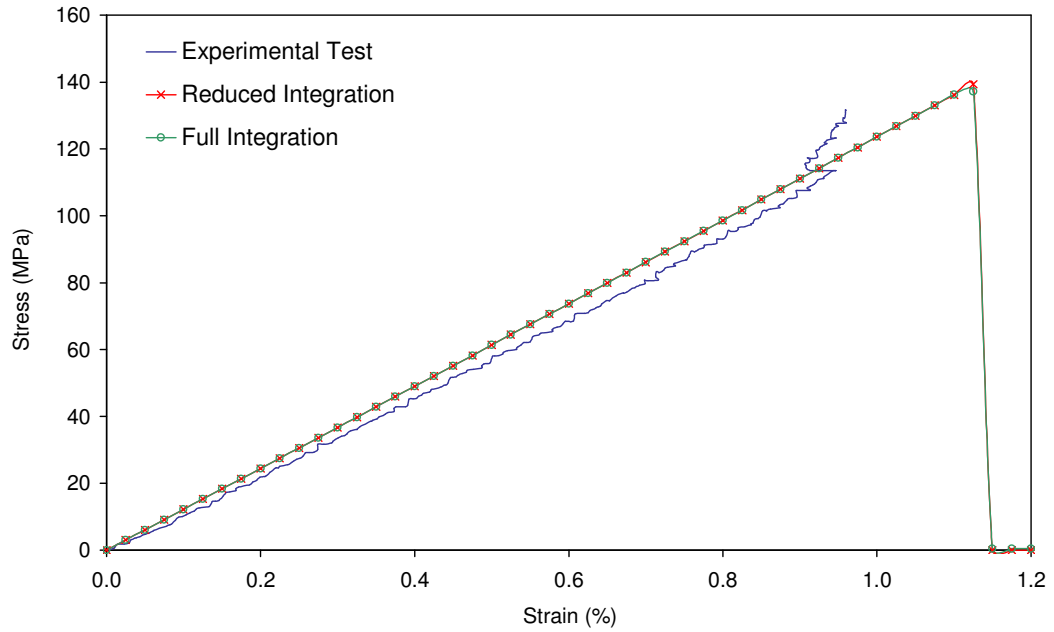


Figure 4.25 0°/90° compressive test simulation - sensitivity to element formulation

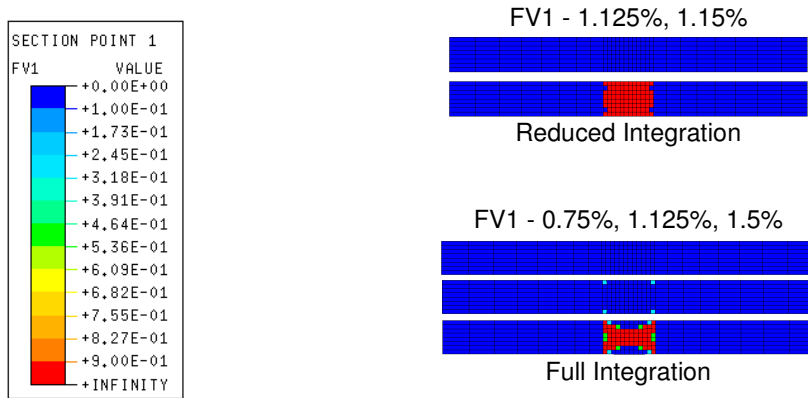


Figure 4.26 0°/90° compressive test simulation - predicted damage

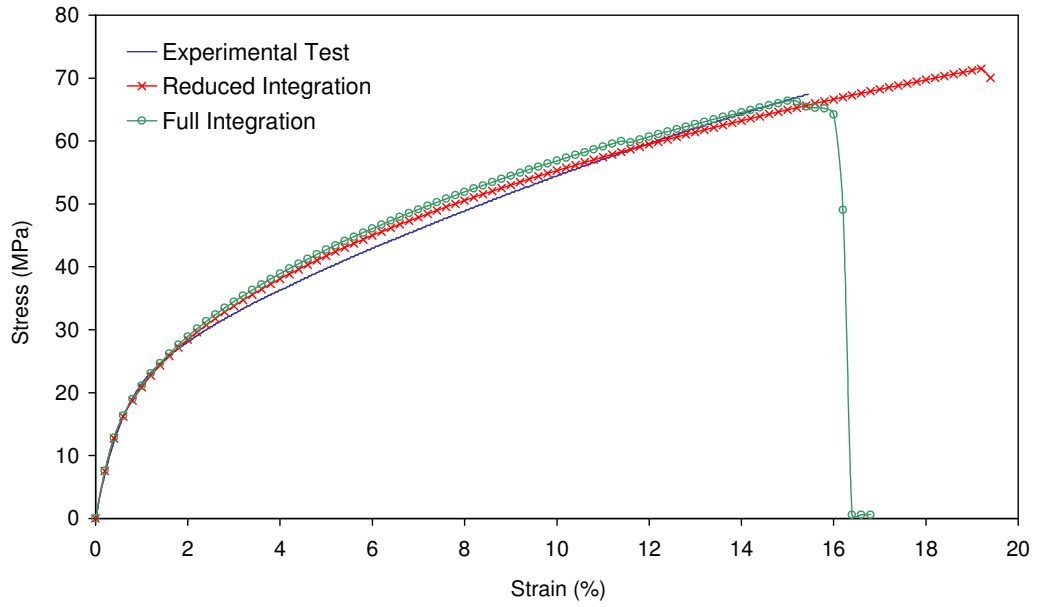


Figure 4.27 +45°/-45° tensile test simulation - sensitivity to element formulation

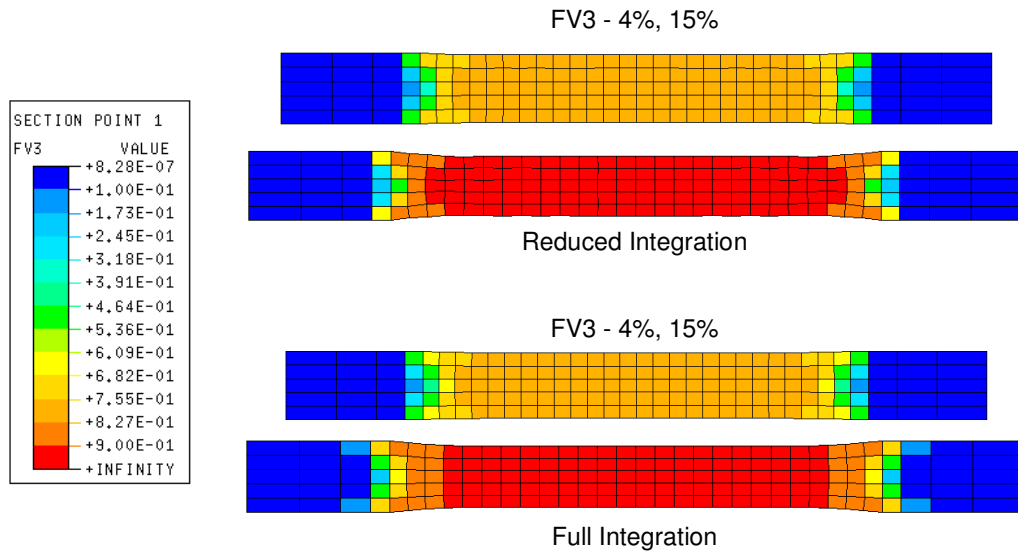


Figure 4.28 +45°/-45° tensile test simulation - predicted damage

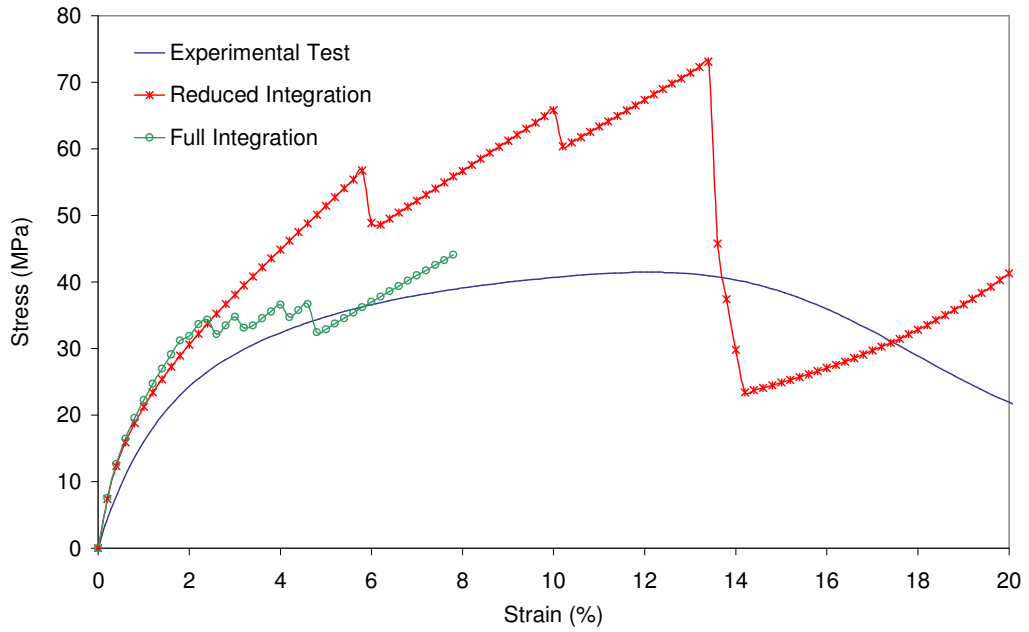


Figure 4.29 +45°/-45° compressive test simulation - sensitivity to element formulation

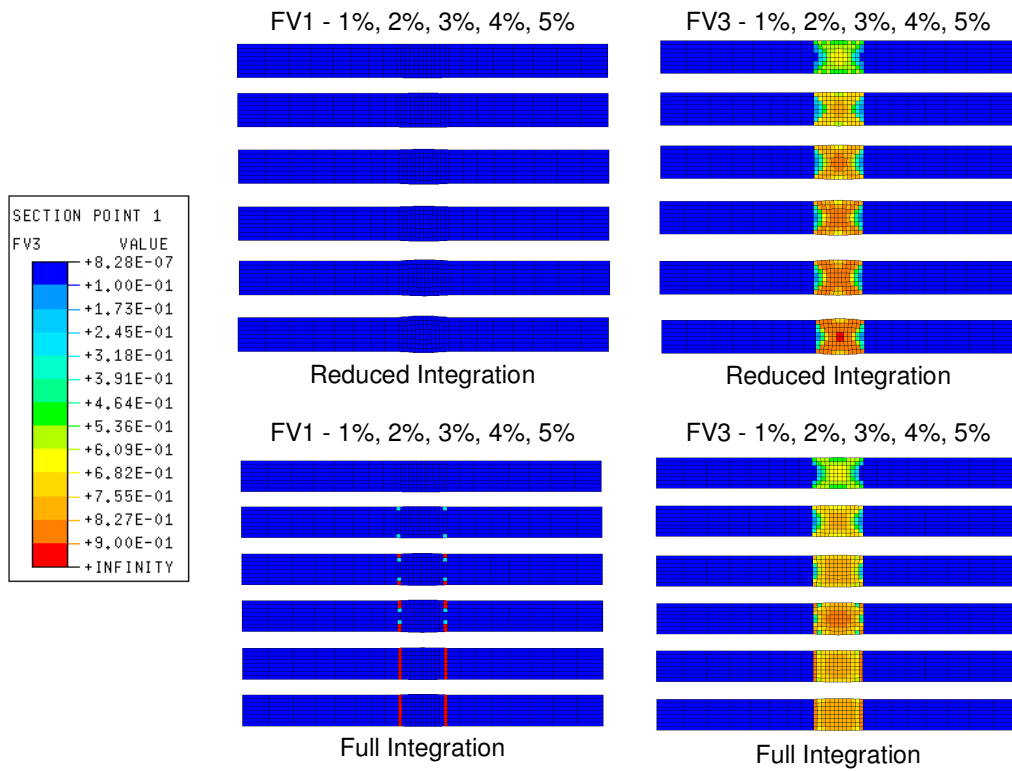


Figure 4.30 +45°/-45° compressive test simulation - predicted damage

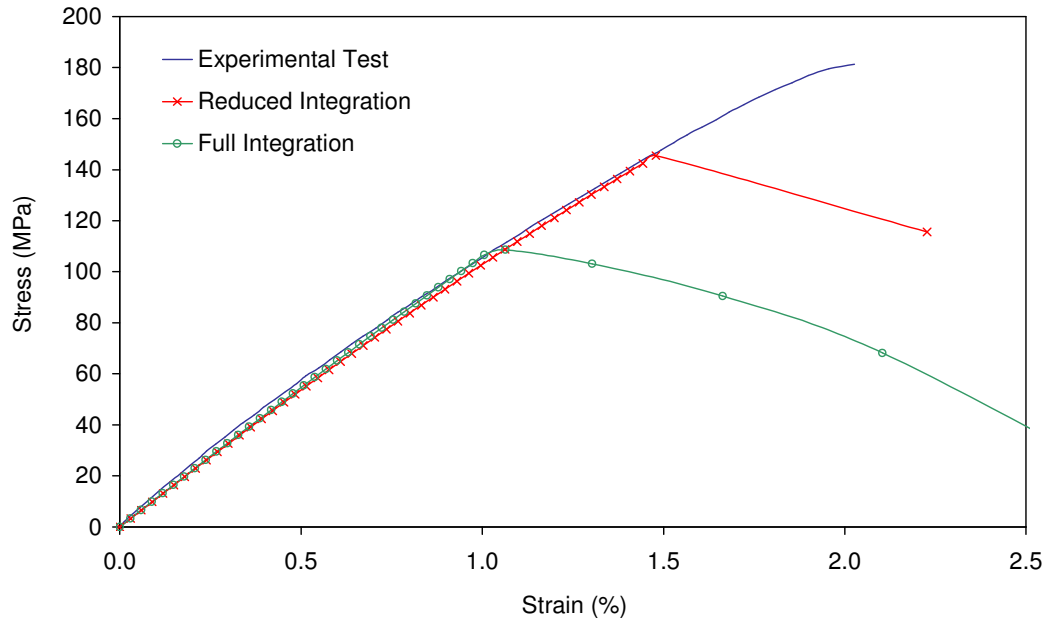


Figure 4.31 0°/90° tensile hole in plate test simulation - sensitivity to element formulation

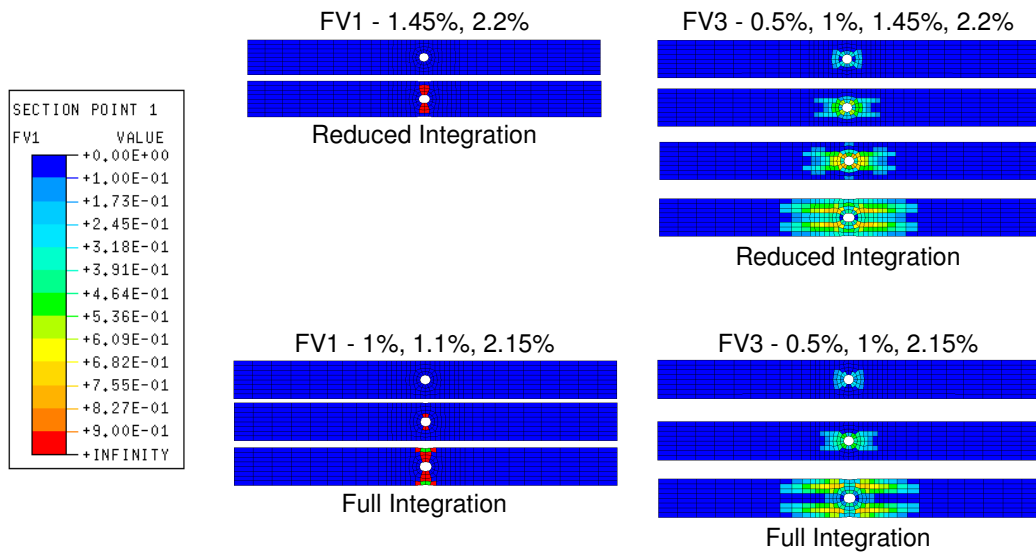


Figure 4.32 0°/90° tensile hole in plate test simulation - predicted damage

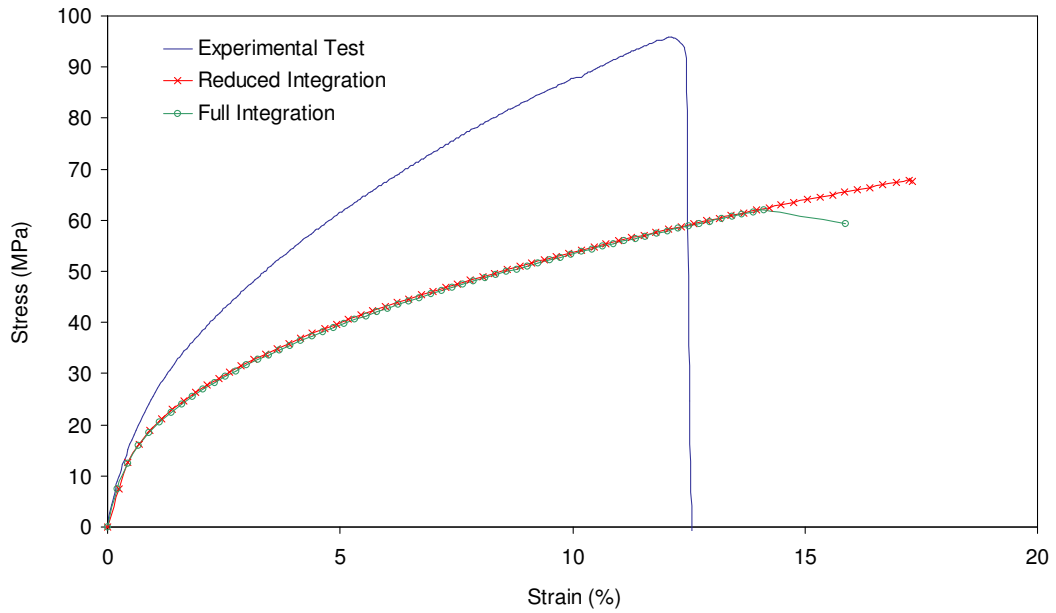


Figure 4.33 +45°/-45° tensile hole in plate test simulation - sensitivity to element formulation

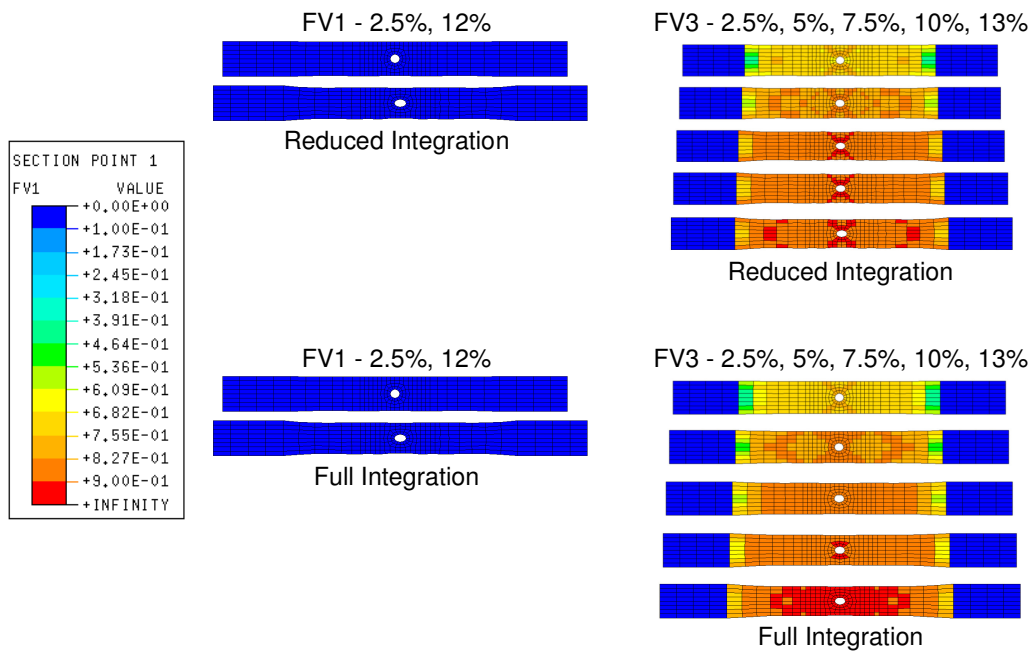


Figure 4.34 +45°/-45° tensile hole in plate test simulation - predicted damage

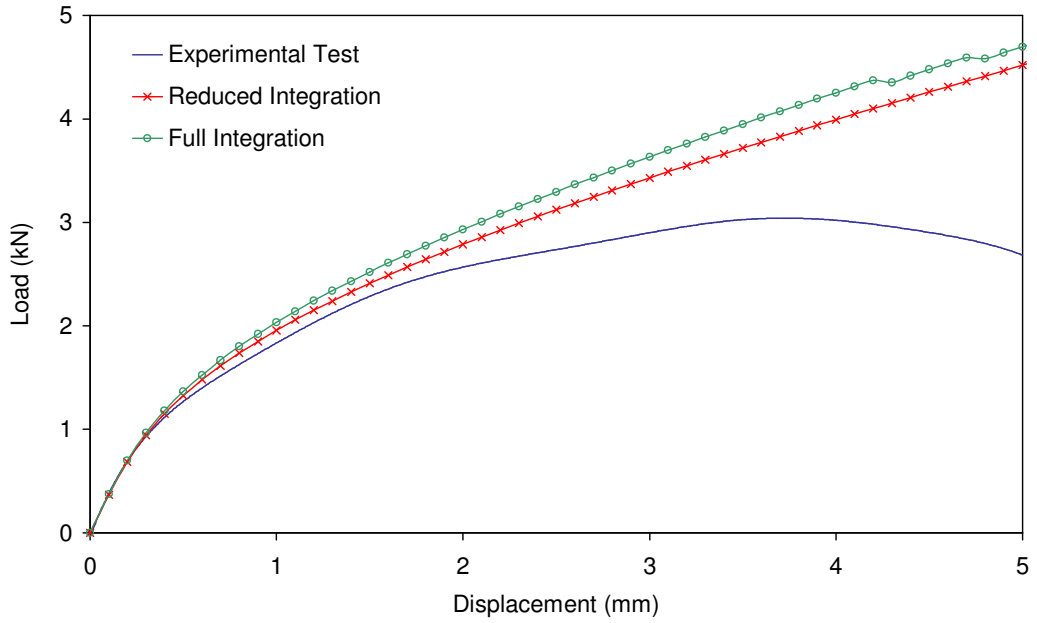


Figure 4.35 +45°/-45° compressive hole in plate test simulation - medium mesh - sensitivity to element formulation

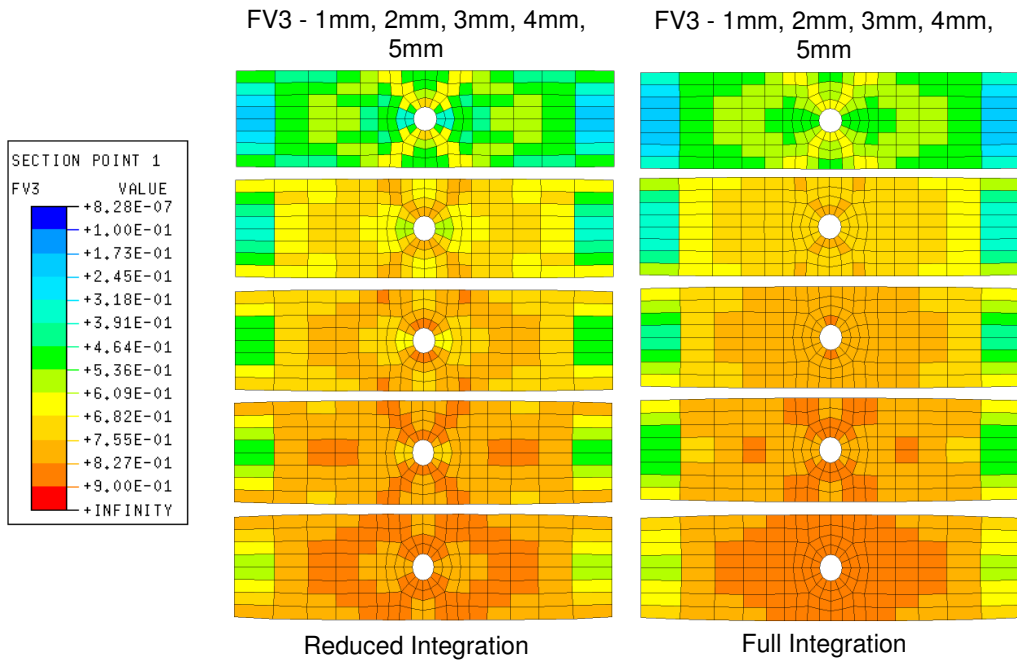


Figure 4.36 +45°/-45° compressive hole in plate test simulation - medium mesh - predicted damage

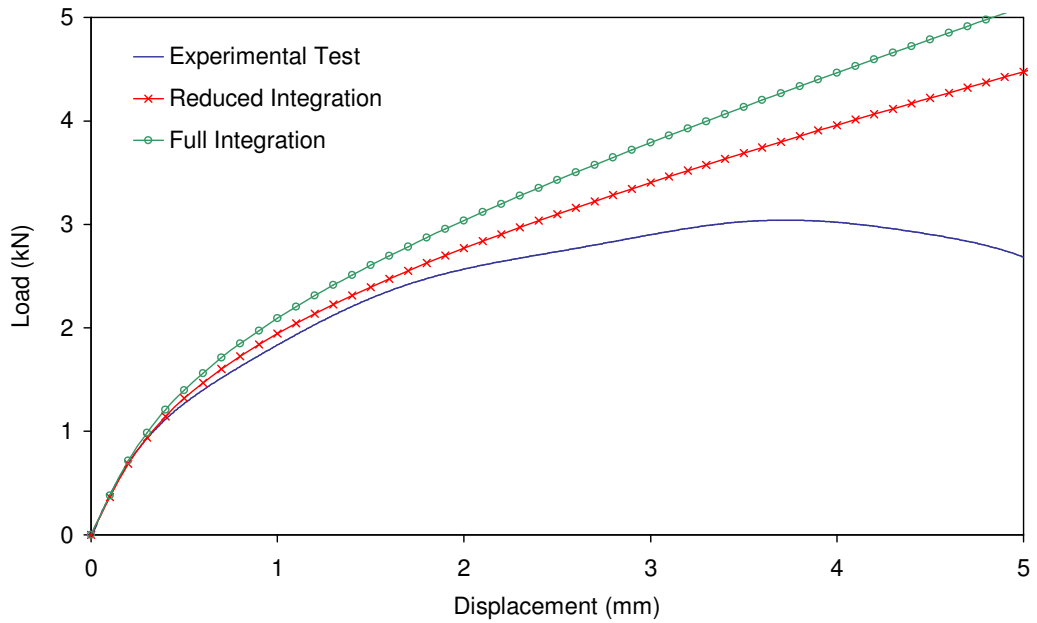


Figure 4.39 +45°/-45° compressive hole in plate test simulation - coarse mesh - sensitivity to element formulation

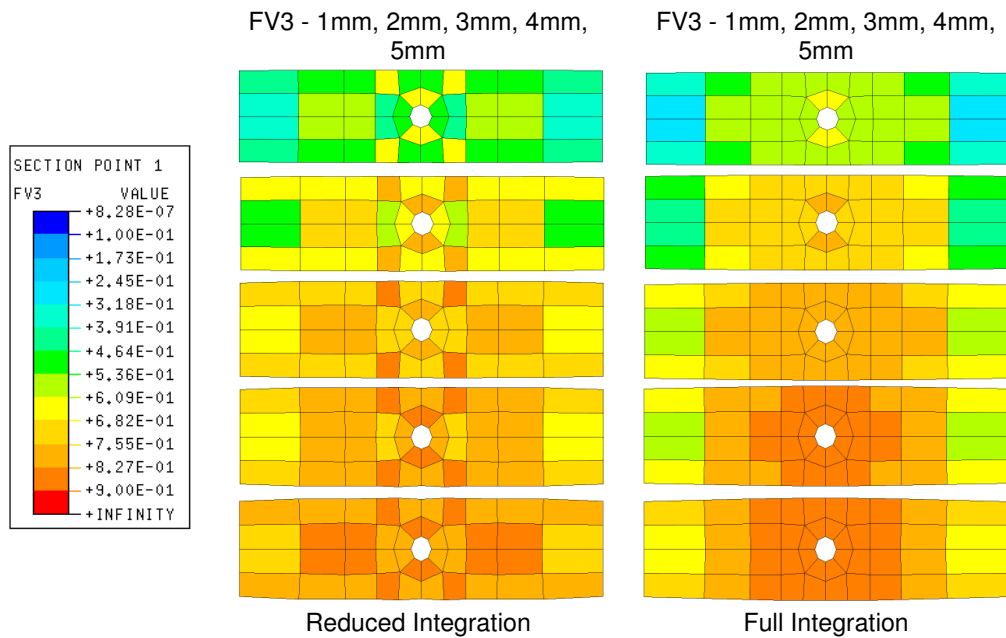


Figure 4.40 +45°/-45° compressive hole in plate test simulation - coarse mesh - predicted damage

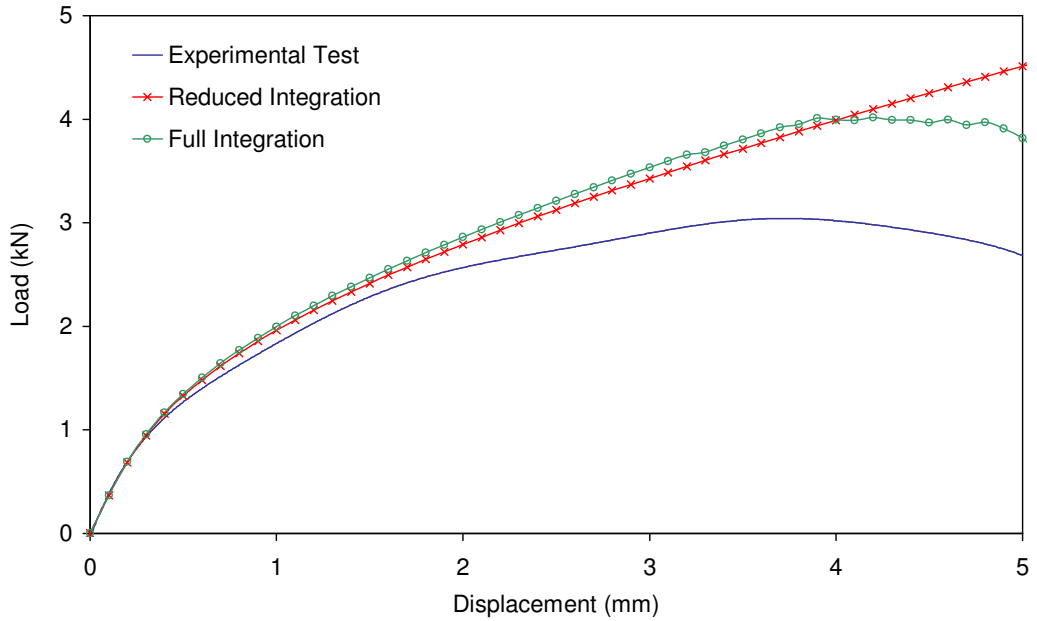


Figure 4.41 +45°/-45° compressive hole in plate test simulation - fine mesh - sensitivity to element formulation

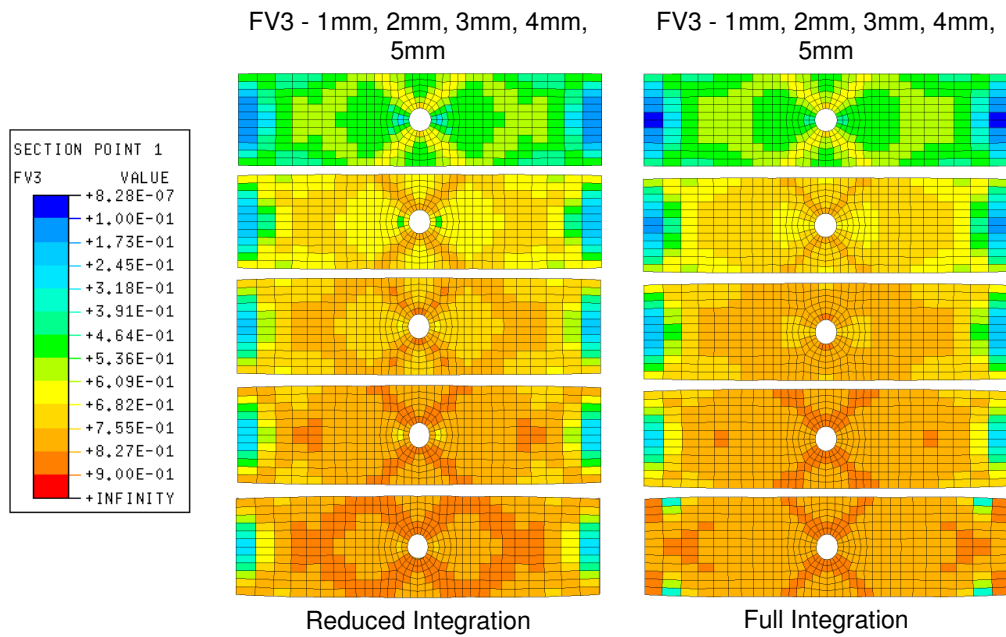


Figure 4.42 +45°/-45° compressive hole in plate test simulation - fine mesh - predicted damage

Chapter 5 Explicit Finite Element Damage Modelling

5.1 Introduction

Explicit finite element codes are used to solve non-linear or dynamic analysis problems. This type of code is therefore ideal for the analysis of composite components where material behaviour can be highly non-linear and large deformations occur.

Commercial codes often include material models specifically developed for the analysis of composites, which include damage models that the user can calibrate. In this part of the work, experimental test and manufacturers published data is used to calibrate one such material model. The model is then validated with the same test specimen data used in the previous, implicit finite element analysis chapter. These include fibre direction and off axis test coupons, both with and without a stress concentration. All the specimens, as described in Chapter 3, were manufactured from balanced weave 60% WF glass reinforced polypropylene Twintex.

5.2 Analysis Technique

The analysis models of coupon test specimens for this part of the work were based on the meshes generated during the implicit analysis damage model development. The use of identical meshes allowed direct comparison of the implicit and explicit codes.

The meshes were generated using HyperMesh 4.0 and exported to the pre-processor, PAM-GENERIS, where boundary conditions, materials and loads were defined and applied. All models were defined using reduced integration shell elements. Post processing was carried out using PAM-VIEW software.

5.2.1 Finite Element Code

The explicit finite element code, PAM-CRASH [81], was selected for this investigation. The code has various material models available for the simulation of general non-linear materials as well as more advanced material and damage models specifically formulated for composites.

The composite material models in PAM-CRASH allow the user to calibrate behaviour based on experimental test results although there is no functionality implemented for adaptation or modification of the models.

5.2.2 Material Model

PAM-CRASH material type 130 was selected for this part of the research programme. This material type defines a multi-layered shell element with ‘composite’ options. The layers can be defined as either elastic damaging fibre-matrix composite or elastic-plastic with damage. For the analysis of woven Twintex, the elastic damaging bi-phase layer definition, ITYP=0, was selected. This damage model is described in further detail in section 5.3.

As discussed in Chapter 2, this material model has been used with some success to model the non-linear damaging behaviour of various thermoset matrix composites, although little research is available validating the model for woven glass/thermoplastic matrix composites.

5.2.3 Element Definition and Formulation

For all the simulations performed using the PAM-CRASH solver, Belytschko-Tsay thin shell elements were used [81]. Shells were selected due to the nature of the test specimens modelled, which all have a small thickness to length ratio. The elements used to model the composite material test coupons in this study are standard, reduced integration four noded elements. No three noded elements were used for the coupon test specimens, although a small number were included in the demonstrator component models.

Shell elements of this type, defined with material type 130 have one integration point per composite layer. The total number of through thickness integration points is therefore dependent on the number of layers in the section definition. For the simulation of in-plane test specimens, this is not critical since no bending is simulated, although in later work, when the demonstrator component is deformed out of plane, simulation of out of plane bending is critical.

5.2.4 Section Definition

The section definition is referenced from the material type 130 input card. Each layer of the shell references a ply card, which contains ply material, thickness and orientation input parameters. For the simulation of coupon test specimens the composite laminate is defined as a number of layers of nominal 0.5mm thickness.

5.2.5 Definition of Orthotropy Direction

The orthotropy directions for all the woven material models are defined in relation to the global coordinate system for the model. For shell elements, only the vector of the principal material direction is required, since the second orthotropy direction is resolved into the plane of the element. Shear of the fabric during forming and the resultant variations in fibre direction are beyond the scope of this investigation. For the geometries analysed here, with little structural complexity, it is assumed that woven reinforcing fibres are tangential to each other.

5.3 Bi-Phase Damage Model

The bi-phase model allows the user to define the fibre properties of a composite as a one-dimensional material phase, separately from the properties of the matrix, which are defined as an orthotropic material. The stiffness of the resulting composite is calculated by superimposing these two material phases. Damage occurs to both the fibre and matrix according to individual laws.

This type of material model is applicable to unidirectional fibre reinforced composite plies. It is less suitable for woven materials such as Twintex.

By neglecting the fibre phase in the bi-phase model, the matrix properties can be used to model the behaviour of an orthotropic composite material. This approach allows the analyst to effectively model the behaviour of a woven composite material such as Twintex.

5.3.1 Degenerate Bi-Phase Damage Model

In its degenerate form, the matrix phase of the bi-phase model is used to model the elastic damaging behaviour of a woven composite material. The model allows

calibration based on a combination of both equivalent volumetric strain and equivalent shear strain dependant damage parameters. For models developed during this study, damage is identified wholly through (deviatoric) equivalent shear strain, rather than the (direct) volumetric equivalent strain. This assumption is possible due to the use of the degenerate form of the bi-phase model, where the fibre is dealt with as part of a homogenous composite material rather than a separate, superimposed one-dimensional fibre phase as in the unidirectional bi-phase model. Damage developed using a purely deviatoric strain based parameter significantly simplifies the calibration of the damage magnitudes and strains, but still allows the user to tailor the damage model accurately for the material.

A single damage parameter, d , is used to quantify the level of damage accumulated by the material during an analysis, based on the deviatoric component of strain. In the degenerate form of the model, this damage parameter is used to calculate reduced elastic properties in the material model for areas where damage has been identified. The parameter is used to reduce all the elastic modulus properties for the composite and therefore does not decouple damage modes, unlike the model developed in Chapter 4. The relationship between strain and damage and subsequently damage and elastic constants is shown in Figure 2.8, in Chapter 2, where the model was first introduced.

To summarise the behaviour of the model, the damage parameter, d , is set at zero and remains at this level until an initial strain threshold is reached. The damage level is then increased linearly in two stages through an intermediate strain level up until a point where an ultimate damage level is deemed to have been reached. All of the composite material elastic moduli are reduced proportionally to the parameter, d , through all the stages of identified damage.

5.4 Calibration

The calibration of this material model requires the input of elastic properties and damage parameters for an orthotropic composite ply in both tension and compression. These, as mentioned in the definition of the degenerate bi-phase model, are input as

the matrix phase properties and are damaged according to the deviatoric strain based damage law.

The calibration parameters were taken from manufacturers published data and from experimental test and are detailed in Chapter 3. The calibrated material cards used for simulations presented in this chapter are given in Appendix D. Investigation of the sensitivity of the model to variation in the damage model calibration was undertaken and results of this sensitivity analysis are presented later in this chapter.

5.4.1 Calibration of Composite Material Elastic Constants

Experimental methods for the determination of the elastic material properties are described in Chapter 3. The in-plane tensile and compressive modulus are assumed to be the same for both orthotropy directions, since the material is a balanced weave reinforced fabric composite. The through thickness modulus for the composite was input from manufacturers published data. Since the work was developing a modelling capability for in-plane damage simulation, the through thickness properties were not critical to the results.

The shear moduli and Poisson's ratio were calibrated from manufacturers' published data, with an adjustment of the shear modulus from 1.2GPa to 1.04GPa, based on results from the previous implicit damage modelling work.

5.4.2 Calibration Of Composite Material Damage Parameters

The damage parameters for the strain based volumetric damage scheme were calibrated using an iterative process. Since the parameters are used to describe an overall damage state rather than specific damage mechanisms it was necessary to develop a calibration, which was applicable to both the fibre direction and shear damage behaviour of the material.

A spreadsheet, developed during previous work by Curtis [15], was used to generate stress/strain curves for the calibrated material model in tension, compression and shear. This allowed comparison with experimental curves and fine adjustment of the damage parameters to best represent all three loading situations.

5.4.3 Simulation of Calibration Coupon Tests

Following the definition of elastic properties and damage parameters, simulations of the tests used to generate calibration data for the material model were performed. This was undertaken to confirm that the procedure had captured the material behaviour as accurately as possible. Throughout this section of the work, simulation results, like the experimental results in Chapter 3, are presented as nominal stress/strain.

5.4.4 Tensile 0°/90° Test Simulation

The 0°/90° tensile test model was run to validate the material and damage calibration for balanced weave Twintex tested in the fibre direction. The mesh of 170 shell elements used to model the specimen, was identical to the mesh used in the implicit simulation, see Figure 5.1. Load was applied as a constant velocity nodal displacement to one end of the specimen. The other end of the specimen was fully constrained. All boundary conditions were applied to 50mm sections of the specimen to represent the jaws used during experimental tests.

A cross section was defined centrally in the specimen, to give cross sectional force output for the simulation. This was used to derive the nominal stress, based on the undeformed cross section, which is compared to experimental results. Output of the damage parameter values for each element was also requested during the simulation. This allowed identification of areas where damage is predicted and where failure occurs. Similar output was requested for all further simulations in this part of the work.

The stress/strain response of the model, shown in Figure 5.2, generally compares well to the experimental results. The experimental result is dominated by the elastic response of the material followed by catastrophic tensile failure. This simulation behaves in a slightly different manner due to the nature of the damage model, which is calibrated to represent a number of damage modes. The damage parameters can be adjusted to tailor the response of the model, although later sensitivity analysis shows that due to the sensitivity of the model, this calibration was the most accurate for general representation of the material.

Figure 5.3 shows the specimen displacement and damage development during the simulation. Damage does not develop during the initial stages of the test, as the specimen is deformed elastically. At approximately 1% strain damage starts to develop throughout the specimen. This builds up until ultimate failure, which occurs in the specimen at approximately 3% strain. This ultimate failure, where the damage level in the specimen approaches 1 occurs across the width of the specimen in the region of the jaws. This mode of failure is similar to that seen during experimental test.

This simple test demonstrated that the tensile material model for behaviour in the fibre direction was calibrated to generally reflect the damaging behaviour of Twintex in fibre direction tension.

5.4.5 Compressive 0°/90° Test Simulation

The mesh used for simulation of the compressive test specimen is shown in Figure 5.4. The majority of the model was constrained to represent the jaws used for loading the specimen. Loading was applied compressively using a nodal velocity boundary condition.

Figure 5.5, shows the load displacement response for 0°/90° Twintex 1:1 in compression. The results from simulation of this test show good correlation up until around 1% strain. In the experimental test, this is the point at which out of plane deformation starts to occur and the gauge used to measure local strain became detached from the specimen. The finite element simulation continues past this point, but with a significant reduction in modulus, as large amounts of damage are predicted in the specimen.

Predicted damage is compared to a failed test specimen in Figure 5.6. It can be seen that the location and shape of the failure zone is predicted accurately, although the strain at ultimate failure cannot be confirmed due to the nature of the data acquisition during the test.

5.4.6 Tensile +45°/-45° Test Simulation

The +45°/-45° tensile test specimen model used an identical mesh and boundary conditions to the 0°/90° tensile model. The critical difference for this analysis was that the material model was oriented at 45° to the axis of load application.

The stress/strain response of the model and experimental results are shown in Figure 5.7. There are two fundamental differences in the response of the finite element model to the experimental results obtained. The first is the observed modulus of the specimens. The model shows that the predicted behaviour of the +45°/-45° specimen is considerably stiffer than that observed. Secondly the strain to failure for the model is lower than the experimentally observed value.

Figure 5.8 shows the specimen displacement and damage development during the test. Damage is initiated at the early stages of the displacement and builds up throughout the specimen. Localised damage is only seen in the later stages of the +45°/-45° model analysis. The failure of the model results from a rapid growth in damage at approximately 2.2% strain, which leads to ultimate failure. This failure is observed in experimental tests, but at considerably higher strain levels.

5.5 Validation

The same range of coupon tests used during the validation of the implicit finite element damage model, in Chapter 4, were used during the validation of the calibration parameters for the PAM-CRASH damage model. During this part of the work no alteration was made to the previously calibrated parameters. The specimens selected were relatively simple geometries, which in most cases contained a stress concentration in the form of a circular hole.

5.5.1 Compressive +45°/-45° Test Simulation

For this simulation, the compressive test specimen model was identical to that used in the 0°/90° compressive specimen, although the material model in this case was oriented at 45° to the axis of the test. The shear behaviour of the material was calibrated from the off-axis tensile test, so the result from this simulation was used only for validation.

The stress/strain response from the simulation and test is shown in Figure 5.9. The simulation, like the off-axis tensile test, shows a stiffer behaviour than experimental test. In the test, the specimen begins to damage at very low strain levels and shows a progressive reduction in stiffness. The simulation shows little reduction in stiffness up to approximately 0.75% strain. After this point, damage development is more rapid in the simulation than in the test and the stiffness reduces significantly. Between 1.5% and 2% strain, the simulation predicts high levels of localised damage and the specimen begins to fail catastrophically.

Figure 5.10 shows the damage build up in the specimen during the simulation. These images confirm the response observed in the stress strain curves. At 2.0% strain, 5 elements in the central area of the specimen have reached a maximum level of damage. This damage progresses rapidly through the specimen, which by 2.5% strain has failed across its whole width.

This result shows a similar behaviour to the tensile of-axis test, highlighting the difficulty in calibrating a set of damage parameters to accurately model both shear and tensile fibre damage. Using the bi-phase model, as shear damage develops, the fibre direction properties are also damaged, resulting in a more brittle failure than that observed in test, where the matrix fails, but the fibres remain intact and continue to function in load bearing up to significantly higher strains than predicted in simulation.

5.5.2 Tensile 0°/90° Hole in Plate Test Simulation

Figure 5.11, shows the finite element mesh used for the simulation of the 0°/90° tensile hole in plate test simulation. The specimen was constrained and simulated using identical boundary conditions to the plain tensile test specimens.

The stress/strain response from test and simulation is shown in Figure 5.12. The simulation correlates well with experiment up to approximately 1% strain and accurately models the elastic behaviour of the specimen. After 1% strain the simulation predicts catastrophic failure in the specimen, which is not observed in the experimental test until approximately 2.0% strain.

Figure 5.13 shows the development of damage during the simulation, compared to the failed experimental test specimen. As expected, damage is initiated at the edge of the stress concentration. In the simulation, this damage leads to rapid catastrophic failure, as the modulus of the elements at the edge of the hole is reduced and load is transferred to adjacent elements. Total failure is predicted across the width of the specimen by 1.2% strain. This result is conservative compared to the experiment, where, although the specimen starts to damage around the stress concentration, catastrophic failure does not occur until 2.0% strain. This result is similar to the behaviour of the implicit finite element damage model observed in Chapter 4, where in tensile fibre direction simulations, localised damage leads to catastrophic failure.

5.5.3 Tensile +45°/-45° Hole in Plate Test Simulation

The off-axis tensile hole in plate specimen uses an identical mesh and boundary conditions to the previous simulation, although the material model is aligned at 45° to the axis of the test.

Figure 5.14 shows the stress/strain response from simulation and experimental test. The model predicts that catastrophic failure will occur at approximately 2.0% strain in the gauge length of the specimen. This is significantly different to the experimentally observed result. The simulation also predicts that the stiffness of the specimen prior to failure will be higher than the test. This increased stiffness was seen in previous off axis simulations and was expected in this analysis. The premature failure was expected and had also been observed in previous simulations and is a combination of over prediction of elastic property reduction resulting from shear damage and load transfer from damaged elements causing rapid failure in adjacent areas of the specimen.

The development of damage in the specimen is shown in Figure 5.15. The rapid failure between 1.5% and 2.0% strain in the specimen gauge length can be clearly observed. Like the fibre direction tensile test with a stress concentrator, as soon as catastrophic damage has occurred around the stress concentration, load transfers to adjacent elements and failure occurs rapidly across the width of the specimen. The shape of the damaged area is significantly different to the fibre direction simulation and shows failure occurring at 45° to the axis of the test.

5.5.4 Compressive +45°/-45° Hole in Plate Test Simulation

The compressive off axis test specimen model, with a stress concentration, is simulated with the mesh shown in Figure 5.16. The stress strain response for the test and simulation is shown in Figure 5.17. As with the other off axis fibre orientation simulations, failure occurs significantly earlier in the simulation than in test and the stiffness of the specimen is predicted to be slightly higher as the specimen is displaced. At 1mm displacement, the test specimen has damaged significantly and the stiffness is reduced, a phenomenon which is not captured accurately by the model. When damage is identified in the simulation, failure is not progressive, as it is in the test, and occurs in two stages with an initial failure at approximately 1.2mm and a catastrophic collapse of the specimen at 2.2mm.

Figure 5.18 shows the damage evolution during the simulation. Between 1mm and 2mm it can be observed that the first reduction in specimen stiffness is caused by damage approaching a level of approximately 0.5 in the elements around the stress concentration. The second, catastrophic failure is shown at 2.6mm where elements all across the specimen are approaching a maximum damage level. This specimen, like the previous simulation, also shows damage evolving at 45° to the axis of the test.

5.6 Model Sensitivity

Since the material model for a composite ply requires extensive calibration, a large proportion of the work undertaken was an assessment of the sensitivity of analysis results to variation in material properties. Although an initial calibration was carried out using a spreadsheet and macro to produce calibration curves based on damage parameters, further adjustment was undertaken during the simulation of the calibration tests, detailed in section 5.4. Both the 0°/90° and +45°/-45° tensile test models were run with variation in a range of selected parameters to ascertain which situations and damage types were most sensitive to the calibration.

Subsequently an investigation of sensitivity to mesh refinement, using the +45°/-45° compressive hole in plate simulation, was performed.

5.6.1 Sensitivity to Damage Model Parameters

For the investigation of the sensitivity of the model to variation in calibration parameters, four models were used. The parameters for these models are detailed in Table 5.1. Initially these models were used to simulate the 0°/90° tensile test. Stress/strain results from these simulations are shown compared against the final calibration and experimental test in Figure 5.19. It can be observed from this comparison that the performance of the model in the fibre direction, as expected, is highly sensitive to the parameters used. The final calibrated model shows the best agreement with experiment. Both Model 2 and Model 4 use the same ultimate damage level, of 0.6, which in the case of this simulation is not high enough to ‘fail’ the specimen.

Figure 5.20 shows the simulation results from the +45°/-45° tensile test, using the same model calibrations given in Table 5.1. The stress/strain results show that this test is far less sensitive to damage model calibration than the fibre direction tensile test. All the models over predict the stiffness of the specimen and reach ultimate failure at significantly lower strain levels than was observed in experiment. This result confirms that the final version of the calibrated model, used in the validation simulations and later demonstrator component models described in Chapter 6, offers the best compromise between accurate simulation of fibre direction and shear damage.

Unlike the model developed in Chapter 4, this model degrades all elastic properties based on the level of damage identified. This leads to reduction in fibre direction properties when shear damage is identified and necessitates careful calibration to capture all damage modes as accurately as possible.

5.6.2 Sensitivity to Mesh Refinement

The model’s sensitivity to mesh refinement was investigated using the compressive +45°/-45° hole in plate specimen simulation. Two further meshes were generated, a coarse mesh shown in Figure 5.21 and a fine mesh shown in Figure 5.22.

Figure 5.23 shows the stress/strain response for the coarse mesh, compared with test and Figure 5.24 shows the damage development in the specimen. The specimen predicts first significant damage at slightly over 1mm of displacement and

catastrophic failure just before 3mm. This result is similar to that seen in section 5.5.4, although failure is predicted slightly later in the simulation and at a higher load.

The stress/strain results and damage plots for the fine mesh, shown in Figure 5.25 and Figure 5.26 respectively show a slight difference in results to the coarse mesh. Failure occurs earlier and at a lower load. From the stress/strain response, it can be seen that the first major damage occurs at just before 1mm displacement and ultimate failure occurs at just before 2mm. These results are very similar to those from the standard mesh simulation performed during the validation phase of the work. This suggests that the damage prediction has converged, as there is little sensitivity or improvement in accuracy of the simulation between the standard and the fine mesh.

5.7 Conclusion

The PAM-CRASH degenerate bi-phase damage model for composite materials has been used to simulate the damaging behaviour of balanced weave Twintex. The model has been calibrated using a range of data from experimental test and manufacturers datasheets.

Calibration tests and a range of validation tests have been simulated to investigate the model's performance in a range of in-plane damage situations. This has shown that the model accurately predicts the behaviour of Twintex damaging in the fibre direction. Shear damage in the specimen has been shown to be less accurately modelled by the technique, with an over prediction of the stiffness of all the off-axis specimens simulated.

Specimens with a hole showed that the model was also sensitive to geometric features. As damage started to develop in the region of the stress concentrator the model often predicted rapid degradation of material properties and lead to catastrophic failure. The sensitivity of the model to the calibration parameters was significant when modelling fibre direction damage. This sensitivity was not observed in the simulation of shear damage.

5.8 Tables

Parameter	Model 1	Model 2	Model 3	Model 4
ϵ_{iT}	0.007	0.01	0.0053	0.0053
ϵ_{lT}	0.02	0.02	0.017	0.017
ϵ_{uT}	0.05	0.08	0.039	0.039
d_{iT}	0.2	0.1	0.5	0.1
d_{uT}	0.8	0.6	0.95	0.6
ϵ_{iC}	0.007	0.01	0.0053	0.0053
ϵ_{lC}	0.02	0.02	0.017	0.017
ϵ_{uC}	0.05	0.08	0.039	0.039
d_{iC}	0.2	0.1	0.5	0.1
d_{uC}	0.8	0.6	0.95	0.6

Table 5.1 Material damage model parameters for sensitivity analysis

5.9 Figures

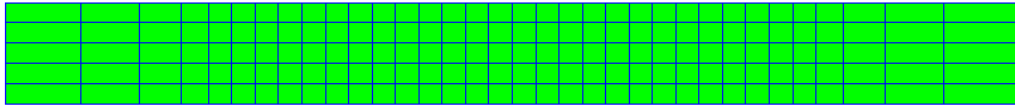


Figure 5.1 Tensile test - shell element mesh

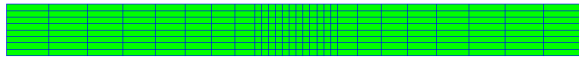


Figure 5.4 Compressive test - shell element mesh

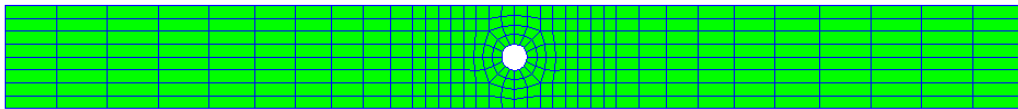


Figure 5.11 Tensile hole in plate test - shell element mesh

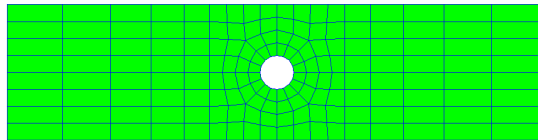


Figure 5.16 Compressive hole in plate test - shell element mesh

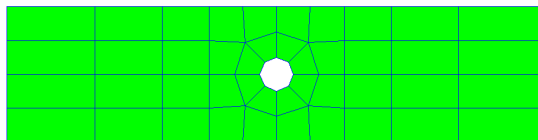


Figure 5.21 Compressive hole in plate test - shell element mesh (coarse)

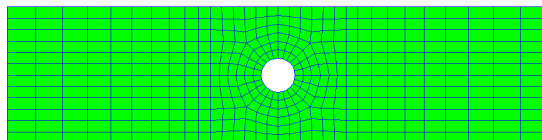


Figure 5.22 Compressive hole in plate test - shell element mesh (refined)

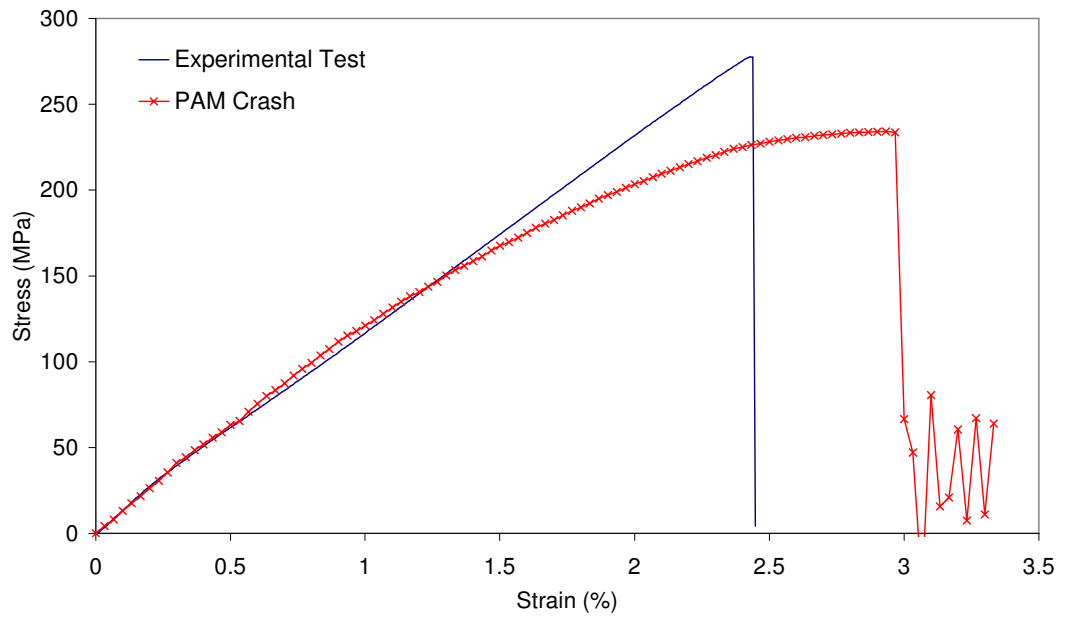


Figure 5.2 0°/90° tensile test simulation - stress/strain

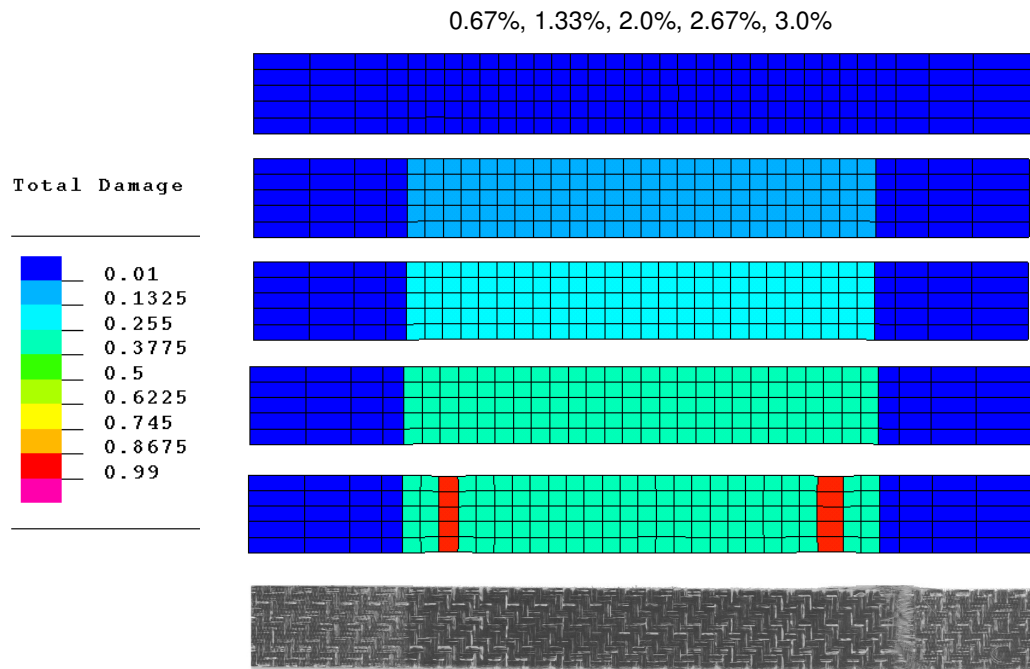


Figure 5.3 0°/90° tensile test simulation - experimental and predicted damage

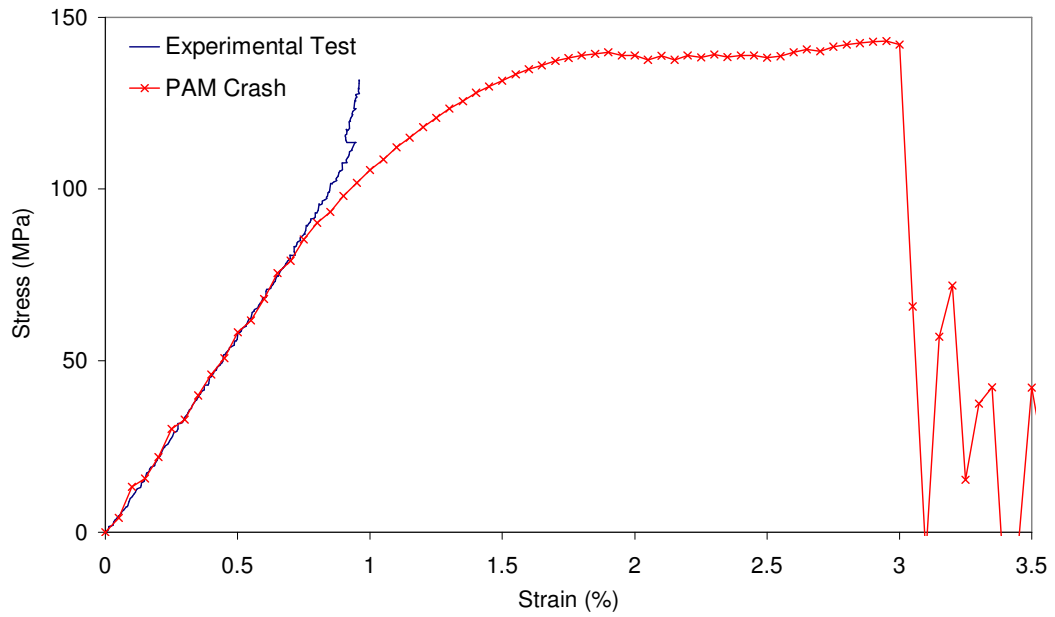


Figure 5.5 0°/90° compressive test simulation - stress/strain

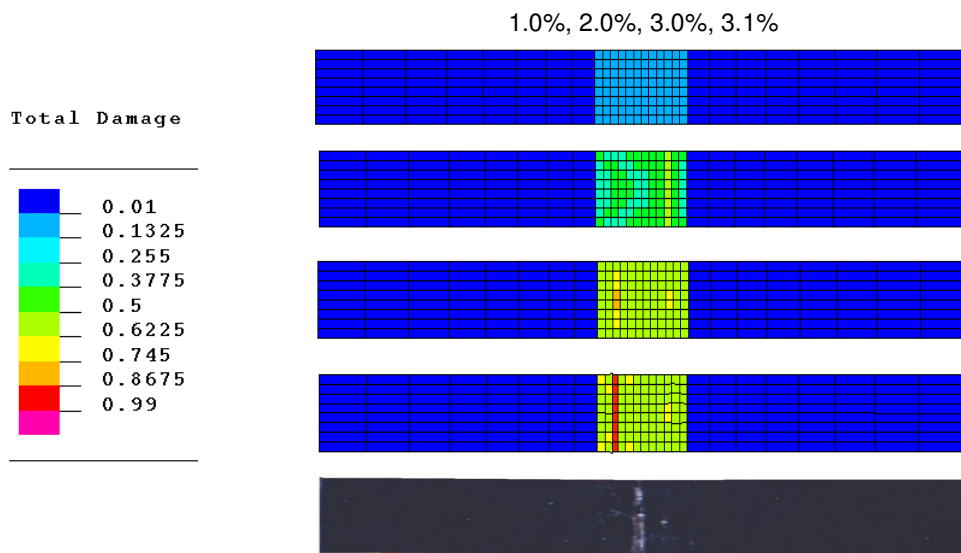


Figure 5.6 0°/90° compressive test simulation - experimental and predicted damage

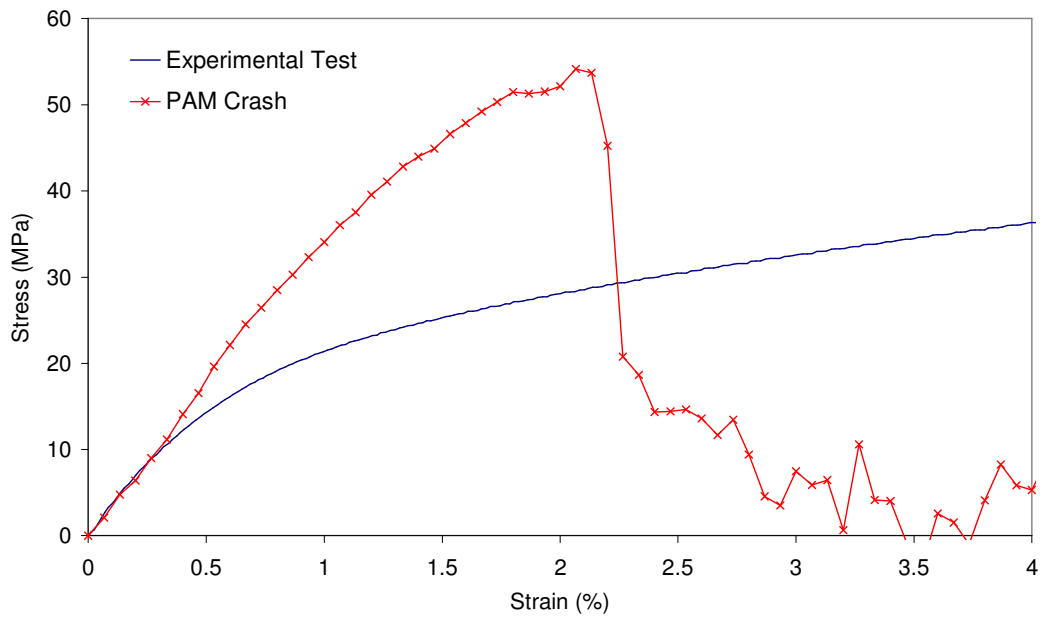


Figure 5.7 +45°/-45° tensile test simulation - stress/strain

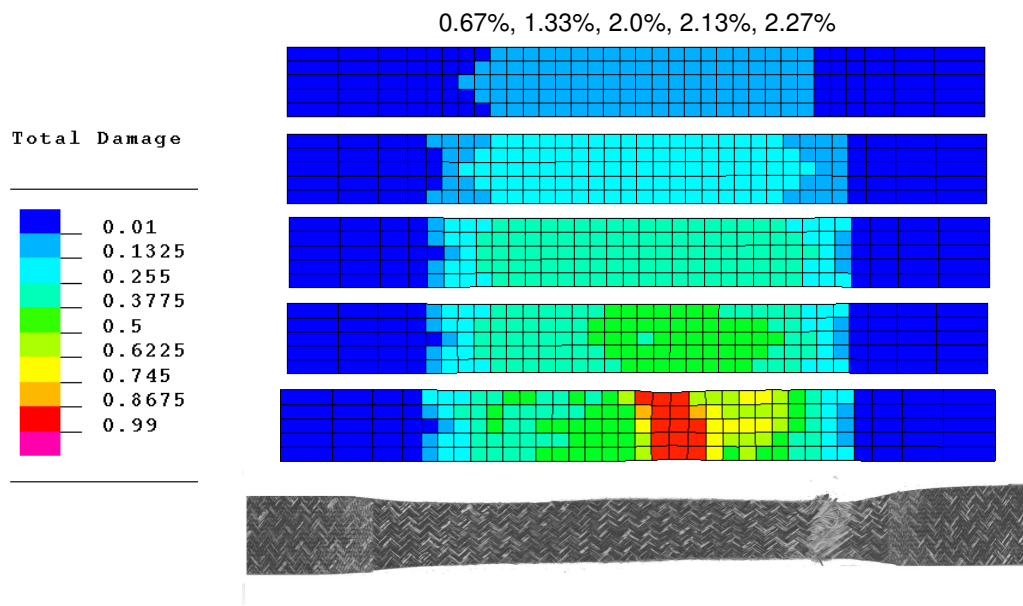


Figure 5.8 +45°/-45° tensile test simulation - experimental and predicted damage

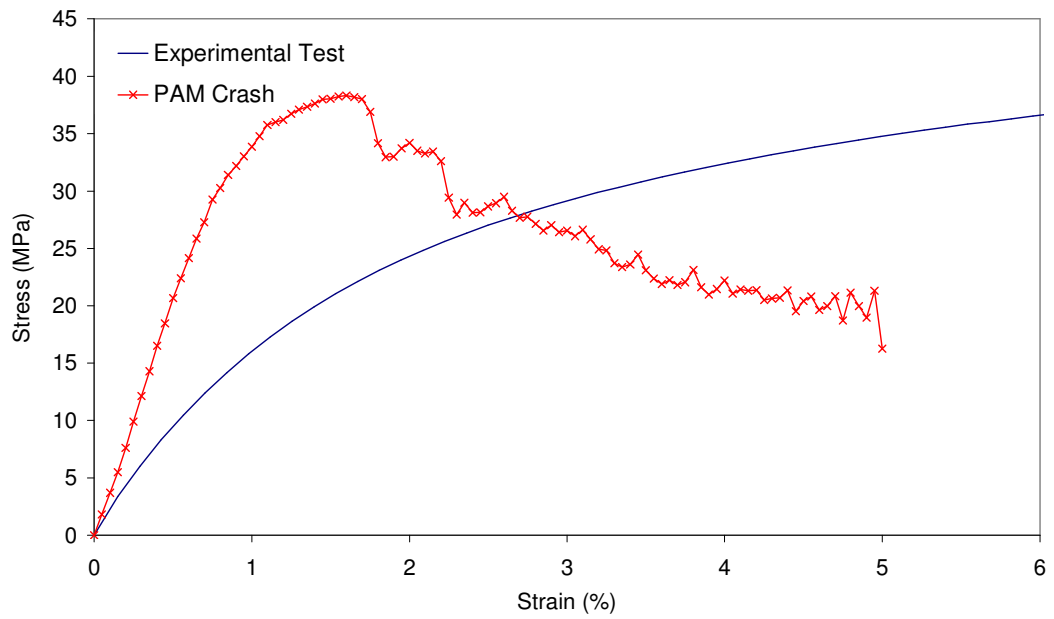


Figure 5.9 +45°/-45° compressive test simulation - stress/strain

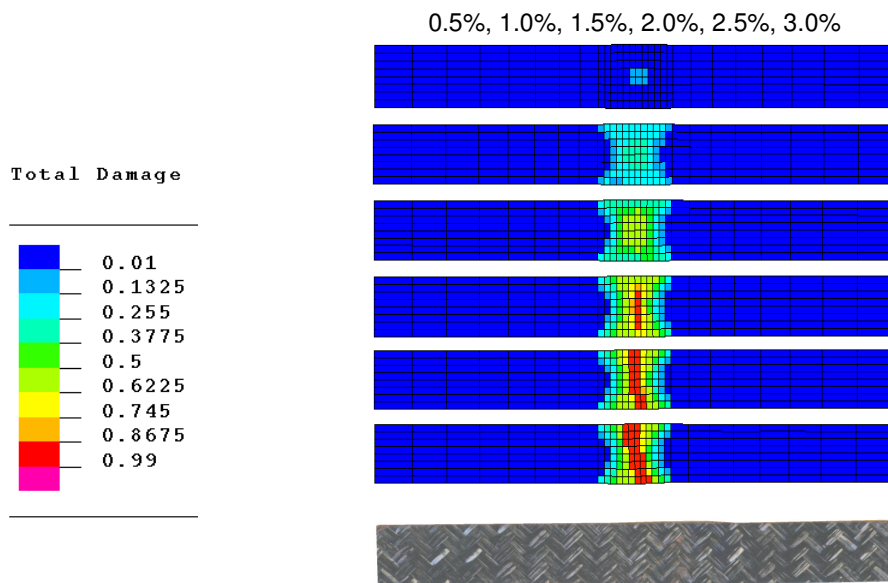


Figure 5.10 +45°/-45° compressive test simulation - experimental and predicted damage

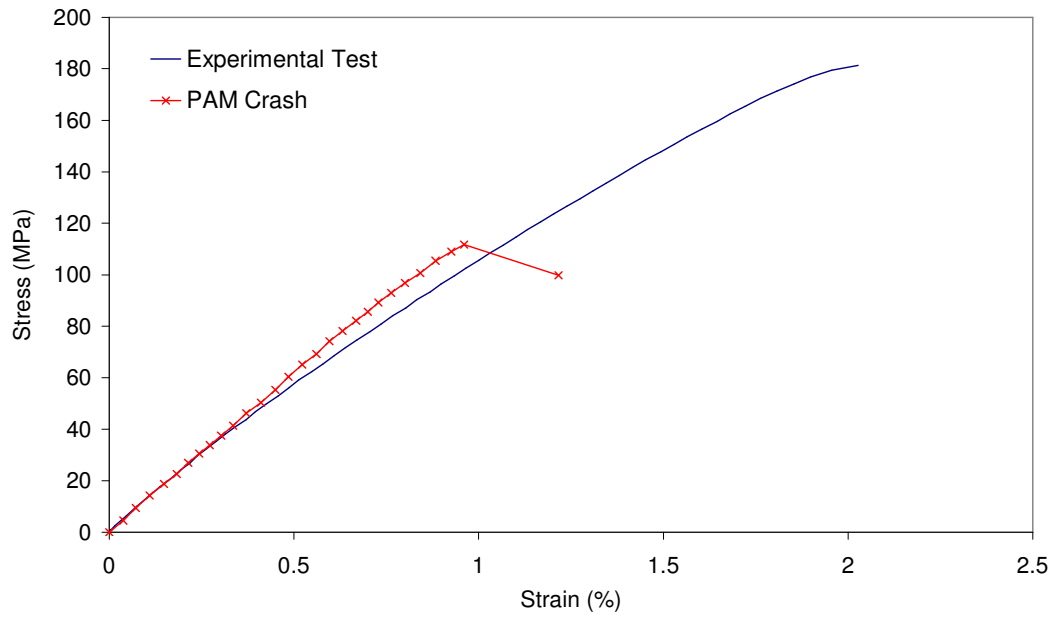


Figure 5.12 0°/90° tensile hole in plate test simulation - stress/strain

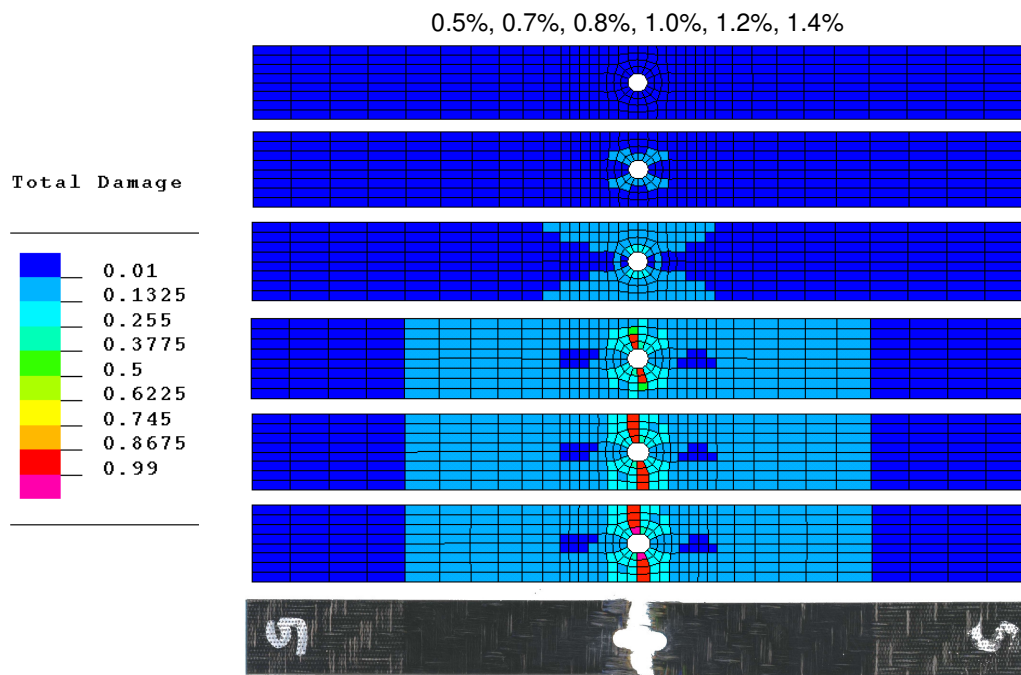


Figure 5.13 0°/90° tensile hole in plate test simulation - experimental and predicted damage

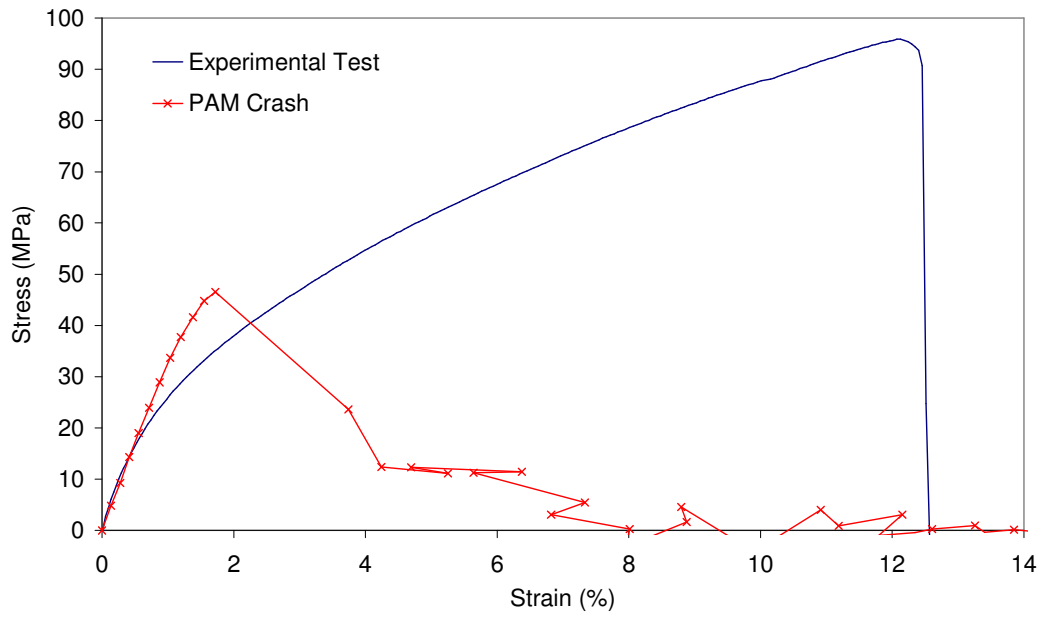


Figure 5.14 +45°/-45° tensile hole in plate test simulation - stress/strain

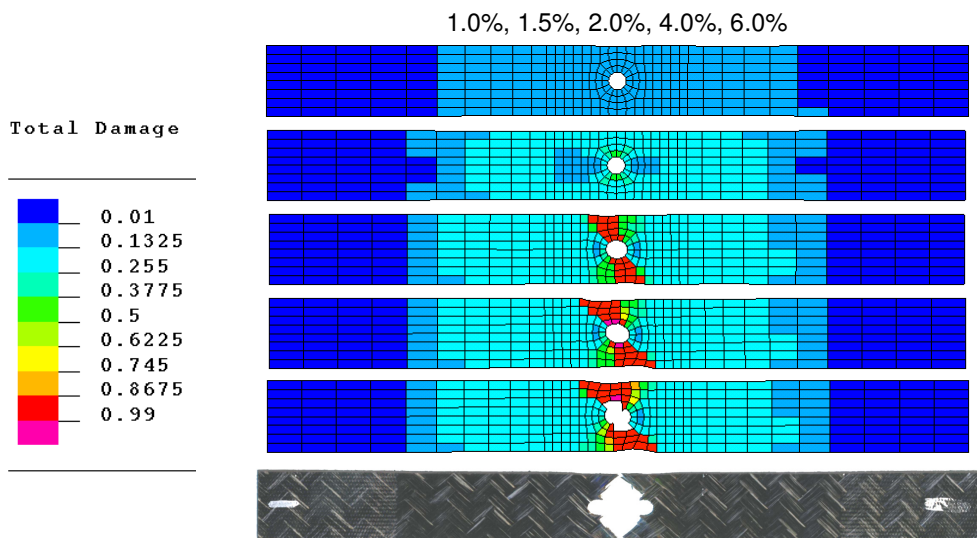


Figure 5.15 +45°/-45° tensile hole in plate test simulation - experimental and predicted damage

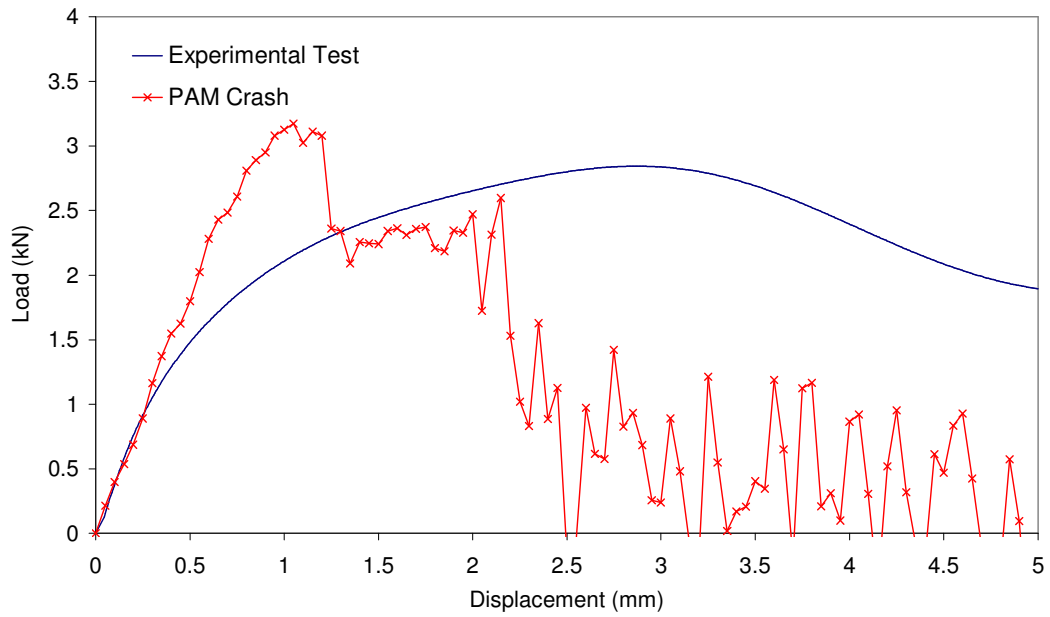


Figure 5.17 +45°/-45° compressive hole in plate test simulation - load/displacement

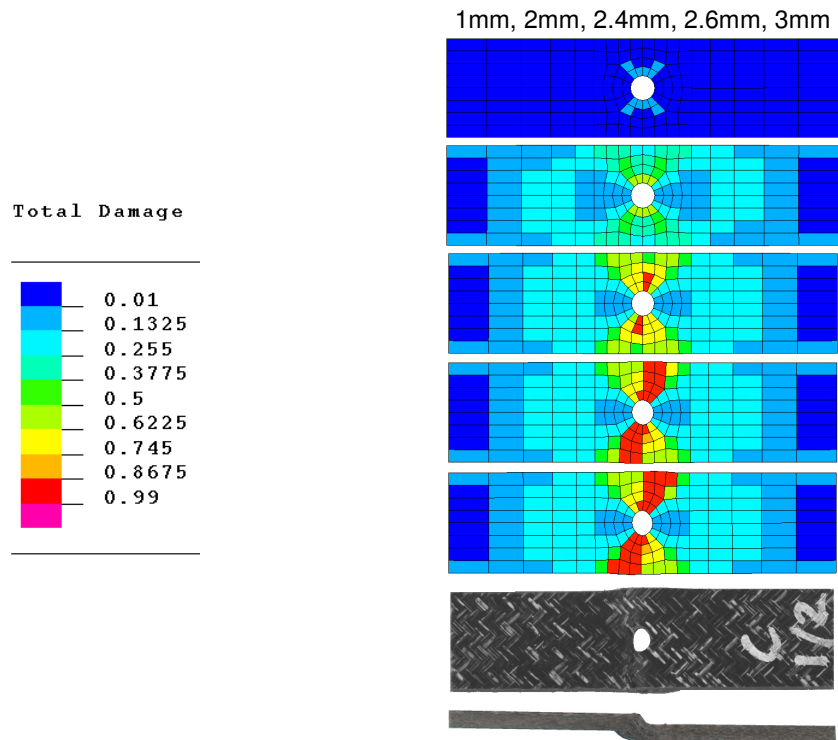


Figure 5.18 +45°/-45° compressive hole in plate test simulation - experimental and predicted damage

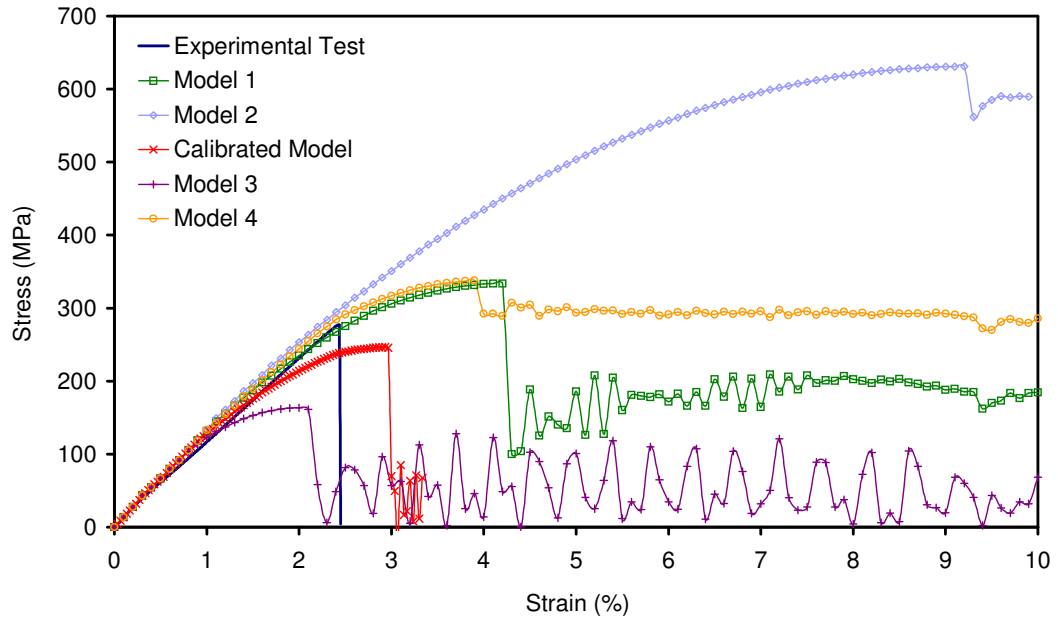


Figure 5.19 0°/90° tensile test simulation sensitivity

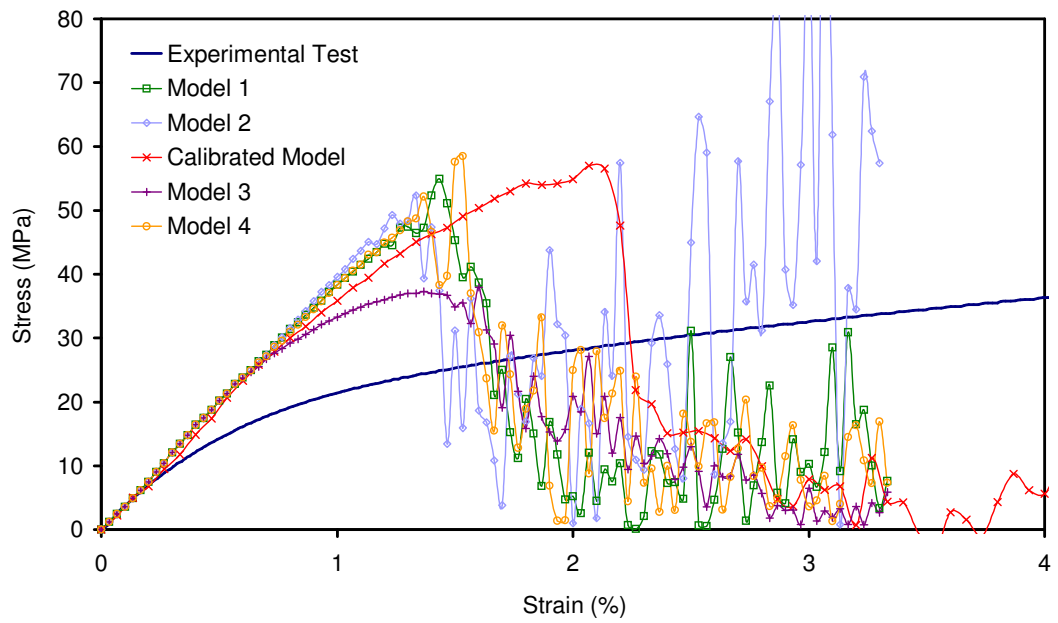


Figure 5.20 +45°/-45° tensile test simulation sensitivity

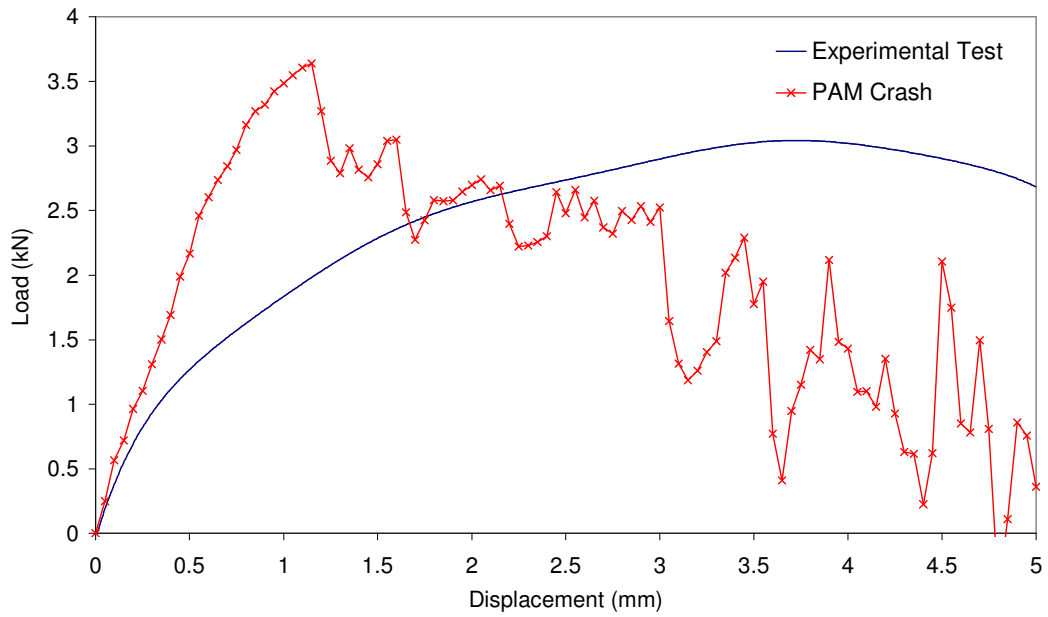


Figure 5.23 +45°/-45° compressive hole in plate test simulation - coarse mesh

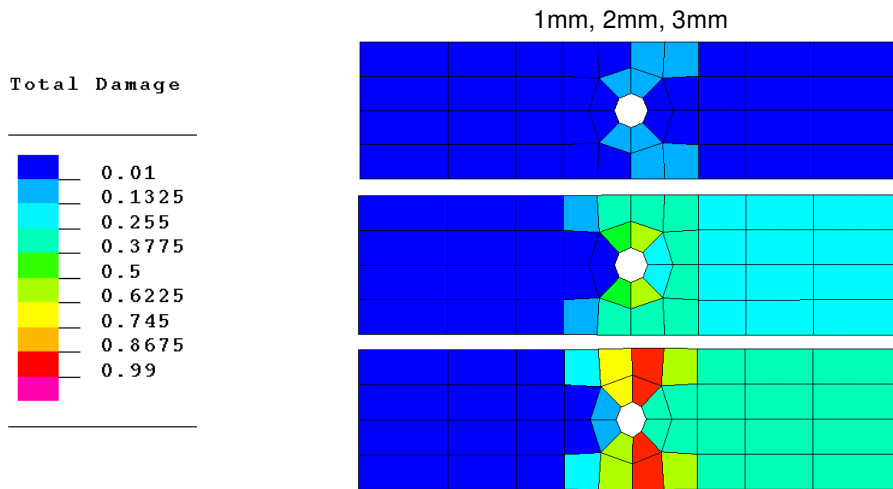


Figure 5.24 +45°/-45° compressive hole in plate test simulation - coarse mesh - predicted damage

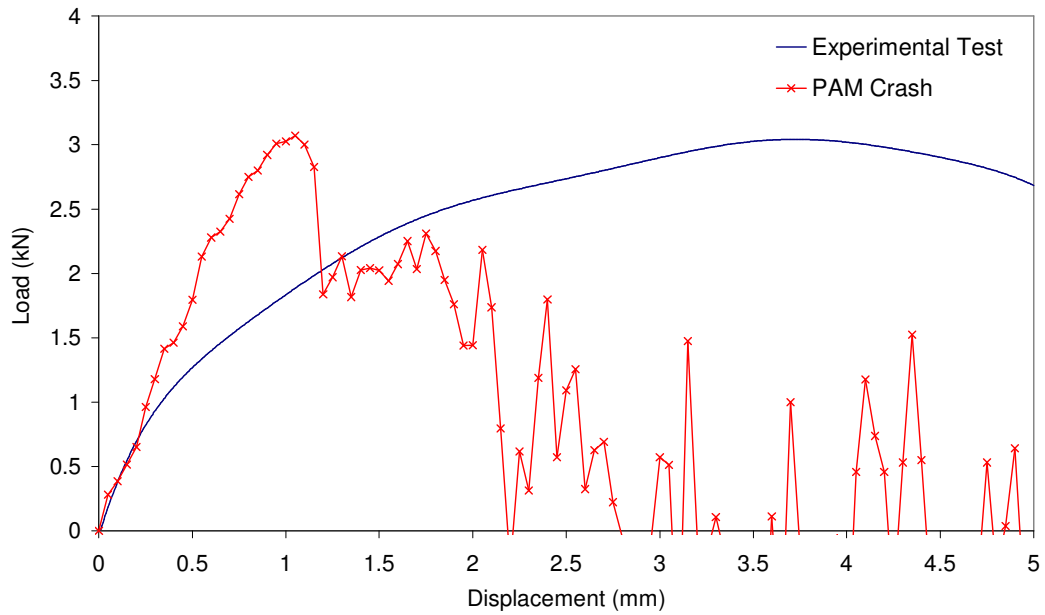


Figure 5.25 +45°/-45° compressive hole in plate test simulation - fine mesh

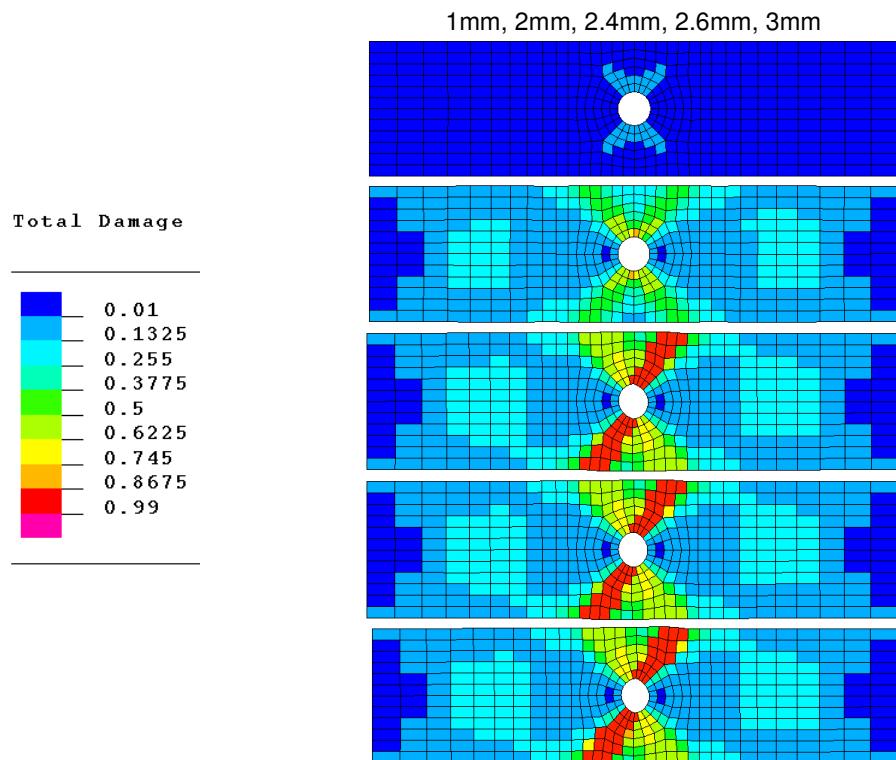


Figure 5.26 +45°/-45° compressive hole in plate test simulation - fine mesh - predicted damage

Chapter 6 Application to an Automotive Demonstrator Component

6.1 Introduction

To validate the manufacturing methods and analysis techniques and to compare the performance of a thermoplastic part with a metallic equivalent, an automotive demonstrator component programme was undertaken. Various factors influenced the choice of demonstrator component, including size, geometry and cost of manufacture and test, as well as the potential viability of introducing the part on future vehicles. For these reasons, a side intrusion protection beam was selected.

Initially, at the start of the research programme, a Phase 1 demonstrator component was designed. At this stage, analysis capability was limited and unvalidated, so the design was based on a simple section geometry designed to offer an acceptable level of stiffness. This beam was thoroughly tested and results were used to validate the finite element damage modelling techniques developed during the core part of the research programme.

The Phase 2 demonstrator component was developed with the aim of installation and test in a full vehicle, to an accepted legislative test method. During the design of the beam, the validated finite element damage models were used extensively to investigate potential geometries and select the most effective. This process reflects the design and simulation stages undertaken during commercial projects developing new components. The Phase 2 demonstrator component was tested and results were compared to those from fully predictive finite element simulations. This testing evaluated the performance of the beam against a current design and further validated the explicit finite element damage modelling technique developed and calibrated in Chapter 5.

For the final full vehicle test a Phase 2 beam was installed in one side of a vehicle along with a thermoplastic door cassette component. Both sides of the vehicle were tested to the Federal Motor Vehicle Safety Standard for side intrusion performance

[45] and results for the composite concept side and the standard steel door configuration were compared.

During the development of the demonstrator component a further two forms of Twintex were also investigated. These were 4:1 plain weave, 60% weight fraction, commingled glass polypropylene Twintex and a double layer, balanced, 2 x 2 twill weave, 60% weight fraction, commingled glass polypropylene with 1% z-axis glass fibres, in this study referred to as 3D Twintex.

6.2 Side Intrusion Beam Test Methods

The Phase 1 demonstrator component, described in section 6.3, was tested using two different 3-point bending test methods, referred to as a small and large-scale 3-point flexure test.

The Phase 2 demonstrator component, described in section 6.4, was tested using the large-scale 3-point flexure test method and was validated in a test vehicle, using the FMVSS 214 [45] quasi-static pole side intrusion test.

6.2.1 Small-Scale 3-Point Flexure Test

For preliminary testing of the Phase 1 beam a 3-point flexure rig was developed for a servo-hydraulic Instron 8500 test machine. Due to the dimensions of the test machine and fixture, the maximum deflection of the beam was limited to 80mm. The load was applied at the middle of the beam through a 2 inch diameter cylindrical impactor and each end of the beam was supported with a 2 inch diameter cylindrical bar.

Aluminium brackets, manufactured from sheet material, were used to mount an extensometer across the centre of beam for measurement of cross-sectional splaying. Measurement of splaying was made up to 5mm during the test. A Phase 1 beam mounted in the test rig is shown in Figure 6.1.

Load data was measured using a 100kN load cell and deflection data was taken from the crosshead of the test machine. The beams were tested at a crosshead displacement

rate of 10mm/minute. Table 6.1 details the thickness, material and lay-up of the Phase 1 beams tested in the small-scale 3-point flexure rig.

6.2.2 Large-Scale 3-Point Flexure Test

To test the beams past the early onset of damage and in the cases of the aligned fibre beams, to ultimate failure, a larger scale 3-point flexure test was developed. The rig used was based on an FMVSS 214 test rig, set up with the beam mounted rigidly at one end and with a compliant steel bracket and restraining chains at the other end. The rig, during Phase 1 beam testing is shown in side view in Figure 6.2 and from the front in Figure 6.3. Figure 6.4 shows the rig during testing of the Phase 2 demonstrator component. A standard steel side intrusion beam from the target vehicle was also tested during the Phase 2 programme to allow comparison with the demonstrator component.

Load data was measured using a load cell mounted behind the 12 inch diameter impactor and displacement was measured using a wire pull displacement transducer attached to the impactor. Both the Phase 1 and Phase 2 beams were tested at a nominal displacement rate of 500mm/minute.

Table 6.2 details the thickness, material and lay-up of the Phase 1 and Phase 2 beams tested in the large-scale 3-point flexure rig.

6.2.3 FMVSS214 Side Intrusion Test

The Phase 2 demonstrator was designed to meet specific load and displacement requirements detailed in FMVSS214, the federal Motor vehicle Safety Standard for side intrusion performance [45]. As part of a wider research programme a semi-structural door cassette was investigated, so this was also used in the final validation test. The door interior panel and steel beam were removed and the composite beam was mounted in the door using steel brackets. The composite door cassette, manufactured from glass mat thermoplastic (GMT) was mounted in place of the standard door trim panel. The assembled door mounted in the test vehicle is shown in Figure 6.5.

The vehicle was constrained by bolting the chassis to a hard floor. The 12 inch diameter impactor used in the large-scale 3-point flexure tests was used to quasi-statically deform the doors centrally, see Figure 6.6. The vehicle was tested at a nominal displacement rate of 500mm/minute. Load displacement data was measured during the test using the same equipment as that used in the large-scale 3-point flexure tests. Table 6.3 details the thickness, material and lay-up of the Phase 2 beam and steel beam tested to FMVSS214.

6.3 Phase 1 Demonstrator Component

The Phase 1 side intrusion beam demonstrator component was developed during the early stages of the project. It was used to validate both the manufacturing and modelling techniques being developed during the research programme. Since modelling tools were not fully developed at the time of the initial design, only basic numerical modelling was undertaken to evaluate the initial stiffness of the component.

A test programme, including small and large-scale flexural testing was undertaken. Results from this testing were compared to simulations performed subsequent to the tests.

6.3.1 Phase 1 Demonstrator Component Design

The component was developed to a generic design envelope, similar to that available for current steel beams, see Figure 6.7, which would allow the beam to be mounted in a typical 3 door vehicle. This approach set constraints on both the length and depth of the beam.

Since the beam was to be tested in flexure, compressing one surface and loading the other in tension, the compressive and tensile strength of Twintex was taken into account. For this reason, the final geometry was developed as a ‘top hat’ section, with approximately double the quantity of material on the compressive face, to take into account the reduction in strength observed in compression during coupon tests. The final design is shown in Figure 6.8 and a section through the centre of the beam is shown in Figure 6.9

6.3.2 Phase 1 Demonstrator Component Manufacture

The beam was manufactured using matched metal tooling and a non-isothermal compression moulding process. The Phase 1 demonstrator component tool included both a sprung blankholder and shear edge, based on the flat plaque tool concept introduced in Chapter 3.

The processing conditions for the demonstrator components were less controllable than those used in the laboratory, due to the industrial scale techniques employed, although where possible, the previously specified optimised parameters, given in Chapter 3, were used.

6.3.3 Phase 1 Demonstrator Component Small-Scale 3-Point Flexure Test

Two 3-point flexure test methods, described in section 6.2, were used to evaluate the performance of the Phase 1 demonstrator component. The first method, a small-scale 3-point flexure test, was performed on four beams: one of each of the four material configurations moulded. The load applied to displace the beam was measured as well as the splaying of the section, since the deformation mode was expected to vary depending on the material configuration.

Figures 6.10 and 6.11 show the results from the $0^\circ/90^\circ$ Twintex beam. The loading is linear during the first stages of the displacement, but starts to show a reduction in stiffness as the beam displaces and the section splays. The first critical failure in the beam occurs in the corner of the lower flange at a displacement of approximately 63mm and a load of 4.7kN. This area continues to damage up until the point at which the test is stopped. No other areas of the beam showed significant levels of visible damage up to this point. The beam had splayed 5mm, the maximum measurable using the extensometer, at a displacement of 47mm.

Figures 6.12 and 6.13 show the results from the $+45^\circ/-45^\circ$ Twintex beam. This beam is less stiff than the $0^\circ/90^\circ$ beam, but displays a similar behaviour, with a reduction of stiffness during loading. The first critical failure occurs at 72mm and a load of 2.8kN, again in the lower flange corner of the beam. The failure was not as marked as that seen in the previous beam and no significant cracking was visible. The splaying of the

section during this test was also significantly lower, with the maximum measurable limit, of 5mm, being reached at a vertical displacement of 65mm.

Figures 6.14 and 6.15 show the results from the 4:1 Twintex beam. As expected, this beam was significantly stiffer than the balanced weave Twintex beam. The first critical failure, in the lower flange corner, occurs at 47mm displacement and a load of 5.4kN. The beam continues to damage in this area up to the end of the test, with no visible damage being observed in any other location. The beam has less transverse fibres than the others tested and exhibits the largest amount of splaying during displacement, with the maximum 5mm being reached at a vertical displacement of only 35mm.

Figures 6.16 and 6.17 show the results from the 3D Twintex beam. This beam exhibits a similar stiffness to the 4:1 Twintex beam, although first critical failure in the flange corner occurred at a higher displacement and load of 67mm and 6.2kN respectively. The beam showed a similar level of section splaying as the 0°/90° Twintex beam, with the maximum 5mm being measured at a displacement of 55mm. Like the previous beams tested, no visible damage was observed in other locations on the beam.

In terms of overall stiffness and integrity of the section, the 3D Twintex beam outperformed all other configurations, with a higher first failure load and displacement and a reduced amount of cross sectional splaying.

6.3.4 Phase 1 Demonstrator Component Large-Scale 3-Point Flexure Test

The second, large-scale 3-point flexure, test was performed on two beams of each of the four configurations.

Figure 6.18 shows the result from the large-scale flexure test on the two 0°/90° Twintex beams. The results initially show a similar behaviour, with a steady increase in load up to a first failure point. After this point, the load rises again and leads to catastrophic failure in the first beam at 225mm displacement. The second beam shows a drop in load at this point, but does not fail and continues to load up to ultimate

failure at 295mm displacement. It was observed that the stiffness of the first beam was significantly higher than the second beam.

Figure 6.19 shows the result from the two $+45^\circ/-45^\circ$ Twintex beams tested. The beams in this test showed a much more progressive loading behaviour, with shear damage gradually building up during the test and very little catastrophic failure in the beams. Beam 2 did show a measurable drop in load at a displacement of 270mm although this did not lead to ultimate failure. After the event the beam continued to perform as previously, suggesting that the load drop was a phenomenon introduced by slip in the test rig rather than failure in the beam. Both beams continued to carry load without failure up to the 305mm maximum displacement in the test. During these tests, the performance of the two beams was almost identical, when compared to the variation seen during the test of the $0^\circ/90^\circ$ beams.

Figure 6.20 shows the result from the two 4:1 $0^\circ/90^\circ$ Twintex beams. Both beams exhibited similar behaviour, with an initial failure at 60mm displacement followed by reloading up to secondary failure at 200mm. Ultimate failure occurred only in Beam 2 at 280mm displacement. Beam 1 did not fail during the 305mm test displacement. The initial stiffness of both beams was very similar although the first failure in Beam 2 appeared more significant with a load drop of 50% which was larger than that observed in Beam 1. Initial failure in both beams occurred at a load of approximately 7kN, which is similar to the initial failure load observed in the $0^\circ/90^\circ$ Twintex beams.

The results from the 3D Twintex beam tests are shown in Figure 6.21. These beams, again, exhibited an initial failure, secondary failure and final failure behaviour. The initial failure for these beams, between 7.5kN and 8kN was slightly higher than that observed in the other tests and occurred in both beams at approximately 70mm displacement. The secondary failure also occurred at a slightly higher load, 10.5kN, and resulted in only a slight drop off in load. Beam 2 was the only beam to fail during the 305mm of the test, at 295mm displacement. The ultimate load for the failed beam was 22.5kN, a significantly higher load than observed in either the failed 1:1 $0^\circ/90^\circ$ and 4:1 $0^\circ/90^\circ$ beams.

Two distinct damage patterns were observed during this stage of the testing. The 1:1 0°/90° Twintex, 4:1 0°/90° Twintex and the 3D Twintex beams, with fibres aligned along the length of the beam, behaved in a similar manner. Initially, as the beams were loaded, bending deformation occurred up until approximately 50mm displacement. At this point a visible and audible damage event occurred, in the lower flange corner in the middle of the beam. This damage zone was similar to that observed during the small scale flexure testing. As the beams continued to displace, a crack progressed up the sidewall of the beams from the damage initiation point and the section began to flatten. By approximately 200mm displacement, the damage had progressed to the upper corners of the beam, adjacent to the top face. At this point a secondary damage zone began to form with a crack in the lower flange progressing up the sidewall approximately 100mm further away from the built-in end of the beam.

The +45°/-45° Twintex beams showed a different damage behaviour to the other beams tested. Damage was developed more progressively in the beams, with no visible cracking on the surface of the beams. Shear damage could be observed during the test, particularly in the sidewall of the beams and splaying of the section was also seen.

Like the results from the small-scale 3-point flexure tests, the larger scale flexure tests showed a significant performance improvement in the 3D Twintex beam compared to the other configurations. These tests showed higher stiffness and failure loads, in addition to an apparent higher damage tolerance.

6.3.5 Phase 1 Demonstrator Implicit Finite Element Damage Modelling

The damage model developed and calibrated for the ABAQUS implicit finite element code, see Chapter 4, was used to simulate the tests performed on both the balanced weave 0°/90° Twintex and the +45°/-45° Twintex beams. The 4:1 and 3D Twintex beam tests were not simulated since a damage model was not calibrated for these configurations, although the model presented in Chapter 4 could be calibrated and used for these materials.

A single layer shell element model, containing 700 elements with a nominal edge length of 15mm, was generated to represent the beam geometry and rigid cylinders

were used to apply a prescribed displacement to the beams. The edge length was selected as the minimum necessary to allow an accurate description of the geometry of the beam. Figure 6.22 shows the mesh and boundary conditions for the small-scale 3-point flexure test models and Figure 6.23 shows the mesh and boundary conditions used for the large-scale test models. In the large-scale test, one end of the beam was fully constrained and the other was constrained in the direction of the load application, but free to move in the longitudinal direction of the beam. In both cases, the load and displacement during the simulation were measured at the rigid wall used to apply the loading.

Figure 6.24 shows the simulation result for the $0^\circ/90^\circ$ Twintex small-scale flexure test, compared to the experimental result. The simulation shows good correlation to test, with accurate prediction of the stiffness of the composite beam. The first failure point is also predicted at the correct load and displacement, although the simulation overestimates the amount of damage and predicts catastrophic failure in the beam. In the test the first failure was not catastrophic and the beam retained structural integrity and load carrying capability. The damage contour plots shown in Figure 6.25 identify compressive failure in the lower flange of the beam, initiating in the corner of the top hat section at around 60mm displacement and progressing rapidly across the beam. The contour plots of FV3 (field variable 3) representing shear damage show that the beam damages due to shear as well as fibre direction stress. This shear damage is not catastrophic and only results in a slight reduction in the beams performance.

Figure 6.26 shows the simulation and experimental result for the $+45^\circ/-45^\circ$ Twintex beam, small-scale flexure test. In this case, the model slightly under-predicts the stiffness of the beam and does not accurately capture the drop off in load seen during the experimental test. This simulation result, showing a lower stiffness, is caused by excessive shear damage development in the model. Figure 6.27 shows FV3 during the simulation, with the maximum amount of shear damage being predicted in the lower flange and a minimal amount predicted in the side webs.

The simulation of the large-scale flexure test for the $0^\circ/90^\circ$ Twintex beam is shown in Figure 6.28. The ABAQUS damage model in this case predicts catastrophic failure in the early stages of the test, at approximately 50mm. The stiffness predicted by the

model is similar to that of Beam 1 although it is higher than Beam 2. The damage contour plots shown in Figure 6.29 identify the ultimate failure in the beam being predicted as a compressive failure in the lower corners of the beam, identified by FV1 reaching a value of 1 at 50mm of displacement in this area. This result is similar to that seen in the small-scale test. The FV3 plots show that a small amount of shear damage is developed during the simulation, but not enough to cause a significant drop in performance.

Figure 6.30 shows the result from the simulation of the large-scale flexure test on the +45°/-45° Twintex beams. The comparison between analysis and experimental results shows that the damage model over-predicts the magnitude of shear degradation in the specimen. The analysis curve shows that the beam is predicted to be significantly less stiff than the physical specimen. Figure 6.31 shows the damage in the specimen during simulation. As expected, shear damage is predicted to occur throughout the central section of the beam and develop rapidly throughout the analysis. There is a small amount of fibre direction damage predicted to occur between 140mm and 200mm displacement, in both the central area of the beam and in the region of the sliding constraint. This damage corresponds to the drop off in load observed at 160mm in the predicted force displacement curve.

6.3.6 Phase 1 Demonstrator Explicit Finite Element Damage Modelling

The damage model, calibrated for the PAM-CRASH explicit finite element code, in Chapter 5 was also used to simulate the balanced weave Twintex demonstrator component tests. The same shell element mesh and boundary conditions, shown in Figures 6.22 and 6.23, used for the implicit finite element models, were also used for the explicit simulation.

Figure 6.32 shows the result from the small-scale flexure test on the 0°/90° Twintex beam. The model accurately predicts the stiffness of the beam, but slightly underestimates the damage developed at around 50mm, where the test shows a load drop off which is not observed in the analysis result. The experimental curve does not show a catastrophic failure in the beam and it is therefore not possible to accurately extrapolate the experimental curve to compare it to the models behaviour between 70mm and 100mm. Figure 6.33 shows the predicted damage in the beam. It is

observed that damage is predicted to occur in a fairly uniform manner throughout the top flange of the beam. In the central section of the beam, the maximum level of damage, 0.5, is observed in the corner of the lower flange. This corresponds to the areas of maximum damage observed in the test specimens.

Figure 6.34 shows the result of the simulation of small-scale test on the $+45^\circ/-45^\circ$ beam. The correlation between analysis and experiment is good, although the simulation slightly under predicts the stiffness of the beam. The plots of damage development during the simulation, shown in Figure 6.35, show that significantly more damage is predicted in this simulation than the previous analysis. The area of maximum damage is also spread more uniformly along the top flange of the beam.

The simulation of the large-scale flexure tests on the Phase 1 demonstrator component show much better correlation throughout the test than the implicit model. The ability of the explicit code and damage model to cope with large deformations and high levels of damage is highlighted by these simulations. Figure 6.36 shows the comparison between experiment and simulation for the $0^\circ/90^\circ$ beam. The prediction accurately captures the stiffness of the beam and the two major failure points at 75mm and 225mm. The damage plots shown in Figure 6.37 identify that the first failure point is caused by material failure in the centre of the beam at the lower corner and the second major failure is a combination of cracking along the lower radius of the beam and failure at the sliding constraint.

Figure 6.38 shows the result from the simulation of the $+45^\circ/-45^\circ$ Twintex beam simulation. The analysis slightly over predicts the stiffness of the beam during the early stage of the analysis, up to 100mm, where a significant failure is predicted. The beam is then predicted to deform and damage progressively, mirroring the result from both experimental tests. The damage plots given in Figure 6.39 show that the first failure predicted is due to localised damage in the centre of the beam. The gradual development of damage is then observed, without the catastrophic failure seen in the $0^\circ/90^\circ$ beam simulation. The final damage plot, at 280mm, shows that damage has developed along the top face of the beam. The total failure at the constraint observed in the previous simulation does not occur during this analysis, although the damage levels in this area are significant, approximately 0.75.

6.4 Phase 2 Demonstrator Component

The Phase 2 demonstrator component was developed, based on the Phase 1 component, specifically for a current model, production vehicle. This component allowed the damage modelling techniques developed and validated during the research, to be assessed as a design tool for composite materials.

Since the beam was to be fitted to a vehicle, packaging constraints led to a modified space envelope compared to the Phase 1 beam. Various geometries were investigated before the final design was selected.

The beam was tested using the large-scale 3-point flexure test method developed for the Phase 1 component and results were compared to predictive simulations. A component was then selected for test in the target vehicle. This test was used to compare the performance of a composite component against the current steel beam used in production and to validate the design.

6.4.1 Phase 2 Demonstrator Component Design

The validated explicit finite element damage model, detailed in Chapter 5, was used extensively during the design of the Phase 2 demonstrator component. Initially a number of geometries were modelled to assess the stiffness of various alternatives. The four geometries identified as potentially offering an acceptable level of performance are shown in Figure 6.40. This design matrix compares first failure load, displacement and mass. This predictive work was used to identify a design to be developed for final testing and installation in the target vehicle.

The results show that Concept 4 is significantly stiffer than the other designs due to the constant section running the length of the beam. This is different to the other concepts investigated, which all taper to a flat section at either end. This design offered the best compromise between stiffness and first failure displacement, although required extra design and development work to mount in the target vehicle.

Figure 6.41 shows the final design of the Phase 2 demonstrator component. A section through the beam is given in Figure 6.42. This shows that like the Phase 1 beam, the

Phase 2 design has a larger area on the compressive face due to the variation in strength when comparing the tensile and compressive performance of Twintex. Since the beam was developed for installation in a specific target vehicle, the CAD geometry was developed as part of a larger model of the vehicle door. Figure 6.43 shows the beam ‘*virtually*’ installed in the door and the clearance between the beam and window glass, confirming that packaging requirements are met. Subsequently, mounting brackets were designed to install the beam in the vehicle. Addition of the brackets caused a small interference in the target door, leading to modification of the beam geometry at one end. This adjustment to the geometry is shown in Figure 6.44 and the steel brackets are shown in Figure 6.45.

6.4.2 Phase 2 Demonstrator Component Manufacture

The Phase 2 demonstrator component used a simpler tool concept, a matched metal tool without a shear edge or blankholder. This second demonstrator component tool was used to investigate the use of inserts to vary thickness without geometry inaccuracy in the radius areas. The beam was initially developed as an 8mm thick section, but was also moulded with 6mm and 4mm sections, through the use of two 2mm thick tool inserts. This allowed further component test data to be generated for comparison with analytical models.

The tool is shown in Figure 6.46, with a 2mm thick insert installed. The inserts were formed from 2mm sheet steel, by compression in the tool. Figure 6.47 shows a closer view of the insert, in the most complex area of the tool, around the step in geometry. A detailed description of the non-isothermal compression moulding process and optimised parameters are given in Chapter 3.

Figure 6.48 shows the industrial moulding process used for the Phase 2 demonstrator component. The process is identical to the laboratory scale plaque moulding technique presented in Chapter 3. Preconsolidated blanks are heated in an infrared oven and transferred to a cool press tool. The component is then formed and consolidated as it cools, before removal from the mould. This process was used for all three forms of Twintex used in the manufacture of demonstrator components.

6.4.3 Phase 2 Demonstrator Component Large-Scale 3-Point Flexure Test

The Phase 2 demonstrator component was tested using the large-scale 3-point flexure test method, employed in the second stage of the testing of the Phase 1 beam. All beams were tested to a nominal 305mm displacement with load data being measured at the impactor. Two beams each of 4mm, 6mm and 8mm thickness, manufactured from 1:1 0°/90°, 1:1 +45°/-45° and 4:1 0°/90° Twintex as well as two 6mm 3D 0°/90° Twintex beams were tested. Typical tested specimens of each of the four material configurations are shown in Figures 6.49 to 6.52. These tested specimens showed characteristic failure types for each material and are compared to predicted damage in section 6.4.4.

Figures 6.53, 6.54 and 6.55 show the results from the three thickness variants of the 0°/90° 1: 1 Twintex beams tested. All six beams showed a similar displacement behaviour, with a linear loading up to the first failure point, a drop in load and then progressive rise up to a second failure point. The 4mm beams did not exhibit a catastrophic failure within the 305mm of test, although beam 2 showed a major failure at 280mm with an 80% drop in load carrying capacity. The 6mm beams exhibited a similar stiffness to the 4mm beams and a first failure point at a significantly higher displacement. This result was unexpected as the extra section thickness was predicted to increase the stiffness of the component over that of the 4mm beams. The 8mm beams did show a significant stiffness increase when compared to the previous results. The first failure point for these beams occurred at approximately 50mm displacement, similar to the 4mm beams. This suggested that the 6mm beam results were uncharacteristically poor when compared to both the 4mm and 8mm beams.

Figures 6.56, 6.57 and 6.58 show the results from the three thickness variants of the +45°/-45° 1: 1 Twintex beams tested. The beams all showed a similar progressive damaging behaviour, with no rapid failure or drop in load carrying capacity. Unlike the 0°/90° beams, the step up in thickness from 4mm to 6mm resulted in a significant increase in stiffness of the beams, as did the step from 6mm to 8mm. The performance when compared for the two beams of each configuration, showed variability in the 6mm and 8mm beams, but a virtually identical performance up to 200mm displacement, for the 4mm beams.

The results from the 4:1 Twintex beams tested are shown in Figures 6.59, 6.60 and 6.61. These tests show a similar result to the $0^\circ/90^\circ$ 1:1 Twintex beams, with a predominantly linear loading behaviour up to the first failure point followed by a drop in load carrying capacity and then a progressive reloading. Both the 8mm beams failed catastrophically within the 305mm of test displacement, at approximately 285mm. This type of failure was not observed in the thinner sectioned beams, where the load progressively increased up to 305mm. Like the $+45^\circ/-45^\circ$ Twintex beams, the 4:1 configuration showed an increase in performance between the 4mm, 6mm and 8mm beams respectively.

The final material configuration tested was the $0^\circ/90^\circ$ 3D Twintex. These beams were only tested in the 6mm configuration. The results from the two tests are shown in Figure 6.62. The load displacement behaviour shows the characteristic initial linear loading followed by failure and reloading. The beams both exhibited catastrophic failure at 280mm, a result not seen in other material configuration 6mm beam tests. The performance of the beams, in general, was significantly better than the standard $0^\circ/90^\circ$ 1:1 Twintex in terms of stiffness and initial failure load. It was also observed that the results showed a consistent behaviour between the two beams tested.

Like the Phase 1 beam tests, two distinct damage behaviours were observed for the Phase 2 beams. The components with fibres aligned along the length beam showed localised damage and failure, whereas the $+45^\circ/-45^\circ$ Twintex beams all showed a progressive shear damaging behaviour in the sidewalls with some splaying of the cross-section at higher displacements. The $0^\circ/90^\circ$ fibre orientation beams, all loaded linearly up until approximately 50mm where the first localised damage occurred in the middle of the beam in the central section of the lower flange. Soon after this event, secondary areas of damage occurred in the outer corners of the lower flange. Cracks then propagated up the sidewalls of the section, as the beam was displaced up to approximately 220mm. At this point, a third damage zone developed approximately 150mm further away from the built in end of the beam. This again produced cracks running up the side wall of the beam, which lead to ultimate failure in the case of the 3D Twintex beams.

6.4.4 Phase 2 Demonstrator Implicit Finite Element Damage Modelling

Although simulation of the Phase 1 demonstrator had shown that the implicit finite element damage model was not ideally suited to large displacement simulations, it was still used to simulate the behaviour of the tested beams. All results presented in this section were produced before the Phase 2 beams had been moulded or tested and are therefore, truly predictive simulations. Since the model was developed and calibrated for 1:1 Twintex, only the $0^\circ/90^\circ$ and $+45^\circ/-45^\circ$ 1:1 Twintex beams were simulated. All three thicknesses were modelled using the properties of the shell elements to simulate the 4mm, 6mm and 8mm variants. The model, containing 1880 shell elements with a nominal edge length of 10mm, and the rigid wall boundary condition for the simulations are shown in Figures 6.63 and 6.64. One end of the beam was constrained rigidly using a nodal constraint and the other was constrained to move only in the longitudinal direction of the beam. These conditions represented the test fixture used for the large-scale 3-point flexure test. The nominal element edge length of 10mm was selected to represent the typical shell element dimensions seen in an automotive finite element crash simulation model.

Figure 6.65 shows the implicit finite element damage model simulation results for the 4mm thick $0^\circ/90^\circ$ Twintex beam. The load displacement result shows that the damage model predicts damage earlier in the displacement than was observed during test. This failure results in a rapid reduction in load carrying capacity and leads to a failure to converge a solution at approximately 90mm. The model also slightly over-predicts the stiffness of the test components during the early stages of the test, from 0mm to 25mm. The damage contour plots, in Figure 6.66, show that the load drop is caused by compressive failure in the lower areas of the beam section. A small amount of shear damage is predicted in the beam, although this does not significantly reduce the structural performance when compared to the level of fibre direction damage identified.

Figure 6.67 shows the predicted result for the 6mm thick $0^\circ/90^\circ$ Twintex beam. The stiffness of the response from the analysis model is significantly higher than that observed during test and like the 4mm beam, failure is predicted in the early stages of the simulation. Figure 6.68 shows that this drop in load is predominantly the result of compressive, fibre direction, failure in the lower flange of the beam. Small amounts of

shear damage are identified in the beam. Again, this does not significantly affect the performance.

The results from the 8mm $0^{\circ}/90^{\circ}$ Twintex beam simulation are shown in Figure 6.69. This analysis, when compared to all the $0^{\circ}/90^{\circ}$ beam simulations, gave the most accurate prediction of beam stiffness, although like previous results, showed a tendency for over-prediction of damage. Failure was predicted at 30mm displacement compared to the experimentally observed 50mm displacement at first failure. The predicted fibre direction damage again lead to a failure to converge a solution, due to deformation in elements in which the modulus had been significantly reduced. This damage is shown in the contour plots given in Figure 6.70. The failure occurs on the compressive face of the beam, but in a more localised area than the previous two simulations.

Figure 6.71 shows the result from the simulation of the 4mm $+45^{\circ}/-45^{\circ}$ Twintex beam. The load displacement behaviour and damage development during the early stages of the test are predicted accurately by the damage model. The ultimate failure, predicted at 120mm is inaccurate, since this was not observed in the test. The plot of damage contours shown in Figure 6.72 shows that shear damage builds progressively across the specimen during the displacement. The ultimate failure is caused by predicted compressive damage in the central section of the beam and results in failure to converge a solution for the analysis.

The simulation result for the 6mm $+45^{\circ}/-45^{\circ}$ Twintex beam shows a similar response to the previous analysis, see Figure 6.73. The stiffness is predicted to reduce progressively due to shear damage up to 130mm where ultimate failure occurs. The damage contours shown in Figure 6.74 identify fibre direction damage on the compressive face of the component occurring between 80mm and 120mm displacement. This corresponds to the ultimate failure predicted by the simulation at 130mm. The shear damage contours also identify a significant amount of shear damage in the specimen, which unlike the fibre direction damage builds progressively throughout the analysis.

The final implicit finite element damage model result is shown in Figure 6.75. The load displacement response predicted for the 8mm +45°/-45° beam, again shows accurate prediction of stiffness and damage up to a failure at approximately 140mm, which halts the simulation. The damage contours in Figure 6.76 show that the ultimate failure in the simulation is caused by fibre direction damage on the compressive face of the beam, whilst shear damage development is progressive and spread across the component. This result, like the other +45°/-45° beams, showed that the shear damaging model is accurate for predicting the structural performance of the beam, but the overall ability of the model is compromised by the inability to converge a solution after small amounts of fibre direction damage are identified.

6.4.5 Phase 2 Demonstrator Explicit Finite Element Damage Modelling

The explicit finite element damage model presented and calibrated in Chapter 5 was also used to predictively model all the 1:1 Twintex beams tested. Like the results presented for the implicit damage model, all the simulations were performed prior to the testing of the beams and therefore give an accurate representation of the predictive modelling capability of the technique. The same mesh and boundary conditions, from the implicit model, were used for the explicit simulations, see Figures 6.63 and 6.64. The rigid wall was displaced with a constant velocity and nodal damping was applied to the model to retain stability and reduce dynamic effects during the simulation. A nodal damping factor of 0.5 was used for all of the Phase 2 demonstrator component explicit finite element simulations. It should be noted that nodal damping, although maintaining stability, can affect the results of a simulation and lead to an over stiff response as well as changing the location and magnitude of damage identified in an analysis.

Figure 6.77 shows the load displacement response predicted for the 4mm 0°/90° Twintex beam compared against the experimental result. The overall performance of the beam is predicted accurately, with first failure identified at 50mm displacement and a load of approximately 10kN. The subsequent performance of the beam is also simulated predictively, with a second major failure occurring just after 200mm displacement. After this point the model predicts a significant reduction in load carrying capacity, which is not observed in the test. The other discrepancy between simulation and experiment is the initial stiffness of the beam, although the analysis

result shows a slight rise in stiffness after the start of the simulation, which could be caused by the stiffening effect of the nodal damping applied to the model. This effect is, as mentioned previously, a potential draw back of using nodal damping as a method for retaining model stability. The damage contours shown in Figure 6.78 predict the initial failure on the compressive face of the specimen and the second major failure at a point along the beam, giving a failed specimen with two distinct areas of critical damage. This compares well to the experimentally observed damage, shown in Figure 6.49.

Figure 6.79 shows the predicted performance of the 6mm 0°/90° Twintex beam against the experimental test results. Like the implicit damage model, the predicted stiffness of the beam is significantly higher than that observed during test. The first major failure is also predicted earlier than was observed, at 50mm rather than 75mm. The subsequent performance of the beam is also predicted to be stiffer and more susceptible to damage than the experiment showed. The predicted damage in the beam, shown in Figure 6.80, suggests that failure occurs initially at the centre of the beam and subsequently in a second concentrated area along the beam, similar to the failures observed during test.

The 8mm 0°/90° Twintex beam simulation result is shown in Figure 6.81. The analysis, like that for the 4mm beam, predicts the behaviour of the component fairly accurately. First major failure is predicted at 50mm and secondary failure at 200mm, which are both observed experimentally, although only one of the 8mm beams showed a secondary failure. The initial stiffness of the beams is over-predicted by the model, but a rise in stiffness in the early stages of the simulation is observed, again potentially a result of the nodal damping applied. Predicted damage for the 8mm 0°/90° Twintex beam is shown in Figure 6.82. Again, the characteristic double damage zone pattern is observed, although damage is more localised in the central area when compared to the thinner beams, due to the increased flexural stiffness of the 8mm beam concentrating the damage zone.

Figure 6.83 shows the result from the first +45°/-45° Twintex beam, the 4mm thick variant. Like the results observed for the Phase 1 demonstrator component, the damage model initially over-predicts the stiffness of the beam, since damage

development is not as rapid in the model as the experimental test. This results in a first failure observed at 50mm for the analysis, which is not seen in the test. After this point the simulation follows the basic form of the test, but again does not accurately predict the magnitude of shear damage and its effect on stiffness. The damage contours shown in Figure 6.84 highlight this, showing localised areas of damage, similar to those seen for the 0°/90° beams. The simulation does show that the section splays more for the predominantly shear damaging beam, which is an effect observed during test, see Figure 6.50.

The 6mm +45°/-45° Twintex beam, load displacement results are shown in Figure 6.85. The general form of the response is similar to the 4mm beam, although the first failure is not as marked and the damage development appears more progressive. The result is close to the experimental result although not identical, due to the nature of the damage predicted. The damage contour plots for the simulation, shown in Figure 6.86, highlight the initial central failure predicted in the beam, causing the load reduction at 50mm displacement. Subsequent damage development is over a larger area than observed in the 4mm beam, although a similar splaying of the section is seen.

The final +45°/-45° Twintex beam simulated had an 8mm section thickness. The result is compared against experiment in Figure 6.87. The simulation curve again shows an over-stiff response initially, followed by a failure at 50mm. Subsequently the load rises and a secondary failure is seen at 250mm displacement. The simulation result again differs from experimental curve due to an over prediction of the beam stiffness and a subsequent failure behaviour that is not observed in the test. The damage plots in Figure 6.88 show that the initial failure is caused by an area of damage in the central section of the beam, which expands during the second stage of the displacement, between 50mm and 200mm. The splaying in the section for the 8mm beam is predicted to be significantly lower than the 6mm and 4mm beams, due to the increased section stiffness.

In general, the ability of the explicit damage model to predict damage in the Phase 2 demonstrator component was good for the fibre direction damaging 0°/90° Twintex beams, but was less accurate for the off axis +45°/-45° beams.

6.5 Vehicle Testing

To fully validate the Phase 2 demonstrator component as an alternative to a steel side intrusion beam, a 6mm thick 0°/90° 4:1 Twintex beam was installed in the target vehicle.

The decision to use the 6mm thick 4:1 Twintex beam was made based on test results for the current steel beam in a large-scale 3-point flexure test, see Figure 6.89. The beam was selected to give a comparable initial stiffness and failure load. The 4mm beam was not structurally strong enough and the 6mm 1:1 Twintex beam had underperformed and shown variability in test and was therefore not suitable.

6.5.1 Installation of Beam in Target Vehicle

The beam was installed using the steel brackets detailed in Section 6.4.1. The skin of the target vehicle door was removed and the brackets were welded to the door structure. The thermoplastic composite beam was then bolted to the brackets and the door skin was replaced. A Glass Mat Thermoplastic (GMT) composite door cassette was mounted on the inside of the door, replacing the steel internal panel. The GMT door cassette, shown in Figure 6.90, was a design developed previously, during a manufacturing process research programme, which had not been validated in a vehicle test [119].

Potentially, a fully thermoplastic door module would be manufactured in a single-shot moulding process, as a door cassette with fully integrated side intrusion protection. This test assembly allowed full assessment of the concept without the requirement for a complex design exercise and the production of expensive tooling.

6.5.2 FMVSS 214 Vehicle Test

The fully assembled door mounted on the target vehicle was tested to the Federal Motor Vehicle Safety Standard for side impact protection. The test specification includes a quasi-static intrusion, with prescribed stiffness and maximum load targets, which was used in this study.

Both a standard, production model, steel door and side intrusion beam and a door with a composite beam and door cassette were tested and the results were compared.

The load displacement results from the two tests performed are shown in Figure 6.91. The initial stiffness, intermediate stiffness and peak load requirements specified in the test standard are also shown on the figure. The overall performance of the two doors is very similar and both beams meet the standard requirements. The door with the composite beam installed shows a drop in load at 75mm displacement, which corresponds to the first failure crack on the compressive face, observed in the large-scale 3-point flexure test. The load continues to rise through to the 305mm maximum displacement of the test. The standard door with a steel beam shows a slightly different load displacement response. The initial loading up to 150mm is very linear, followed by a relatively smooth drop in load, corresponding to the yielding of the section of the steel beam. The steel beam then re-loads as a tensile strap and yields significantly again at a displacement of approximately 240mm.

Although the response is different for the two beams, the performance, in terms of the pass/fail test criteria is very similar. Both the initial and intermediate stiffnesses and the peak load of the composite beam/door are within 10% of the standard steel door.

6.6 Conclusion

Two demonstrator components have been used during this part of the research, to further validate the modelling techniques described in Chapter 4 and Chapter 5.

Initially, a first phase component was designed to develop a test methodology and modelling technique for the beams. The results from an extensive test programme were compared to simulations using both the ABAQUS and PAM-CRASH models described earlier in this work. The ABAQUS model was shown to predict the behaviour of shear damaging components accurately over large displacements, although for fibre direction damage, the technique was not as applicable. The PAM-CRASH model was calibrated predominantly to predict the onset of fibre direction damage and was therefore more applicable to the 0°/90° Twintex beam configurations.

For the second phase of the demonstrator component programme, the PAM-CRASH model was used as a predictive design tool, to develop a new, Phase 2, beam geometry for a target vehicle. This beam was manufactured and tested using the same techniques as the Phase 1 beam and results were compared to simulation, which had been performed predictively, prior to the test work. This allowed the model to be validated in an 'industrial' type design, manufacture and test exercise. The results showed that the PAM-CRASH model again performed well when damage was predominantly in the fibre direction and that the ABAQUS model was less suited to components where large amounts of damage occur.

To conclude the work, validating the material as a potential alternative to steel for side intrusion protection and proving the structural integrity of a 'composite door' concept, a composite beam and door cassette were installed in a target vehicle. This vehicle was quasi-statically tested to Federal Safety Standard and shown to meet all the target requirements, with both a steel and composite door.

6.7 Tables

Beam Geometry	Material	Orientation	Nominal Thickness	Quantity Tested
Phase 1	1:1 Twintex	0°/90°	7.5mm	1
Phase 1	1:1 Twintex	+45°/-45°	7.5mm	1
Phase 1	4:1 Twintex	0°/90°	7.5mm	1
Phase 1	3D Twintex	0°/90°	7.5mm	1

Table 6.1 Beams tested in small-scale 3-point flexure rig

Beam Geometry	Material	Orientation	Nominal Thickness	Quantity Tested
Phase 1	1:1 Twintex	0°/90°	7.5mm	2
Phase 1	1:1 Twintex	+45°/-45°	7.5mm	2
Phase 1	4:1 Twintex	0°/90°	7.5mm	2
Phase 1	3D Twintex	0°/90°	7.5mm	2
Phase 2	1:1 Twintex	0°/90°	8mm	2
Phase 2	1:1 Twintex	0°/90°	6mm	2
Phase 2	1:1 Twintex	0°/90°	4mm	2
Phase 2	1:1 Twintex	+45°/-45°	8mm	2
Phase 2	1:1 Twintex	+45°/-45°	6mm	2
Phase 2	1:1 Twintex	+45°/-45°	4mm	2
Phase 2	4:1 Twintex	0°/90°	8mm	2
Phase 2	4:1 Twintex	0°/90°	6mm	2
Phase 2	4:1 Twintex	0°/90°	4mm	2
Phase 2	3D Twintex	0°/90°	6mm	1
Original Beam	Steel	-	-	1

Table 6.2 Beams tested in large-scale 3-point flexure rig

Beam Geometry	Material	Orientation	Nominal Thickness	Quantity Tested
Phase 2 & Cassette	4:1 Twintex GMT	0°/90° Random	6mm	1
Original Beam	Steel	-	-	1

Table 6.3 Beams tested to FMVSS214

6.8 Figures

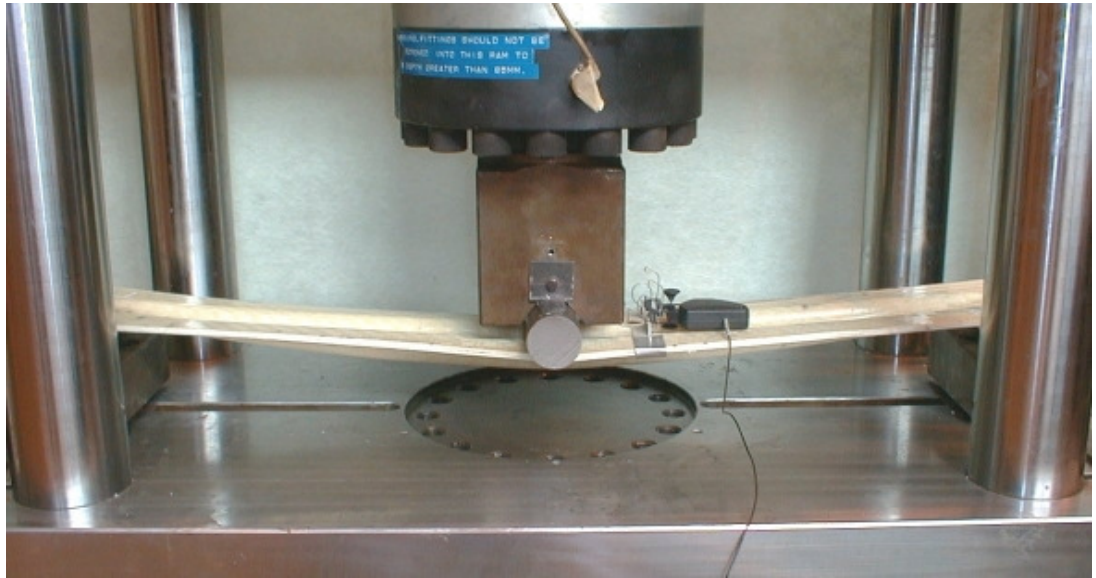


Figure 6.1 Small-scale 3-point flexure test

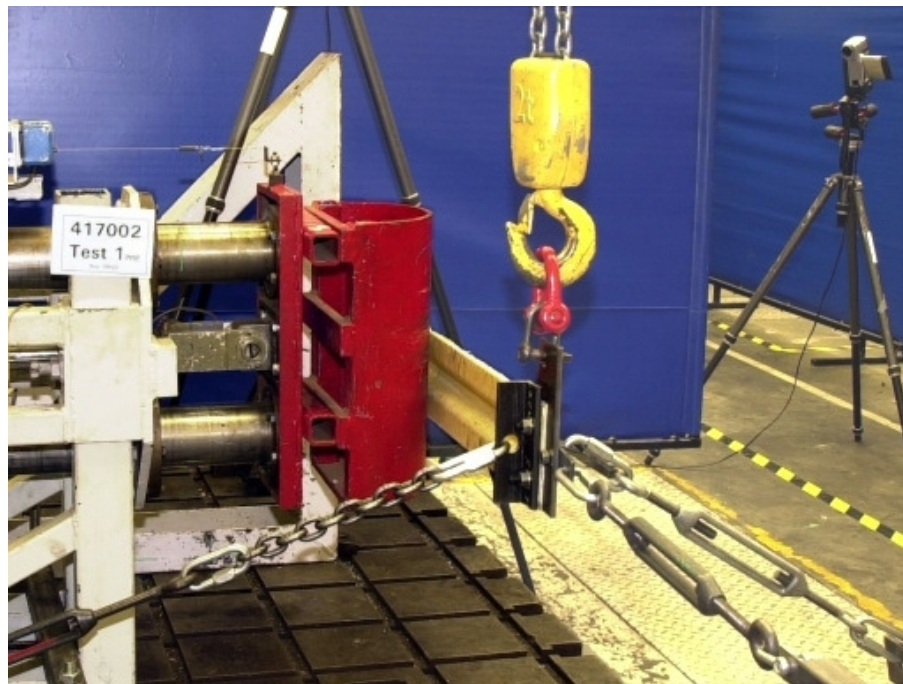


Figure 6.2 Large-scale 3-point flexure - Phase 1 beam



Figure 6.3 Large-scale 3-point flexure - Phase 1 beam



Figure 6.4 Large-scale 3-point flexure - Phase 2 beam



Figure 6.5 Demonstrator component test vehicle with door cassette fitted



Figure 6.6 FMVSS214 test rig



Figure 6.7 Typical tubular steel and pressed steel side intrusion beams

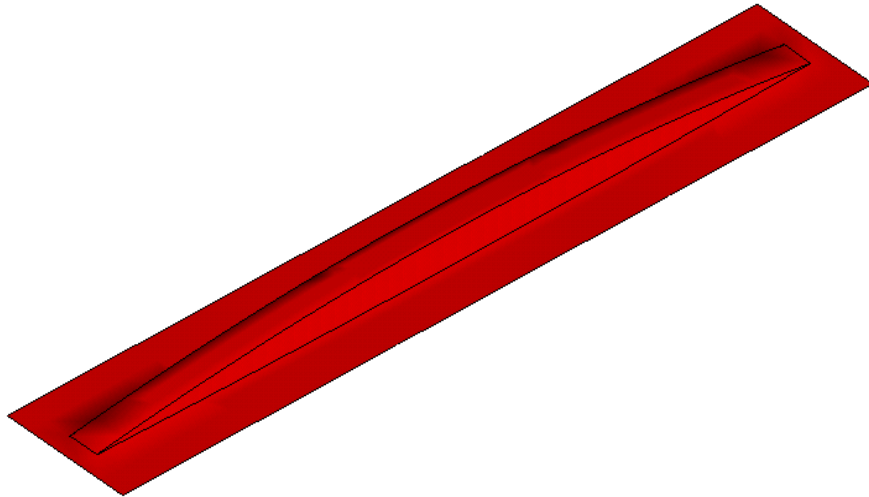


Figure 6.8 Phase 1 demonstrator component geometry, 1050mm x 150mm x 48mm

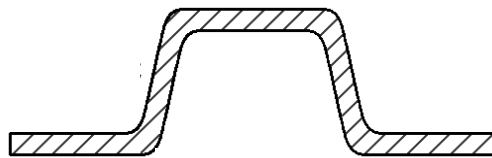


Figure 6.9 Phase 1 demonstrator component central cross section

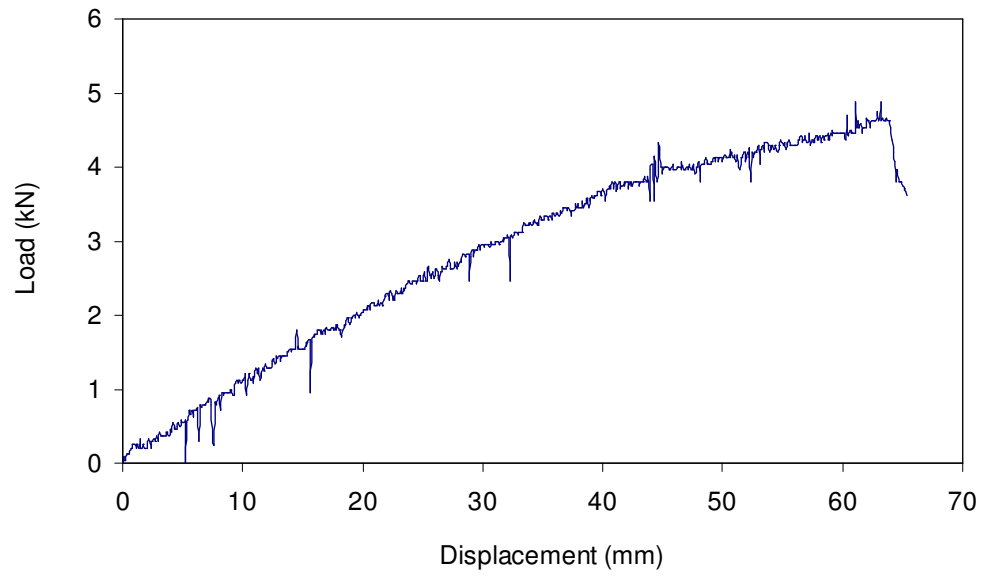


Figure 6.10 1:1 Twintex 0°/90° Phase 1 demonstrator small-scale 3-point flexure test result

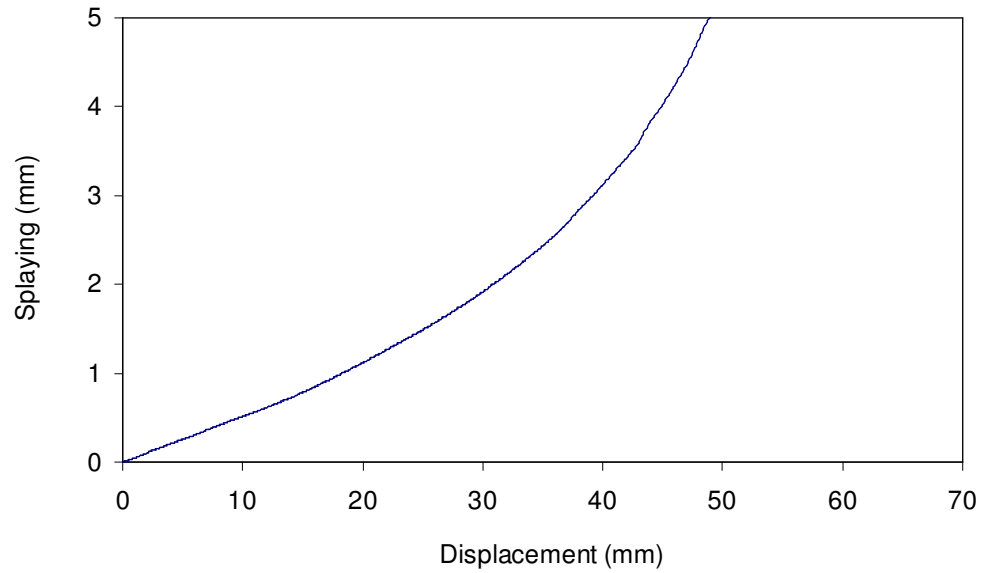


Figure 6.11 1:1 Twintex 0°/90° Phase 1 demonstrator small-scale 3-point flexure test section splaying

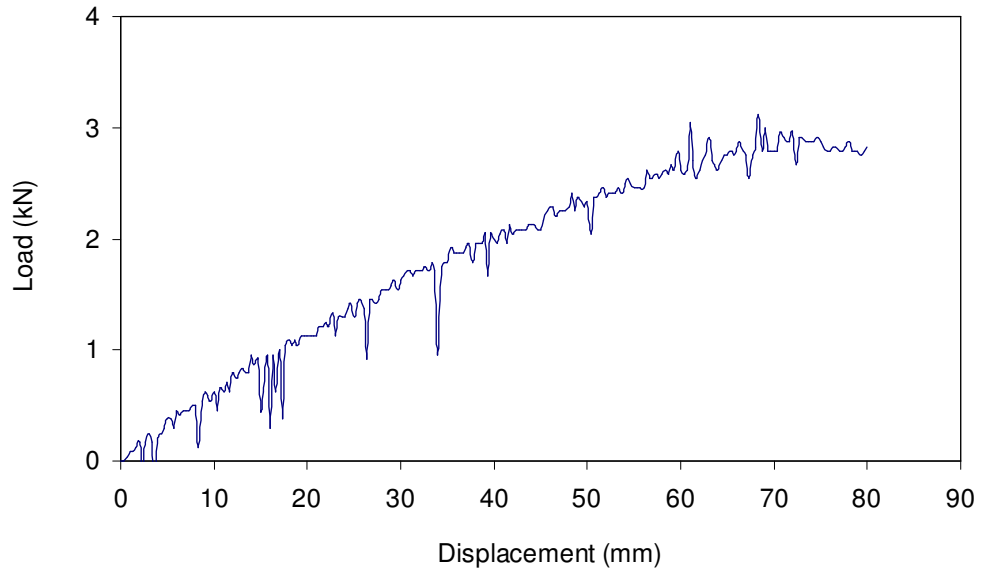


Figure 6.12 1:1 Twintex +45°/-45° Phase 1 demonstrator small-scale 3-point flexure test result

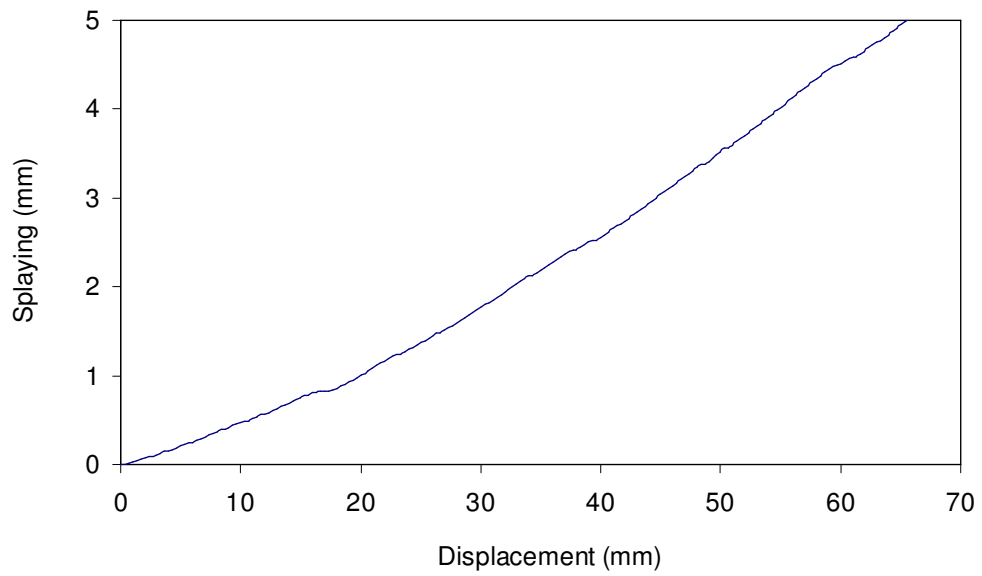


Figure 6.13 1:1 Twintex +45°/-45° Phase 1 demonstrator small-scale 3-point flexure test section splaying

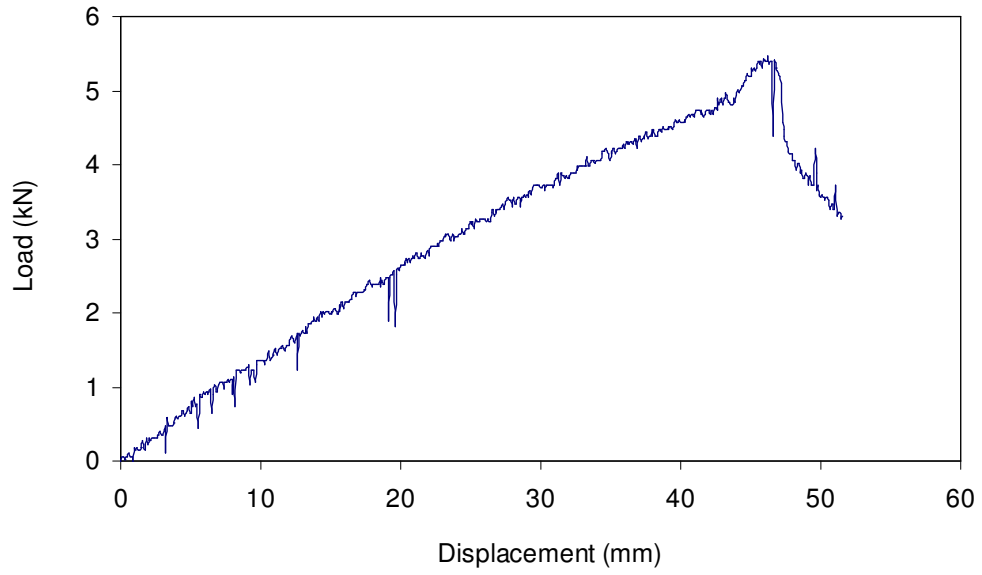


Figure 6.14 4:1 Twintex 0°/90° Phase 1 demonstrator small-scale 3-point flexure test result

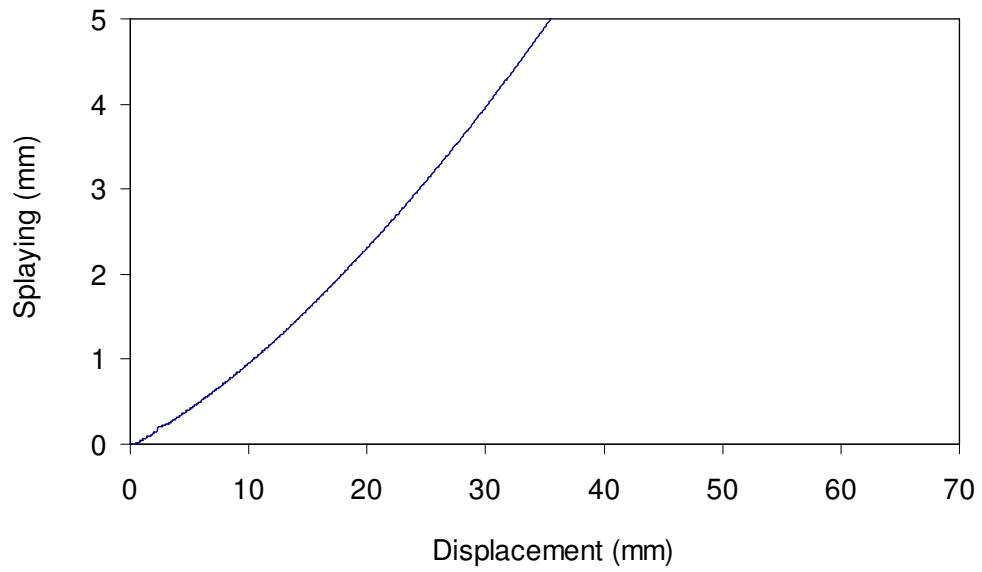


Figure 6.15 4:1 Twintex 0°/90° Phase 1 demonstrator small-scale 3-point flexure test section splaying

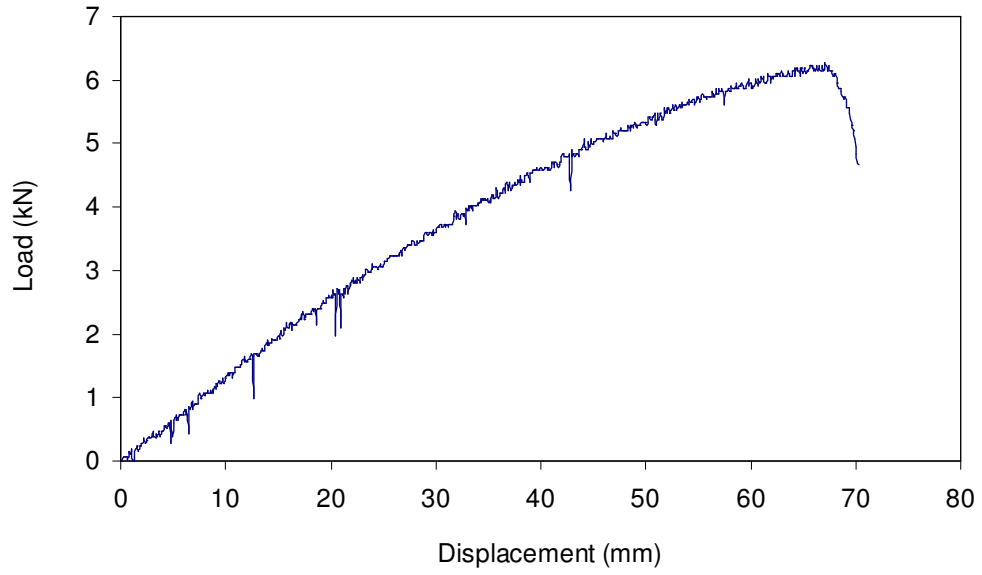


Figure 6.16 3D Twintex 0°/90° Phase 1 demonstrator small-scale 3-point flexure test result

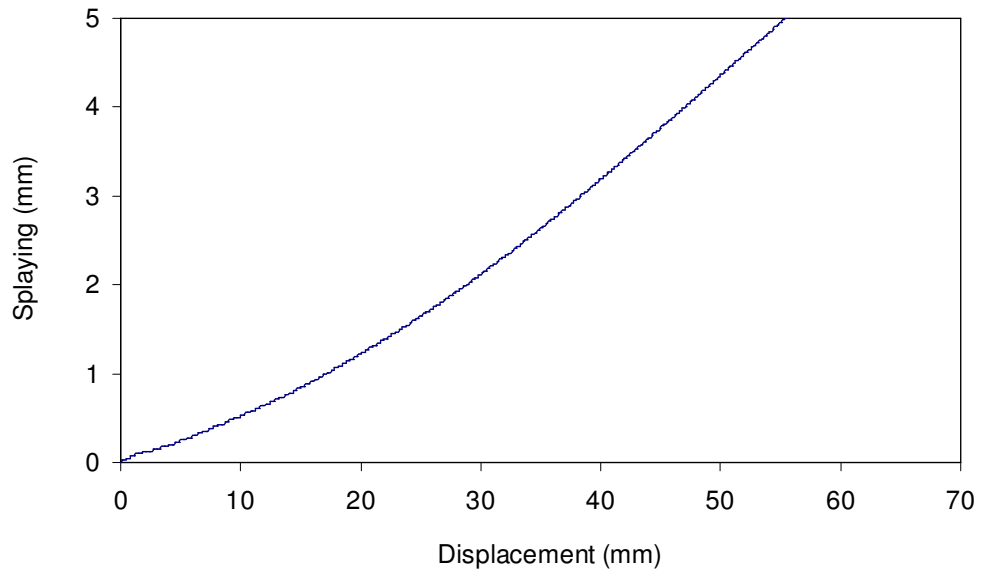


Figure 6.17 3D Twintex 0°/90° Phase 1 demonstrator small-scale 3-point flexure test section splaying

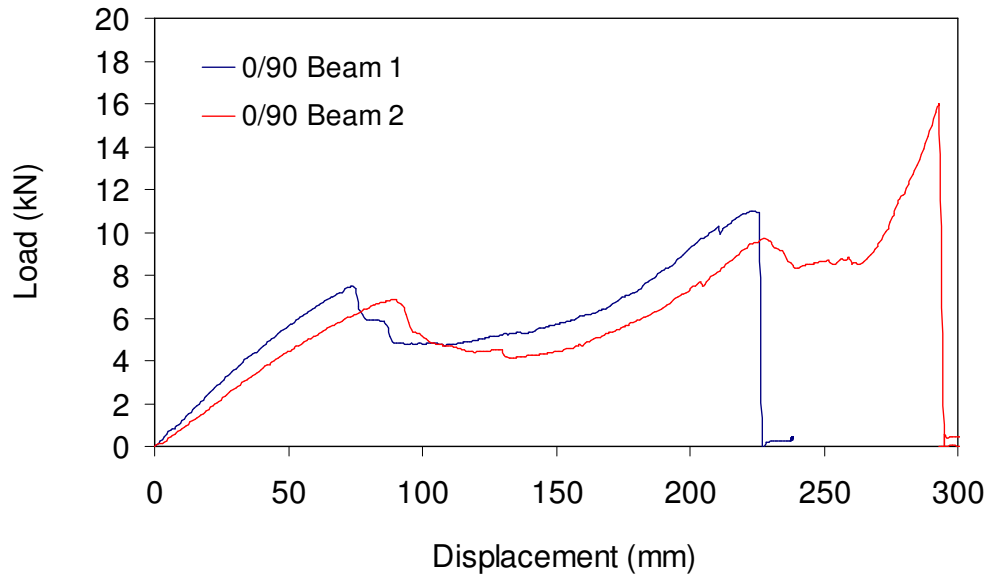


Figure 6.18 1:1 Twintex 0°/90° Phase 1 demonstrator large-scale 3-point flexure test results

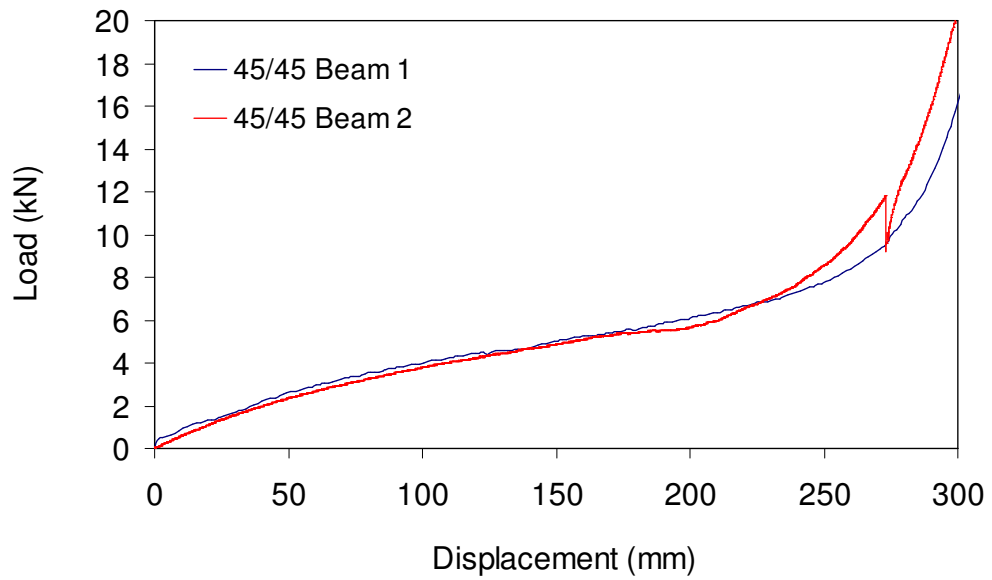


Figure 6.19 1:1 Twintex +45°/-45° Phase 1 demonstrator large-scale 3-point flexure test results

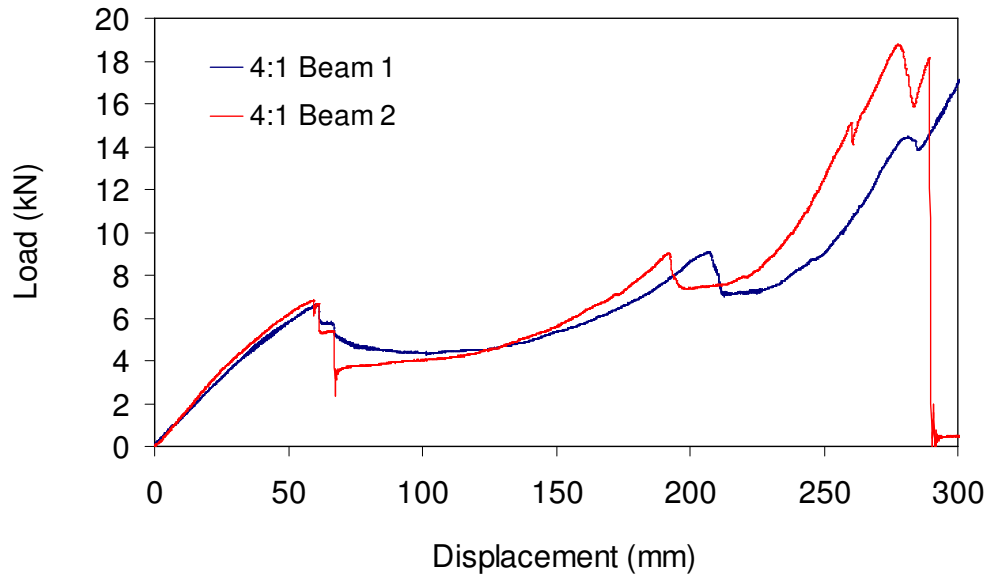


Figure 6.20 4:1 Twintex 0°/90° Phase 1 demonstrator large-scale 3-point flexure test results

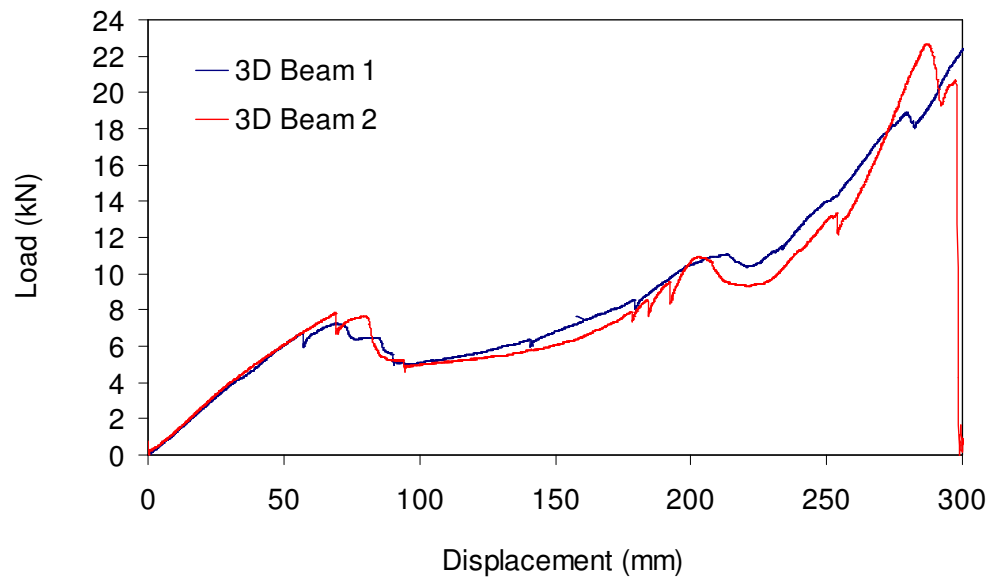


Figure 6.21 3D Twintex 0°/90° Phase 1 demonstrator large-scale 3-point flexure test results

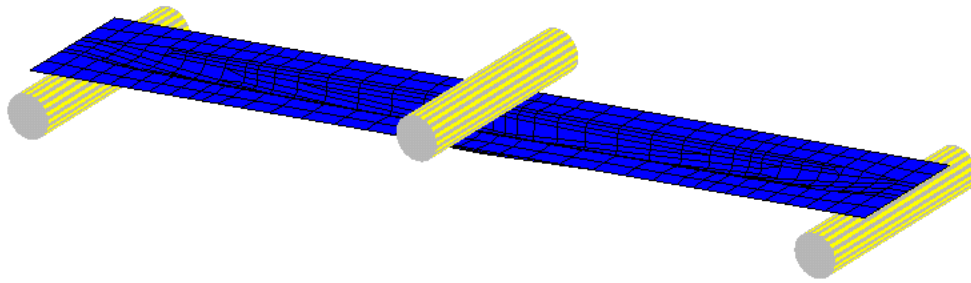


Figure 6.22 Phase 1 demonstrator small-scale 3-point flexure model

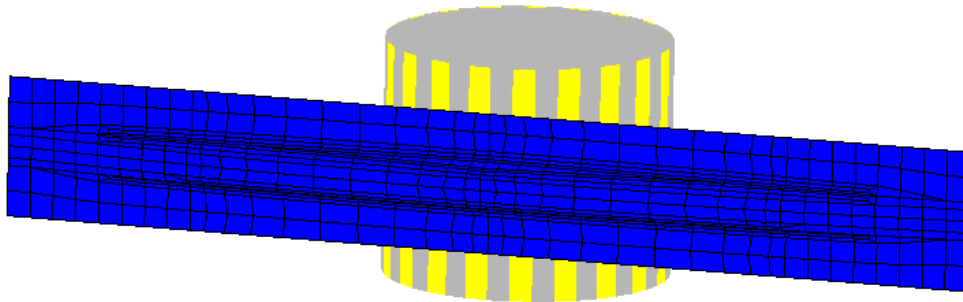


Figure 6.23 Phase 1 demonstrator large-scale 3-point flexure model

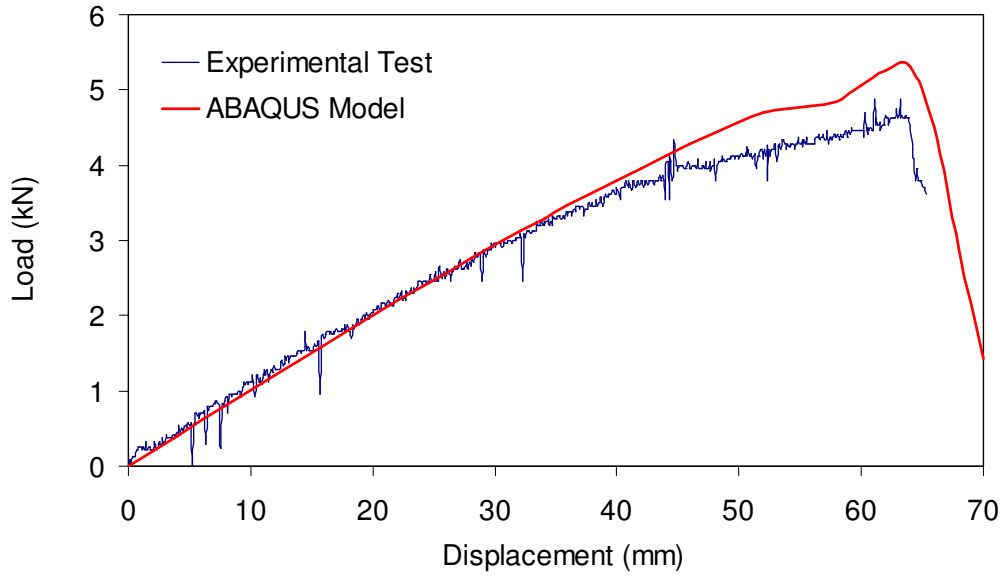


Figure 6.24 1:1 Twintex 0°/90° Phase 1 demonstrator small-scale 3-point flexure test implicit finite element simulation

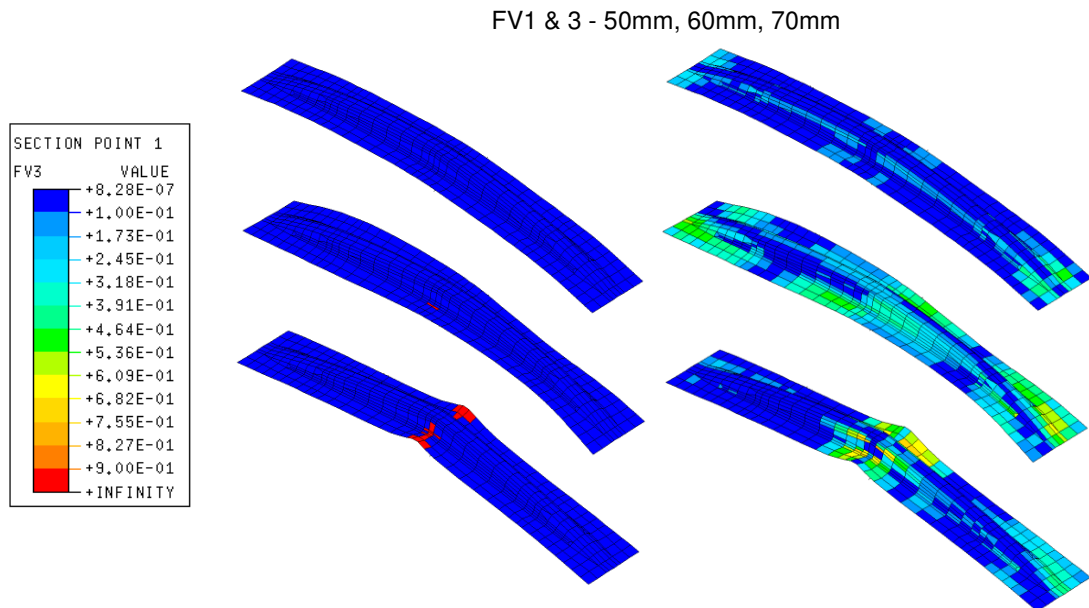


Figure 6.25 1:1 Twintex 0°/90° Phase 1 demonstrator small-scale 3-point flexure test implicit finite element simulation - predicted damage

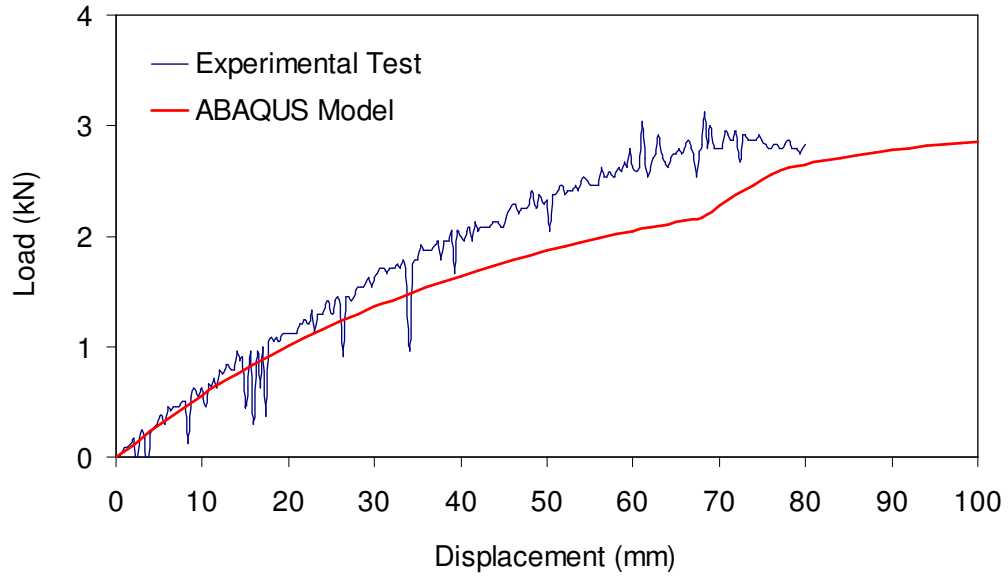


Figure 6.26 1:1 Twintex +45°/-45° Phase 1 demonstrator small-scale 3-point flexure test implicit finite element simulation

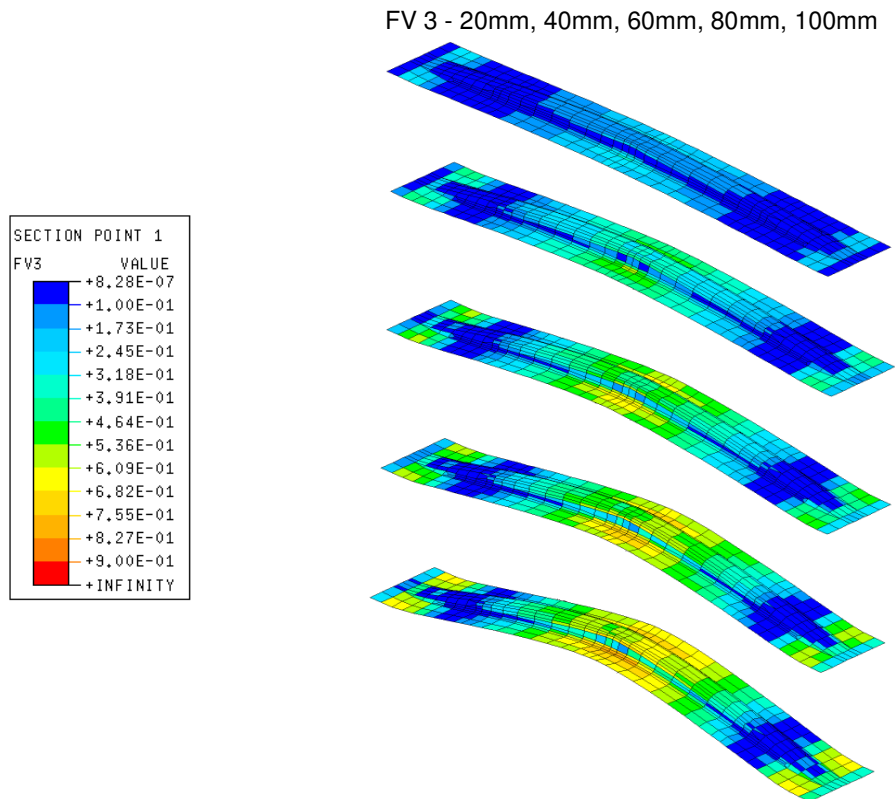


Figure 6.27 1:1 Twintex +45°/-45° Phase 1 demonstrator small-scale 3-point flexure test implicit finite element simulation - predicted damage

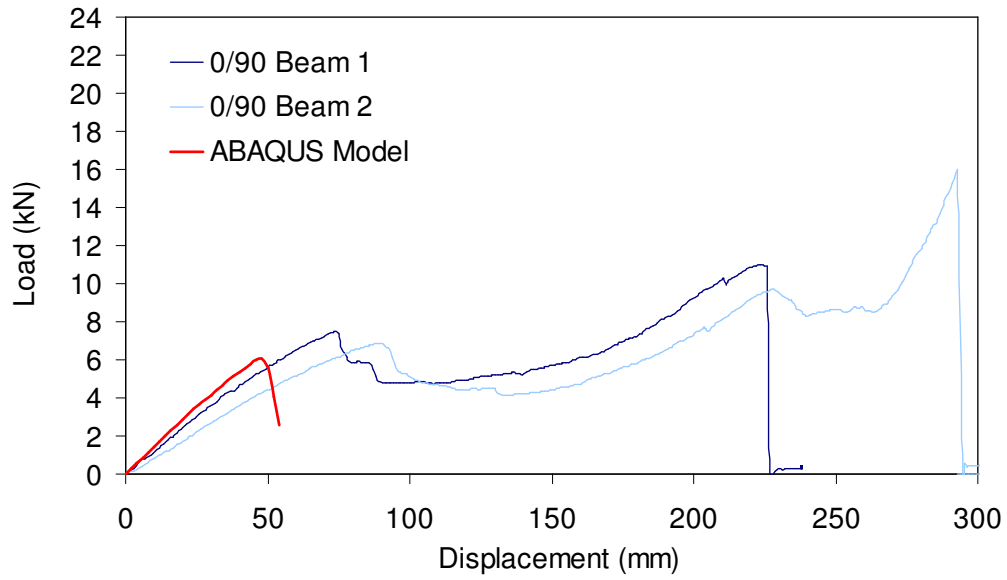


Figure 6.28 1:1 Twintex 0°/90° Phase 1 demonstrator large-scale 3-point flexure test implicit finite element simulation

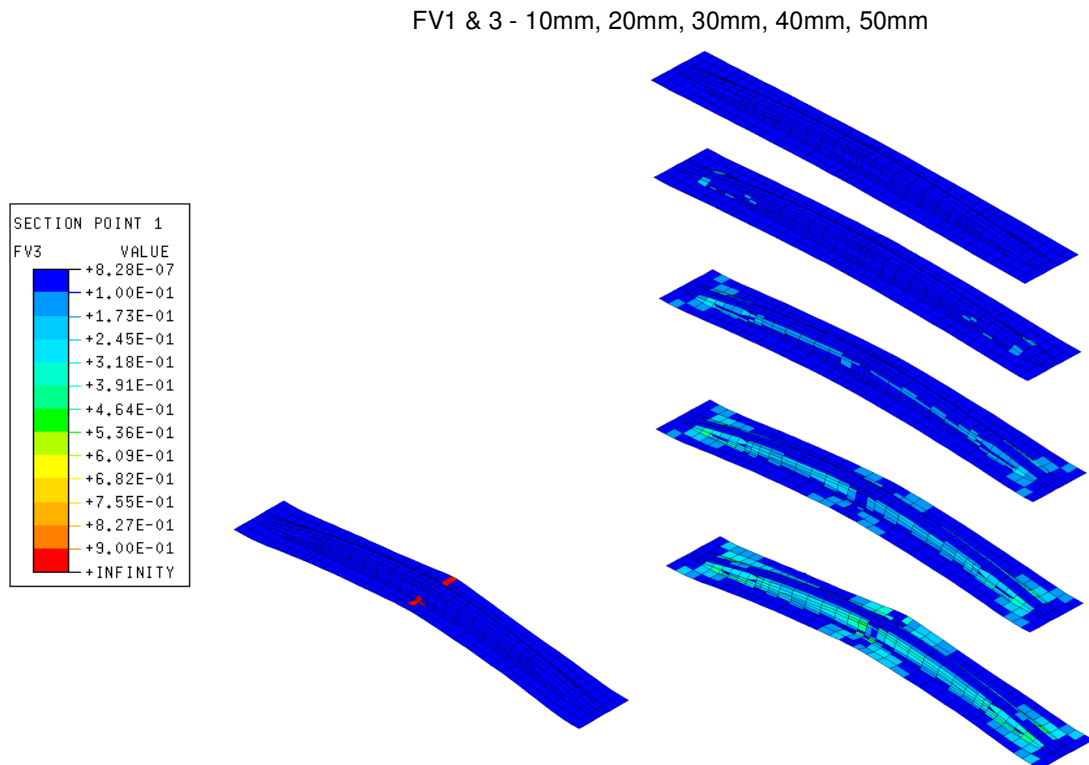


Figure 6.29 1:1 Twintex 0°/90° Phase 1 demonstrator large-scale 3-point flexure test implicit finite element simulation - predicted damage

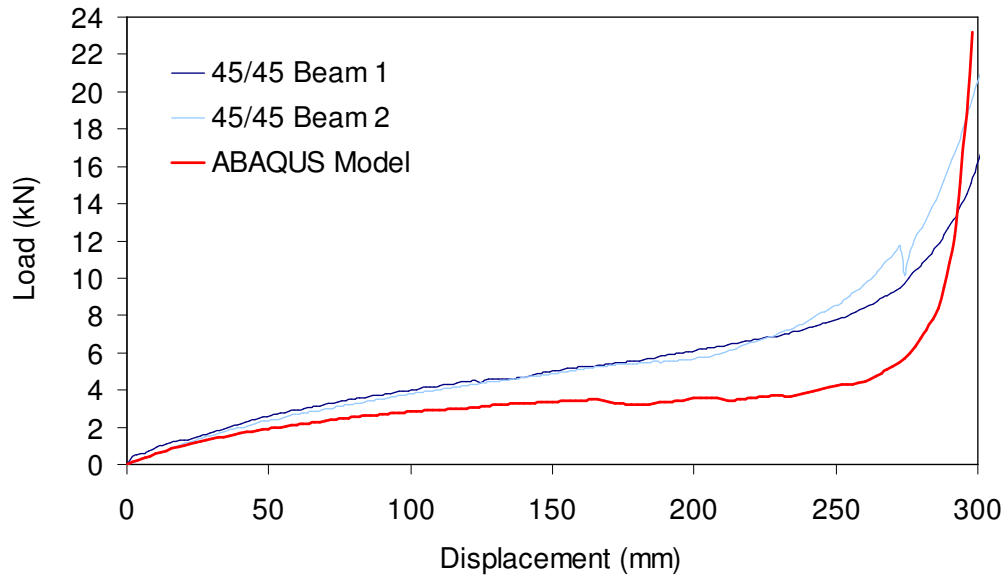


Figure 6.30 1:1 Twintex +45°/-45° Phase 1 demonstrator large-scale 3-point flexure test implicit finite element simulation

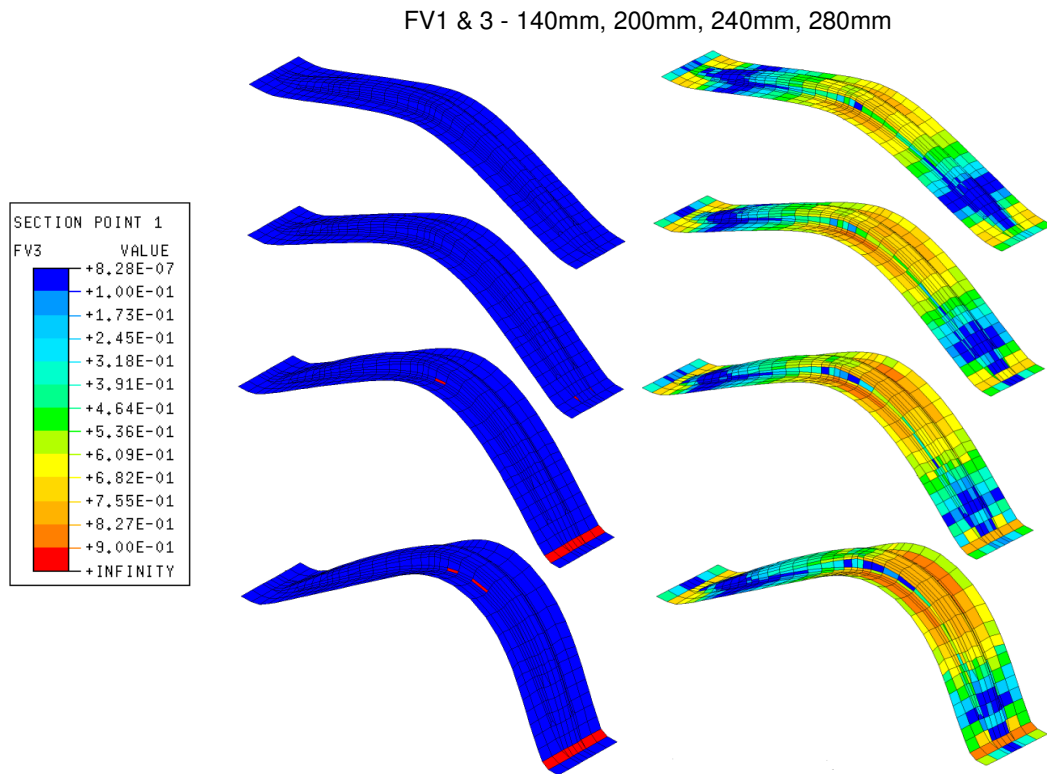


Figure 6.31 1:1 Twintex +45°/-45° Phase 1 demonstrator large-scale 3-point flexure test implicit finite element simulation - predicted damage

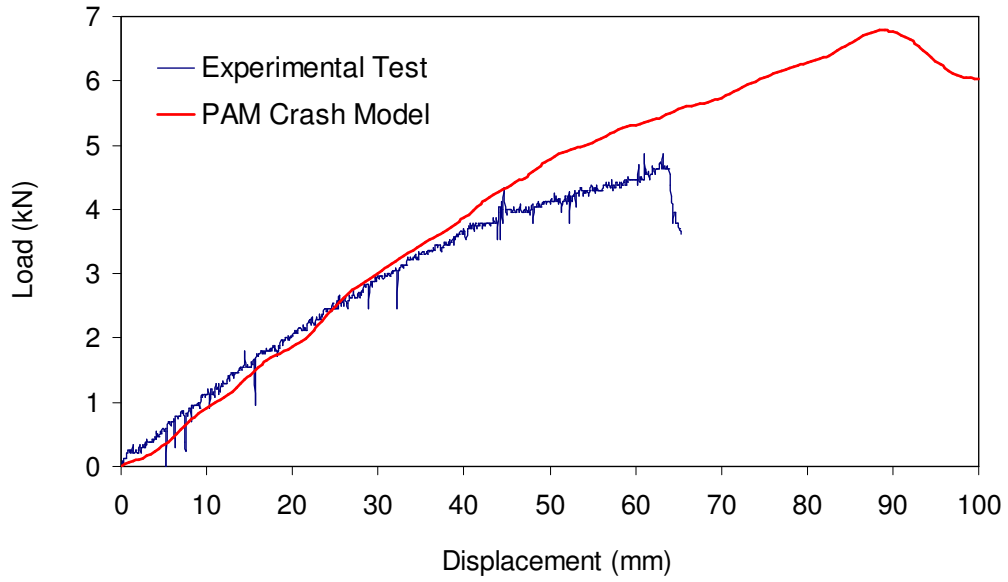


Figure 6.32 1:1 Twintex 0°/90° Phase 1 demonstrator small-scale 3-point flexure test explicit finite element simulation

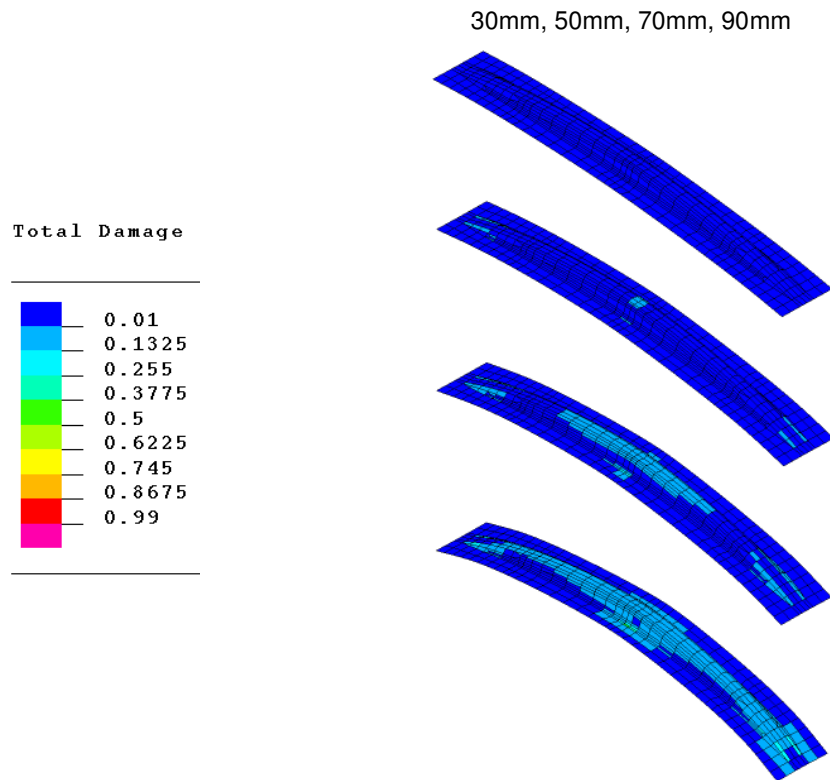


Figure 6.33 1:1 Twintex 0°/90° Phase 1 demonstrator small-scale 3-point flexure test explicit finite element simulation - predicted damage

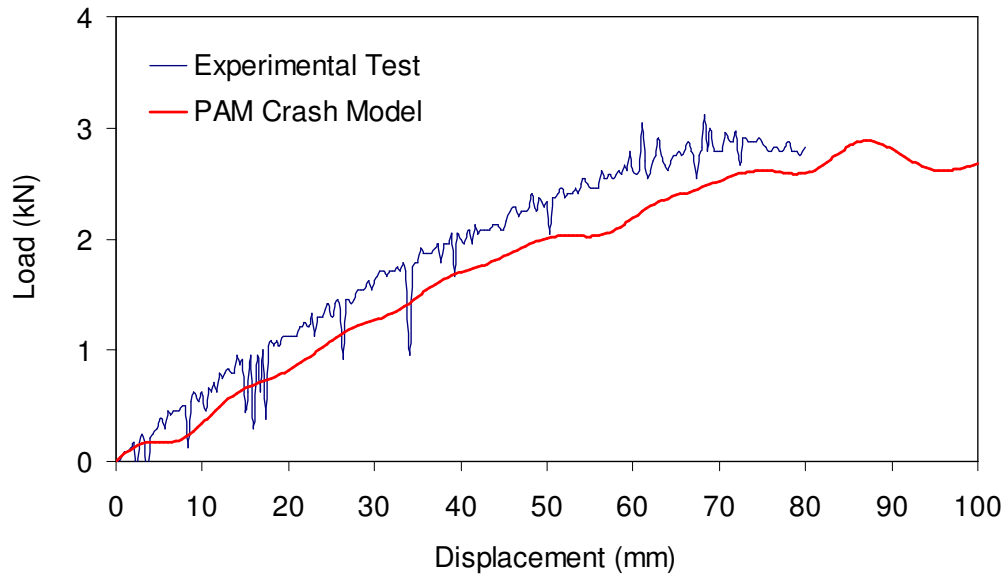


Figure 6.34 1:1 Twintex +45°/-45° Phase 1 demonstrator small-scale 3-point flexure test explicit finite element simulation

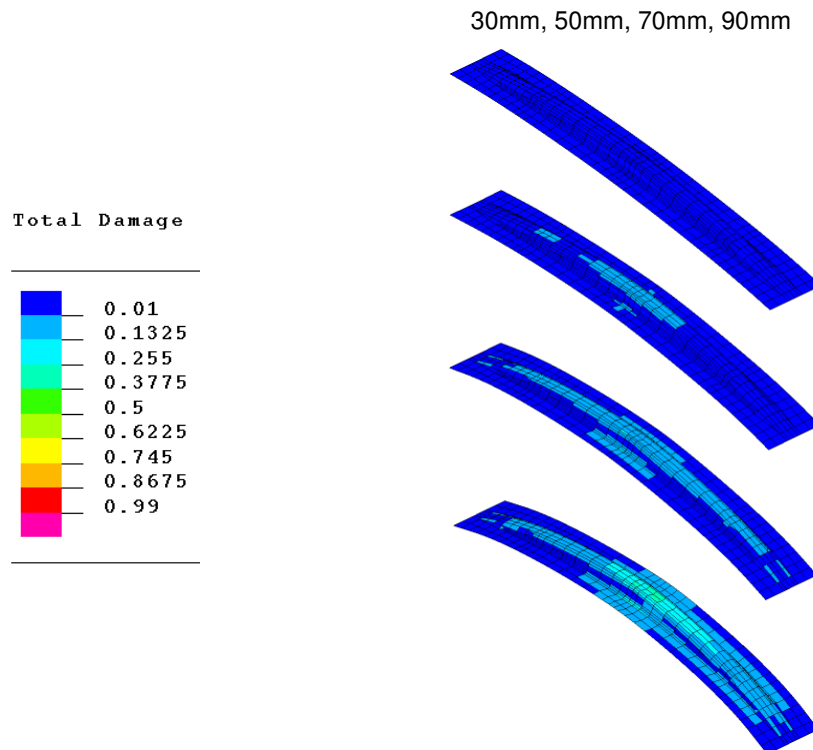


Figure 6.35 1:1 Twintex +45°/-45° Phase 1 demonstrator small-scale 3-point flexure test explicit finite element simulation - predicted damage

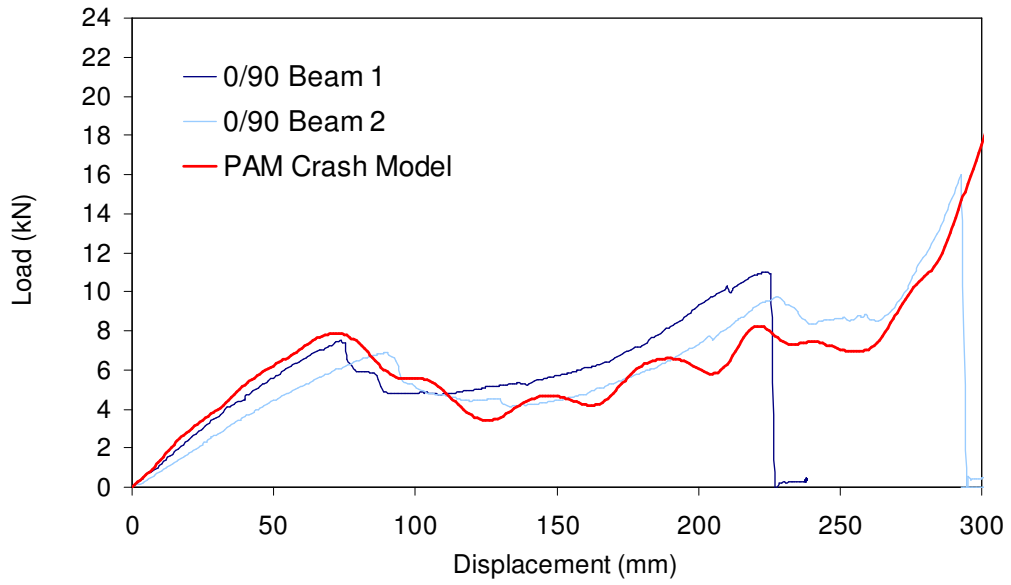


Figure 6.36 1:1 Twintex 0°/90° Phase 1 demonstrator large-scale 3-point flexure test explicit finite element simulation

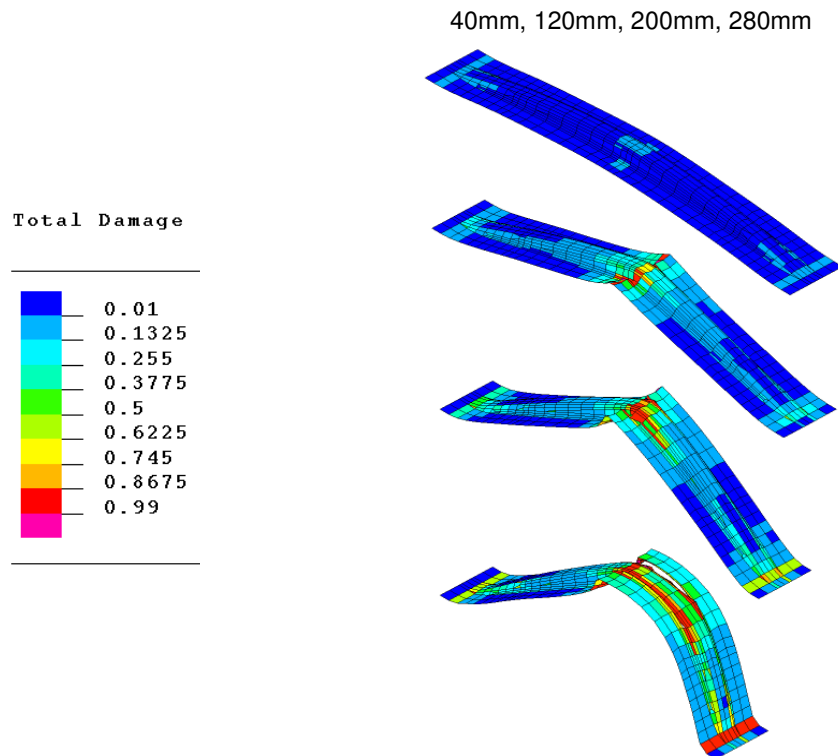


Figure 6.37 1:1 Twintex 0°/90° Phase 1 demonstrator large-scale 3-point flexure test explicit finite element simulation - predicted damage

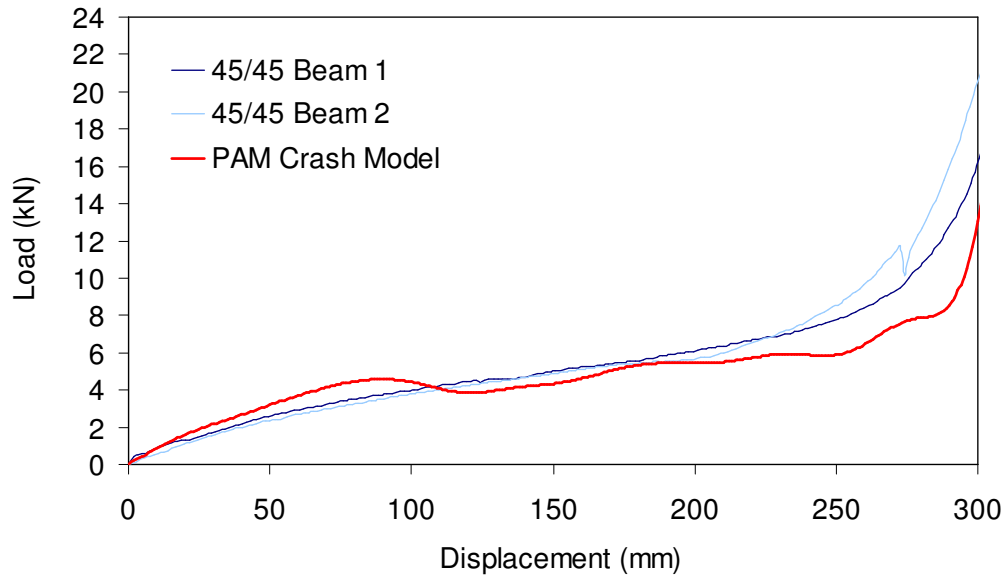


Figure 6.38 1:1 Twintex +45°/-45° Phase 1 demonstrator large-scale 3-point flexure test explicit finite element simulation

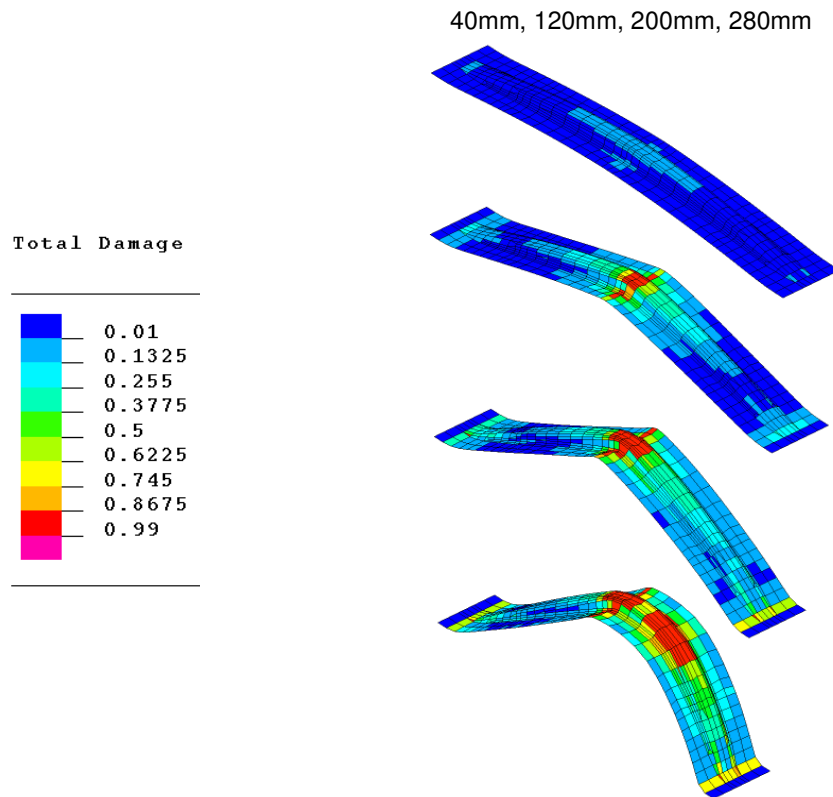


Figure 6.39 1:1 Twintex +45°/-45° Phase 1 demonstrator large-scale 3-point flexure test explicit finite element simulation - predicted damage

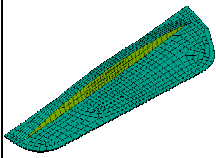
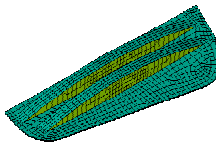
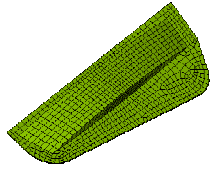
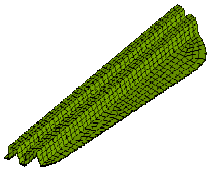
Concept	1	2	3	4
Geometry				
Thickness (mm)	8.0	8.0	8.0	8.0
Mass (kg)	3.3	3.5	3.9	4.0
1 st Failure Load (kN)	12.5	19.5	13.0	24.0
1 st Failure Disp. (mm)	78	83	60	52

Figure 6.40 Summary of concept development analysis results for Phase 2 demonstrator component

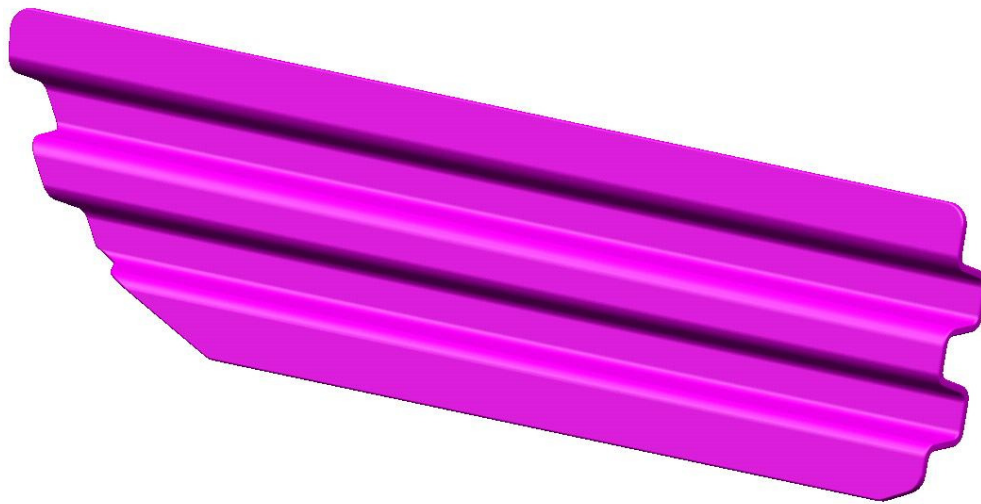


Figure 6.41 Phase 2 demonstrator component geometry, 1020mm x 268mm x 55mm

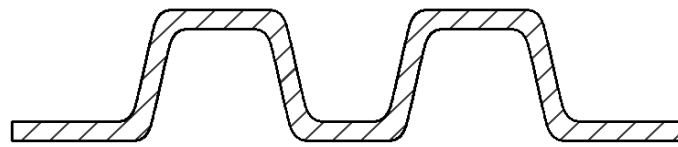


Figure 6.42 Phase 2 demonstrator component central cross section

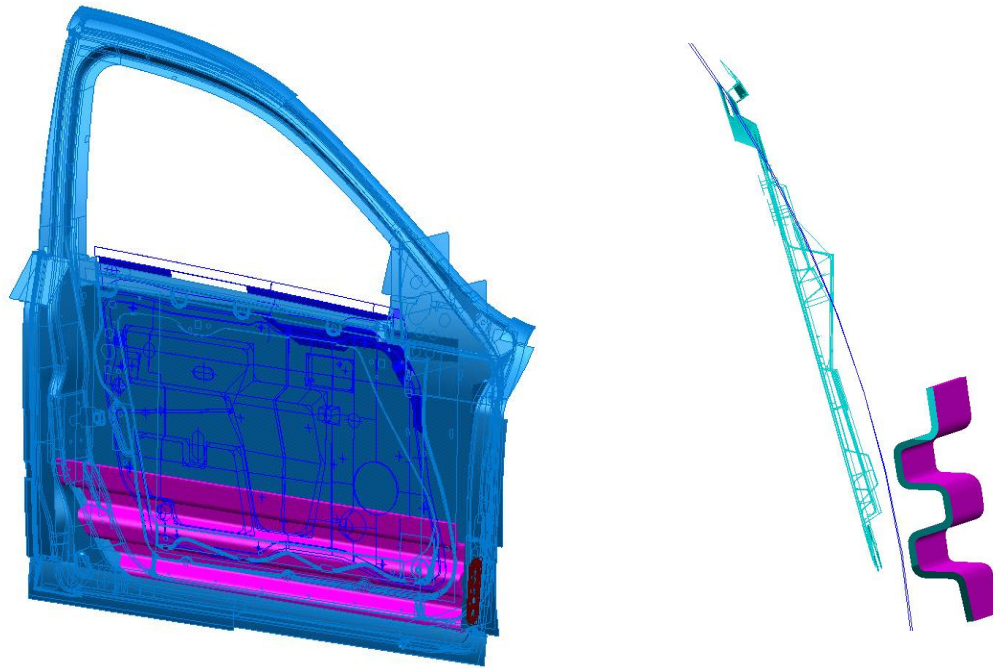


Figure 6.43 Phase 2 demonstrator component installation in target vehicle CAD model

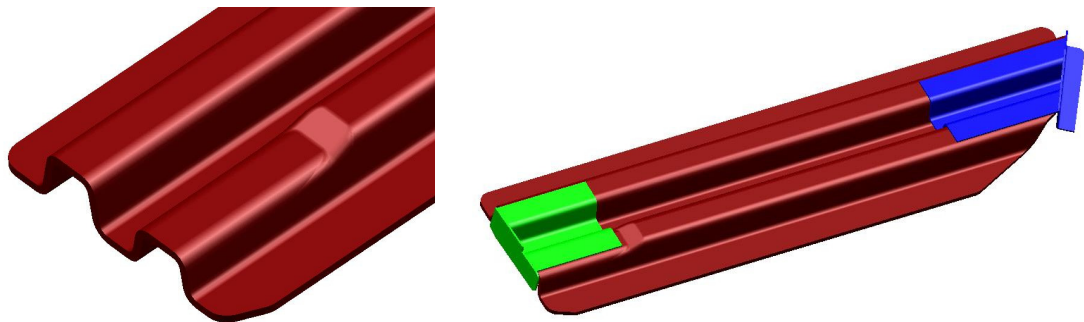


Figure 6.44 Phase 2 demonstrator component profile modification for vehicle installation

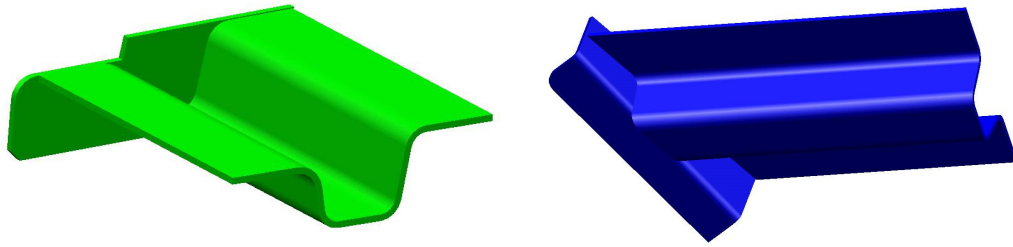


Figure 6.45 Phase 2 demonstrator steel brackets for vehicle installation

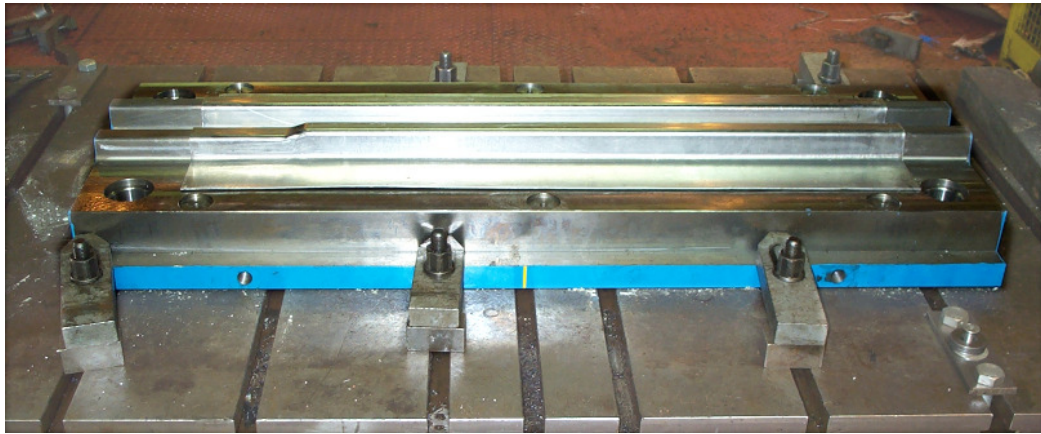


Figure 6.46 Phase 2 demonstrator tool showing insert to reduce component thickness

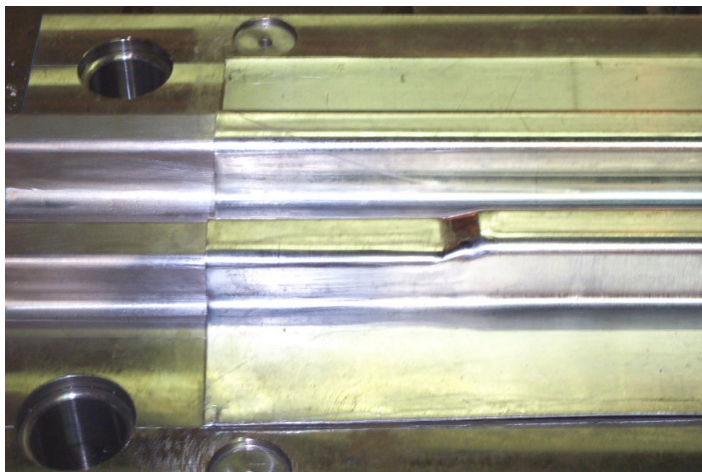


Figure 6.47 Phase 2 demonstrator tool showing insert to reduce component thickness

1.



Preconsolidated blanks heated to 200°C in oven.

2.



Material transferred to cool tool.

3.



Pressure applied for 90s as material cools.

4.



Tool opened and formed part removed.

Figure 6.48 Moulding process for Phase 2 demonstrator component



Figure 6.49 1:1 Twintex 0°/90° 4mm Phase 2 demonstrator large-scale 3-point flexure tested specimen



Figure 6.50 1:1 Twintex +45°/-45° 4mm Phase 2 demonstrator large-scale 3-point flexure tested specimen



Figure 6.51 4:1 Twintex 0°/90° 4mm Phase 2 demonstrator large-scale 3-point flexure tested specimen



Figure 6.52 3D Twintex 0°/90° 6mm Phase 2 demonstrator large-scale 3-point flexure tested specimen

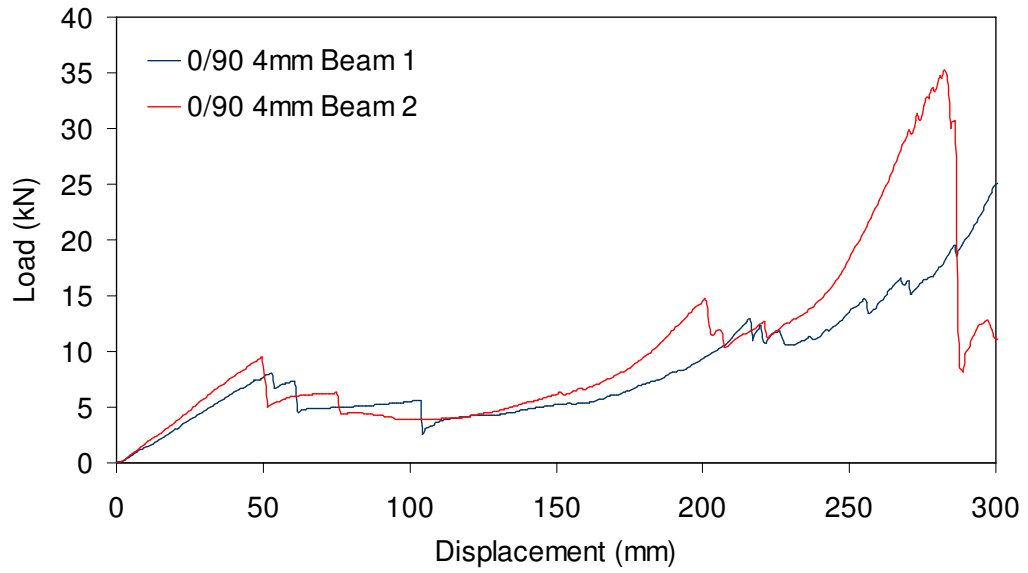


Figure 6.53 1:1 Twintex 0°/90° 4mm Phase 2 demonstrator large-scale 3-point flexure test results

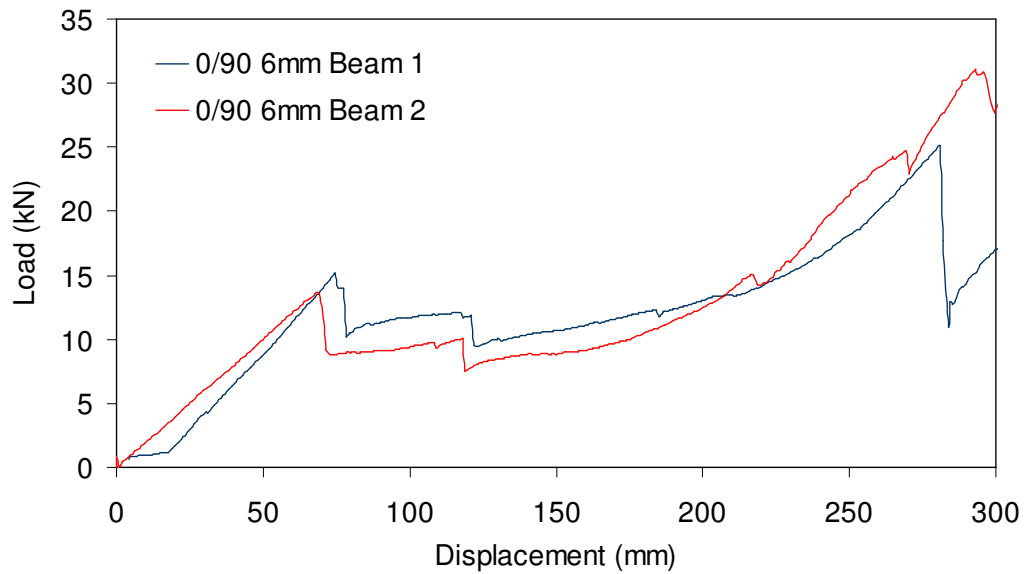


Figure 6.54 1:1 Twintex 0°/90° 6mm Phase 2 demonstrator large-scale 3-point flexure test results

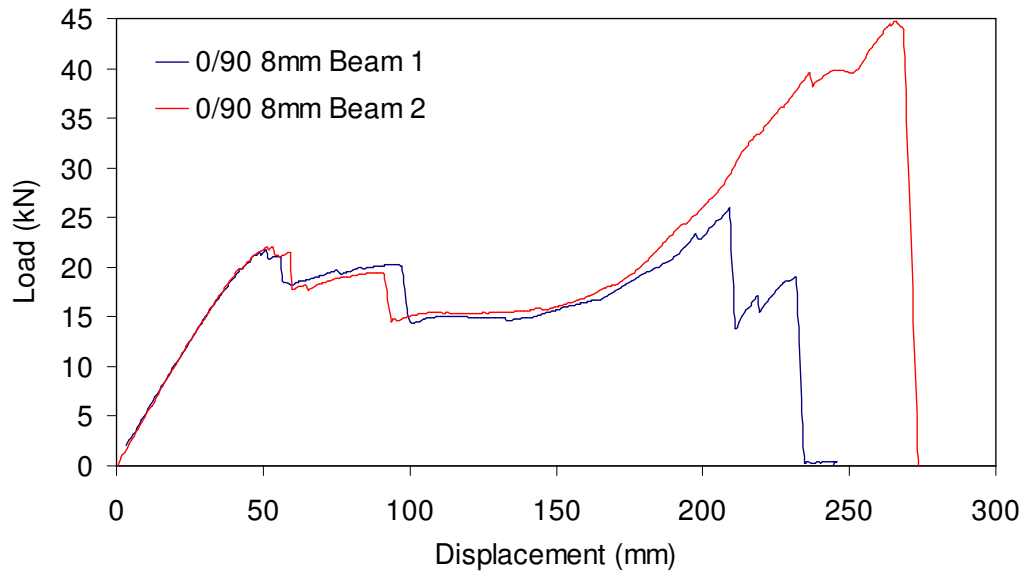


Figure 6.55 1:1 Twintex 0°/90° 8mm Phase 2 demonstrator large-scale 3-point flexure test results

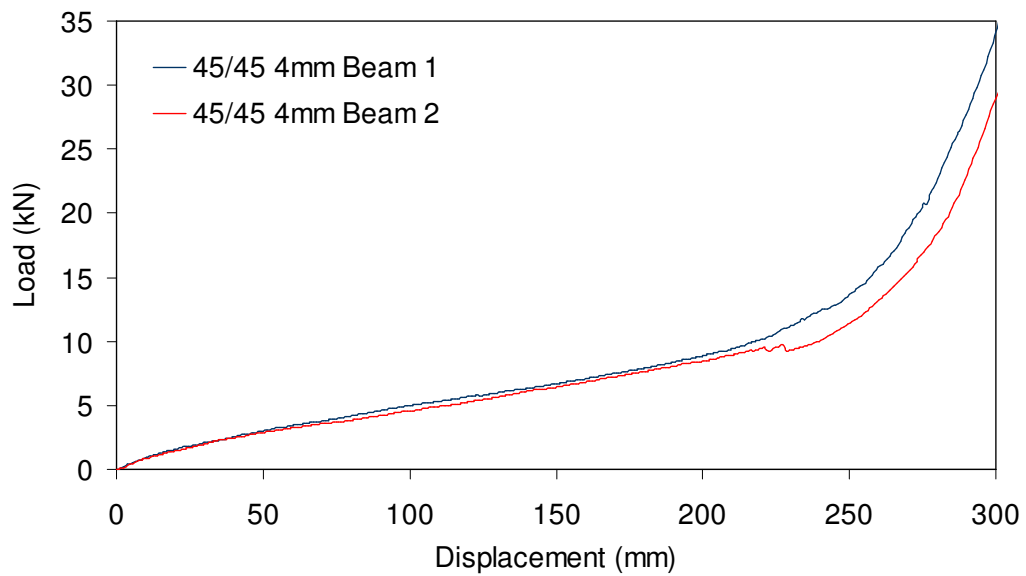


Figure 6.56 1:1 Twintex +45°/-45° 4mm Phase 2 demonstrator large-scale 3-point flexure test results

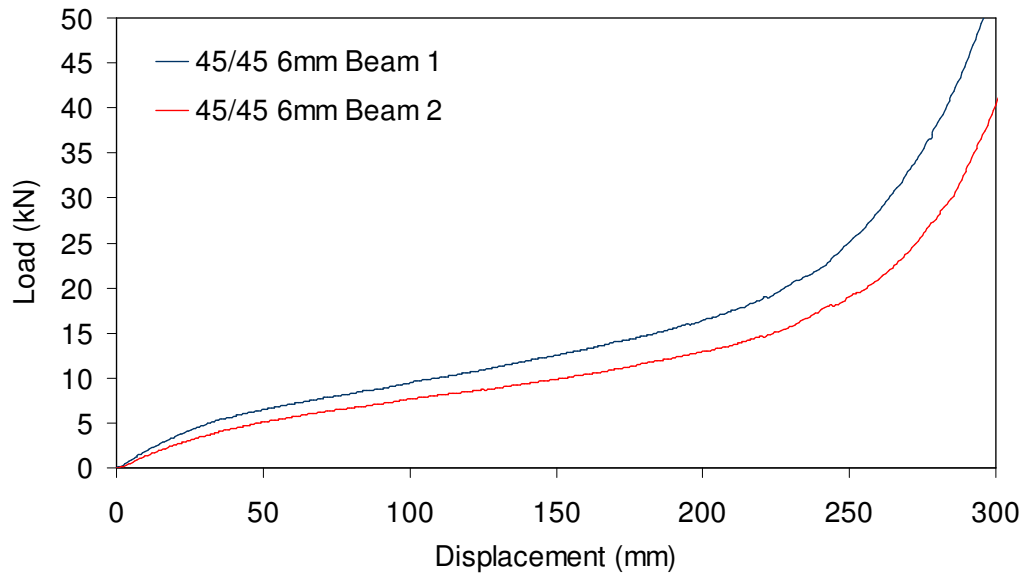


Figure 6.57 1:1 Twintex +45°/-45° 6mm Phase 2 demonstrator large-scale 3-point flexure test results

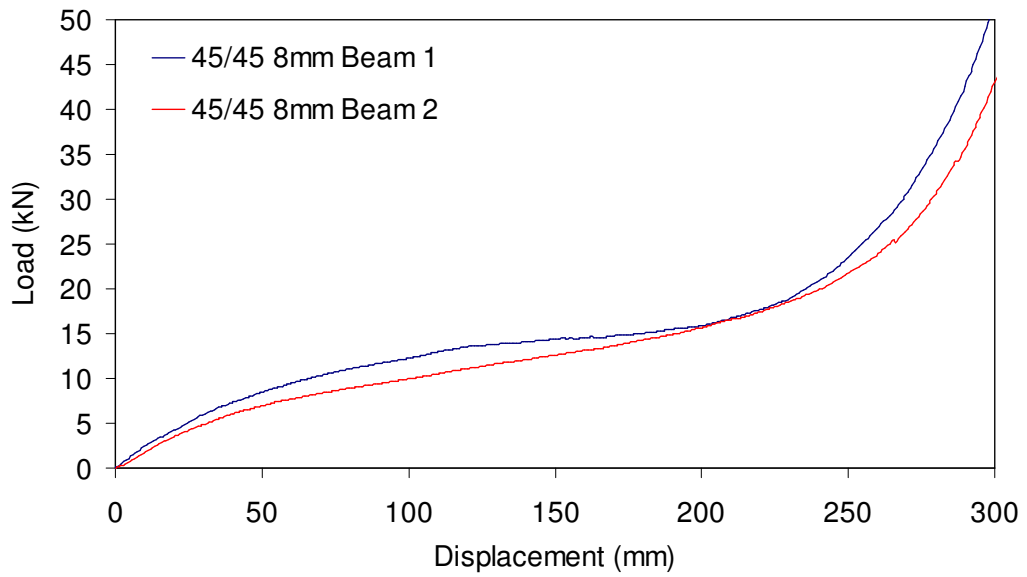


Figure 6.58 1:1 Twintex +45°/-45° 8mm Phase 2 demonstrator large-scale 3-point flexure test results

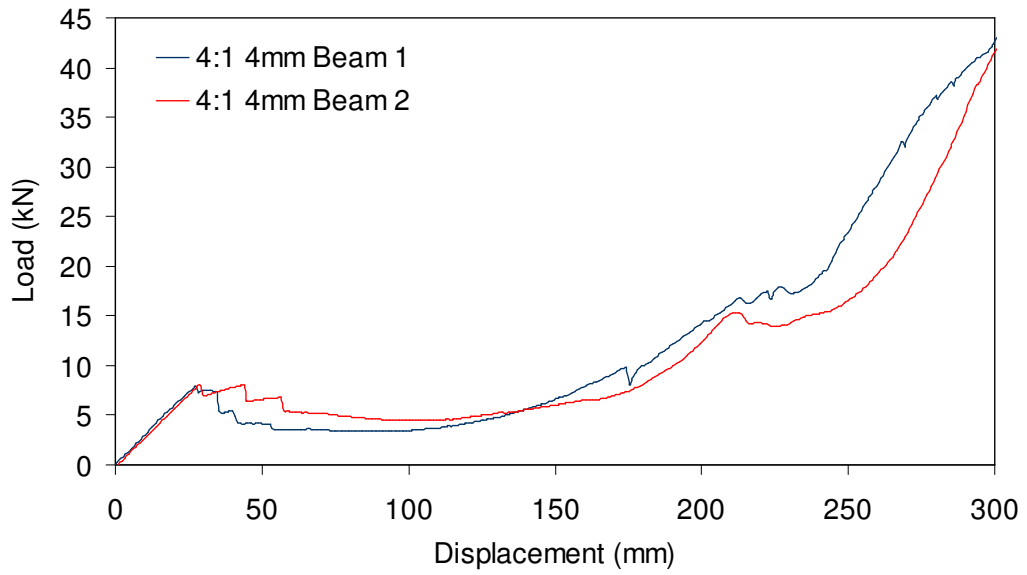


Figure 6.59 4:1 Twintex 0°/90° 4mm Phase 2 demonstrator large-scale 3-point flexure test results

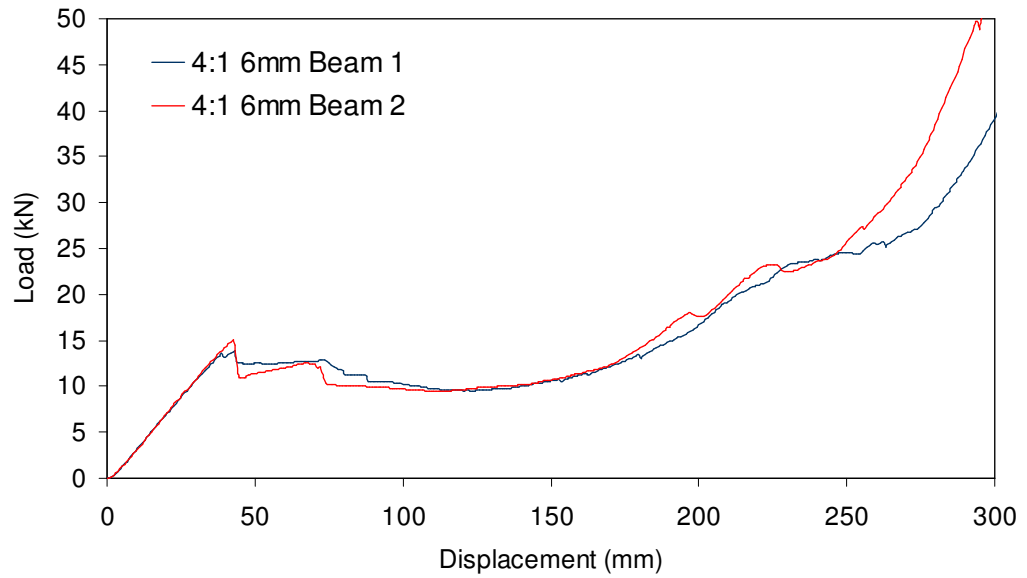


Figure 6.60 4:1 Twintex 0°/90° 6mm Phase 2 demonstrator large-scale 3-point flexure test results

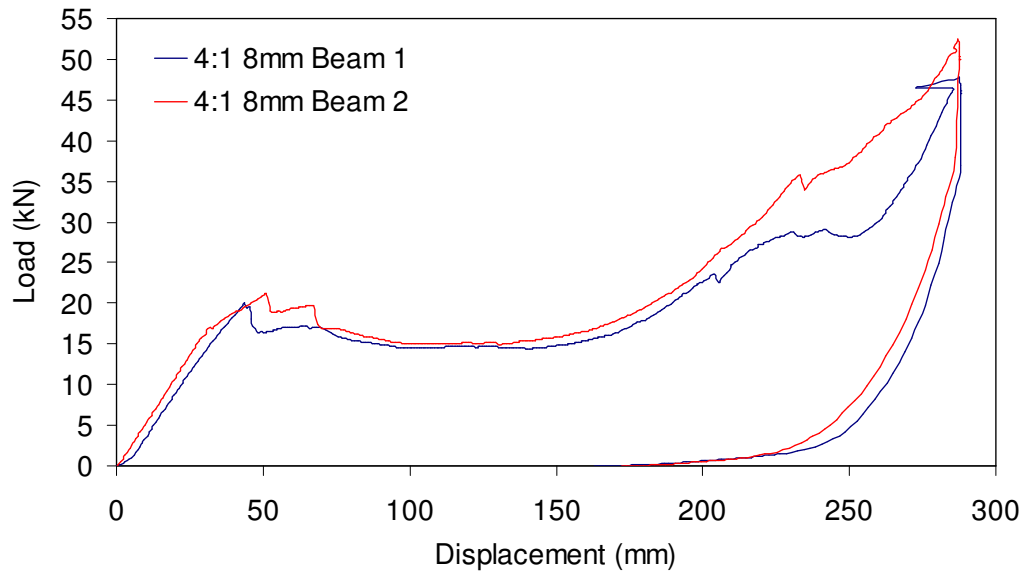


Figure 6.61 4:1 Twintex 0°/90° 8mm Phase 2 demonstrator large-scale 3-point flexure test results

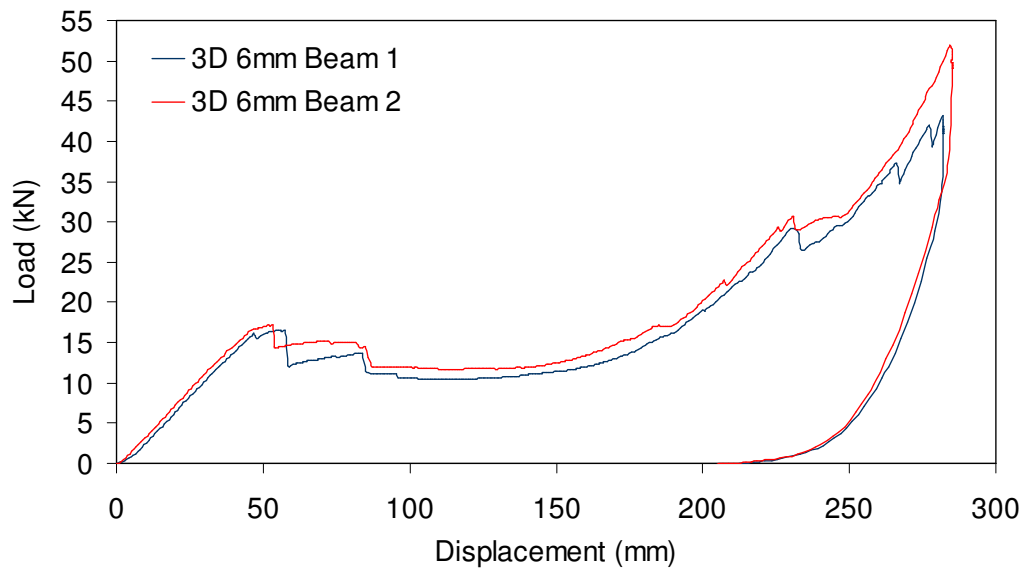


Figure 6.62 3D Twintex 0°/90° 6mm Phase 2 demonstrator large-scale 3-point flexure test results

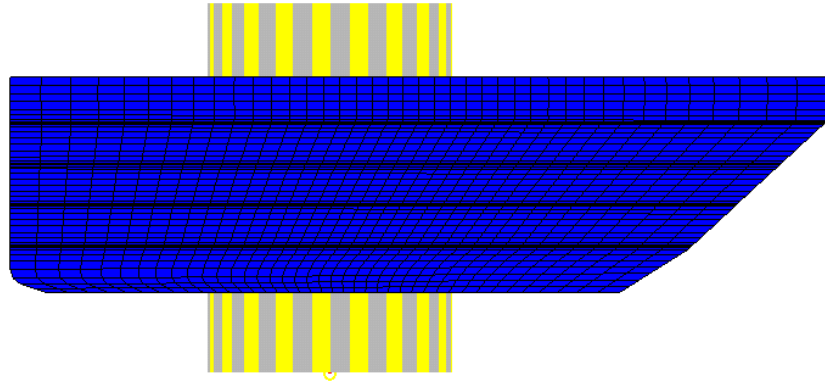


Figure 6.63 Phase 2 demonstrator large-scale 3-point flexure model

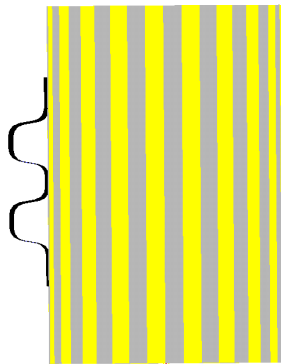


Figure 6.64 Phase 2 demonstrator large-scale 3-point flexure model

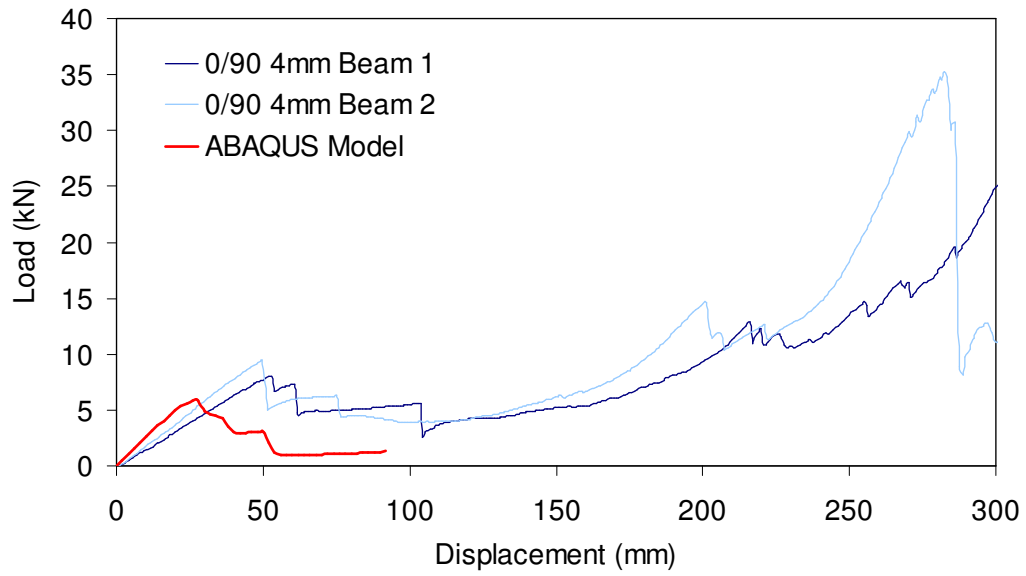


Figure 6.65 1:1 Twintex 0°/90° 4mm Phase 2 demonstrator large-scale 3-point flexure implicit finite element simulation

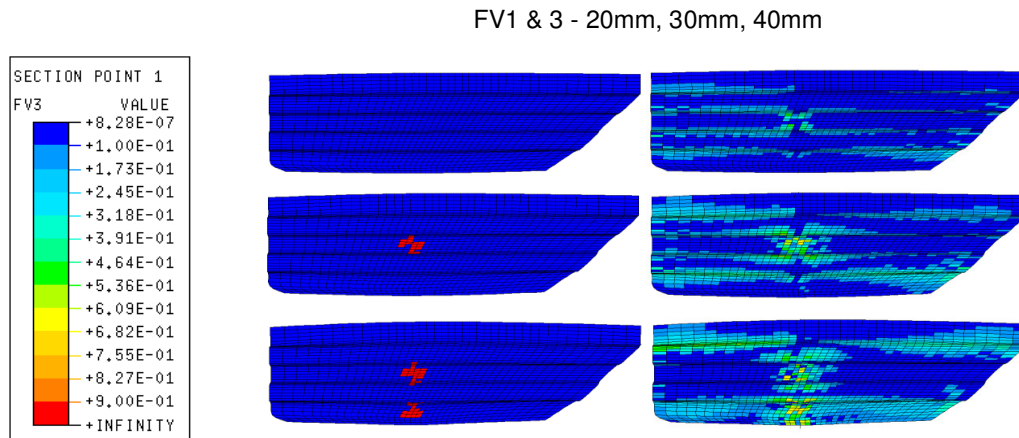


Figure 6.66 1:1 Twintex 0°/90° 4mm Phase 2 demonstrator large-scale 3-point flexure implicit finite element simulation - predicted damage

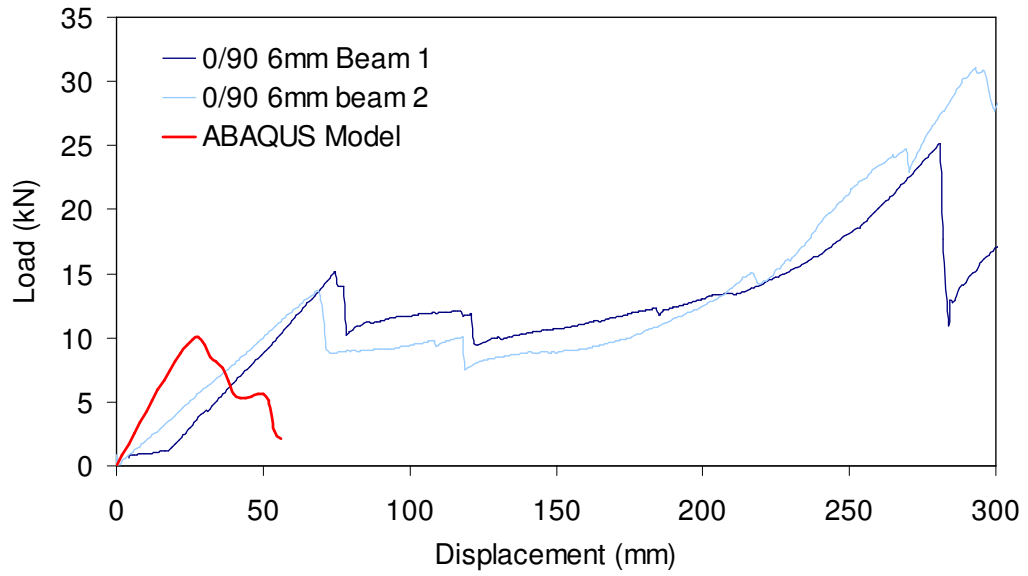


Figure 6.67 1:1 Twintex 0°/90° 6mm Phase 2 demonstrator large-scale 3-point flexure implicit finite element simulation

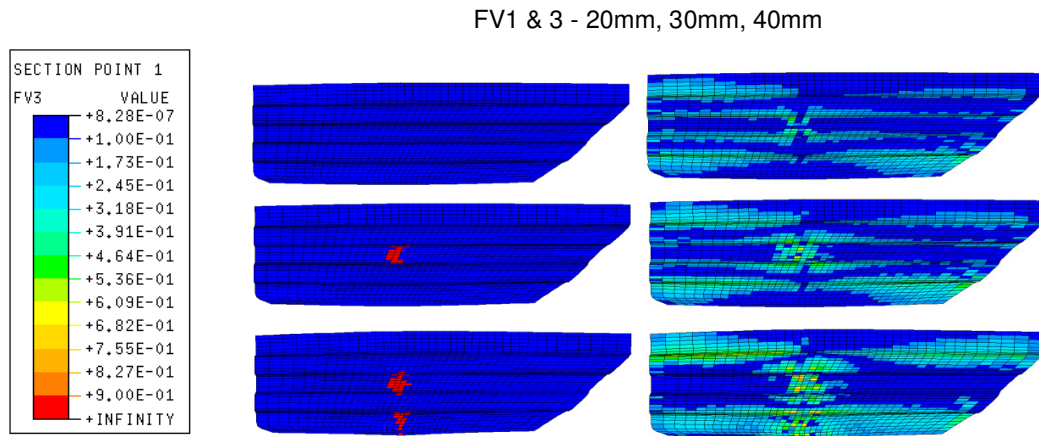


Figure 6.68 1:1 Twintex 0°/90° 6mm Phase 2 demonstrator large-scale 3-point flexure implicit finite element simulation - predicted damage

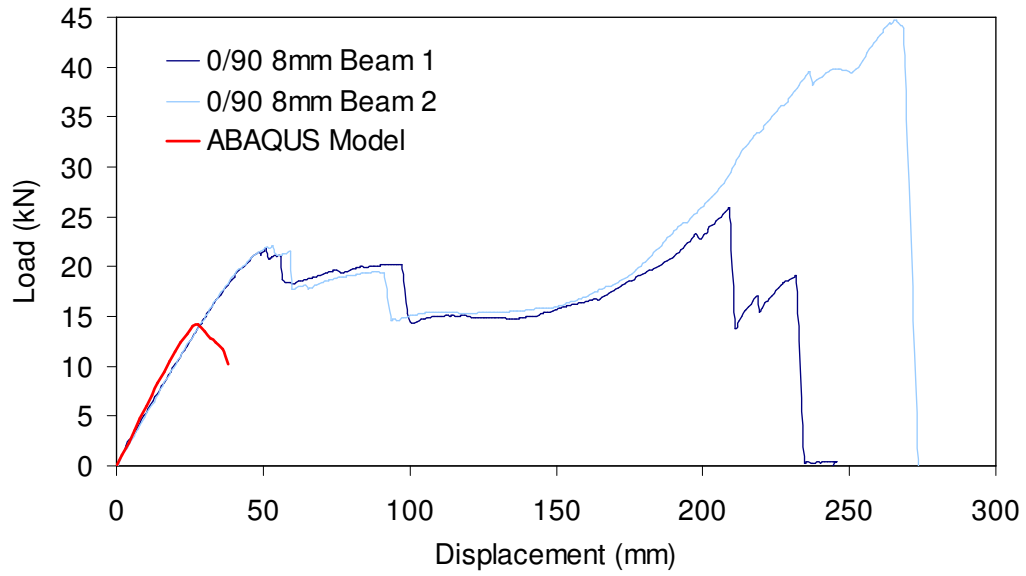


Figure 6.69 1:1 Twintex 0°/90° 8mm Phase 2 demonstrator large-scale 3-point flexure implicit finite element simulation

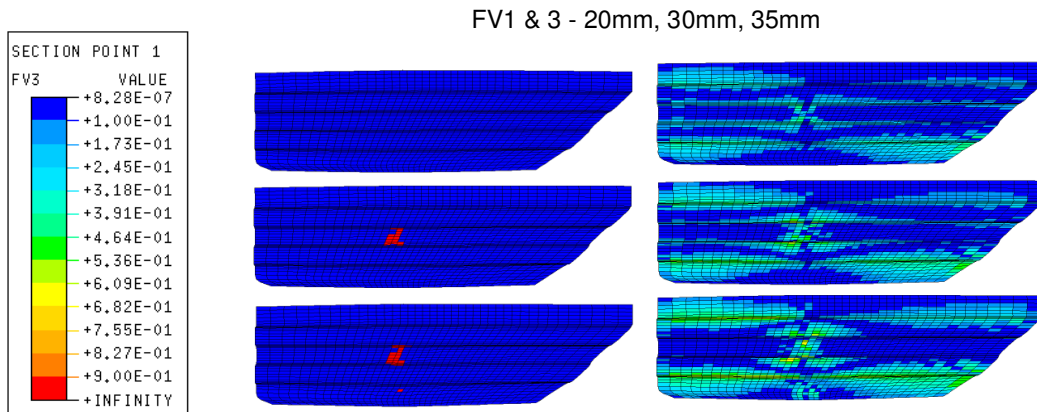


Figure 6.70 1:1 Twintex 0°/90° 8mm Phase 2 demonstrator large-scale 3-point flexure implicit finite element simulation - predicted damage

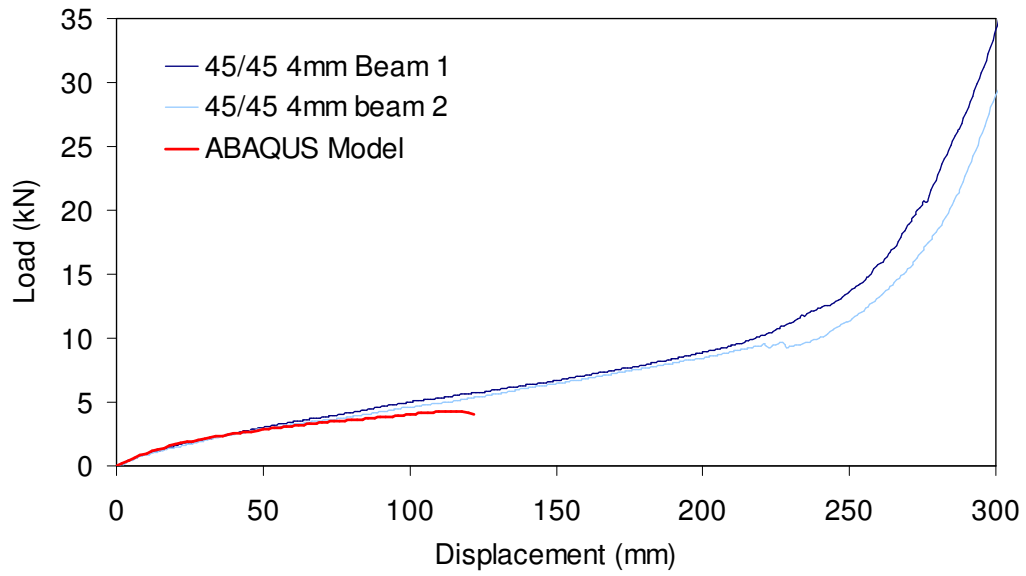


Figure 6.71 1:1 Twintex +45°/-45° 4mm Phase 2 demonstrator large-scale 3-point flexure implicit finite element simulation

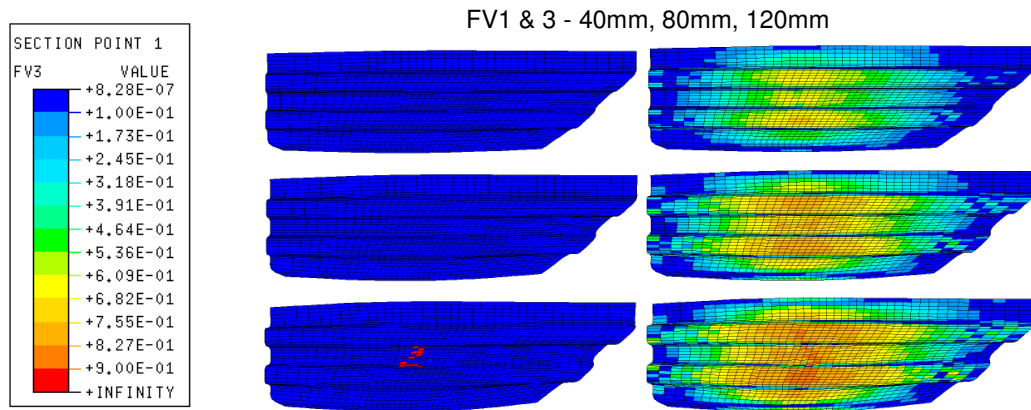


Figure 6.72 1:1 Twintex +45°/-45° 4mm Phase 2 demonstrator large-scale 3-point flexure implicit finite element simulation - predicted damage

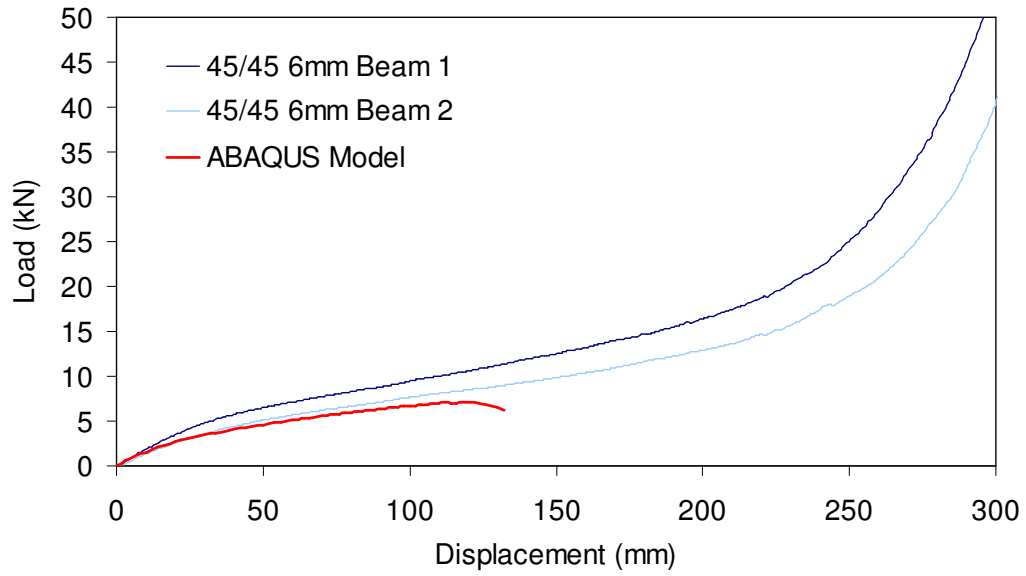


Figure 6.73 1:1 Twintex +45°/-45° 6mm Phase 2 demonstrator large-scale 3-point flexure implicit finite element simulation

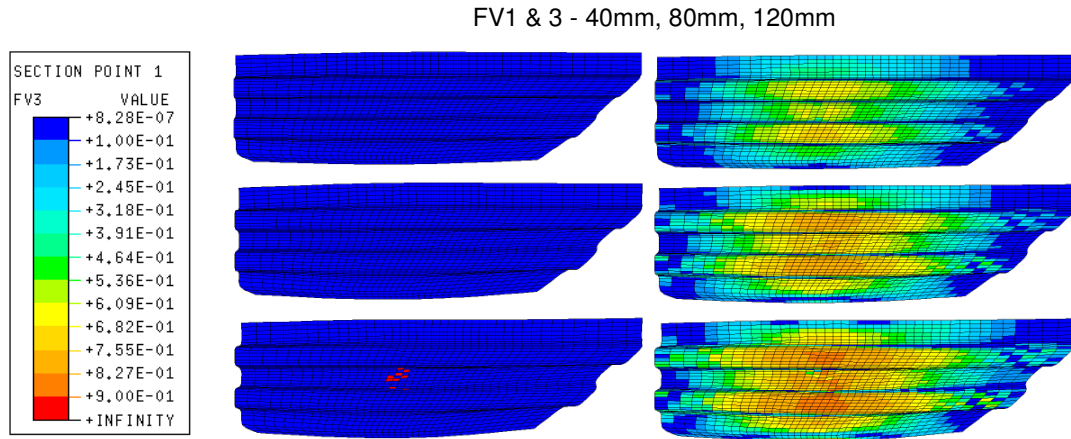


Figure 6.74 1:1 Twintex +45°/-45° 6mm Phase 2 demonstrator large-scale 3-point flexure implicit finite element simulation - predicted damage

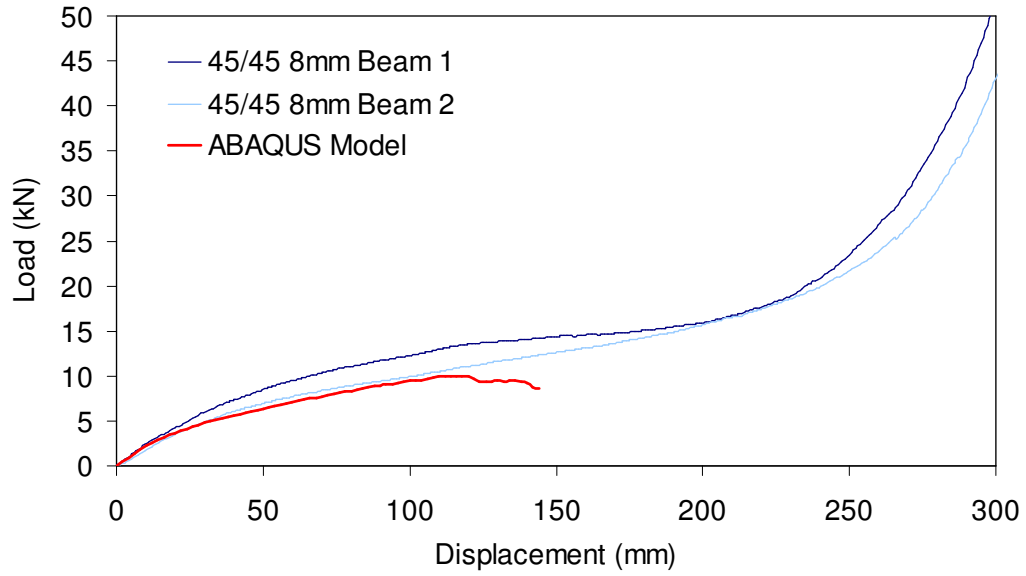


Figure 6.75 1:1 Twintex +45°/-45° 8mm Phase 2 demonstrator large-scale 3-point flexure implicit finite element simulation

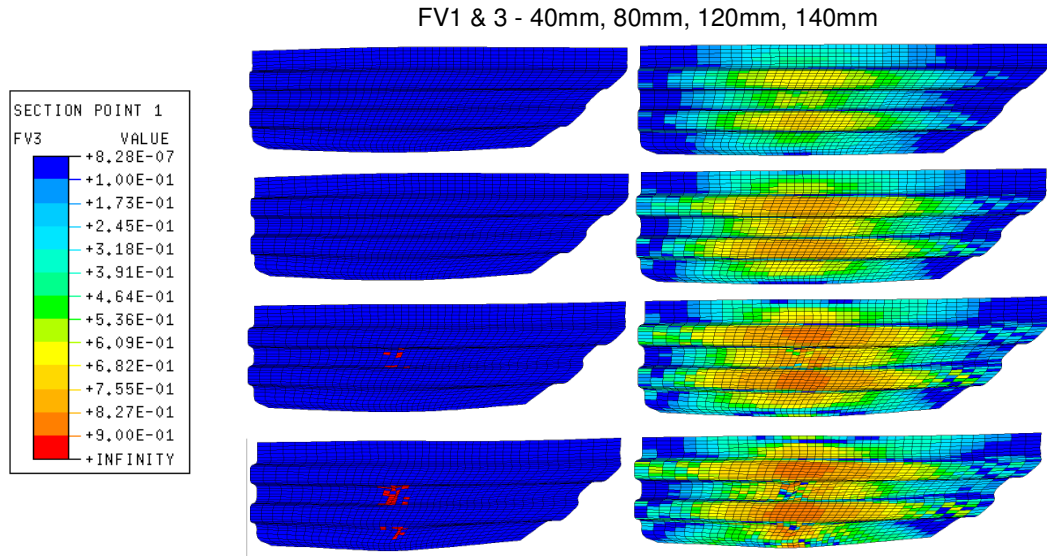


Figure 6.76 1:1 Twintex +45°/-45° 8mm Phase 2 demonstrator large-scale 3-point flexure implicit finite element simulation - predicted damage

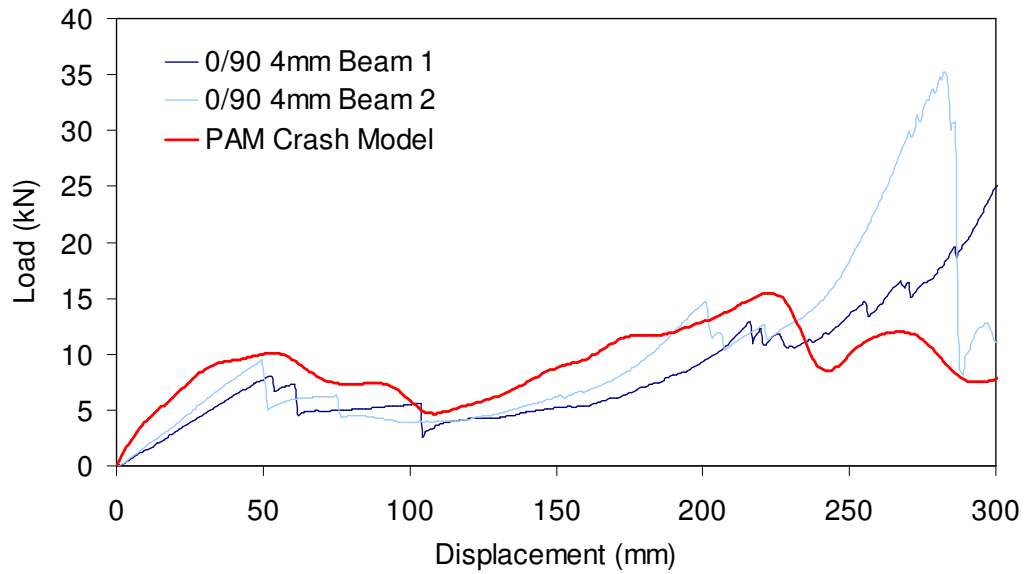


Figure 6.77 1:1 Twintex 0°/90° 4mm Phase 2 demonstrator large-scale 3-point flexure explicit finite element simulation

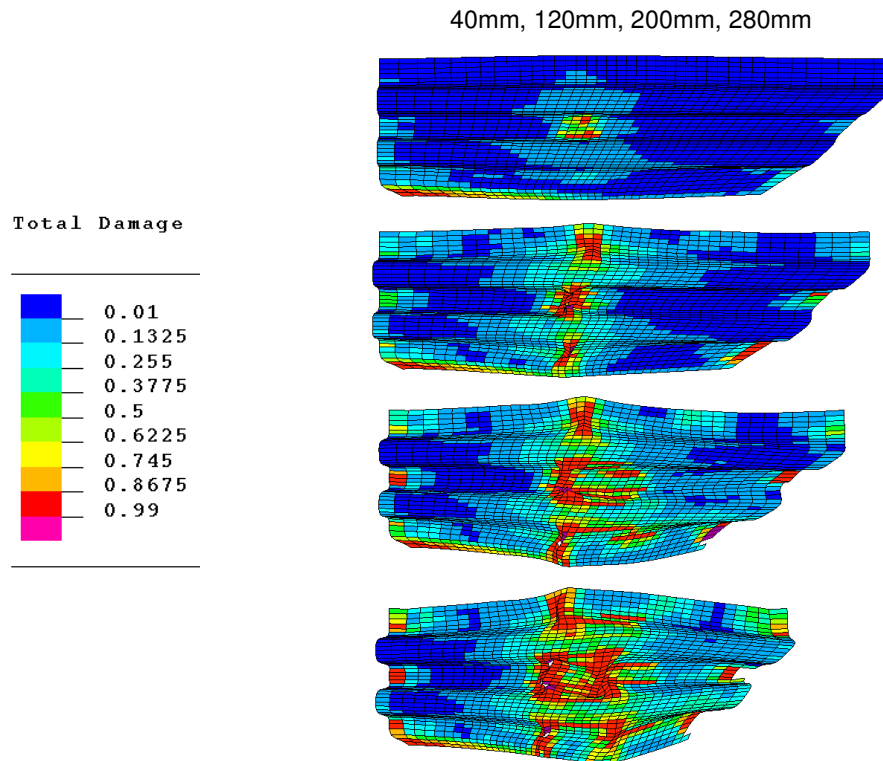


Figure 6.78 1:1 Twintex 0°/90° 4mm Phase 2 demonstrator large-scale 3-point flexure explicit finite element simulation - predicted damage

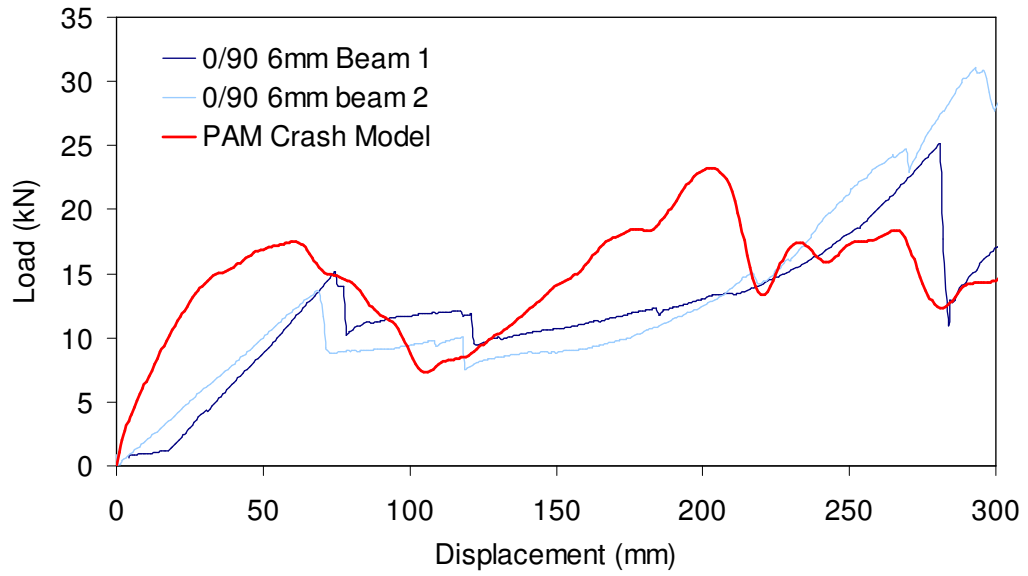


Figure 6.79 1:1 Twintex 0°/90° 6mm Phase 2 demonstrator large-scale 3-point flexure explicit finite element simulation

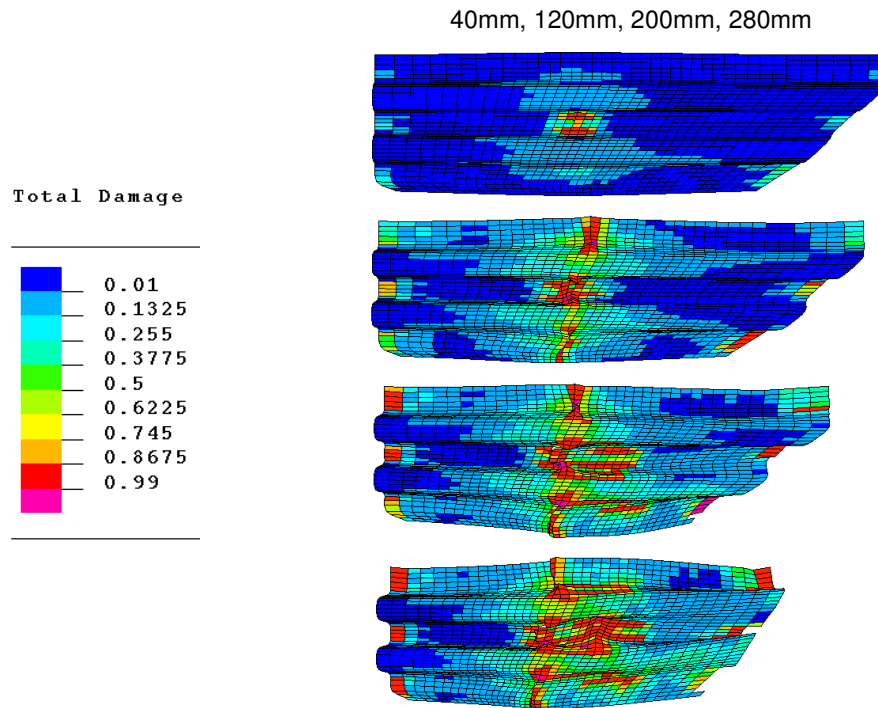


Figure 6.80 1:1 Twintex 0°/90° 6mm Phase 2 demonstrator large-scale 3-point flexure explicit finite element simulation - predicted damage

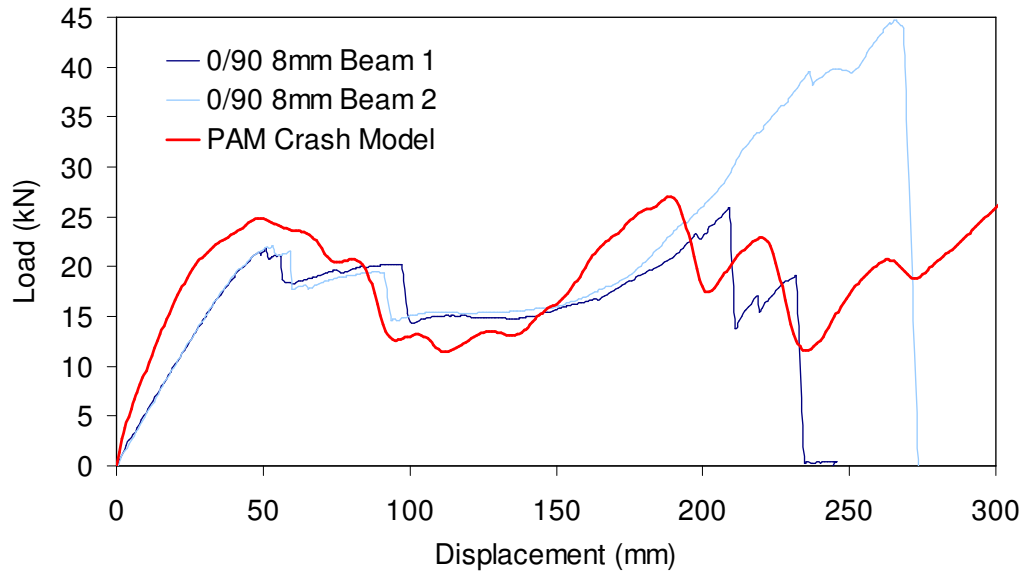


Figure 6.81 1:1 Twintex 0°/90° 8mm Phase 2 demonstrator large-scale 3-point flexure explicit finite element simulation

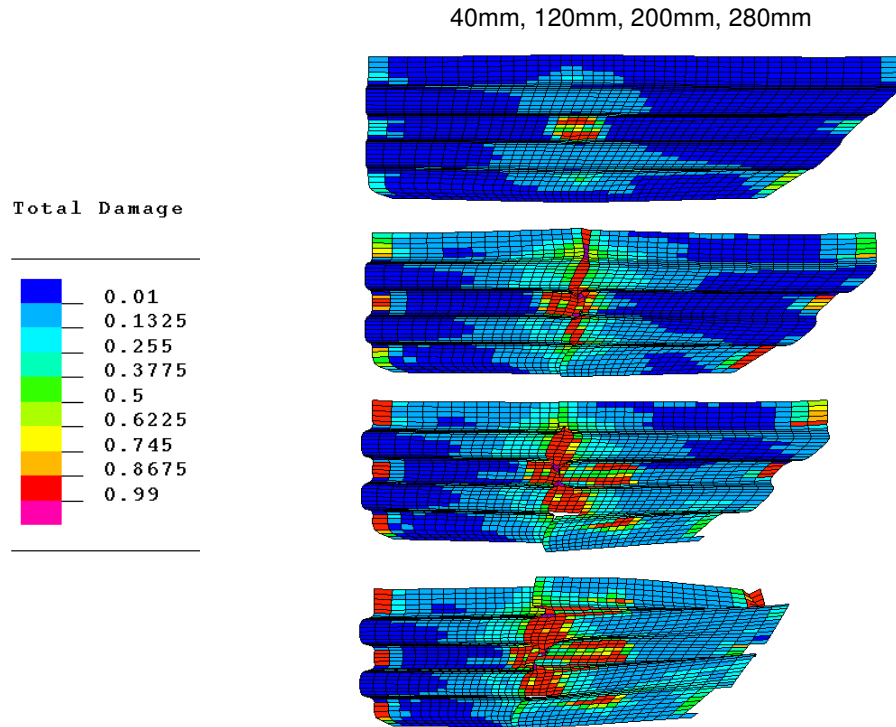


Figure 6.82 1:1 Twintex 0°/90° 8mm Phase 2 demonstrator large-scale 3-point flexure explicit finite element simulation - predicted damage

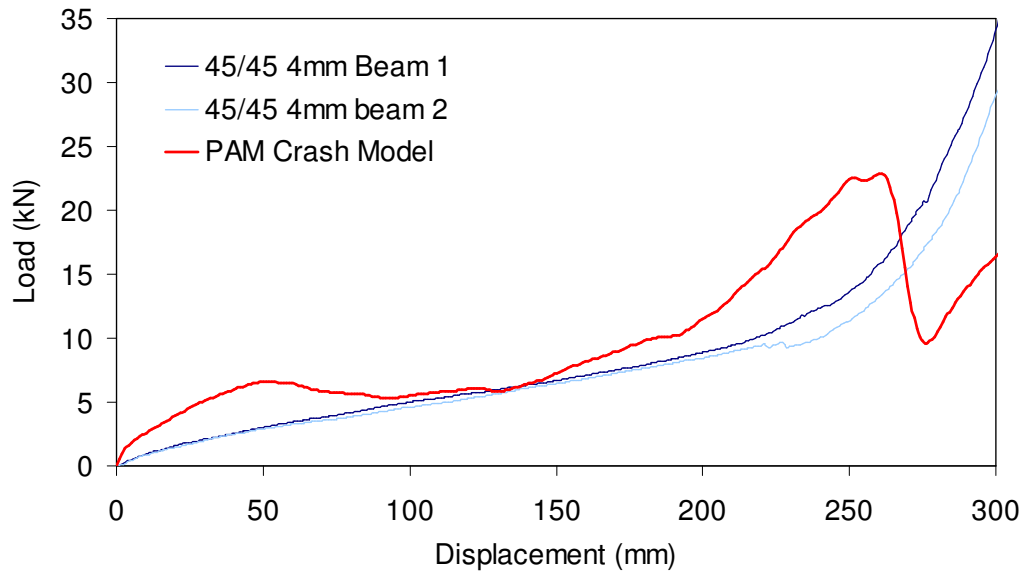


Figure 6.83 1:1 Twintex +45°/-45° 4mm Phase 2 demonstrator large-scale 3-point flexure explicit finite element simulation

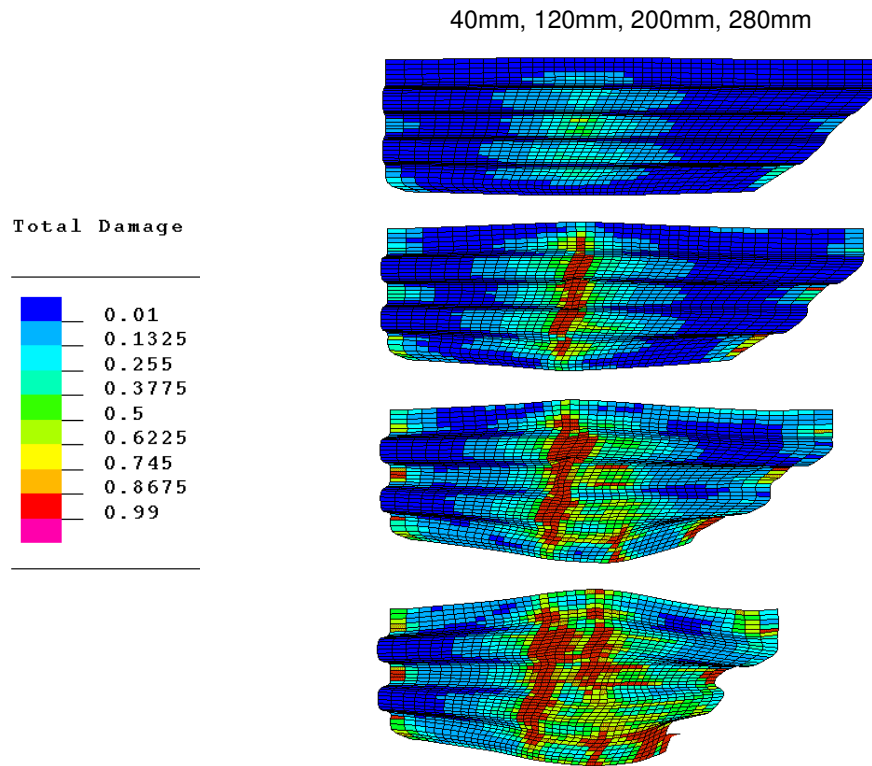


Figure 6.84 1:1 Twintex +45°/-45° 4mm Phase 2 demonstrator large-scale 3-point flexure explicit finite element simulation - predicted damage

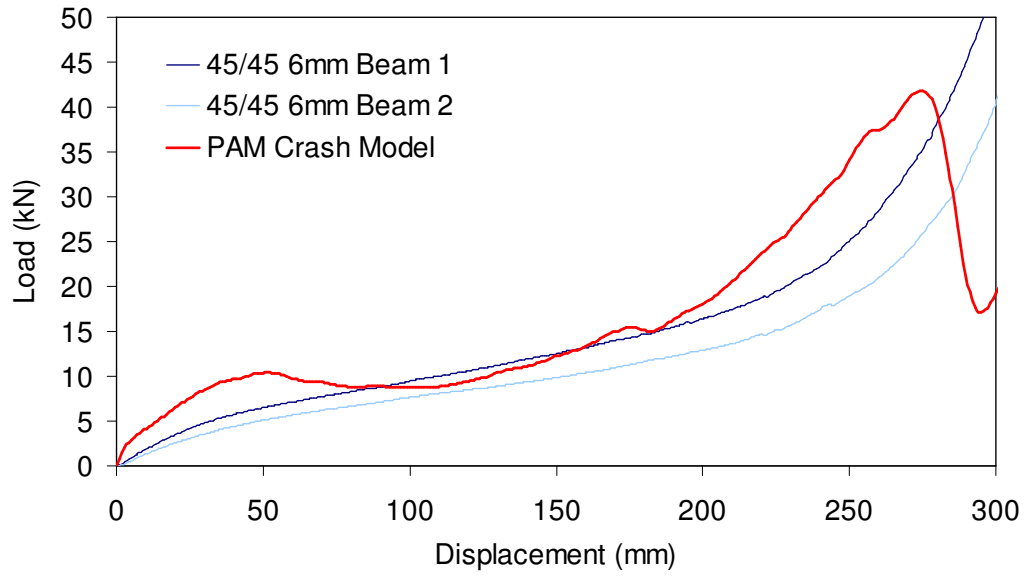


Figure 6.85 1:1 Twintex +45°/-45° 6mm Phase 2 demonstrator large-scale 3-point flexure explicit finite element simulation

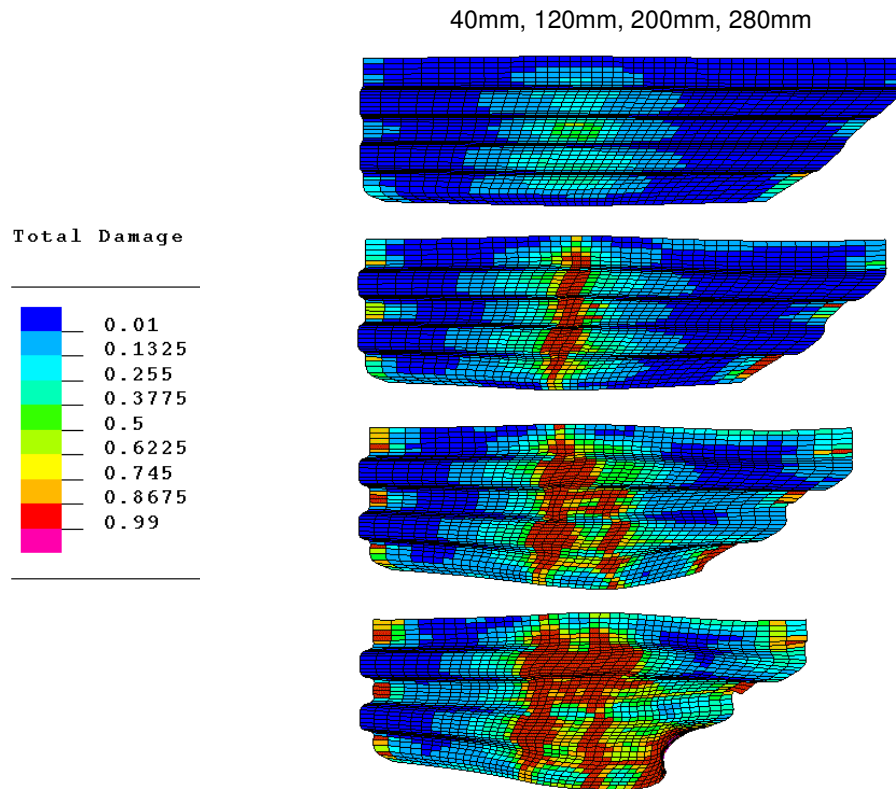


Figure 6.86 1:1 Twintex +45°/-45° 6mm Phase 2 demonstrator large-scale 3-point flexure explicit finite element simulation - predicted damage

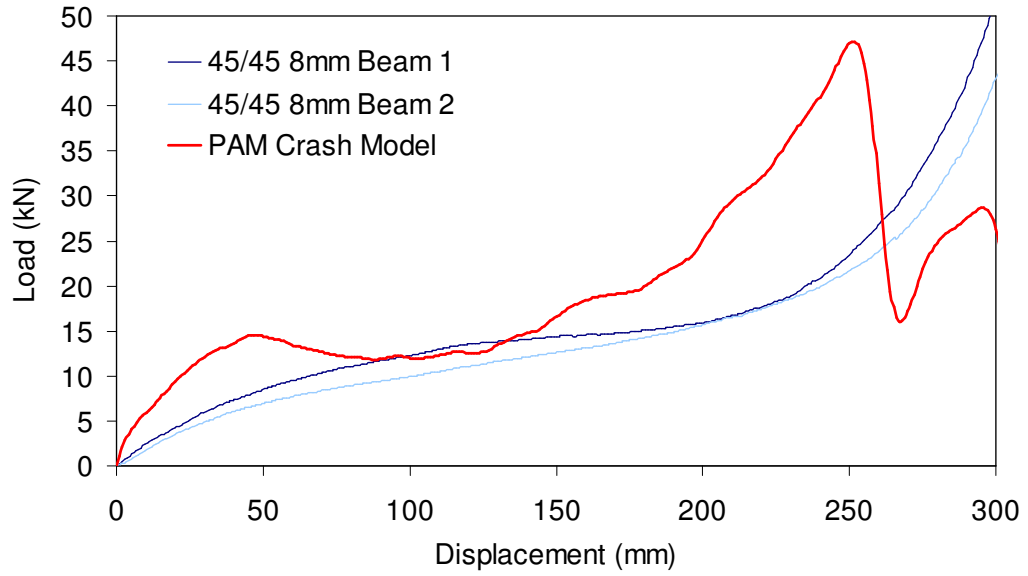


Figure 6.87 1:1 Twintex +45°/-45° 8mm Phase 2 demonstrator large-scale 3-point flexure explicit finite element simulation

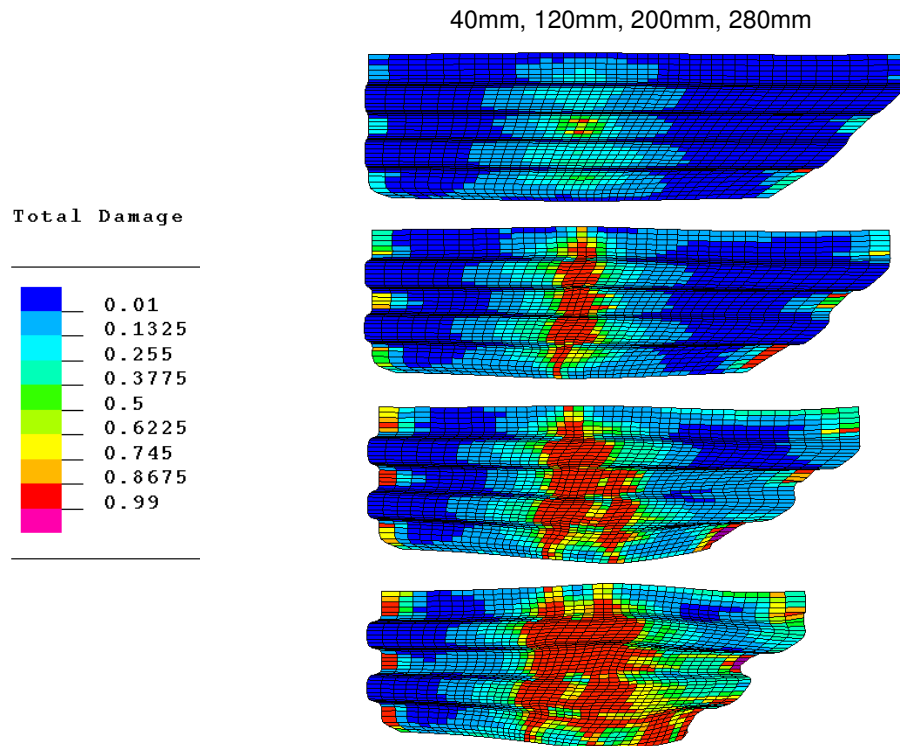


Figure 6.88 1:1 Twintex +45°/-45° 8mm Phase 2 demonstrator large-scale 3-point flexure explicit finite element simulation - predicted damage

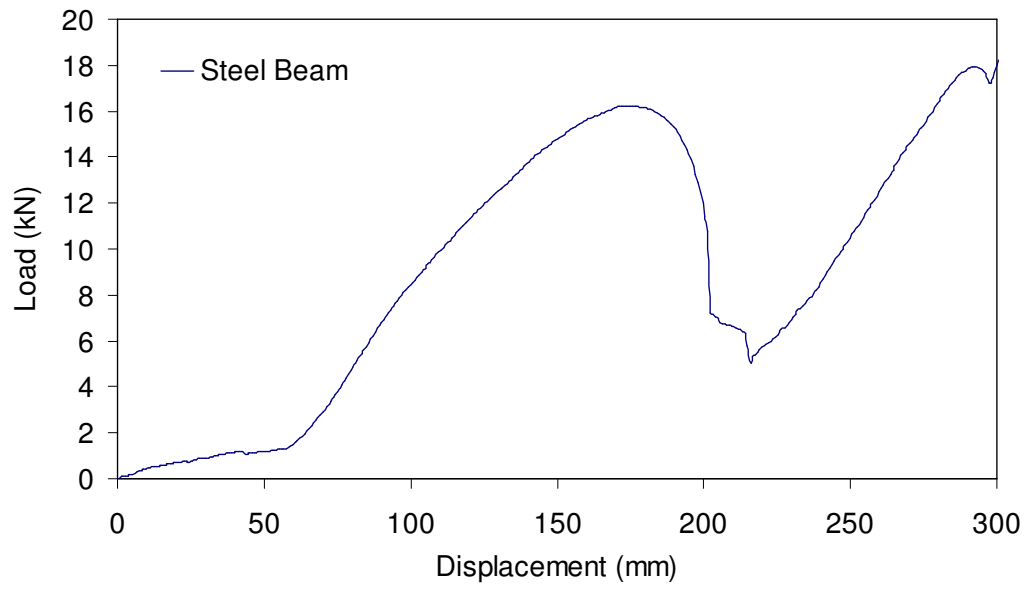


Figure 6.89 Steel side intrusion beam large-scale 3-point flexure test



Figure 6.90 GMT door cassette component used in FMVSS214 composite beam test

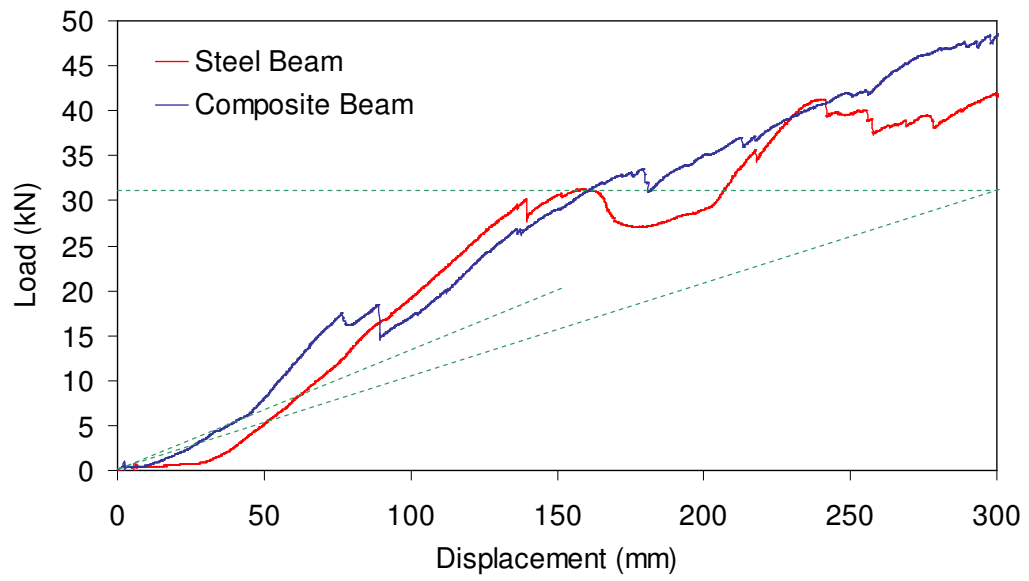


Figure 6.91 FMVSS214 vehicle side intrusion test - load displacement results

Chapter 7 Discussion and Conclusions

7.1 Introduction

Thermoplastic composite materials are becoming a viable alternative to steel and aluminium for use in semi-structural applications in the automotive industry. Limitations in the current understanding of their damaging behaviour and a lack of fully validated modelling tools, is though, a barrier to their application in fully crashworthy components. The aim of this work was to develop a predictive damage modelling capability for a thermoplastic composite material, namely Twintex and to use the results for the design and test of a structural crashworthy component.

Two approaches to damage modelling have been investigated, the first using an implicit finite element code and the second using an explicit finite element code. Both have been calibrated with a combination of published and experimental test data and validated for a range of in-plane damage scenarios.

In general, testing numerous specimens for calibration of complex material models is costly in terms of both time and expense. It is therefore important, for the purposes of industrial acceptance, that it is as simple as possible to gather the necessary data to facilitate the accurate calibration of damage models. It is also imperative, that where applicable, material data that is already available can be used for these purposes. It is for this reason, that the current body of work has not been an exercise in the development of calibration regimes or a thorough characterisation of the candidate material. In fact, the author has where possible, used currently available data and where not, used what was judged to be the least complex test standard or method to gather the necessary data.

The validated models have then been applied to the design of an industrial demonstrator component to investigate the potential applications and limitations of the techniques. The demonstrator component has finally been tested to prove that thermoplastic composite materials, if designed correctly, can offer an alternative to high strength steel for crashworthy applications.

In this section, the calibration test methods, damage models used and component testing undertaken are discussed. Limitations with the current work are investigated and suggestions are made for further work to improve the techniques developed.

7.2 Coupon Test Methods for Calibration and Validation of Finite Element Damage Models

Since Twintex, is a $0^\circ/90^\circ$ balanced weave fabric reinforced composite, there are only three basic tests required to calibrate the critical parameters for the in-plane behaviour of the material. These are, a 0° tensile tests, a 0° compression test and a shear test. In the current work, a $+45^\circ/-45^\circ$ tensile test was selected for the shear characterisation, as both specimen preparation and test rig development were significantly simpler. This method has been validated by previous authors [19] and has also been published as an ISO standard method [120]. Developments of these tests, using specimens with stress concentrations were used to further validate numerical models after calibration.

7.2.1 Quantity of Specimens Tested and Scatter of Results

Material availability for preparation of test specimens was an important factor throughout the research, up until the demonstrator component programme, when increased stocks became available. In general for each test undertaken, at least five specimens were prepared to allow for variation in material performance. Ideally, more specimens of each type would have been tested, although this was not possible.

For the tensile $0^\circ/90^\circ$ test, results from 11 successful tests from 15 specimens are presented. Since the same method was used for all subsequent tensile tests, both with and without stress concentrations, it is hypothesised that the variability observed during the $0^\circ/90^\circ$ tensile test would be similar to the levels observed in subsequent tests. In this first set of tests, ultimate strength ranged from 244 MPa to 302 MPa, which equates to approximately $\pm 10\%$ about the mean value of 279 MPa. This suggests that the variable nature of the manual transfer, non-isothermal processing method could introduce a certain amount of scatter in observed test results. In consequence, the exact prediction of the performance of a component, using numerical methods will always be dependant on, not only the quality of the simulation

techniques, but also on the quality of the composite material, which has in turn been shown to be highly dependant on manufacturing process [11][12].

7.2.2 Strain Measurement Techniques

In terms of experimental technique, the method for measurement of strain during test was where the present authors approach differed from previous studies [15][16]. In all of the tensile tests undertaken, strain measurement was performed using an extensometer mounted on the specimen, measuring nominal strain over a 50mm gauge length. This was essential for two reasons. Firstly the quality of bond achievable between a strain gauge and a polypropylene matrix composite specimen is highly variable, depending on the surface treatment and preparation and secondly, even with excellent bond quality, the gauge will only measure over a short strain range before becoming detached. When investigating a thermoset matrix composite, where behaviour is often elastic with a brittle failure, strain gauges are acceptable for material characterisation. In the case of polypropylene Twintex, especially in shear-dominated tests, where behaviour was highly non-linear and the extension over a 50mm gauge length was observed to be greater than 15%, strain gauges are less applicable.

The only characterisation test to use a strain gauge rather than an extensometer, was the $0^\circ/90^\circ$ compressive test. This test captured the linear portion of the material behaviour accurately, but failed to give strain behaviour after the first critical failure, when the strain gauge became detached. This resulted in a phase of specimen compressive damage not being captured by the test result.

7.2.3 Shear Behaviour During Off Axis Tests

The shear damaging behaviour of Twintex, was difficult to model. In the early stages of the work, testing of tensile and compressive specimens manufactured from $+45^\circ/-45^\circ$ mouldings, showed similar results, in terms of the modulus and shear damaging behaviour. This allowed modelling, especially using the implicit technique described in Chapter 4, to be calibrated to reflect observed material performance.

When comparing these results to the behaviour of the $+45^\circ/-45^\circ$ specimens with stress concentrations, an interesting phenomenon is observed. The compressive off-axis test

with a stress concentration appears to behave in a similar way to the plain compressive specimen, with some initial shear deformation followed by a combination of shear deformation and out of plane buckling. The tensile $+45^\circ/-45^\circ$ specimen with a stress concentration, on the other hand, provides results which are more difficult to predict. In these specimens, a stiffer than expected response is observed, with failure occurring at significantly lower strain than in the specimen without a stress concentration. This result is due to the method of strain measurement, over a 50mm gauge length. When the gauge is measuring a strain of 5%, strain levels could be locally higher than 25% if all the deformation is concentrated around the hole.

7.2.4 Out of Plane Deformation During Compressive Test

Due to the nature of the polypropylene matrix material, it was particularly difficult to characterise the damaging behaviour during compressive tests. The damage models are predominantly concerned with single, multi-layered, shell element representations of the composite and as such do not accurately model the complex out of plane and buckling damage seen during test. This, for thermoset matrix composites is not a particularly critical issue, since the material is loaded and deforms linearly until delamination, fibre buckling or catastrophic matrix failure occur and the specimen fails. With a polypropylene matrix the specimen starts to deform out of plane, without a catastrophic drop in load carrying capability. For this reason it was difficult in some cases to differentiate the contribution of in-plane and out of plane damage development during these tests.

7.2.5 Damage Development in Hole in Plate Specimens

The hole in plate specimen as a method for investigation of damage in a non-uniform geometry and as a validation for numerical studies has been shown to be a valuable tool. The specimen itself is little more complex than a standard tensile or compressive specimen and requires virtually no modification in method for testing.

If it is accepted that the step from standard test specimen results for material characterisation to prediction of composite component behaviour is too great for current simulation techniques, the hole in plate type specimen could be an economically viable midway point. This is especially true when considering the

results of the later stages of this work, which show that for thermoplastic composite materials, an accurate in-plane model for the fibre direction behaviour can yield encouraging results in terms of the prediction of damage development in complex geometries.

7.3 Implicit Finite Element Damage Modelling

The purpose of this section of the work was to consider the potential of a previously proposed damage model for thermoset matrix composites, for the simulation of accumulated damage in thermoplastic composites. During the initial stages of the investigation it was quickly identified that the model's treatment of the brittle matrix material and shear failure criteria yielded poor results when applied to thermoplastics. This led to the development of a simplified model for thermoplastic matrix composites, using a ply based maximum strength criteria for the fibre direction and a shear degradation regime and ultimate failure strain. The only component of the model retained from the work of Chang [68][79] was the shear modulus degradation relationship.

Subsequent work was then undertaken to validate the new model and investigate the potential of such an approach to be used as a composite material design tool. It should be noted that the purpose of this work was not to provide an alternative to explicit dynamic modelling techniques, but to investigate the potential for an implicit code to be used to provide a complementary solution and a numerically less expensive design capability.

7.3.1 The Treatment of Fibre Direction and Shear Damage

The most interesting feature of this model when comparing to the other model investigated during this research programme is the separate treatment of fibre direction and shear damage. When considering a brittle matrix composite, where failure strains in both fibre direction and shear are within similar ranges, it is possible to consider a damage state for a unit volume and degrade the elastic constants accordingly. In a woven fibre reinforced thermoplastic matrix composite, this can potentially lead to situations where shear damage, which in reality would result in fairly minimal reduction in fibre direction properties, results in levels of damage that

significantly reduce the load carrying capacity of the ply. The separation of the two avoids this situation and in the case of coupon test simulations, offered promising results.

7.3.2 Accuracy of Fibre Direction Damaging Behaviour

Using the implicit damage model it was possible to gain excellent agreement between tensile experiment and test in the fibre direction. It was also possible to accurately model the compressive behaviour of Twintex, where simulation again matches closely experimentally observed behaviour. The implicit model does however fail catastrophically at the point when stress levels reach the calibrated compressive failure level. This appears to match the experimental result well, although it should be noted that, as mentioned previously, the specimen in reality continued to deform out of plane after this first ply failure, which resulted in a significant load drop, but not in catastrophic collapse.

This result, for the compressive damage prediction, becomes more significant when considering more complex geometries, where ultimate failure in a localised region would not necessarily lead to global collapse of a structure.

For the fibre direction specimen with a stress concentration, ultimate failure is also predicted prematurely, at a stress level approximately 15% below that observed in test. This suggests that inclusion of a residual strength in the model could improve the stability of the solution.

7.3.3 Accuracy of Shear Damaging Behaviour

The accuracy of the shear damaging behaviour of the model, was good for the +45°/-45° tensile test specimen. This was expected, since this test was used to calibrate the shear damage parameter α . In the off-axis compression test, the result of simulation was not as encouraging. As mentioned previously, the specimen deformed both in and out of plane during this test, resulting in a damaging behaviour that was not wholly captured by the model. This result was also seen in the +45°/-45° compression specimen with a hole, where, especially at high levels of displacement, the model predicts a stiffer response. It is interesting to note, that the 5mm displacement

observed at the completion of this test, equates to a global strain level of approximately 4 %, when considering the whole specimen. Similar work presented by Chang and Lessard [79] shows results up to between 0.6% and 1.6% strain. If these levels were considered for the work presented here, excellent agreement would be seen. It is therefore concluded that the model is accurate for in-plane damaging modes, although buckling deformation, as expected, cannot be accounted for accurately.

The result for the tensile +45°/-45° specimen with a hole is less encouraging. The model significantly under predicts the response of specimen in terms of stiffness and ultimate failure load. This is due in part to the model predicting shear damage throughout the specimen, which to a certain extent was not observed in test, where the deformation was more localised around the hole. It is also possible that fibre re-orientation around the hole, which is not accounted for accurately by the model, could influence the performance at high strain levels. In this case as the fibres shear in the area of the hole, they become oriented in the direction of the test. Due to the ductility of the matrix, the composite can still function as a homogeneous material and hence the local stiffness can remain high.

7.3.4 Application of the Implicit Damage Model to a Complex Component

During the development of the automotive demonstrator components manufactured and tested during this research programme, the model was used to predictively simulate the damage behaviour, with varying degrees of success. For the Phase 1 demonstrator geometry, the model accurately predicted the small-scale 3-point flexure behaviour of both the 0°/90° and the +45°/-45° lay-up beams. These results were for relatively small displacement, around 80mm, compared to later tests up to 300mm.

It is in these later tests that limitations of the technique become apparent, for the 0°/90° beams in particular, where the model predicts catastrophic failure at a displacement of 50mm. In reality, although damage had occurred, the beams continued to carry load until an ultimate failure displacement of up to 300mm. This limitation of the model is in part due to the inability of an implicit code to converge a solution when elements have deformed significantly due to reduction in load carrying

capacity and also due to the nature of the damage model, where compressive failure leads to a reduction of the modulus to a nominal value.

In the case of the $+45^\circ/-45^\circ$ Phase 1 beam simulations, the results are more encouraging. Although the model under predicts the stiffness of the beam towards the end of the test, the solution remains stable and converges up to a displacement of 300mm.

For the Phase 2 beam geometry, similar results are observed. The $0^\circ/90^\circ$ beam simulations all predict failure to occur catastrophically during the early stages of the test, a phenomenon that was not observed experimentally. It is also interesting to note that for the 6mm beam, the stiffness, even during the initial stages of test is not correctly predicted. It is felt that this was due to moulding issues associated with the 6mm beam, which will be discussed later, and not due to the modelling technique.

The $+45^\circ/-45^\circ$ Phase 2 beam simulations, like the Phase 1 results, show good correlation with test, although the simulations all predict failure at incorrect displacements. In all cases, fibre direction damage predicted in the beams is resulting in failure to converge a solution at approximately 120mm displacement.

7.3.5 Suitability of the Implicit Finite Element Method for Large Displacements

In general, attempting to capture and model highly non-linear material behaviour using an implicit finite element code could be seen as a futile exercise. The nature of the technique is such that if failure is predicted and large displacement is expected, the step size of each iteration, which has to be small enough to allow the solution to converge, could potentially result in a numerically uneconomical solution.

Results from this work have shown that this assumption does not necessarily hold true for all situations. The progressive nature of the shear damage model allows the technique to work effectively in certain cases, producing stable results for the $+45^\circ/-45^\circ$ Phase 1 side intrusion beam simulation. For components where damage is predominantly in the fibre direction the model is less effective. Although it is based on observed phenomena, the failure model causes instability, by reducing elastic

constants to levels where a solution cannot be converged satisfactorily in the specified step.

7.4 Explicit Finite Element Damage Modelling

In the second part of the numerical modelling research work presented, the degenerate bi-phase damage model implemented in a commercial finite element analysis code was investigated. This model, as discussed in Chapter 2, has been used with a certain degree of success to model thermoset matrix composites with various fibre reinforcements, but little work has been published on its use to predict the behaviour of thermoplastic matrix composites.

The aim of the work was to calibrate and validate a model for polypropylene Twintex, with the in-plane damaging behaviours observed in simple tests and to then use this calibrated model for the analysis of more complex geometries.

7.4.1 The Treatment of Fibre Direction and Shear Damage

Unlike the previous numerical modelling work, the calibration of this model was limited to the parameters and material law available in the PAM-CRASH code. For this reason, the model was calibrated to offer a general representation of the material behaviour and does not appear to show as good an agreement with experiment for the coupon tests as the implicit damage model developed by the author.

This however, it is shown, does not necessarily compromise the ability of the model when considering more complex geometries.

7.4.2 Accuracy of Fibre Direction Damaging Behaviour

The nature of the bi-linear damage law and relation between damage and elastic constant degradation lead to a characteristic, curved response, from a simulation of the tensile test for a $0^\circ/90^\circ$ specimen. Although this is not an exact representation of the linear-elastic and then catastrophically damaging behaviour observed during test, the energy to failure is similar for both curves. During the calibration of the model, it was not possible to achieve a 'better fit' for this simulation.

For the $0^\circ/90^\circ$ compressive test simulation, the linear behaviour up to the point of major failure is captured accurately. It is however noted that in the simulation, the specimen is predicted to carry load up until failure at 3% strain. It is difficult to confirm this behaviour against test, since the stress/strain data available is up till the point at which the strain gauge became detached and not ultimate failure in the specimen.

The tensile $0^\circ/90^\circ$ specimen with a hole stress concentration also shows an interesting result. Here, at approximately 1% strain, when the first damage is identified in the specimen, catastrophic failure occurs rapidly. This is due to load redistribution across the central section of the specimen as damage accumulates around the hole. The nature of the damage model, with an initial damage point marking the start of a progressive failure behaviour, is such that this type of simulation, for a specimen with a hole will always yield a similar result, with catastrophic failure occurring soon after damage initiation. In more complex geometries, where load redistribution is possible without catastrophic consequences, this type of behaviour is not of great concern.

7.4.3 Accuracy of Shear Damaging Behaviour

The shear damaging response of the material model was more difficult to calibrate accurately, since any variation in the damage parameters to obtain an accurate shear damage behaviour, had repercussions in terms of the response of the fibre direction damage model. It was also very difficult, regardless of the parameters selected, to calibrate the model to remain stable at higher strain levels. In fact after an extensive calibration simulation programme the final set of parameters selected were chosen primarily based on the fibre direction damage.

This difficulty in calibrating the degenerate bi-phase model to accurately capture shear damaging behaviour, especially for woven fabric reinforced composites, has been discussed by McCarthy and Wiggeraad [113]. The phenomenon which has previously been observed for thermoset matrix composites was expected and seen to be more pronounced for thermoplastic composites where the matrix is tougher and displays a more ductile behaviour during deformation.

Since the behaviour of the $+45^\circ/-45^\circ$ tensile test simulation was compromised due to the calibration of the model, it was expected that a similar result would be observed for the off-axis compression test. This was the case, with the same, over stiff response, and premature ultimate failure.

The combination of this inaccuracy in the modelling of shear damage and the instability of the test simulations with a stress concentration, yielded poor agreement with the results for the off axis tensile and compressive test with a stress concentration. Again, this phenomenon was both expected and unavoidable due to the nature of the model and the tests.

7.4.4 Sensitivity to Calibration Parameters

During the calibration phase of the model, as previously discussed, it was the objective of the work to develop and propose a calibration scheme, which accurately captured the full range of in-plane damage modes for Twintex. During the study, it became apparent that this would not be fully achievable. Eventually a calibration scheme was developed to primarily reflect the fibre direction damage of the composite, whilst remaining stable during shear damage, since it was felt that in a structural component, the fibre direction damage behaviour would be dominant.

The sensitivity analysis presented shows the effect of variation in the various parameters, for the simulation of the $0^\circ/90^\circ$ and $+45^\circ/-45^\circ$ tensile test. It was shown in this part of the work that there was little possibility for the model to accurately capture shear behaviour without significantly compromising the fibre direction behaviour, as the $0^\circ/90^\circ$ simulation result is clearly more sensitive to the variation of damage parameters.

7.4.5 Application of the Explicit Damage Model to a Complex Component

Although the model had been shown to be truly accurate only for coupon simulations with predominantly fibre direction damage, the calibrated model was used to simulate all the 1:1 balanced twill weave demonstrator components tested. This included beams with $0^\circ/90^\circ$ and with $+45^\circ/-45^\circ$ fibre architectures.

The results from the Phase 1 demonstrator component showed excellent agreement for the $0^\circ/90^\circ$ beams, both in the small-scale and large-scale 3-point flexure tests. In the large-scale test simulations, the prediction of the first critical damaging event and subsequent load drop and reloading behaviour closely matched the experimental result. The predicted damage zones also match closely, suggesting that the model is highly applicable to damaging situations of this type. The $+45^\circ/-45^\circ$ beam simulations, as expected, do not show as good agreement with experimental test. In this case, the predicted behaviour is over stiff with subsequent damage resulting in a drop in load carrying capacity. This is a similar effect to that seen in the coupon test simulations and is due to the model not capturing the shear damaging behaviour of the composite correctly. It was therefore concluded from this part of the demonstrator component programme that the predictive simulation of shear damage development in a component was not accurate using the current calibration of the model.

For the Phase 2 demonstrator component, where the model was being used fully predictively, the simulation results for the $0^\circ/90^\circ$ beams, again showed good agreement with test. The 6mm beam analysis did however highlight that the test had provided results which were uncharacteristically poor in terms of bending stiffness. The $+45^\circ/-45^\circ$ beam simulations in this phase of the demonstrator work, again showed poor correlation with test, as expected.

In general, the model, which was calibrated primarily for fibre direction damage behaviour, performed well. In the second phase of the demonstrator component programme, the model was used fully predictively and yielded acceptable results.

7.4.6 Applicability of Damage Model to Thermoplastics

The degenerate bi-phase model has been shown to be applicable to thermoplastic matrix composites, but with certain limitations, which have been highlighted by this work. The damage model is not particularly suitable for woven fabric reinforced composites, especially with ductile matrix materials, which was highlighted during the calibration, validation and demonstrator component simulations.

In summary, during the calibration of the damage parameters it had been shown that capturing shear and fibre direction damage with a single range of parameters was not

possible for Twintex, due to the woven fabric reinforcement and the ductile matrix. This was confirmed by the demonstrator component simulations. The discrepancy between test and analysis for the $+45^{\circ}/-45^{\circ}$ beams was however not as great as initially expected. This suggests that if the limitations of the technique are considered and it is used in situations where damage is predominantly in the fibre direction, there is potential to use the model as a predictive design tool.

7.4.7 Suitability of the Explicit Finite Element Method for Large Displacements

Although the damage model was implemented in a commercial code and the user had no specific control over the numerical treatment of the damage development in the composite, the method yielded interesting and in certain cases, successful results. In particular, when considering a complex component, the explicit finite element technique was clearly far more suited to dealing with damage and material non-linearity than the previous implicit finite element damage modelling work.

7.5 Application of Thermoplastic Composites to Crashworthy Automotive Structures

Polypropylene matrix based composite materials have previously been used successfully in semi-structural automotive applications. The demonstrator component programme undertaken during this study has shown that they also have the potential to be used in fully crashworthy applications. A glass reinforced polypropylene composite side intrusion beam has been shown to offer a similar level of performance to that of a current steel beam design. There is a potential weight penalty if the composite beam is used as a direct replacement for a current steel component, but if the beam is considered as part of a structural thermoplastic composite door module it may become a viable alternative. Typically, the masses of the Phase 2 demonstrator beams tested ranged from 2.1kg to 4.3kg, with the final vehicle test performed on an 8mm thick, 4.2kg beam. This is a significant weight penalty when directly comparing the composite beam to the 1.9kg steel beam from the target vehicle, even when considering that the geometry and lay-up of the composite design had not been fully optimised.

7.5.1 Industrial Processing Techniques for Thermoplastic Composite

Various authors have presented idealised processing parameters for thermoplastic composite materials, to give optimum material properties and produce mouldings of the highest quality. This can be achieved through careful control of preheat time and temperature, transfer time, moulding pressure, tool temperature and consolidation time. These idealised parameters may be more difficult to achieve in an industrial process. During most of the moulding that was undertaken for this work, a semi-automated procedure was used, where pre-heat was controlled using an industrial oven, measuring material surface temperature and the press closure cycle was automated.

Slight over prediction of strength and stiffness, during the modelling of the demonstrator components could be explained by these parts having a marginally poorer moulding quality than the laboratory manufactured test specimens, used for material model calibration. This is reinforced when considering the quality of moulded specimens using optical microscopy. Typically the void content observed in the 1:1 Twintex beams, manufactured for the Phase 1 demonstrator component programme, ranged from 1.8% to 6.8% across the section of the beam [121], which compares to 2% observed in 1:1 Twintex plaques manufactured using a laboratory scale process [27]. It is also noted that the 3D Twintex beams, which consistently showed higher performance when compared to 1:1 Twintex beams, also had the lowest void content, with a range of between 0.5% and 4.5% across a typical beam [121]. It is likely that this is due to the two stage moulding technique applied to the 3D Twintex, where an extra pre-consolidation of the fabric was included prior to final moulding. This was not required for either the 1:1 or 4:1 Twintex beams, as the material blanks were supplied pre-consolidated.

The development of tooling including a combined sprung blankholder and shear edge was novel in terms of industrial application. This technical innovation allows variable thickness co-moulding of fabrics and flowing thermoplastic composites, for example Twintex and GMT. Although shown to work on a laboratory scale, the technology had not been industrialised until the development of the Phase 1 demonstrator component tooling. The technique was implemented successfully, with a number of mouldings being produced, although the work did highlight the need for tool

temperature to be considered, since heating of the tool during moulding caused interference issues with the sprung shear edge. The blankholder had no such problems and produced reliable results. Fabric wrinkling was not seen in any of the components manufactured, in part due to the geometry of the component, but potentially also due to the tension in the fibres during forming, applied by the blankholder.

7.5.2 The Effect of Process Variability

The only demonstrator component where manufacturing issues potentially compromised performance was the 6mm Phase 2 demonstrator component. Test results showed that the beam was significantly less stiff than expected, when tested in 3-point bending. After investigation of various potential explanations, the preheating technique was identified as the cause. Both the 4mm thick beam and the 8mm thick beam were manufactured from stacks of blanks preheated in units of four, containing four 1mm thick layers of Twintex (one for the 4mm beam and two for the 8mm beam). The 6mm beam was manufactured from a single stack of six 1mm layers, preheated using the same technique as for the 4mm and 8mm beam. The measurement of surface temperature both on the top and bottom of the stack meant that the internal temperature had to be assumed to be high enough for moulding. The results for the 4mm and 8mm beams show that this was the case, but the result from the 6mm beams suggest otherwise. The 6mm beams were moulded with a lower temperature in the middle of the stack and therefore significantly underperformed.

It would be essential that if the process were to be industrialised, thorough moulding trials were undertaken to optimise the processing parameters for each thickness of beam. This would reduce variability and could also increase the performance of all the beam geometries and thicknesses developed.

7.5.3 The Need for Part Integration

Thermoplastic composite components with polypropylene matrix materials, due to their cost and mechanical properties need to be carefully designed to achieve maximum benefit. This work has shown that, in principle, the concept of a crashworthy Twintex part is a valid one, when considering performance alone. This however is not the only criteria which an automotive manufacturer uses to assess candidate materials. Composites, and in particular, 'non-exotic' composites, need to

display a range of advantages before they are considered. One such advantage, touched upon only briefly during this study and in general outside of the scope of the research, is part integration.

Polypropylene is available in a range of forms, from the basic polymer through to aligned fibre reinforced structural composite materials. These can all potentially be combined in a single part and manufactured in a single moulding process. This is therefore the area where not only the research engineer, but also the commercial engineer, see their objectives converging. The potential to mould, in a single 'shot', a pre-coloured door module, with trim, outer skin, inner structural reinforcement, crashworthiness and lifetime corrosion resistance built in, is an attractive concept. This is especially true since the biggest hurdle, that of matching the structural performance of current steel designs, has been shown to be achievable in a relatively short timescale and with relatively low investment in tooling and development costs.

7.6 Recommendations for Future Work

This research has covered a wide range of topics, including processing, modelling and industrial component manufacture and design. It is proposed that the following areas of further work be considered. Some of the proposals are minor changes to method or approach, which have been highlighted when considering this work as a whole, whilst others are suggestions of larger units of research, which could be undertaken to further the knowledge and understanding of thermoplastic composites.

7.6.1 Inclusion of Residual load Carrying Capacity in the Implicit Model

Having assessed the results from the implicit finite element damage modelling work, it is suggested that a residual strength be implemented in the model, in an attempt to resolve stability issues associated with fibre direction damage in complex components.

7.6.2 Implementation of the Implicit Damage Model in an Explicit Code

The implicit finite element damage model developed has been shown to account for the predominant in-plane damage modes observed in Twintex and could therefore potentially be implemented in an explicit finite element code. An explicit code could

deal with non-linearity and large displacement more effectively than the implicit solution could, potentially allowing the model to be developed and improved.

7.6.3 Assessment of Alternative damage Models

The field of material modelling, in particular using explicit finite element codes, is constantly evolving. It is therefore suggested that new models, becoming available specifically for the characterisation of fabric composites, should be investigated. Potentially these could be more suitable for composite materials with woven glass fibre reinforcement, such as Twintex.

7.6.4 Assessment of Relevance of Delamination as a Damage Mechanism

It is felt that neglecting delamination as a damaging mode in thermoplastics, could lead to incorrect prediction of performance. Although potentially not as critical for thermoplastic matrix composites as it is for thermoset matrix composites the phenomenon should be investigated, to confirm the validity of the current approach.

7.6.5 Rate Dependency

If Twintex is to be used in fully crashworthy structures, the material rate dependency must be assessed. This was beyond the scope of the current work and not included in the material models developed and investigated.

7.6.6 Development of a Fully Thermoplastic Door Concept

In terms of the industrial continuation of this work, it is felt that the next step is the development of a fully thermoplastic door concept. The component parts, and in particular the crashworthy structure, have been shown to work effectively. Therefore the logical conclusion would be prototype development leading to maturity of the technology into commercial applications.

7.7 Conclusions

Initially after a review of current literature, three areas were identified as requiring further work. These have been investigated and the following conclusions are drawn.

Implicit finite element damage modelling techniques can be developed to account for the damage and failure modes observed in a woven glass fibre reinforced polypropylene composite. The de-coupling of shear and fibre direction damage can result in a model that is applicable to a range of test scenarios. This approach can be used as a design tool for more complex components, but is limited when considering high levels of material non-linearity and damage development, due to the stability of the implicit finite element method.

Current explicit finite element damage modelling techniques and in particular the bi-phase material model, implemented in PAM-CRASH, are applicable to aligned glass fibre reinforced polypropylene composite materials, but with significant limitations, especially when considering shear damaging behaviour. The application of this model to a complex geometry has shown that the bi-phase model can be calibrated and validated as a design tool for thermoplastic composite components, but only if considering damage development that occurs predominantly in the fibre direction.

Finally, it is concluded that aligned glass fibre reinforced polypropylene composite materials are suitable for structural automotive applications, such as side impact protection and perform to a similar standard as steel components. If the weight penalty observed at a component level is overcome by modularisation then this technology could potentially be used commercially in crashworthy automotive applications.

Chapter 8 References

- [1] Harrison, A., "Driving Composites - Weighting For Improved Vehicle Fuel Economy", *5th International Conference on Automated Composites - ICAC '97*, Glasgow, September 4-5, 1997, pp. 3-12.
- [2] Jambor, A. and Beyer, M., "New Cars - New Materials", *Materials & Design*, Vol. 18 (4/6), 1997, pp. 203-209.
- [3] McConnell, V. P. "Robust Growth Predictions Outlined at SAE 2000", *Reinforced Plastics*, May, 2000, pp. 34-38.
- [4] Quadrant Plastic Composites AG (Formerly Symalit AG) "Thermoplastic Composites for Your Car as Well", <http://www.quadrantcomposites.com/English/idqpc102.asp>, Lenzburg, 2003.
- [5] Saint-Gobain Vetrotex, "Twindex Markets and Applications - Transportation", http://www.twintex.com/markets_app/tw_trans.html, France, 2003.
- [6] Cole, G. S. and Sherman, A. M., "Lightweight Materials for Automotive Applications", *International Metallographic Society Symposium on 'Microstructural Characterization of Lightweight Materials for Transportation'*, Montreal, July 24-25, 1994, pp. 3-9.
- [7] Svensson, N., Shishoo, R. and Gilchrist, M., "Manufacturing of Thermoplastic Composites from Commingled Yarns - A Review", *Journal of Thermoplastic Composite Materials*, Vol. 11, 1998, pp.22-56.
- [8] Ye, L., Friedrich, K. and Kastel, J., "Consolidation of GF/PP Commingled Yarn Composites", *Applied Composite Materials*, Vol 1, 1995, pp. 415-429.

- [9] Klinkmuller, V., Um, M., Friedrich, K. and Kim, B., “Impregnation and Consolidation of Different GF/PP Co-mingled Yarn”, *Tenth International Conference on Composite Materials*, Whistler, Vol. 3, 1995, pp. 397-403.
- [10] Klinkmuller, V., Um, M. K., Steffens, M., Friedrich, K. and Kim, B. S., “A New Model for Impregnation Mechanics in Different GF/PP Commingled Yarns”, *Applied Composite Materials*, Vol. 1, 1995, pp. 351-371.
- [11] Wakeman, M., Cain, T., Rudd, C. D., Brooks, R. and Long, A. C., “Compression Moulding of Glass and Polypropylene Composites for Optimised Macro- and Micro-Mechanical Properties - 1 Commingled Glass and Polypropylene”, *Composites Science and Technology*, Vol 58, 1998, pp. 1879-1898.
- [12] Wakeman, M., “Non-Isothermal Compression Moulding of Glass Fibre Reinforced Polypropylene Composites”, Ph.D. Thesis, University of Nottingham, UK, 1997.
- [13] Osten, S., St. John, C., Guillon, D., Zanella, G. and Renault, T., “Compression Molding of Twintex and Random Fiber Thermoplastic Molding Materials”, *ANTEC '97*, The Annual Technical Conference of the Society of Plastics Engineers, Toronto, 1997, pp. 2432-2436.
- [14] Bruer, U. and Neitzel, M. “High Speed Stamp Forming of Thermoplastic Composite Sheets”, *Polymers and Polymer Composites*, Vol. 4, No. 2, 1996, pp 117-123.
- [15] Curtis, C., “Energy Absorbtion and Crush Behaviour of Composite Tubes”, Ph.D. Thesis, University of Nottingham, UK, 2000.
- [16] Lourenço, N. S. F., “Predictive Finite Element Method for Axial Crush of Composite Tubes”, Ph.D. Thesis, University of Nottingham, UK, 2002.
- [17] Saint-Gobain Vetrotex, “Physical Properties for FEA Modelling - TPEAT4460K”, www.twintex.com/matprop/tw_physical.html, France, 2003.

- [18] Saint-Gobain Vetrotex, "Data Base for 2-D Woven fabrics - DCC1", France, 1998.
- [19] Pierron, F. and Vautrin, A., "Accurate Comparative Determination of the In-Plane Shear Modulus of T300/914 by the Iosipescu and 45° Off-Axis Tests", Composites Science and Technology, Vol. 52, 1994, pp. 61-72.
- [20] Synamit AG, "GMT Data Sheet", Personal Communication, 1998.
- [21] Borealis A/S, "PLYTRON GN638T Unidirectional Glass-Fibre/Polypropylene Composite, Physical Properties", Denmark, 1997.
- [22] Gibson, R. F., "Principles of Composite Material Mechanics", McGraw Hill Inc., 1994.
- [23] Hull, D. and Cline, T. W., "An Introduction to Composite Materials", 2nd Edition, Cambridge University Press, 1996.
- [24] Cantwell, W. J. and Morton, J., "The Impact Resistance of Composite Materials - A Review", Composites, Vol. 22, No. 5, 1991, pp. 347-362.
- [25] Srinivasan, K., Jackson, W. C., Smith, B. T. and Hinkley, J. A., "Characterization of Damage modes in Impacted Thermoset and Thermoplastic Composites", Journal of Reinforced Plastics and Composites, Vol. 11, October 1992, pp. 1111-1126.
- [26] Jouri, W. S. and Shortall, J. B., "Impact Testing of Long Fibre reinforced Thermoplastic Composites", Journal of Thermoplastic Composite Materials, Vol. 4, July 1991, pp. 206-226.
- [27] Santulli, C., Brooks, R., Long, A. C., Warrior, N. A. and Rudd, C. D., "Impact Properties of Compression Moulded Commingled E-glass-Polypropylene Composites", Plastics, Rubber and Composites, Vol. 31, No. 6, 2002, pp. 270-277.

- [28] Ramakrishna, S. and Hamada, H., “Energy Absorption Characteristics of Crash Worthy Structural Composites”, *Key Engineering Materials*, Vols. 141-143, 1998, pp. 585-620.
- [29] Sabic Europe, “BMW Mini Front End Carrier”, StaMax Commercial Application Datasheet, Dec, 2001.
- [30] Anon, “Mini Cooper has StaMax Front-End Carrier”, <http://www.sae.org/automag/material/12-2001/>, Dec, 2001.
- [31] Anon, “OC Showcases SUV Applications at SAE 2003”, http://www.reinforcedplastics.com/WZ/RPlastics/market_focus/automotive/000017/show/, 2003.
- [32] Sabic Europe, “Ford Fiesta Door Modules”, StaMax Commercial Application Datasheet, Dec, 2001.
- [33] Bricout, A., “Composite materials: Performance of Twintex for Automotive Weight Saving”, www.twintex.com, 1998.
- [34] Hexcel Composites, “TowFlex Fabric Products Provide Performance and Manufacturing Benefits for BMW M3 Bumper Beams”, TowFlex thermoplastics – Applications, <http://www.hexcelcomposites.com/Markets/Products/Thermoplastics/Applications/Bumper>, 2001.
- [35] Anon, “Hexcel Thermoplastic TowFlex featured in BMW M3 Bumper”, <http://composite.miningco.com/library/PR/2001/blhexcel21.htm>, 2001.
- [36] Warrior, N., “Polymer Composites for Automotive Crashworthiness”, *Automotive Composites*, Warwick University IMC, Coventry, June 10, 2003.
- [37] Pitrof, S. M. and Merrifield, R. A., “Engineering Development of a Composite Cross Car Beam”, SAE Technical Paper 970727, 1997.

- [38] Manwaring, D., Chan, A. and Marks, M., "A Structural Instrument Panel from Glass-Mat thermoplastic for the Small-Car Market ", SAE Technical Paper 970726, 1997.
- [39] Anon, "Plastic/Metal Hybrid Composite technology IP Support Beam", Bayer Corporation, CLN Case Study, <http://www.lightspeed.com/csstudies/links/ipbeam.html>, 2000.
- [40] Anon, "Composite B-Post Passes the Test", European Automotive Design, March 199, pp 11.
- [41] Sherman, K. C. and Florence, R., "Design and Development of an Engineering Thermoplastic Energy Absorbing System for Automotive Knee Bolsters ", SAE Technical Paper 970725, 1997.
- [42] Davis, R., Ford Motor Company, Personal Communication, 24 Feb 1999.
- [43] European Commission, "ELV - End of Life Vehicle Directive", Proposal COM(97)358 amended COM(99)1761997, <http://europa.eu.int/comm/environment/docum/index.html>.
- [44] EURO NCAP, "EURO NCAP Side Impact - How the Tests are Done", <http://www.euroncap.com/tests.htm>, 2003.
- [45] National Highway Traffic Safety Administration, "Federal Motor Vehicle Safety Standard (49 CFR Part 571) MVSS214 Side Impact Protection", Federal Register, Vol. 58, No. 225, Issue 3, December 1995.
- [46] Lie, A. and Tingvall, C., "How Does Euro NCAP Results Correlate to real Life Injury Risks - A Paired Comparison Study of Car-to-Car Crashes", *IRCOBI, International Conference on the Biomechanics of Impact*, Montpellier, France, Sept 20, 2000.

- [47] Kahane, C., "An Evaluation of Side Structure Improvements in Response to Federal Motor Vehicle Safety Standard 214", NHTSA Report Number DOT HS 806 314, Nov 1982.
- [48] Ray, M. H., "Impact Conditions in Side-Impact Collisions with Fixed Roadside Objects", Accident Analysis and Prevention, Vol. 31, 1999, pp. 21-30.
- [49] Miltner, E. and Salwender, H. J., "Injury Severity of Restrained Front Seat Occupants in Car-to-Car Side Impacts", Accident Analysis and Prevention, Vol. 27, No. 1, 1995, pp. 105-110.
- [50] Farmer, C. M., Braver, E. R. and Mitter, E. L., "Two-Vehicle Side Impact Crashes: The Relationship of Vehicle and Crash Characteristics to Injury Severity", Accident Analysis and Prevention, Vol. 29, No. 3, 1997, pp. 399-406.
- [51] Mizuno, K. and Kajzer, J., "Compatibility Problems in Frontal, Side, Single Car Collisions and Car-to-Pedestrian Accidents in Japan", Accident Analysis and Prevention, Vol. 31, 1999, pp. 381-391.
- [52] Uduma, K., "Innovations in Auto Safety design, a Key to Quality Improvement", Technological Forecasting and Social Change, Vol. 64, 2000, pp. 197-208.
- [53] Koehr, R., "ULSAC - Lightweight Steel Automotive Closures", AutoTechnology, Vol. 1, 2001, pp. 74-77.
- [54] Cheon, S. K., Lee, D. G. and Jeong, K. S., "Composite Side-Door Impact Beams for Passenger Cars", Composite Structures, Vol. 38, No. 1-4, 1997, pp. 229-239.
- [55] Kamil, R. and Saunders, E., "Side Impact Beam Design", MAE226 - Mechanics of Composite Materials, Project Report, 2000, http://spline.mae.wvu.edu/Courses...6/projects_S96/ERIC/sidebeam.html.

- [56] Adam, H., Patberg, L., Philipps, M. and Dittmann, R., "Testing of New composite Side Door Concepts", SAE Special Publications, 980859, Vol. 1320, Feb 1998, pp. 23-30.
- [57] Erzen, S., Ren, Z. and Anzel, I., "Analysis of FRP Side-Door Impact Beam", Faculty of Mechanical Engineering, University of Maribor, Slovenia, 2002, http://www.sussex.ac.uk/automotive/tut2002/15_erzen.pdf.
- [58] Clemo, K., "SACTAC Project: Door Beam Design Sub-group, Progress Reports 1-5", MIRA/University of Nottingham, Dec 1996-Jan 1998.
- [59] Clemo, K. and Price, C., "Developing Composite Material Side-Impact Beams", MIRA New Technology, 2000, pp. 184-190.
- [60] Priston, A-M., "Evaluation of Stress Induced Damage in Composite Material", PhD Thesis, Nottingham Trent University, UK, 1997.
- [61] Cheikh, M., "Reanalysis of Structures with Modification of the Stiffness, Application to the Modelling of Damage in Unidirectional Composites", Composites and Structures, Vol. 78, 2000, pp. 725-736.
- [62] Belingardi, G., Gugliotta, A. and Vadori, R., "Numerical Simulation of fragmentation of Composite Material Plates due to Impact" International journal of Impact Engineering, Vol. 21, No. 5, 1998, pp. 335-347.
- [63] Feng, Z.-N., Allen, H. G. and Moy, S. S. J., "Theoretical and Experimental Investigation of Progressive Failure of Woven Composite Panels", Journal of Composite Materials, Vol. 33, No. 11, 1999, pp. 1030-1047.
- [64] Gamble, K., Pilling, M. and Wilson, A., "An Automated Finite Element Analysis of the Initiation and Growth of Damage in Carbon Fibre Composite Materials", Composite Structures, Vol. 32, 1995, pp. 265-274.

- [65] Tan, S. C. and Perez, J., “Progressive Failure of Laminated Composites with a Hole Under Compressive Loading”, *Journal of Reinforced Plastics and Composites*, Vol. 12, 1993, pp. 1043-1056.
- [66] Padhi, G. S., Sheno, R. A., Moy, S. S. J. and Hawkins, G. L., “Progressive Failure and Ultimate Collapse of Laminated Composite Plates in Bending”, *Composite Structures*, Vol. 40, Nos. 3-4, 1998, pp. 277-291.
- [67] Ozden, O. O. and Engblom, J. J., “Analysis of Progressive Failure in Composites”, *Composites Science and Technology*, Vol. 28, 1987, pp. 87-102.
- [68] Chang, F. and Chang, K., “A Progressive Damage Model for Laminated Composites Containing Stress Concentrations”, *Journal of Composite Materials*, Vol. 21, Sept 1987, pp. 834-855.
- [69] Chow, C. L. and Yang, F., “Inelastic Finite Element Analysis of Fibre-Reinforced Composite Laminates with Damage”, *Proceedings of the IMechE*, Vol. 212, Part C, pp. 717-729.
- [70] Williams, K. V., Floyd, A. M., Vasiri, R. and Poursartip, A., “Numerical Simulation of In-Plane Damage Progression in Laminated Composite Plates”, *12th International Conference on Composite Materials - ICCM 12, Paris, 1999*.
- [71] Vang, L., Baubakar, M. L., Trivaudey, F. and Perreux, D., “Coupled Damage Elasto-Dissipative Models for Numerical Analysis of Laminate Shells”, *13th International Conference on Composite Materials - ICCM 13, Beijing, 2000*.
- [72] Oytana, C., “Damage Indicators – Part I” *Mechanics and Mechanisms of damage in Composites and Multi-Materials*, ESES11 (Edited by D. Baptiste), 1991, Mechanical Engineering Publications, London, pp. 215-232.

- [73] Coats, T. W., Harris, C. E., Lo, D. C. and Allen, D. H., "Progressive damage Analysis of Laminated Composite (PDALC) - (A Computational Model Implemented in the NASA COMET Finite Element Code) Version 2.0", NASA Technical Report NASA/TM-1998-208718, 1998.
- [74] Coats, T. W. and Harris, C. E., "A Damage-Dependant Finite Element Analysis for Fiber-Reinforced Composite Laminates", NASA Technical Paper, 1998.
- [75] Harris, C. E., Coats, T. W. and Glaessgen, E. H., "Experimental Verification of Computational Models for Laminated Composites", NASA Technical Paper, 1998.
- [76] Iannucci, L., "Failure Propagation Modelling Using Explicit Codes" *NAFEMS Awareness Seminar – Advances in Composites Analysis & Design*, London, 20th June 2001.
- [77] Iannucci, L. and Willows, M. J., "Progressive Failure Modelling of Woven Carbon Composites Under Impact", *Euromech 40, European Mechanics Society Colloquium*, Imperial College, London, 27-29 Sept 1999.
- [78] Iannucci, L., Dechaene, R., Willows, M. J. and Degrieck, J., "A Failure Model for the Analysis of Thin Woven Glass Composite Structures Under Impact Loadings", *Composites and Structures*, Vol. 79, 2001, pp. 785-799.
- [79] Chang, F. and Lessard, L. B., "Damage Tolerance of Laminated Composite Plates Containing an Open Hole and Subjected to Compressive Loadings: Part I - Analysis", *Journal of Composite Materials*, Vol. 25, Jan 1991, pp. 2-43.
- [80] Ladeveze, P., "On a Damage Mechanics Approach", *Mechanics and Mechanisms of damage in Composites and Multi-Materials*, ESES11 (Edited by D. Baptiste), 1991, Mechanical Engineering Publications, London, pp. 119-141.
- [81] E.S.I. Group, "PAM-CRASH/PAM-SAFE Solver Notes Manual, Version 1998", France, 1998.

- [82] Hahn, H. T. and Tsai, S. W., “Nonlinear Elastic Behaviour of Unidirectional Composite Laminates”, *Journal of Composite Materials*, Vol. 7, 1973, pp. 102-110.
- [83] Lessard, L. B. and Chang, F., “Damage Tolerance of Laminated Composite Plates Containing an Open Hole and Subjected to Compressive Loadings: Part II - Experiment”, *Journal of Composite Materials*, Vol. 25, Jan 1991, pp. 44-64.
- [84] Chang, K., Liu, S. and Chang, F., “Damage Tolerance of Laminated Composites Containing an Open Hole and Subjected to tensile Loadings”, *Journal of Composite Materials*, Vol. 25, March 1991, pp. 274-301.
- [85] Avalle, M., Belingardi, G. and Vadori, R., “Numerical Simulation of Impact Damage in Composite Material Structures”, *Impact and Dynamic Fracture of Polymers and composites, ESES19* (Edited by J. G. Williams and A. Pavan), 1995, Mechanical Engineering Publications, London, pp. 329-340.
- [86] Shahid, I. and Chang, F., “An Accumulative Damage Model for tensile and Shear Failure of Laminated Composite Plates”, *Journal of Composite Materials*, Vol. 29, No. 7, 1995, pp. 274-301.
- [87] Davila, C. G., Ambur, D. R. and McGowan, D. M., “Analytical Prediction of Damage Growth in Notched Composite Panels Loaded in Axial Compression”, Paper AIAA-99-1435, *40th AIAA/ASME/ASCE/AHS/ASC Structures, Structural Dynamics and Materials Conference*, St. Louis, April 12-15, 1999.
- [88] Hibbitt, Karlsson and Sorenson Inc. “ABAQUS Examples Manual”, USA, 1998.
- [89] Ladeveze, P., “A Damage Computational Method for Composite Structures”, *Computers and Structures*, Vol. 44, No. 1/2, 1992, pp. 79-87.
- [90] Ladeveze, P., “A Damage Computational Approach for Composites: Basic Aspects and Micromechanical Relations”, *Computational Mechanics*, Vol. 17, 1995, pp. 142-150.

- [91] Ladeveze, P. and le Dantec, E., "Damage Modelling of the Elementary Ply for Laminated Composites", *Composites Science and technology*, Vol. 43, 1992, pp. 257-267.
- [92] Allix, O., Daudeville, L. and Ladeveze, P., "Delamination and Damage Mechanics", *Mechanics and Mechanisms of damage in Composites and Multi-Materials*, ESES11 (Edited by D. Baptiste), 1991, Mechanical Engineering Publications, London, pp. 143-157.
- [93] Allix, O., Ladeveze, P. and Corigliano, A., "Damage Analysis of Interlaminar Fracture Specimens", *Composite Structures*, Vol. 31, 1995, pp. 61-74.
- [94] Allix, O., Guedra-Degeorges, D., Guinard, S. and Vinet, A., "3D Damage Analysis Applied to Low-Energy Impacts on Composite Laminates", *12th International Conference on Composite Materials - ICCM 12*, Paris, 1999.
- [95] Ladeveze, P., Allix, O., Deu, J. and Leveque, D., "A Mesomodel for Localisation and Damage Computation in Laminates", *Computer Methods in Applied Mechanics and Engineering*, Vol. 183, 2000, pp. 105-122.
- [96] Touchard, F., Lafarie-Frenot, M. C. and Guedra-Degeorges, D., "Mechanical Behaviour Characteristics of a Thermoplastic Composite Used in Structural Components", *Composites Science and Technology*, Vol. 56, 1996, pp. 785-791.
- [97] Coutellier, D. and Rozycki, P., "Multi-Layered Multi-Material Finite Element for crashworthiness Studies", *Composites: Part A*, Vol. 31, 2000, pp. 841-851.
- [98] Hochard, C., Auborg, P.-A. and Charles, J.-P., "Modelling of the Mechanical Behaviour of Woven-Fabric CFRP Laminates up to Failure", *Composites Science and technology*, Vol. 61, 2001, pp. 221-230.

- [99] Johnson, A. F. and Simon, J., “Modelling Fabric Reinforced Composites Under Impact Loads”, *Euromech 400, European Mechanics Society Colloquium*, Imperial College, London, 27-29 Sept 1999.
- [100] de Rouvray, A. and Haug, E., “Failure of Brittle and Composite Materials by Numerical Methods”, Chapter 7 in ‘Structural Failure’, Editor T. Wierzbicki, John Wiley & Sons, 1989.
- [101] de Rouvray, A., Haug, E. and Stavrinidis, C., “Composite material damage and fracture Models for Numerical Simulations in Support of Fracture Control”, *International Conference on ‘Spacecraft Structures and Mechanical testing’*, Noordwijk, April 24-26, 1991.
- [102] Pickett, A., Ruckert, J., Ulrich, D. and Haug, E., “Material damage Law Suitable for Crashworthiness Investigation of Random Fibre Composite Materials”, *XVIII International Finite Element Congress*, Baden-Baden, Nov 20-21, 1989.
- [103] de Rouvray, A., Dowlatyari, P. and Haug, E., “Validation of the PAMM-FISS/Bi-Phase Numerical Model for the Damage and Strength Prediction of LFRP Composite Laminates”, *Mechanics and Mechanisms of Damage in Composite and Multi-Materials*, ESIS11, Editor D. Baptiste, Mechanical Engineering Publications, London, 1991, pp. 183-202.
- [104] Haug, E. and de Rouvray, A., “Crash response of Composite Structures”, *3rd International Symposium on Structural Crashworthiness*, Liverpool, April 14-16, 1993, pp. 237-294.
- [105] Haug, E. and Jamjian, M., “Numerical Simulation of the Impact Resistance of Composite Structures”, Chapter 8 in ‘Analysis and Modelling of Composite Materials’, 1996.
- [106] Haug, E. and Jamjian, M., “Industrial Crashworthiness Simulation of Automotive Structures and Components Made of Continuous Fiber Reinforced Composite and Sandwich Assemblies”, *ESI SA Paper No. 94UL026*, France, 1994.

- [107] Haug, E., Watanabe, M. and Nakada, I., “Numerical Crashworthiness Simulation of Automotive Structures and Components Made of Continuous Fiber Reinforced Composite and Sandwich Assemblies”, *SAE International Congress and Exhibition*, Detroit, Feb, 1991.
- [108] Nakada, I. and Haug, E., “Numerical Simulation of Crash Behaviour of Composite Structures for Automotive Applications”, *Tech’Mat 92 - Euro-Japan Exchanges on Materials*, Paris, 1992.
- [109] Johnson, A. F., Kindervater, C. M., Kohlgruber, D. and Lutzenburger, M., “Predictive Methodologies for the Crashworthiness of Aircraft Structures”, *American helicopter Society 52nd Annual Forum*, Washington D.C., June 4-6, 1996.
- [110] Kohlgruber, D. and Kamoulakos, A., “Validation of Numerical Simulation of Composite Helicopter Sub-Floor Structures Under Crash Loading”, *American helicopter Society 54th Annual Forum*, Washington D.C., May 20-22, 1998.
- [111] Deletombe, E., Delsart, D., Kohlgruber, D. and Johnson, A. F., “Improvement of Numerical methods for Crash Analysis in Future Composite Aircraft design”, *Aerospace Science and Technology*, Vol. 4, 2000, pp. 189-199.
- [112] McCarthy, M. A., Harte, C. G., Wiggenraad, J. F. M., Michielsen A. L. P. J., Kohlgruber, D. and Kamoulakos, A., “Finite Element Modelling of Crash response of Composite Aerospace Sub-Floor structures”, *Computational Mechanics*, Vol. 26, 2000, pp. 250-258.
- [113] McCarthy, M. A. and Wiggenraad, J. F. M., “Numerical Investigation of a Crash Test of a Composite Helicopter Subfloor Structure”, *Composite Structures*, Vol. 51, 2000, pp. 345-359.
- [114] BS EN ISO 527-4, “Plastics - Determination of tensile properties - Part 4: Test conditions for isotropic and orthotropic fibre-reinforced composites”, 1997

[115] ASTM D 3410 – 75, “Standard Test Method for Compressive Properties of Oriented Fiber Composites”, 1975

[116] Wan, T. and Tham, L. “Data for Modelling the Impact of Automotive Laminates”, BEng Final Year Project Thesis, University of Nottingham, UK, 2002.

[117] Duckett, M. J., “Rate Dependent Effects on the Energy Absorption and Material Properties of Polymer Composites”, PhD Thesis, University of Nottingham, UK, October 2001.

[118] Hibbitt, Karlsson and Sorenson Inc. “ABAQUS/Standard User’s Manual - Volume I”, USA, 1998.

[119] Thomas, A. V., “SACTAC Project: Modular Door Cassette Design Sub-group, Progress Reports 1 & 2”, Jaguar Cars Limited, March 1996-June 1996.

[120] EN ISO 14129, “Fibre-reinforced Plastic Composites - Determination of In-plane Shear Stress/Shear Strain Response, Including the In-plane Shear Modulus and Strength, by the $\pm 45^\circ$ Tension Test Method”, 1997.

[121] Santulli, C., CRACTAC Project Progress Update, Internal Communication, University of Nottingham, 2000.

[122] Pickett, A., "Design and Manufacture of Textile Composites", Ed. A. C. Long, Ch. 8, Woodhead Publishing Ltd, (in press).

Appendix A ABAQUS/Standard User Defined Field

The following source code, adapted from a previously implemented algorithm [88], was used to implement the damage model proposed in Chapter 4 and calculate the field variables for an ABAQUS/Standard user defined material.

```
** -----
** USER-DEFINED FIELD
** -----
*USER SUBROUTINES
  SUBROUTINE USDFLD(FIELD, STATEV, PNEWDT, DIRECT, T, CELENT, TIME, DTIME,
  1 CMNAME, ORNAME, NFIELD, NSTATV, NOEL, NPT, LAYER, KSPT, KSTEP, KINC,
  2 NDI, NSHR)
  C
    INCLUDE 'ABA_PARAM.INC'
  C
  C SHEAR MODULUS AND DAMAGE PARAMETER
    PARAMETER(G12=1.04D3, ALPHA=1.4D-5)
  C
    CHARACTER*80 CMNAME, ORNAME
    CHARACTER*8 FLGRAY(15)
    DIMENSION FIELD(NFIELD), STATEV(NSTATV), DIRECT(3,3), T(3,3), TIME(2)
    DIMENSION ARRAY(15), JARRAY(15)
  C
  C INITIALIZE FAILURE FLAGS FROM STATEV.
    EFF = STATEV(1)
    EFS = STATEV(2)
    DAMAGE = STATEV(3)
  C
  C GET STRESSES FROM PREVIOUS INCREMENT
    CALL GETVRM('S', ARRAY, JARRAY, FLGRAY, JRCD)
    S11 = ARRAY(1)
    S22 = ARRAY(2)
    S12 = ARRAY(4)
  C
  C GET SHEAR STRAIN FROM PREVIOUS INCREMENT
    CALL GETVRM('E', ARRAY, JARRAY, FLGRAY, JRCD)
    E12 = ARRAY(4)
  C
  C SHEAR DAMAGE INDEX: = 0 IF NO STRAIN TO PREVENT DIVIDE BY ZERO
  C
    IF (E12.NE.0) THEN
      DAMAGE = (3.D0*ALPHA*G12*S12**2 - 2.D0*ALPHA*(S12**3)/E12) /
    & (1.D0 + 3.D0*ALPHA*G12*S12**2)
    ELSE
      DAMAGE = 0.D0
    ENDIF
  C
  C
  C PLY TENSILE/COMPRESSIVE FAILURE
  C
    IF (EFF .LT. 1.D0) THEN
      IF (S22 .LT. -137) THEN
        EFF=2
      END IF
      IF (S22 .GT. 279) THEN
        EFF=2
      END IF
      IF (S11 .LT. -137) THEN
        EFF=2
      END IF
      IF (S11 .GT. 279) THEN
        EFF=2
      END IF
      STATEV(1) = EFF
    ENDIF
  C
  C
```

```

C
C PLY ULTIMATE SHEAR FAILURE
C
  IF (EFS .LT. 1.D0) THEN
    IF (E12 .GT. 0.45) THEN
      EFS=2
    ELSE IF (E12 .LT. -0.45) THEN
      EFS=2
    ELSE
      EFS=0
    ENDIF
    STATEV(2) = EFS
  ENDIF

C
C UPDATE FIELD VARIABLES
C
FIELD(1) = 0.D0
FIELD(2) = 0.D0
IF (EFF .GT. 1.D0) FIELD(1) = 1.D0
IF (EFS .GT. 1.D0) FIELD(2) = 1.D0
FIELD(3) = DAMAGE
STATEV(3) = FIELD(3)

C
RETURN
END

```

Appendix B Derivation of Shear Damage Formulation

The shear damage model implemented in the ABAQUS/Standard user defined field given in Appendix A, was based on the model proposed by Chang and Lessard [79]. The algorithm used was adapted to improve stability during analysis. This adaptation was developed from a previous implementation of the model [88] and is included here for completeness.

The original form of the model,

$$\epsilon_{12} = \frac{\sigma_{12}}{G_{12}} + \alpha\sigma_{12}^3 \quad (\text{B.1})$$

can be rearranged to:

$$\epsilon_{12} = G_{12}^{-1}\sigma_{12} + \alpha\sigma_{12}^3 \quad (\text{B.2})$$

For an increment, i , the shear stress can then be expressed as a linear function of strain,

$$\epsilon_{12}^{(i+1)} = \left(G_{12}^{-1} + \alpha(\sigma_{12}^{(i)})^2 \right) \sigma_{12}^{(i+1)} \quad (\text{B.3})$$

which is inverted to:

$$\sigma_{12}^{(i+1)} = \left(\frac{G_{12}}{1 + \alpha G_{12} (\sigma_{12}^{(i)})^2} \right) \epsilon_{12}^{(i+1)} \quad (\text{B.4})$$

This gives an algorithm which will allow the definition of effective shear modulus over an increment, i .

This algorithm is not stable at higher strain levels [88]. This can be demonstrated by considering an increment where strain is constant, such that:

$$\epsilon_{12}^{(i+1)} = \epsilon_{12}^{(i)} = \epsilon_{12} \quad (\text{B.5})$$

If the stress at increment i is considered to have a small perturbation from the exact solution at that increment $\sigma_{12}^e{}^{(i)}$, then the solution at that increment is,

$$\sigma_{12}^{(i)} = \sigma_{12}^e{}^{(i)} + \Delta\sigma_{12}^{(i)} \quad (\text{B.6})$$

and similarly at an increment $i+1$ is:

$$\sigma_{12}^{(i+1)} = \sigma_{12}^{e(i+1)} + \Delta\sigma_{12}^{(i+1)} \quad (\text{B.7})$$

For the algorithm to be stable $\Delta\sigma_{12}^{(i+1)}$ should be no larger than $\Delta\sigma_{12}^{(i)}$.

The perturbation at $i+1$ is calculated by substituting $\sigma_{12}^{(i)}$ into equation B.4 and linearising about $\sigma_{12}^{e(i)}$:

$$\Delta\sigma_{12}^{(i+1)} = \frac{-2\alpha G_{12}^2 \sigma_{12} \varepsilon_{12}}{1 + \alpha G_{12} \sigma_{12}^2} \Delta\sigma_{12}^{(i)} \quad (\text{B.8})$$

where $\sigma_{12} = \sigma_{12}^{e(i)}$.

The perturbation at $i+1$ is larger than at i if:

$$2\alpha G_{12}^2 \sigma_{12} \varepsilon_{12} > (1 + \alpha G_{12} \sigma_{12}^2)^2 \quad (\text{B.9})$$

Eliminating ε_{12} from equation B.9 gives.

$$\alpha\sigma_{12}^3 > G_{12}^{-1}\sigma_{12} \quad (\text{B.10})$$

Instability occurs at strain levels where the non-linear part of the shear strain is larger than the linear part. This would significantly reduce the effectiveness of the algorithm in the current study.

To obtain a more stable algorithm the nonlinear stress/strain law is written including a coefficient β [88].

$$\varepsilon_{12} + \beta\sigma_{12}^3 = G_{12}^{-1}\sigma_{12} + (\alpha + \beta)\sigma_{12}^3 \quad (\text{B.11})$$

Equation B.11 can be linearised to the form,

$$\left(1 + \beta(\sigma_{12}^{(i)})^3 / \varepsilon_{12}^{(i)}\right) \varepsilon_{12}^{(i+1)} = \left(G_{12}^{-1} + (\alpha + \beta)(\sigma_{12}^{(i)})^2\right) \sigma_{12}^{(i+1)} \quad (\text{B.12})$$

which when inverted gives:

$$\sigma_{12}^{(i+1)} = \frac{1 + \beta(\sigma_{12}^{(i)})^3 / \epsilon_{12}^{(i)}}{1 + (\alpha + \beta)G_{12}(\sigma_{12}^{(i)})^2} G_{12} \epsilon_{12}^{(i+1)} \quad (\text{B.13})$$

Following the same procedure as the original algorithm it can be shown that a small perturbation $\Delta\sigma_{12}^{(i)}$ in increment i , is reduced to zero in $i+1$ if $\beta = 2\alpha$.

The stable algorithm can be expressed as:

$$\sigma_{12}^{(i+1)} = \frac{1 + 2\alpha(\sigma_{12}^{(i)})^3 / \epsilon_{12}^{(i)}}{1 + 3\alpha G_{12}(\sigma_{12}^{(i)})^2} G_{12} \epsilon_{12}^{(i+1)} \quad (\text{B.14})$$

which can be rearranged into the form:

$$\sigma_{12}^{(i+1)} = (1 - d_s) G_{12} \epsilon_{12}^{(i+1)} \quad (\text{B.15})$$

where the shear damage level d_s is defined as:

$$d_s = \frac{3\alpha G_{12}(\sigma_{12}^{(i)})^2 - 2\alpha(\sigma_{12}^{(i)})^3 / \epsilon_{12}^{(i)}}{1 + 3\alpha G_{12}(\sigma_{12}^{(i)})^2} \quad (\text{B.16})$$

It is in this form, in equation B.15, that the model is implemented in the user defined field FORTRAN subroutine.

Appendix C ABAQUS/Standard Material Cards

The following ABAQUS/Standard elastic laminate material control cards, with three field dependencies, were calibrated from experimental test data, for balanced weave, 60% weight fraction glass reinforced polypropylene Twintex.

```
**
** MATERIAL: NONLINEAR SHEAR WITH BUILT-IN EXPLICIT FAILURE
**
** FV1: PLY COMPRESSIVE/TENSILE FAILURE
** FV2: PLY SHEAR FAILURE
** FV3: SHEAR DAMAGE (NONLINEARITY) PRIOR TO FAILURE
** TOTAL OF 2^3 = 8 STATES
**
*MATERIAL, NAME=TWIN11
*ELASTIC, TYPE=LAMINA, DEPENDENCIES=3
12.17E3, 12.7E3, 0.08, 1.04E3, 1.52E3, 1.52E3, 0., 0., 0., 0.
1.00, 1.00, 0.00, 1.04E3, 1.52E3, 1.52E3, 0., 1, 0., 0.
12.17E3, 12.7E3, 0.00, 1, 1.52E3, 1.52E3, 0., 0., 1, 0.
1.00, 1.00, 0.00, 1, 1.52E3, 1.52E3, 0., 1, 1, 0.
12.17E3, 12.7E3, 0.08, 25, 1.52E3, 1.52E3, 0., 0., 0., 1
1.00, 1.00, 0.00, 25, 1.52E3, 1.52E3, 0., 1, 0., 1
12.17E3, 12.7E3, 0.00, 1, 1.52E3, 1.52E3, 0., 0., 1, 1
1.00, 1.00, 0.00, 1, 1.52E3, 1.52E3, 0., 1, 1, 1
*DEPVAR
3
**
```

Appendix D PAM-CRASH Material Cards

The following PAM-CRASH degenerate bi-phase material control cards were calibrated from experimental test data, for balanced weave, 60% weight fraction glass reinforced polypropylene Twintex.

```

$
$ MATERIAL DATA CARDS
$
$---5---10---5---20---5---30---5---40---5---50---5---60---5---70---5---80
MATER /          1      130          1.5e-06          1

Ply
  0          0          0.01          0.01          0.01          0.8333
  1  1  1  1  1  1  1  1  0  0  0  0  0  0  0  0
  0  0  0  0  0  0  0  0  0  0  0  0  0  0  0  0
  0  0  0  0  0  0  0  0  0  0  0  0  0  0  0  0
  0.800  40  0  0  0
  1  1  1  2  1  3  1  4  1  5  1  6  1  7  1  8
  1  9  1  10  1  11  1  12  1  13  1  14  1  15  0  0
  0  0  0  0  0  0  0  0  0  0  0  0  0  0  0  0
  0  0  0  0  0  0  0  0  0  0  0  0  0  0  0  0
  0  0  0  0  0  0  0  0  0  0  0  0  0  0  0  0
  0  0  0  0  0  0  0  0  0  0  0  0  0  0  0  0
$---5---10---5---20---5---30---5---40---5---50---5---60---5---70---5---80
PLY /          1      0          0      0
Twintex 1:1 0/90
  12.70  12.70  5.30
  1.040  1.520  1.520  0.080  0.080  0.360
  0.0053  0.017  0.039  0.25  0.9
  0  0  0  0  0
  0  0  0  0  0
  1  1  0  0  0  0  1  0  0  0.5
  11.40  11.40  5.30
  1.040  1.520  1.520  0.080  0.080  0.360
  0.0053  0.017  0.039  0.50  0.9
  0  0  0  0  0
  0  0  0  0  0  0  0
$

```

Appendix E CRACTAC Project Publications

[i] Rudd, C. D., Brooks, R., Long, A. C., Warrior, N. A., Wilson, M. J. and Santulli, C., “Development of a Crashworthy Composite Side Intrusion Beam Using Long Glass Fibre Reinforced Polypropylene for the Foresight Vehicle Programme”, *SAE2002*, Detroit, 2002.

[ii] Santulli, C., Brooks, R., Long, A. C., Warrior, N. A. and Rudd, C. D., “Impact Properties of Compression Moulded Commingled E-glass-Polypropylene Composites”, *Plastics, Rubber and Composites*, Vol. 31, No. 6, 2002, pp. 270-277.

[iii] Warrior, N. A., Rudd, C. D., Brooks, R., Long, A. C., Wilson, M. J. and Santulli, C., “Development Of A Thermoplastic Composite Side Intrusion Beam”, *Materials for Lean Weight Vehicles 4*, Motor Heritage Centre, Gaydon, October 30-31, 2001.

[iv] Warrior, N. A., Wilson, M. J., Brooks, R. and Rudd, C. D., “Modelling of Glass Reinforced Thermoplastic Composite Side Impact Structures”, *International Journal of Crashworthiness*, Vol. 6, No. 4, 2001.

[v] Santulli, C., Brooks, R., Long, A. C., Rudd, C. D., Wilson, M. J. and Warrior, N. A., “Impact Properties of Thermoplastic Laminates for Automotive Applications”, *Automotive Composites and Plastics ACP 2000*, Ford Motor Company, Dunton, 5-6 December, 2000.

[vi] Wilson, M. J., Warrior, N. A., Brooks, R. and Rudd C. D., “Post First-Ply Failure Modelling of Glass Reinforced Thermoplastic Composites”, *FRC 2000 - ‘Composites for the Millennium’*, Newcastle, September 13-15, 2000, pp. 505-511.

[vii] Warrior, N. A., Wilson, M. J., Brooks, R. and Rudd, C. D., “Modelling of Glass Reinforced Thermoplastic Composite Side Impact Structures”, *ICrash 2000*, London, September, 2000.